Quantification de l'évolution de glissements de terrain argileux par des techniques de télédétection. Application à la région du Trièves (Alpes Françaises)

Ulrich Kniess

UNIVERSITÉ DE GRENOBLE

THÈSE

Pour obtenir le grade de

DOCTEUR DE L'UNIVERSITÉ DE GRENOBLE

Spécialité : **Sciences de la Terre, de l'Univers et de l'Environnement**

Arrêté ministérial : 6 janvier 2005

Présentée par

Ulrich KNIESS

Thèse dirigée par **Denis Jongmans**
et codirigée par **Erwan Pathier et Stéphane Schwartz**

préparée au sein du **Institut des Sciences de la Terre**
dans **Terre, Univers, Environnement**

Quantification de l'évolution de glissements argileux par des techniques de télédétection. Application à la région du Trièves (Alpes Françaises occidentales)

Thèse soutenue publiquement le **24 octobre 2011**,
devant le jury composé de :

Christophe Basile
ISTerre, Grenoble, Président
Benoit Deffontaines
Université Paris-Est Marne-la-Vallée, Rapporteur
Michel Jaboyedoff
Université de Lausanne, Rapporteur
Jean-Philippe Malet
Institut de Physique du Globe de Strasbourg, Examinateur
Pascal Allemand
Université Claude Bernard, Lyon1, Examinateur
Denis Jongmans
ISTerre, Grenoble, Directeur de thèse
Erwan Pathier
ISTerre, Grenoble, Co-Directeur de thèse
Stéphane Schwartz
ISTerre, Grenoble, Co-Directeur de thèse

Abstract

Three remote sensing techniques, Lidar, satellite radar interferometry and aerial photogrammetry are applied to quantify the spatial and temporal evolution of two clayey landslides (Avignonet and Harmalière, located in the Trièves area, French Alps) in complement to in-situ instrumentations. A geomorphological analysis based on Lidar-derived filtered DEM, coupled to analysis of ortho-photos dating back to 1948 and geophysical investigations, shows that the different evolution of the neighbouring landslides could be partly controlled by the paleotopography of the bedrock underlying the clay layer. Directional roughness is shown to help distinguishing between landsliding and gully erosion patterns. Cross-correlation technique adapted to DEMs has been developed to derive 3D-displacement-vectors between two Lidar acquisitions (2006 and 2009), paying attention on measure quality assessment. The displacement map reveals that, at the Harmalière landslide, the main sliding channel, very active from 1981 - 2001, is now relatively slow (< 0.4 m over 3 years), in contrast with four surrounding distinct areas of large movements (up to 3 m) partly with rotational components. At the Avignonet landslide, displacements generally increase towards the toe (up to 1 m near the drainage outlets). Persistent Scatterers Interferometry technique allows to derive new reliable displacement-rates (1992 - 2000) at 16 points of the Avignonet landslide, consistent with GPS time-series. The long-term average headscarp retreat rates are estimated to 1 - 5 cm/y at Avignonet and 7 - 14cm/y at Harmalière. The retreat of the Avignonet landslide seems to be controlled by the erosion of the top of the underlying compacted alluvial layers. The presence of a paleovalley (Drac river) below the Harmalière toe could explain the difference of kinematics between the two landslides.

Résumé

Trois méthodes de télédétection (Lidar, interférométrie radar satellitaire et photogrammétrie aérienne) ont été appliquées pour quantifier les évolutions spatiales et temporelles de deux glissements argileux (Harmalière et Avignonet, situés dans la région du Trièves, Alpes françaises) en complément d'instrumentation in-situ. Une analyse géomorphologique a été réalisée à partir d'ortho-photos (depuis 1948) et du MNT Lidar filtré. Couplée à des reconnaissances géophysiques, elle a montré que la cinématique différente des deux glissements contigus était partiellement contrôlée par la paléotopographie sur laquelle s'est déposée la couche d'argile. La rugosité directionnelle a permis de distinguer les processus d'érosion résultant de mouvements gravitaires et de ravinement. Une technique de corrélation d'images adaptée aux MNT a été développée pour obtenir les vecteurs de déplacement 3D entre deux acquisitions Lidar (2006 - 2009), avec une attention particulière portée à l'évaluation de la qualité des mesures. La carte des déplacements obtenue montre que la zone la plus active du glissement de Harmalière entre 1981 et 2001 est maintenant relativement lente (déplacement < 0.4 m en 3 ans), contrairement à d'autres zones proches montrant des mouvements importants atteignant 3m avec une composante rotationnelle. Pour le glissement d'Avignonet, les déplacements déduits augmentent généralement vers le pied du glissement et peuvent atteindre 1 m. La technique des réflecteurs permanents en interférométrie radar a permis de déterminer de nouvelles valeurs de taux de déplacements (entre 1992 et 2000) en 16 points du glissement, qui sont cohérentes avec les données GPS existantes. Le taux moyen de recul à long terme de l'escarpement principal a été estimé à 1-5 cm/an à Avignonet et entre 7 et 14 cm/an à l'Harmalière. La régression du glissement d'Avignonet semble contrôlée par l'érosion du sommet de la couche d'alluvions compactes reposant sur le substratum. La présence d'une paleovallée du Drac sous le pied du glissement de l'Harmalière pourrait expliquer cette différence de cinématique entre les deux glissements.

Contents

List of Figures

List of Tables

Acknowledgements

After a long way through various landscapes, wide plains, high mountains, deep waters and dark forests, the journey is coming to an end.

I would like to thank my family, Nadja and Elisabeth, for their strong support, especially during long times of physical or mental absence.

Many people at different places very kindly helped me to navigate on the right path, explore new adventures and finding warm shelter. I am highly grateful to all of them:

At Grenoble, Denis Jongmans and Erwan Pathier for their endless efforts solving my hundreds of scientific, administrative and motivational issues. My dear fellows and friends Celine, Clara, Gideon and especially Mikael ("You gotta do what you gotta do!"). Thierry Villemin and Stéphane Schwartz for their help to get the Lidar data. Grégory for the nice collaboration. All the people from the Ecole Doctorale, the Lab-administration and computer department for their collaboration. Merci bien!

At Enschede, I would like to thank Cees can Westen for his scientific guiding and the organisation of my carefree stay. Many thanks also to the most helpful contributions from Enrique and Antonio. Dank je wel!

At Florence, many thanks for the warm welcome to Nicola Casagli and Veronica Tofani, the Rigini family for the nice accommodation, Francesca for the countless help when struggling with Gamma and all the other nice people of the Arcetri outpost. Mille Grazie!

And last but not least I would like to thank all the members of the Mountain Risks project which made this work possible, especially Jean-Philippe for the great coordination in general and all the other scientific leaders for the powerful workshops, meetings and fieldtrips. Special thanks also to Jacopo, Marjory, Melanie, Ping and all the other young fellows for the nice time we had together.

I also thank the European Space Agency for providing the SAR-data through the project CAT-1 6124.

CHAPTER 1

Introduction

A landslide evolution is characterised by spatial and temporal change at different scale. The efficient quantification of landslide evolutions is important, because landslides increasingly causing risks, among other natural hazards, to the modern society worldwide due to the increasing spatial demands by society and partly due to climate change (Kjekstad, 2007; Sidle and Ochiai, 2006). Landslides are slope movements of soil or rock controlled by gravity. Reliable numbers of the socio-economic impact from landslides are difficult to obtain on a global scale, because they are often caused by other natural hazards like floods and earthquakes. According to the EM-DAT database[1] about 17% of fatalities from natural disasters can be accounted for landslides(Sassa and Canuti, 2008). After a World Bank report (Dilley, 2005) are 3.7 million km^2 populated by 300 million people are exposed to landslide hazards and from that 820 000 km^2 with 66 million people within high risk areas. Petley (2008) reports for the year 2007 that 90% of the world wide landslide fatalities were due to precipitation triggered landslides, 3.4% due to construction, 1.8% due to mining, only 0.7% due to earthquakes and 3.4% due to unknown causes. This might have changed significantly within years of large earthquakes like the Sichuan earthquake of 2008 in China which caused many big landslides with lots of fatalities.

In order to manage the risk for economic values it is usual helpful to make a cost-benefit analysis determining useful counter-measures to landslides. When dealing with human lives the analysis is more sensitive and the notion of an acceptable risk has to be defined, which depends on culture, risk perception, availability of alternative building land, etc. (Glade et al., 2005). Usually, less developed countries show high fatality rates with natural disasters, while higher developed countries are more vulnerable in terms of economic values. However, compared to the gross domestic product (GDP), low developed countries are also more vulnerable in terms of economic values (Smith and Petley, 2009). Also the majority of undeveloped countries are prone to tropical storms and earthquakes, the main trigger factors for landslides and usually building codes, spatial planning and education are less advanced causing high fatalities due to landslides (Petley, 2008).

[1] EM-DAT database of the Centre for Research of Epidemiology of Disasters (CERD) - `emdat.be`

Type	Rock	Debris	Soil
Fall	Rockfall	Debris fall	Soil fall
Topple	Rock topple	Debris topple	Soil topple
Slide (rotational)	Multiple	Multiple	Multiple
	Successive	Successive	Successive
Slide (translational)	Block slide	Block slide	Slab slide
	Rock slide	Debris slide	Mudslide
Lateral spreading	Rock spreading	Debris spread	Soil spreading
Flow	Rock flow	Debris flow	Soil flow
Complex (change of behaviour downslope)	e.g. rock avalanche	e.g. flow slide	e.g. slump-earthflow

Table 1.1: Landslide Classification after (Dikau et al., 1996). The materials are based on an engineering definition, meaning that instead of soil also earth can be used.

Velocity class	Description	Velocity (m/sec)	Typical velocity	Human response
7	Extremely Rapid			Nil
		5	5 m/s	
6	Very Rapid			Nil
		$5 \cdot 10^{-2}$	3 m/min	
5	Rapid			Evacuation
		$5 \cdot 10^{-4}$	1.8 m/h	
4	Moderate			Evacuation
		$5 \cdot 10^{-6}$	13 m/month	
3	Slow			Maintenance
		$5 \cdot 10^{-8}$	1.6 m/a	
2	Very Slow			Maintenance
		$5 \cdot 10^{-10}$	16 mm/a	
1	Extremely Slow			Nil

Table 1.2: Landslide velocity classification after (Cruden and Varnes, 1996)

1.1 Landslide classification and terminology

The term landslide covers a large variety of mass movements, and can be classified using different characteristics like the type of movement, the involved material, the status of activity or the sliding velocity (Varnes, 1978; Cruden and Varnes, 1996; Dikau et al., 1996). Table 1.1 shows the classification after Dikau et al. (1996), which subdivides landslides depending on the source material (rock, debris, soil) and the type of movement (fall, toplle, slide, etc.). Figure 1.1 illustrates some of the most common landslide types. They can be further described by the status of activity (active, suspended, reactivated, inactive, dormant, stabilised, relict (Varnes, 1978)) or the sliding velocity as listed in Table 1.2, reaching from extremely rapid to extremely slow.

Other less commonly used classifications can be according to age, morphology, geography, topography, climate or cause of the movement.

This work focuses on clayey landslides, which usually exhibit extremely slow to slow movements (see Tab. 1.2), but can sometimes accelerate and evolve into rapid

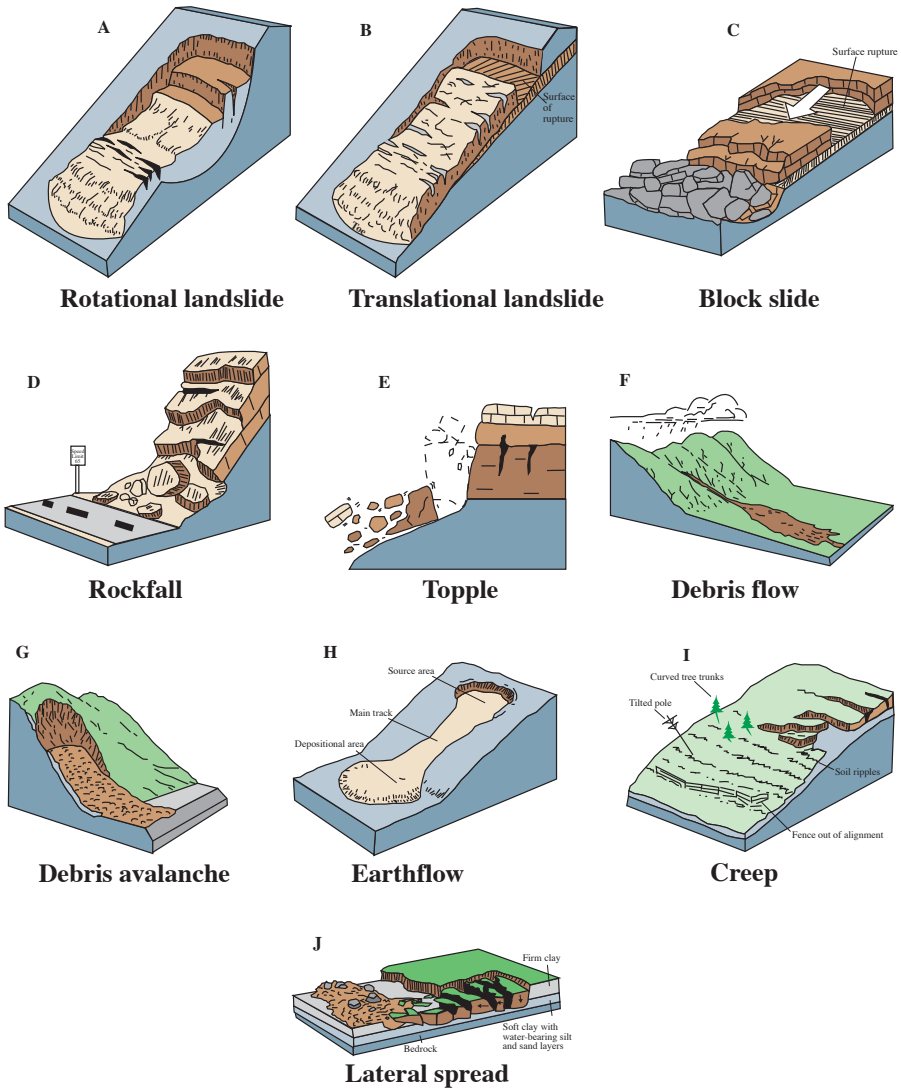

Figure 1.1: Most frequently occurring landslide types. Source: USGS (United States Geological Service), fact sheet 2004-3072 `http://pubs.usgs.gov/fs/2004/3072/`.

catastrophic earthflows causing severe damages to the society (e.g. Zogning et al., 2007). Figure 1.2 shows the schematic of a typical complex slump-earthflow including the terminology for different observable features.

The difficult to predict transition from slower to higher velocities is what makes these type of landslide dangerous. On the other hand the often continues but very slow movements can be used to detect and analysis the spatial and temporal kinematics for a better understanding of the underlying mechanisms before larger hazards occur.

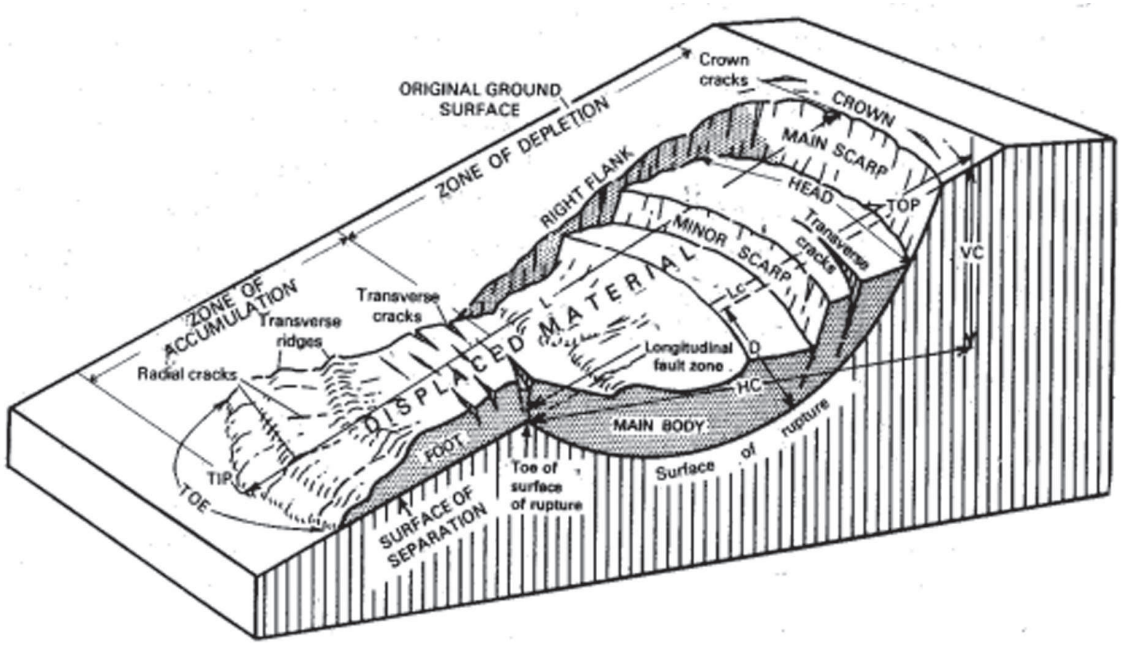

Figure 1.2: Terminology of features of a slump-earthflow (rotational landslide + mudslide) after (Cruden and Varnes, 1996)

1.2 Study site: the Avignonet and Harmalière landslide

This work is focusing on two adjacent typical clayey landslides in the French Alps (Fig.1.3). They are located in the northern part of the Trièves (Fig. 1.3a) at the westside of the Lake Monteynard (Fig. 1.3b). The area consists of a plateau (S), bordered by a mountain range in the West and five erosion valleys, which retreat into the plateau from North, East and South. The Drac River flows from South to North and is dammed-up at the North end of the artificial Lake Monteynard. The Avignonet landslide (1.3c) is covered by agricultural fields, forests and some rural settlements (about 50 buildings including abandoned ones).The Harmalière landslide is predominantly covered by forest with major parts exposing bare soil due to landslide activity. Just from looking at the photos, one can see the different landslide activity between both landslides. The fundamental question wether the Avignonet landslide can develop such high activity like the Harmalière landslide (which had a catastrophic event in 1981) asks for the better understanding of the mechanisms of the two landslides. A detailed description about the geological setting and history of the study site can be found in Section 3.1.

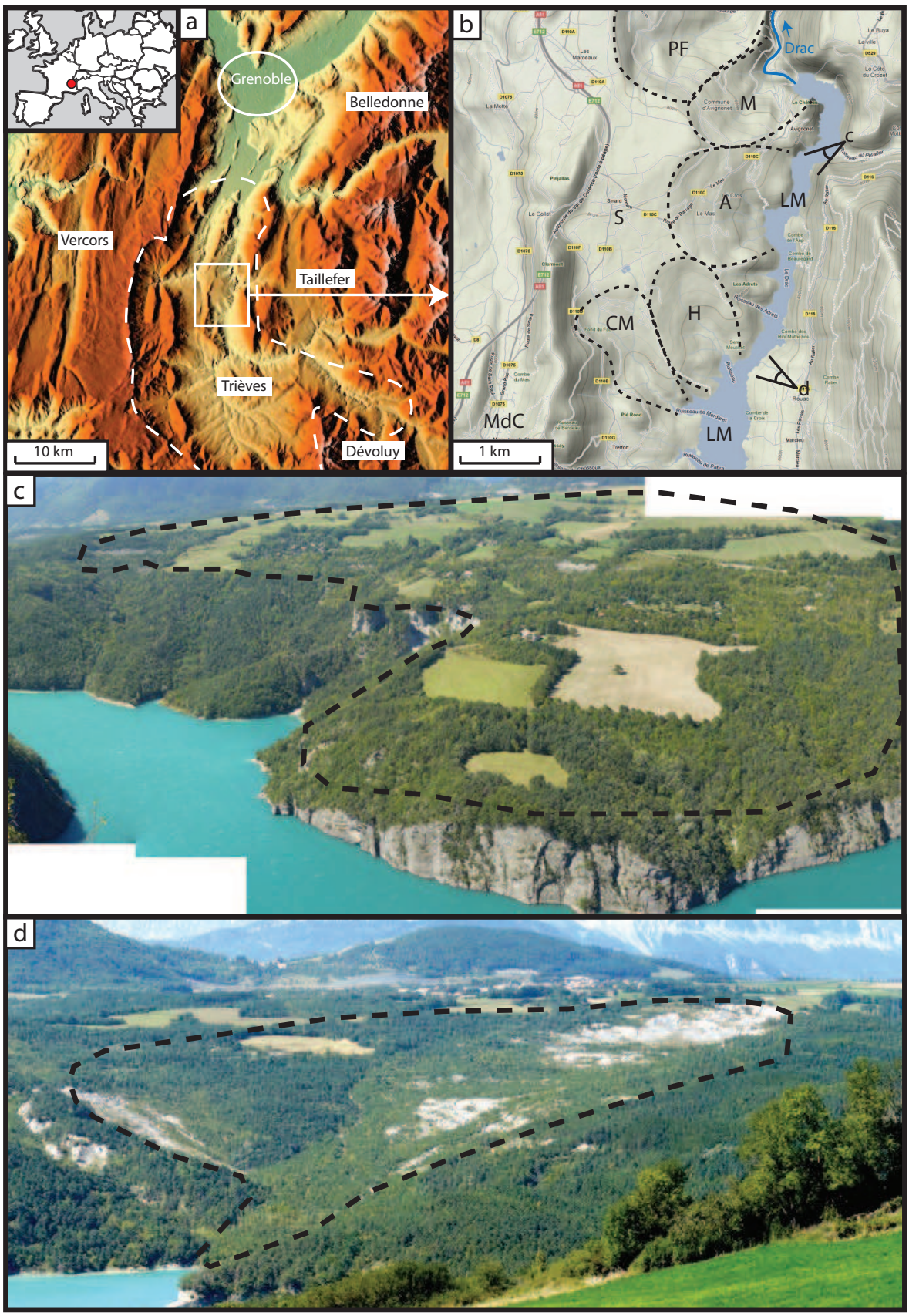

Figure 1.3: Location of the study site. a) Relief map of the Trièves valley and surrounding massifs. b) Topographic map of the study site. LM - Lake Monteynard, villages: S - Sinard, MdC - Monestier-de-Clermont, erosion valleys (combe): PF - Pierre Feu, M - Mitraire, A - Avignonet, H - Harmalière, CM - Champ du Mouton, c and d) Panorama photos of the Avignonet and Harmalière landslide (landslide limits as dashed line), the orientation of the views are indicated in Subfig. b.

1.3 Objectives of the thesis

The evolution of landslides through time can be examined using geotechnical (extensiometer, inclinometer), geodetic (GPS) or remote sensing techniques, where the latter one is the focus of this thesis. In particular, three remote sensing techniques are investigated: Lidar, Insar and aerial photogrammetry.

The first main objective is the evaluation and enhancement of those techniques for a better quantification of the evolution of slow moving landslide. This includes in particular:

- Production of high resolution bare-earth DEMs from aerial Lidar acquisitions.
- Production of different DEM-derivatives for geomorphological interpretations.
- Extraction and analysis of surface displacements from multi-temporal Lidar-DEMs.
- Production and analysis of ortho-photos and DEMs from aerial photogrammetry,
- Extraction of surface displacements from spaceborne SAR-images (i.e. PS-Insar)

The challenge lies in the fact that the expected surface velocities of the study site are near the limits of accuracy of the methods. Figure 1.4 shows the expected velocities of the Avignonet landslide (gray) in relation to the predicted velocities obtainable from the given datasets. For the PS-Insar technique the particular problems are coming from the unfavourable reflective properties of the rural study site.

The second main objective of the thesis is to use the increased knowledge about the past and present of the study site to explain the different behaviour of the Avignonet and Harmalière landslide and the general driving mechanisms. This includes more particular

- the spatial and temporal evolution of the landslides,

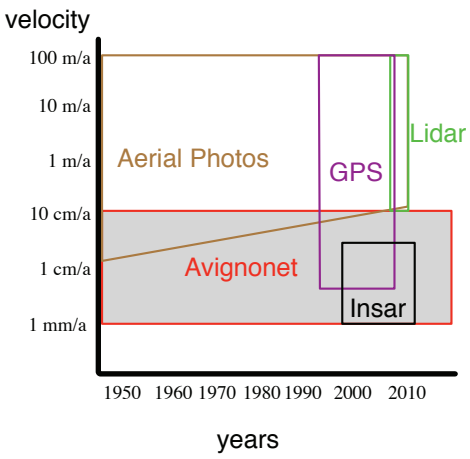

Figure 1.4: Approximately detectable surface velocities through time from the investigated datasets for the Avignonet landslide. The assumed methods for displacement extractions are Aerial photos: Feature-tracking on ortho-photos, Lidar: Cross-correlation of DEMs, Insar: Persistent Scatterer Insar, GPS: biannual campaigns using differential GPS

- the short and long term history of the landslides (since the last glacial maximum, the last decades and the last few years),
- the differences between Avignonet and Harmalière in terms of activity and controlling factors,
- the evaluation of probable future scenarios

1.4 Structure of the thesis

The thesis is structured in three main chapters: methods, geomorphology/geology and kinematics, framed by an introduction and a summary. Chapter 2 (Methods) gives an overview about the state of the art of remote sensing techniques on landslides and some background information for all methods and processing concepts, which are used in the following chapters. Chapter 3 (geomorphology and geology) deals with the static information extracted from datasets. The first part is basically a published paper containing an introduction in the geomorphology and geology of the study site; it focusses then on the different behaviour of the Avignonet and Harmalière landslide and discusses the reasons, with the help of the paleotopography, obtained by geophysical investigations. The second part of that chapter contains the analysis and discussion of different derivatives of the DEM like slope, shaded relief, drainage system and roughness. Chapter 4 (Kinematics) deals with the results obtained from the temporal analysis using aerial photogrammetry (Sec. 4.1), aerial Lidar (Sec. 4.2) and permanent scatterer interferometry (Sec. 4.3). The methodical limits and possibilities are discussed for each method separately in its section and the results are then summarised and discussed in Section 4.4. Finally Chapter 5 gives a summary and conclusion over the whole thesis. Appendix A contains more detailed informations about some datasets (i.e. aerial photos, GPS-displacements, Lidar). They are referenced in the text when a particular dataset is used.

1.5 Framework of the thesis

The research of this thesis was embedded and mainly funded through the European project "Mountain Risks: from prediction to management and governance"[2], a Marie Curie Research Training Network (RTN) of the 6th Marie Curie framework from 2007-2010. Figure 1.5 shows the main organisation structure of that project with the four working blocks Hazard Analysis, Quantitaive Risk Assessment, Risk management and Risk Governance. The main objective of this project were:

- To provide high-level training, teaching and research in the field of hazard and risk management.
- To overcome the fragmentation of the research on mountain natural processes.
- To strengthen and expand collaboration between the teams.
- To promote scientific and technological excellence in the science of hazard and risk.

[2]Mountain Risks Project - `www.mountain-risks.eu`

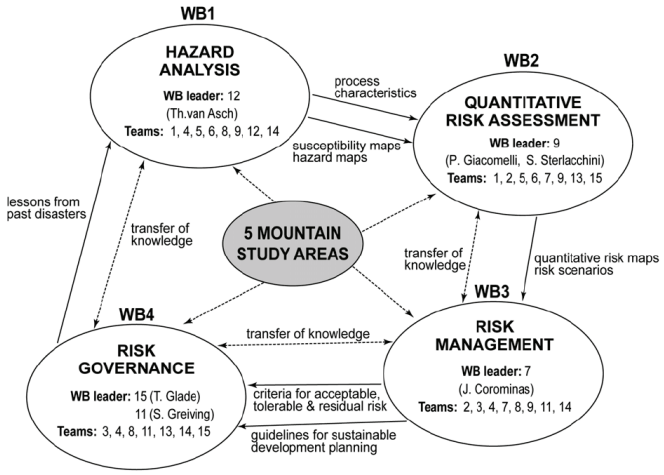

Figure 1.5: Organisation scheme of the Mountain risks project.

The project was concentrated on specific study sites in Spain, France, Italy, Switzerland and Germany. The research in the scope of this thesis was mainly embedded in WB1, partly in WB2 and focussed on the Avignonet and Harmalière landslides in the Trièves Plateau (French Alps).

This study site is also part of the French collaborative network OMIV[3], a union of six French scientific institutes focusing on four landslides in the French Alps in order to intensify the technical and scientific findings from slow and rapid moving landslides. This includes mainly the exchange of equipment, data and technical expertise concerning geodesy, inclinometers, extensiometers, aerial and satellite imagery, microseismic, regional seismic, hydrology and meteorology.

[3]OMIV (Observatoire Multidisciplinaire des Instabilités de Versants) - `http://www-lgit.obs.ujf-grenoble.fr/observations/omiv/omiv.html`

CHAPTER 2

Methods

Conventional geodetic methods have been widely used for monitoring the kinematics of slow moving landslides (centimetres per year to centimetres per day). Ground velocities are derived from successive field surveys measuring positions of reference stations by geodetic techniques like triangulation and tacheometry (Angeli et al., 2000) or using GPS (Jackson et al., 1996; Malet et al., 2002). Such techniques can achieve millimetric positioning and allow to choose specific points to measure the distribution of such data is temporally and spatially limited and needs human intervention in the field for the measurement. Remote sensing imagery instead is a powerful tool due to its capability to get a synoptic view of a landslide that can be repeated at different time intervals and its efficiency at various scales from a single landslide to regional scale (Metternicht et al., 2005; van Westen et al., 2008; Delacourt et al., 2007).

An overview of the Remote-sensing techniques used for quantifying landslide evolution is given in Section 2.1. Then, the aim of this chapter is to present the different methods used in the study of the Avignonet and Harmalière landslides. Most of the remote sensing approaches benefit from the GPS technique at different levels (acquisition, processing or analysis step). That is why the fundamentals of GPS will be explained in Section 2.2 in this chapter, even if the GPS is usually not classified as a "remote sensing" technique because, although it is based on satellites, it requires in situ instrumentation. The ways optical imagery and Lidar are used for the study of the Avignonet and Harmalière landslides are detailed in sections Sec. 2.3 and 2.4. One of the main product that can be derived from these two methods are Digital Elevation Models (DEM). These DEMs are used through quantitative analysis like slope or roughness maps. Section 2.5 describes how these DEM derivatives are obtained and gives illustration of their usefulness. Another important part of this thesis is dealing with ground displacement measurement from the remote sensing data. This is done through two main approaches: correlation technique applied on DEM acquired at different times and SAR interferometry (INSAR). The principles of the correlation technique that can also be applied on remote-sensing images are described in section 2.6. The last Section 2.7 explains the fundamentals of spaceborne Radar imagery techniques and then focusing on the Permanent Scatterer technique used in this study.

This thesis deals with data from different sources and different times and the geographical informations are not always given in the same coordinate system and projection. A description of the different projections and datums used in France and

the methods to transform between them (for instance from NTF to RGF93 geodetic systems) can be found in the Appendix B.

2.1 Overview of Remote-Sensing on landslide

Several remote sensing techniques have been used to get information about landslide like optical imagery, Lidar and radar imagery. However, their performances are very variable from one technique to another and from one dataset to another. The balance between spatial coverage and spatial resolution is a typical example: for instance, on one hand satellite Landsat images are not suitable to detect landslides smaller than 250 m (Eyers et al., 1998), but they cover a swath of 185 km, on the other hand aerial photos obtained from an airplane at low altitude (500 m) can be used to compute DEMs with an accuracy of 50 cm (Henry et al., 2002), but the spatial extent is quite limited. Imaging techniques currently used for landslide monitoring can be divided in passive and active methods. The passive methods are measuring the electromagnetic radiation from the sun reflected from the earth surface or from the own thermal radiation from the ground. For landslide studies, mainly optical sensors are used at different bands covering the visible part of the electromagnetic spectrum up to the mid infrared or thermal bands (wavelength from 0.4 μm up to 15 μm). The active methods are measuring the backscattered signal of an artificially emitted pulse. For that, different wavelengths can be used, near-infrared (NIR) in the case of topographic Lidar (LIght Detection And Ranging) and microwaves (1 mm - 1 m wavelength) for Synthetic Aperture Radar (SAR). The sensors are operated from mobile platforms like satellites, airplanes, helicopters, drones or from fixed ground based stations. Table 2.1 gives a comparison of the performance between different optical and radar imagery techniques (Lidar is not included in the table but is detailed in Section 2.1.3).

Ground based remote sensing methods, like Terrestrial Laser Scan (TLS), Ground based SAR or fixed camera), need to be installed on a good view-point not to far from the landslide (typically less than 1 km), which makes them sometimes inappropriate, especially for low slope (<30°) landslides. In addition they require electrical supply, not easy to implement for a landslide monitoring over several months or years.

2.1.1 Optical Images

Optical images are used either directly for visual, semi-automatic or automatic interpretation (Kääb, 2002; Hervas et al., 2003; Leprince, 2008; Delacourt et al., 2009) or to obtain DEMs using the stereo geometry of multiple images if available (Baltsavias et al., 1996; Lee and Lee, 2006; Pesci et al., 2007). Optical Imagery from satellites exists for about 40 years. Up to the 21st century, the spatial resolution of civil spaceborne optical sensors was typically not adequate for identifying single landslides, except very big ones (e.g. Landsat Thematic Mapper sensor can only achieve 30 m spatial resolution). But terrain conditions associated with landslides like lithology, differences in vegetation and soil humidity were derived from Landsat and SPOT images (Mantovani et al., 1996). Since about 10 years new developments of optical sensors from satellites with higher resolutions onboard IKONOS (0.8 m), Quickbird (0.6 m), SPOT5 (2.5 m) and Geoeye (0.5 m) allow studying kinematic details even inside of single landslides (Delacourt et al., 2007). Usually the higher the resolution the smaller the spatial coverage (e.g. meteorological satellites NOAA cover a swath of 2400 km with a resolution of 1.1 km and Geoeye covers 15 km with a resolution of 0.5 m).

	Radar sensor		
	Satellite		Ground-based
Technique	**DInsar**	**PS**	**DInsar**
Measurement Type	**1D component along the line of sight**		
Spatial Resolution	~10 m	~10 m	better than 10 cm
Accuracy	~ mm to ~ cm	mm	better than 1 mm
Swath	100 x 100 km		
Temporal resolution	1 to 178 days		
Archive	ERS (1991-2001); JERS (1992-1998); RADARSAT (1995); ENVISAT (2002)		
Major references	Fruneau *et al*. [1996]; Rott *et al*. [1999]; Kimura and Yamaguchi [2000]; Squarzoni *et al*. [2003]; Strozzi *et al*. [2005]	Ferretti *et al*. [2001]; Colesanti *et al*. [2003]; Hilley *et al*. [2004]	Antonello *et al*. [2004]

	Optical sensor			
	Satellite	**Aerial**	**Remote-controlled**	**Fixed Camera**
Measurement Type	**2 D horizontal displacement or 3D if DEMs available**			
Spatial Resolution	0.6 m to 80 m	0.5 m to 2 m	< mm to 1 m	~ cm to ~ m
Accuracy	~1/5 to 1 pixel	2-3 pixels	A few pixels	1/5 pixel
Swath	10 x 10 km to 60 x 60 km	5 x 5km	10 x 10 m to 300 x 300 m	10 x 10 m to 1 x 1 km
Temporal resolution	a few days to 30 days	5-7 years for France (IGN-coverage)	On request	1 s to 1 day
Archive	SPOT1-4 (1986); SPOT5 (2002); IKONOS (1999); QUICKBIRD (1999)	1950 - ongoing for France		
Major references	Scambos *et al*. [1992]; Kääb [2002]; Kääb *et al*. [2005]; Berthier *et al*. [2005, 2006]	Kääb *et al*. [2002]; Casson *et al*. [2003]; Delacourt *et al*. [2005]		

Table 2.1: Characteristics of the radar and optical remote-sensing sensors, platforms and techniques for landslides surface displacement measurements.(from Delacourt et al. (2007))

Another trend in optical imagery in the last two decade has been the development of airborne (e.g. Aviris, Hymap) and spaceborne (e.g. hyperion) hyperspectral imagery with measurement in tens of bands from visible to infrared (Kruse et al., 2003). However only a few studies have been done over landslides using hyperspectral imagery (Crowley et al., 2003; Mondino et al., 2009). This may be explained by the balance between spectral resolution and spatial resolution (due to the relatively small extent of landslides, the priority is still on the spatial resolution), the lack of long time series, the restricted availability of the data and their costs.

The temporal resolution is another important factor. One should distinguish between the return time and the revisit time. The time a satellite returns to the same position can vary between 1 day (NOAA, Terra) and 46 days (ALOS) depending on the height and the orbits inclination (return time). Usually optical sensors look perpendicular to the earth surface, but some newer satellites can change the incidence angle up to 60° and therefore are able to shorten the revisiting time for a desired target without flying at the same orbit (e.g. IKONOS) by looking from aside (revisiting time). If the revisiting time is usually shorter than the return time, as the images are not taken exactly from the same point of view, they can be more difficult to compare.

Before the availability of high resolution satellite images the alternative source were photos from airplanes. The availability varies a lot from one country to another, for France aerial photos are available since 1948 every 5-7 years with scales between 1:15 000 and 1:30 000. Optical imagery has been successfully used for landslide assessment. Some studies are based on automatic classification of single time satellite images (Barlow et al., 2006) and aerial photos (Weirich and Blesius, 2007) to support landslide susceptibility mapping. Stereo-images from satellites and aerial photos are used to build DEMs for landslide interpretation (Nichol et al., 2006). Multi-time aerial

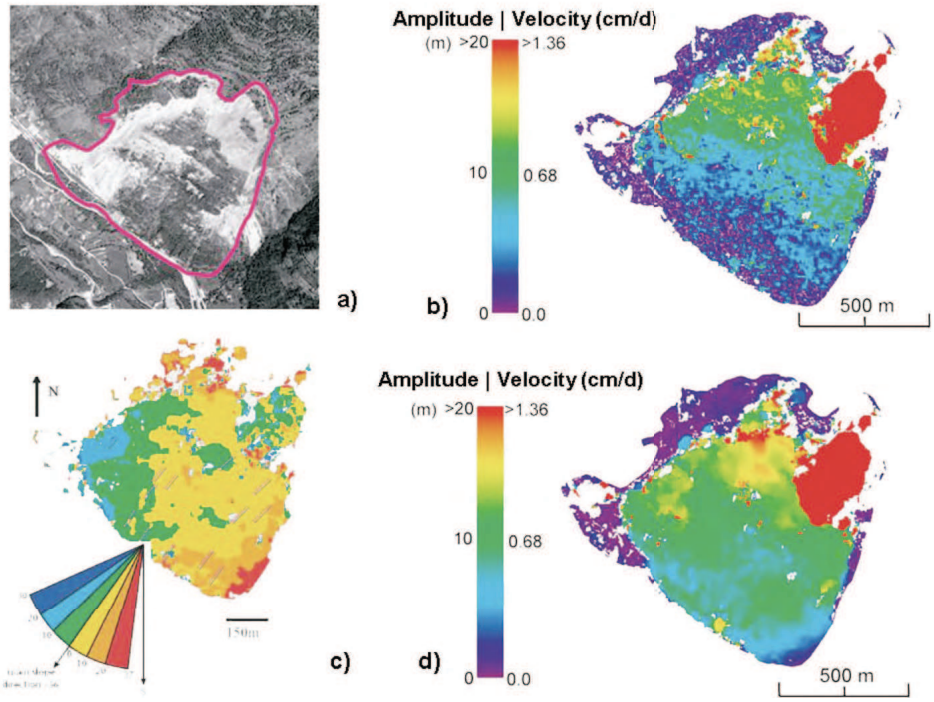

Figure 2.1: Displacement and velocity maps calculated by Aerial photo correlation using images from 1995-1999 at La Clapière - landslide. a) Aerial photo. b) Horizontal velocity. c) Horizontal displacement orientations. d) Vertical velocity map. (Delacourt et al., 2007)

photos (Casson et al., 2003; Walstra et al., 2004), satellite images (Cheng et al., 2004; Lee and Evangelista, 2006) or both (Kääb, 2002), acquired at multiple time for the same area, are used to compute radiometric and DEM differences between acquisitions of different times on landslides. These changes in time can also be horizontally tracked visually using image control points (Chadwick et al., 2005) or automated using cross-correlation techniques (Delacourt et al., 2004) (see Fig. 2.1 for an illustration).

Very high resolution aerial photos for landslide investigations and other morphology studies have been also derived using unmanned drones (helicopter, hang-glider, airplanes) (Henry et al., 2002; Lejot et al., 2007). Multi-temporal image analysis on landslides has also been done using fixed cameras on the ground (Delacourt et al., 2007), which can give much higher accuracies using image-correlation because the view angle is always the same and the images do not have to be geometrical corrected.

This study will only focus on the use of aerial photos as they are available since 1948 at relatively low costs and provide spatial resolution of about 30-100 cm over the whole studied area. Indeed, low resolutions satellite images could not serve the necessary resolutions to resolve the expected velocities in the studied landslides and high resolution satellite images would only cover at maximum the last 10 years, which would not include the years of the highest reported activities since 1981 at Harmalière. Acquisitions from drones are may be feasible, despite the large extents of the landslides, but expensive and the technology was not available. Ground based cameras would lack a good terrain-point with a complete view on the landslides within a range allowing resolutions of the images to track changes. The treatment of the aerial photos is described in section 2.3.

2.1.2 InSAR

Synthetic Aperture Radar (SAR) is an active microwave device capable of recording the amplitude and phase of electromagnetic echoes backscattered from the Earth surface and of arranging it in a 2D image map. With respect to optical sensors, SAR offers several unique opportunities like all-weather and day-night capability, but also presents considerable data processing and interpretation difficulties.

To derive information about landslide displacements from SAR imagery, four main approaches are possible: visual interpretation, image correlation, DEMs generation and comparison and differential SAR interferometry (InSAR). The three first approaches are quite similar to those applied in optical imagery. Regarding the visual interpretation, as optical imagery gives generally a better spatial resolution than radar imagery and because optical imagery are easiest to interpret, optical images are preferred even if the all-weather capability of SAR images provide more regular time-series of exploitable images compared to optical time-series often affected by cloud coverage. The resolution issue also favours optical imagery for image correlation or DEM generation. By contrast, the ability of SAR instruments to record the phase of the coherent backscattered signal makes interferometric methods (InSAR) possible by combining phase images acquired at different time. The INSAR method has the potential to measure ground displacements up to millimetric scale. This accuracy is not achievable by optical imagery.

Despite some severe limitations (high vegetation density leading to signal decorrelation, high variation of topography and high deformation rate leading to loss of coherence (Vanderbecq, 2000)), the capability of InSAR to detect movement fields in landslide areas has been demonstrated using spaceborne SAR (Fruneau et al., 1996; Rott et al., 1999; Hilley et al., 2004; Colesanti and Wasowski, 2006) and using ground based SAR (Antonello et al., 2004; Tarchi et al., 2003). By using ground based InSAR some of the problems arising from spaceborne observations can be solved by adapting view angles, acquisition intervals and distance to single landslides resulting in displacement fields of higher accuracy and resolution (Tarchi et al., 2003).

Using ground based InSAR spatial resolutions at metric scale can be reached. The viewing geometry and re-observation time can be freely adapted to the expected velocities and directions of the assessed landslides. Successful studies included observation distances of 500 to 2 000 km. This is above all useful to supervise emergency cases (Antonello et al., 2004).

Spaceborne SAR images can achieve resolution in range direction up to 1 m with a 10 km swath (e.g. mode spotlight of CosmoSkymed and TerraSarX). The swath can be extended up to 500 km in ScanSAR mode (Envisat, Radarsat) but with a degraded resolution of about 100 m. The most common mode is the stripmap mode that typically achieve a resolution in range of 5-10 m with a 100 km swath (ERS, ENVISAT, RADARSAT, ALOS...). The return time varies from 11 days to 44 days for single satellites (see Fig. 2.2) but can be reduced when a constellation of satellites is available. For instance for the period 1995-2000 ERS-1 and ERS-2, that have similar acquisition parameters, were on the same orbit (35 days cycle) with one day timeshift. Consequently it was possible to get pairs of images (called Tandem) with one day interval every 35 days. A summary of some sensor specific parameters can be found in Table 2.1 and Figure 2.2 gives an overview of civil satellites from the past and planned for the future carrying SAR imager suitable for interferometry.

For this study ERS-1 and ERS-2 data is used because they provide the longest (up to 1992) and most dense time series and are affordable (compared to Radarsat) thanks

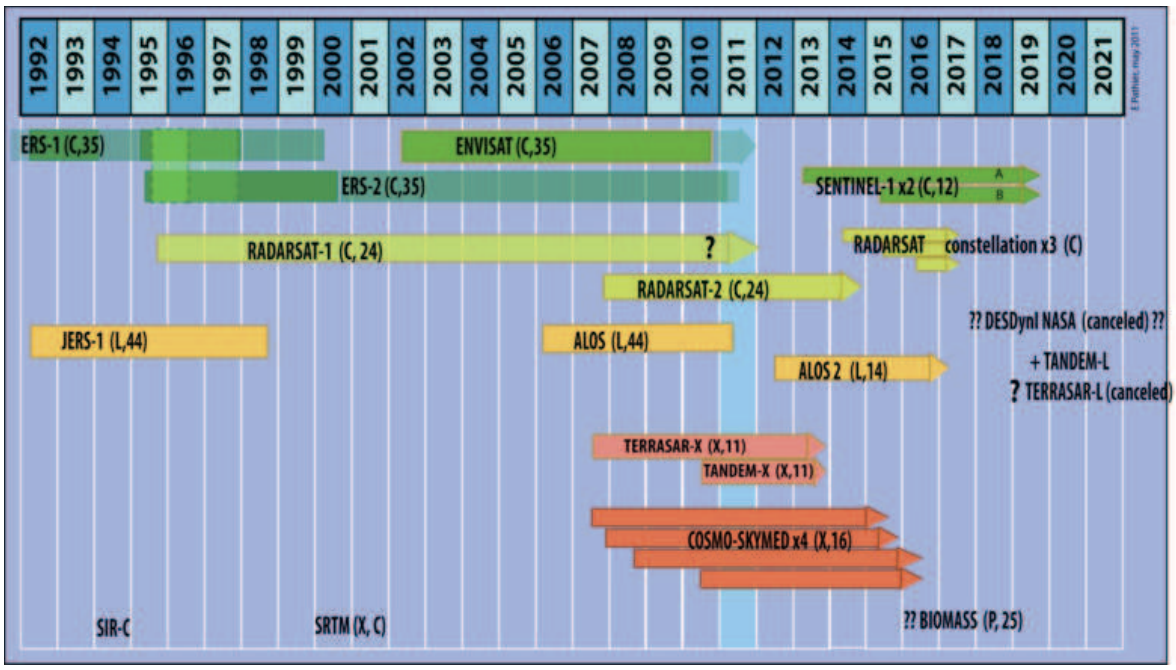

Figure 2.2: Past and future civil satellites carrying a Synthetic Aperture Radar imager suitable for interferometry. The letter and number in brackets indicate the band frequency of the SAR and the return time in days respectively. C-band corresponds to 4 - 8 cm wavelength, X-band 2 - 4 cm, L-band 15 - 30 cm and P-band 1 m. Note that for satellite constellation the return time is divided by the number of satellite (e.g. for Cosmo-Skymed constellation with 4 satellites the return time is 4 days). From E. Pathier (unpublished).

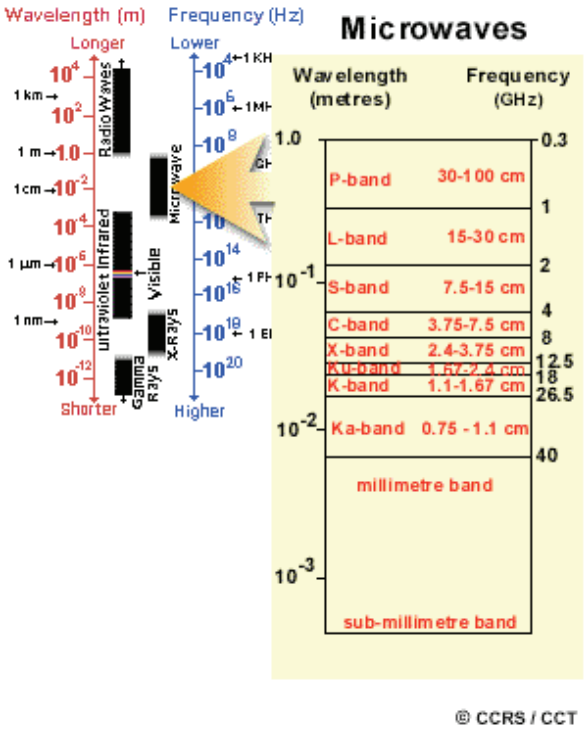

Figure 2.3: Spectrum of microwaves. SAR systems using microwaves in the C-, X- and L-band. Frequencies of commonly used in spaceborne SAR systems are in the C-band (5.30 GHz at ERS-1/2 and Radarsat, 5.33 GHz at Envisat), in the X-band (9.65 Ghz at TerraSAR-X) or L-band (JERS). Figure from CCRS (Canada Centre for Remote Sensing - `http://www.cct.nrcan.gc.ca/resource/tutor/fundam/chapter1/03_e.php`).

to the ESA distribution policy (CAT-1 projects).

Major difficulties arising from the side looking geometry of SAR instruments in mountainous areas because of shadowing and layover effects (details in section 2.7) at steep slopes (>15°), which can sometimes be mitigated by choosing images acquired with the most adapted geometric configuration (ascending or descending path, incidence angle) to the topography of the investigated landslide.

To derive ground displacements from InSAR, several methods are possible. The simplest is to consider pairs of images, making single interferogram that give information about the displacement between two dates. However interpretation of single interferograms are always difficult, because the deformation signal is mixed with other sources, such as atmospheric effects, orbital errors or decorrelation noises. When using C-band data like ERS1 and ERS2 data, over rural area, the various change in vegetation cover make the deccorelation problem critical. To overcome these limitations time-series approaches have been developed since a decade. They can be classified in two types : Small-Baselines (Usai, 2001; Berardino et al., 2002) and Permanent Scatterers (PS) (Ferretti et al., 2000; Werner et al., 2003; Hooper et al., 2004). The main difference between the two methods is that the small-baseline approach tries to optimise the signal for all the pixels but needs to start with interferograms showing a good spatial coherence, in contrast the PS approach aims to work only with points that are less sensitive to variations in the acquisition geometry but then can deal with low spatial coherence interferograms. Some mixed approaches have been recently proposed (Hooper, 2008; Ferretti et al., 2011).

Figure 2.4 shows an example of PS analysis used to determine long-term trends at discrete point networks. Permanent scatterers often correspond to man-made features or rock outcrops, so that the number of observation points can vary a lot between hundred thousands of points per square kilometre in urban areas to large rural soil and vegetation covered areas without any point. As the interest of landslide investigation is often more focused in areas where they interfere with manmade structures or previous activity of the landslide expose rock outcrops, this techniques is feasible for landslide assessment.

For this thesis the PS approach is chosen, because most of the studies done on landslide so far has used this approach and because in the framework of the Mountain Risks project a collaboration with University of Florence (Italy) using this approach with the Gamma Software[1] has been developed. Section 2.7 will give more details on the ERS data and their PS processing to measure ground displacement of the Avignonet and Harmalière landslide.

2.1.3 Lidar

Lidar has been increasingly used since about 2000 for landslide investigations (Jaboyedoff et al., 2010). It is mainly used to derive high resolution DEMs even in highly vegetated areas, where for example stereo-photogrammetry cannot be very successful (at small scales) due to geometrical distortions and vegetative "noise". It can be done by terrestrial laser scans (TLS) observing single landslides (Kasperski et al., 2010) or by aerial laser scans (ALS) from aircrafts like airplanes and helicopter covering larger areas. Such DEMs are well-suited to support geomorphological mapping and updating landslide inventories especially in highly vegetated terrain (Rowlands et al., 2003;

[1]Gamma Software by Gamma Remote Sensing `http://www.gamma-rs.ch/`

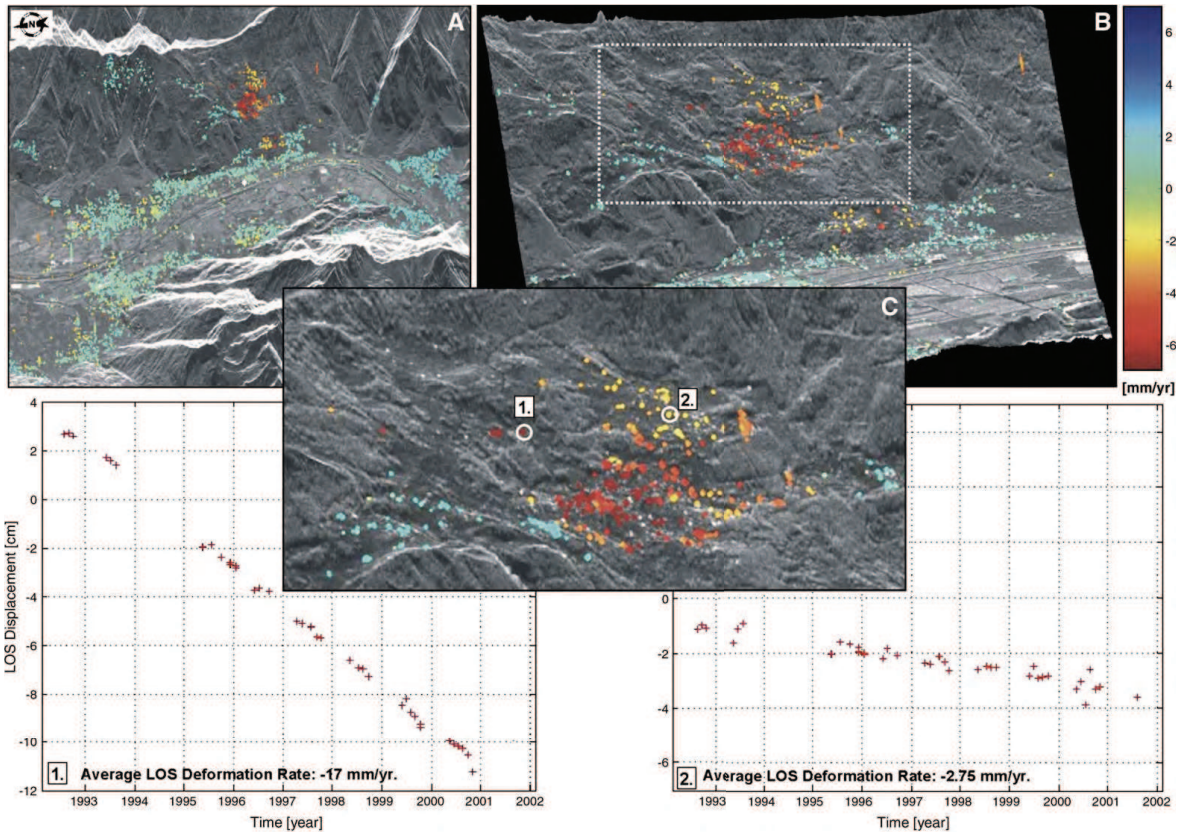

Figure 2.4: PS-InSAR results at the Triesenberg-Triesen landslide in the Rhine valley from Colesanti and Wasowski (2006) showing positions and average Line Of Sight (LOS) displacement rates of the Permanent Scatterers (marked by colour dots). A) SAR image showing the landslide location within the Rhine river valley; white square near the centre of the image marks the reference PS supposed motionless; B) SAR image showing the landslide slope; white dotted rectangle indicates the area represented in C); C) SAR image showing locations of two representative PS located on the landslide (marked 1., 2.). The images are in SAR co-ordinates, with 4 times oversampling applied along range. The pixel size amounts, therefore, to 4 m in azimuth and 3 to 5 m (depending on the local slope) in ground range. LOS velocity has been saturated at $\pm 7\,mm/yr$ for visualisation purposes only. The graphs show LOS displacement time series of the PS 1 and 2.

Schulz, 2007; Van den Eeckhaut et al., 2007). The high resolution DEMs allow to determine spatial distributions of morphological properties inside single landslides or landslide complexes like slope, roughness and drainage networks (McKean and Roering, 2004; Haneberg et al., 2005; Glenn et al., 2006). The example from McKean and Roering (2004) in Figure 2.5 illustrate the distinction of kinematic units from a shaded relief representation derived from an aerial Lidar scan of a landslide complex.

Using multiple laser scans differential DEMs can be derived showing accumulation and depletion of material through time (Chen et al., 2006; Corsini et al., 2008). Often an ALS is combined with aerial photo acquisition, so that both methods can be complementary combined, for example to produce high resolution ortho-photos using the Lidar-DEM or producing realistic 3D-views by draping the ortho-photos on the derived DEM. An extensive review about the use of Lidar for landslide investigations is given by Jaboyedoff et al. (2010).

In this study aerial Lidar scans have been used, because the area of the two landslides is too large to cover it by multiple terrestrial laser scans (TLS) and furthermore it does not exist exposed locations in the terrain from where scans of larger areas of the landslides would be possible within reasonable distance. The acquisition and

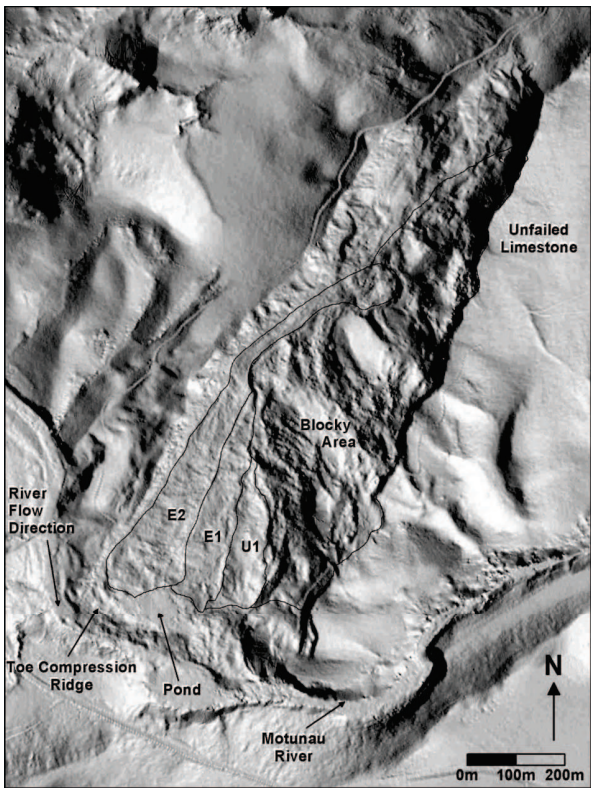

Figure 2.5: Shaded relief representation of the Coringa Landslide near Christchurch, New Zealand derived by Lidar. The primary kinematic units within the slide are earthflows E1 and E2, the area of compression U1 and the Blocky area with incorporated limestone blocks.

processing of the aerial Lidar used in this study is described in section 2.4.

2.2 Global Positioning System (GPS)

GPS is usually not classified as a remote-sensing tool because it requires receiver on the ground. However, we dedicate a subsection to this method, because not only the GPS is a common tools to measure surface displacements of landslides, but it is also useful for remote sensing technique like LIDAR and aerial photogrammetry in providing reference and ground control points. To measure ground displacements, it can be done continuously by permanent stations (Pambrun and Nocquet, 2005; Rutledge et al., 2001; Malet et al., 2002) or by repeated campaigns measuring marked points throughout the area (Squarzoni et al., 2005). Both methods are applied to Avignonet. Three permanent GPS-stations are operational since 2007 and 30 reference points were measured biannual since 1995 by RTM (*Restauration de Terrains en Montagne*, a french public service) (see App. A.5). Differential GPS has been used to derive ground control points for the processing of the aerial photos. Because GPS-processing for displacement measurements is not the main scope of this study, GPS techniques are explained as far as it is necessary to understand the processing of the ground control points and to judge the accuracies of displacement data from GPS. Further details (principle, applicability, procedures of measurements, equipment, accuracy) are given in Hofmann-Wellenhof et al. (2001) and for the explicit application on landslides in Malet et al. (2002).

First the basic concept of positioning using GPS is explained, followed by a presentation of differential GPS a method more difficult to implement but increasing the positioning accuracy. Section 2.2.3 describes the strategy for acquiring the ground control points needed for the processing of the aerial photos covering the study area (Sec. 2.3).

2.2.1 GPS concept

GPS or more precise "Navstar GPS" is a global navigation satellite system (GNSS) developed by the United States of America, besides the not yet operational systems GLONASS (Russia) and Galileo (Europe). The GPS system is made up of at least 24 satellites (currently 30). They are distributed on 6 different orbits at altitudes of approximately 20 000 km, with 4 satellites on each. This configuration assures visibility from every point on the earth surface to at least 4 satellites at the same time. These satellites send continuously information about their position and time coded on two frequencies (L1 = 1.2 GHz and L2 = 1.5 GHz). In order to determine its position the GPS-receiver at the point of interest (POI) needs to receive the position and time from at least 4 satellites (Fig. 2.6a). The time information is used to calculate the travel time of the signal from the satellite to the receiver, from which the distance can be estimated. To determine the position of the receiver by trilateration in 3D-space, only three distances would be enough, but it requires a very accurate timing in the receiver and the satellites. To achieve this the satellites contain an atomic clock, which would be not practicable on the receiver side. The signal from a fourth satellite is used to solve the equation-system of four equations and four unknown variables (three directions and time error). The accuracy of the positioning depends on one hand on the properties of the receiver (code and phase measurements, mono- or dual-frequency) and the strategy of calculation. On the other hand the accuracy is limited by physical factors like selective availability of satellites, ephemerides, precision of the orbits and alterations of the travel time of the signal due to atmospheric conditions (Hofmann-Wellenhof et al., 2001). Lastly, the use of special antennas and their installation on

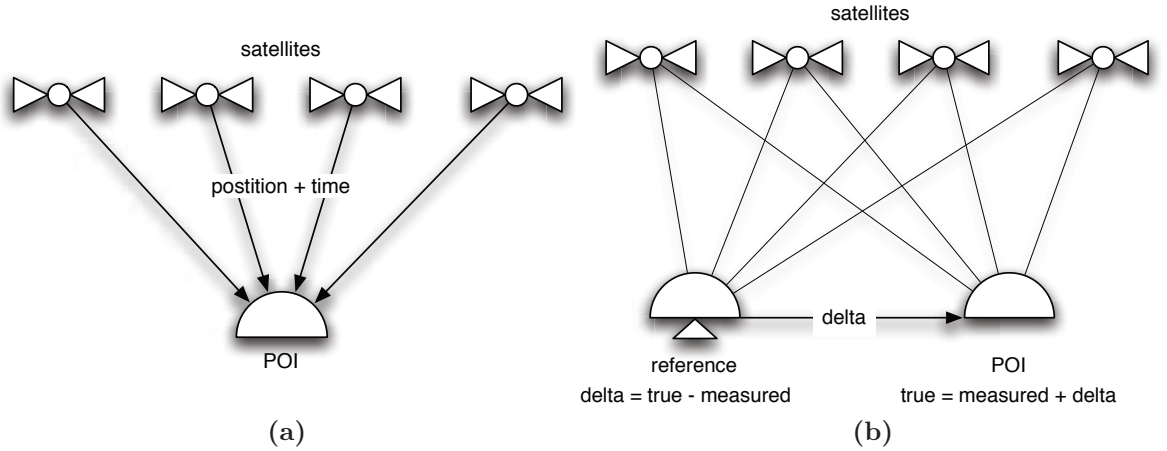

Figure 2.6: GPS basic concept. (a) Single GPS: A minimum of 4 GPS-satellites send their positions and time to the receiver at the POI. The receiver calculates the distances to the satellites and from that its own position. (b) Differential GPS: The reference station has known coordinates and measures the position by GPS. The receiver at the POI measures a position by GPS, which can be corrected using the difference (delta) from the known and measured position of the reference station. This can be done directly in the field by a data link between the reference and the POI-stations or in post-processing using the raw data received from the satellites.

sites with an open view must limit the multipath effects, which introduce additional errors in the resolution of the equations (Gili et al., 2000). Typical accuracies of single (handheld) GPS receivers are about 5 m horizontally and 15 m vertically.

2.2.2 Differential GPS

To overcome some limitations of the positioning by a single GPS receiver, differential GPS can be used to obtain more accurate coordinates at the POI (rover) relative to a second GPS receiver (reference). If the coordinates of the reference station are known (e.g. from long-term GPS measurements or other geodetic methods), precise absolute coordinates can be calculated at the rover station. The basic principle of differential GPS is shown in Figure 2.6b. The difference (delta) between the expected and received signals at the reference station is used to correct the measured signal at the rover station. For this method the two stations have to see the same satellites at the same time, meaning that the rover and reference station should have an open view to the same part of the sky. With this method errors introduced from delays of the signal in the ionosphere and troposphere can be minimised as the introduced error in the signal will be about the same at the reference station and the rover station. As the constellation of satellites changes over time, the relative orientations of the satellites towards the GPS receiver changes, giving new geometrical information. Therefore the accuracy of the positioning increases over time. The example of (Malet et al., 2002) in Figure 2.7 shows the improvement of the positioning with the increased duration of measurements for a differential GPS setting.

2.2.3 Ground control points

For the processing of the aerial photos, described in section (2.3), ground control points with accuracies close to the images resolution (< 0.5 m) was needed. Therefore two

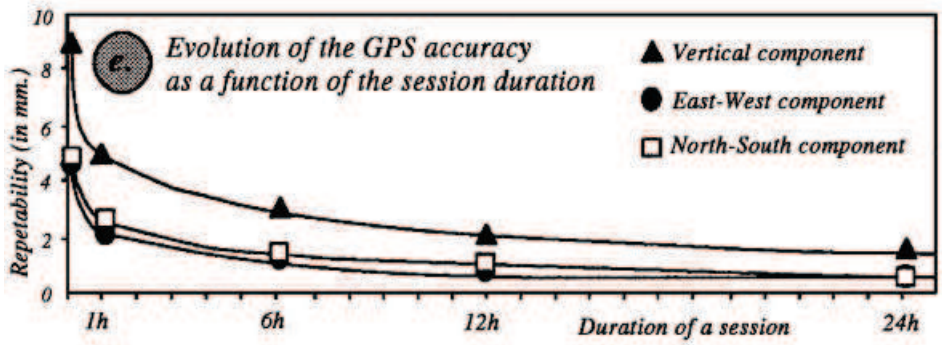

Figure 2.7: Repeatability as a function of measurement duration between two single-frequency GPS stations using differential GPS techniques. The baseline between the stations is 1.1 km. (Malet et al., 2002)

campaigns were realised in 2006 (1 day) and 2007 (3 days) using differential GPS techniques. In order to be able to use the ground control points in all aerial photos, before the actual field campaigns, the aerial photos of three different times (1948, 1985, 2003) were examined in details searching for landmarks (cross-roads, field-borders, houses, walls, etc.) existent over time (see an example in Fig. 2.8a). These points were chosen as ground control point candidates and surveyed during the campaigns. Each point was measured by GPS for at least 15 min in static mode with a sampling frequency of 2 s. Several parameters of the acquisition were reported in a datasheet including receiver properties, sample interval, antenna height, date, time and duration (Fig. 2.8b). Furthermore one or more photos were obtained (Fig. 2.8c) to illustrate the measurement conditions in order to be able to judge causes of errors maybe arising in the later post-processing (e.g. field of free view to the sky, wrong reported parameters).

In both campaigns the same location for the reference station was chosen to minimize shifts between the two campaigns by using the same fixed coordinates for this station. The reference station was recording over the whole time-span when the GCPs were measured (local reference in Fig. 2.9). In order to calculate the coordinates of the GCPs the recorded raw GPS-data was post-processed with Ashtech Solutions[2]. To derive accurate absolute coordinates for the local reference station REF1, its coordinates were calculated using two permanent GPS stations at Avignonet (with unknown coordinates) and the geodetic permanent GPS station CHAM of the RENAG-network[3]. Because all these three stations were only available since 2007, first the coordinates at REF1 were calculated at 2007 and the obtained coordinates where used as fixed coordinates for 2006 (Fig. 2.9). During the calculations it took out that some rover stations were not observing the same satellites as the reference station and therefore it was not possible to derive valuable coordinates for them. Because of that the geodetic reference stations were included in the calculations for the GCPs. As this was also the case for the measurements of 2006 and the permanent stations of Avignonet as well as the CHAM station were not available for that time, four stations of the RGP-network[4] about 100 km away were used instead (Fig. 2.9). To optimize the final solution for the coordinates the IGS final orbits[5] were used, which hold more precise orbit solutions

[2]Ashtech Solutions from Ashtech (`ashtech.com`), version 2.70

[3]RENAG - Réseau National GPS from collaborating french science institutes - `renag.fr`

[4]RGP - Réseau GNSS permanent from the IGN - `rgp.ign.fr`

[5]Final IGS orbit solutions are available from the US National Geodetic Service (NGS) at `www.ngs.noaa.gov/orbits/` about 2 weeks after the day of interest

(a)

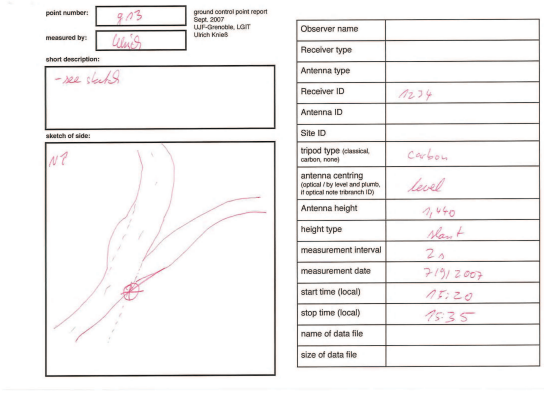

(b)

(c)

Figure 2.8: Example of a report of a ground control point (G013) including (a) an extraction around the GCP from aerial photos of three different years (1948, 1985 and 2003), (b) a datasheet containing a description and a sktech of the site, the time and several acquisition parameters and (c) a photo of the site showing the GPS-receiver position and the surrounding conditions.

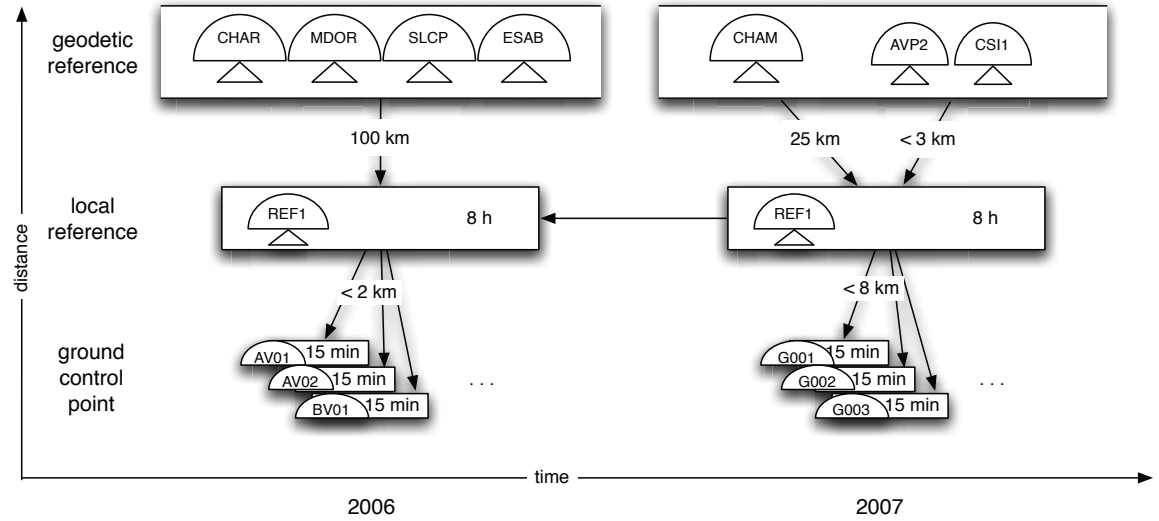

Figure 2.9: Time - distance sketch of the ground control point campaigns. The campaigns were operated by installing a reference station (Ref1) for a whole day (8h) and measuring points in the area for 15 minutes each. In the post-processing for 2007 the RENAG-station CHAM was included as well as two permanent stations at Avignonet (AVP2, CSI1)). For 2006 four stations of the RGP-network of the IGN were included and the coordinates for Ref1 derived from 2007. See chapter 2.2.3 for details.

of the GPS satellites during the dates of measurements. The influence of the use of different combinations of permanent stations and precise orbit files on the final solution of the GCP coordinates is presented in section 4.1.1.

2.3 Aerial Photogrammetry

Aerial photos are a powerful source of information to investigate the evolution of landslides in the past decades. Depending on the country, regular acquisition campaigns may be available by national public services. In France aerial photos are available since the Second World War approximately every 5-7 years from the IGN at scales from 1:15 000 to 1:30 000. A typical acquisition scheme is shown in Figure 2.10. Photographs are vertically shot from a plane flying at 0.7-4.5 km altitude on parallel flight strips so that the resulting photos are overlapping about 60% in flight direction and 20-30% between the flight strips. At IGN until recently these photos were acquired with analog cameras resulting in approximately squared film negatives with a size of 23 cm. For further digital processing they were scanned with a calibrated photogrammetric scanner with a resolution of 21 $\mu m/pixel$ for panchromatic images and 28 $\mu m/pixel$ for coloured images. The digital scale of the final image is therefore between 0.3 and 0.9 m/pixel depending on the analog scale, but the "real" physical resolution is worse due to atmospheric distortions, optical resolution of the camera and the physical resolution of the film (film grains).

Aerial photos are geometrically distorted with respect to a map projection and need to be corrected for further quantitative analysis. These geometrical distortions are on one hand due to alterations of the optical rays inside the camera (interior) and on the other hand due to the viewing geometry from the camera relative to the terrain (exterior) (see 2.11). In order to correct these distortions or to get information about the topography, the interior and exterior orientation of the camera is modelled (see next sections 2.3.1 and 2.3.2). After simulating the acquisition positions of the camera,

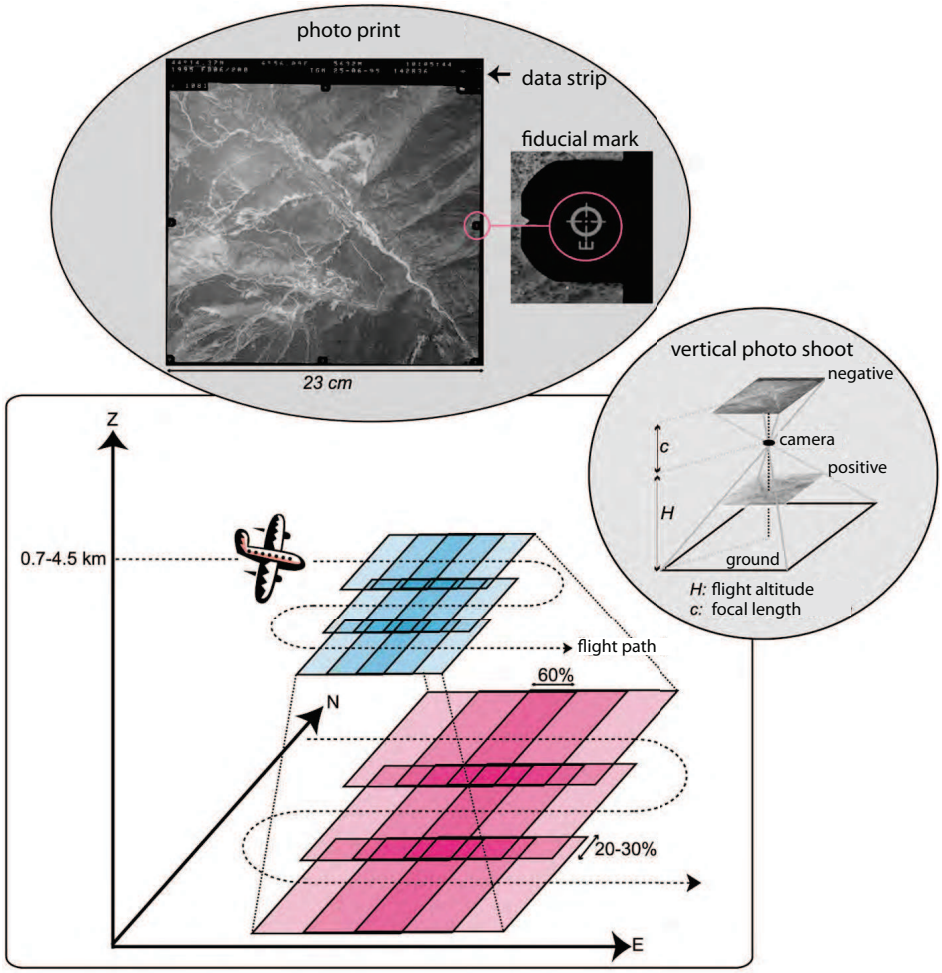

Figure 2.10: Aerial photo acquisition scheme of the regular french aerial photo acquisitions from the IGN showing the flight path configuration, a photo print example with a fiducial mark and the fundamental parameters of the vertical photo shoot. (Figure from Casson (2004)

DEMs can be computed from overlapping photos covering the same area (Section 2.3.3). Finally these DEM's or external DEM's can be used to produce ortho-photos, that are corrected photos simulating a parallel view perpendicular to the reference plane of a map projection (Section 2.3.4) (Paine and Kiser, 2003). In this study the processing of the aerial photos is done using Geomatica Orthoengine[6]

2.3.1 Interior orientation

The interior orientation is the reconstruction of a bundle of image rays with respect to the image center. As part of the interior orientation process the geometric influence of the lens system is calibrated. The properties of the camera are measured and delivered with the images in the calibration report (also called calibration certificate). The main calibrated parameters provided in such report are the focal length, positions of the fiducial marks, fiducial center, point of autocollimation, point of symmetry and dial and tangential distortions. An aerial photo has fiducial marks at the borders (crosses, circles, lines) and/or in the corners. The center of the fiducial marks is the fiducial center (FC). The principle point of autocollimation (PPA) is the point where the optical

[6]Geomatica Orthoengine 10.1.3 from PCI Geomatics - `www.pcigeomatics.com`

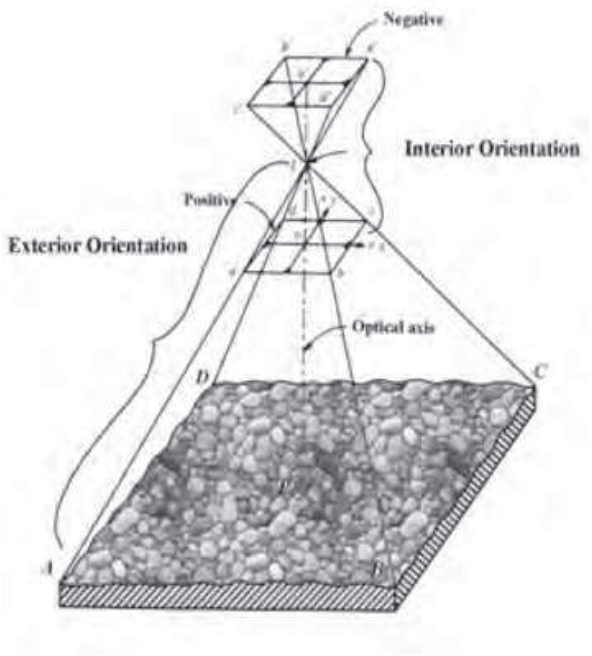

Figure 2.11: Interior and exterior orientation of aerial photos. The rays from the ground (ABCD) passes the lens L in the camera and hit the film producing a negative (a'b'c'd'). The interior orientation describes the geometry of the ray traces inside the camera. The exterior orientation describes the camera position and looking direction relative to the ground. (Figure from `http://ralph.swan.ac.uk/glaciology/projects/slices/Photography/`)

axis crosses the image plane (point "o" in Figure 2.11). This is usually the origin of the coordinate system in which all the other positions are given. Sometimes it is just called the principle point (PP). The image contains distortions coming from the lenses. As the lenses are made using rotational processes, these distortions are mainly radial. The point in the image from where the best compensation for these radial distortions is possible is the principle point of symmetry (PPS). This compensation is done using a polynomial function defining the radial expansion or contraction circular around the PPS. This function can be calculated from the radial distortion parameters given in the calibration report as a table of distances from the PPS and deviation from the expected distance. The FC, PPA and PPS are usual very close to each other and can be assumed equal if not available. Other sources of errors are often not taken into account, like tangential distortions coming from divergences of multiple lenses relative to the optical axis, undulations of the photo-film or deviations of all the parameters due to thermal variations during the flight. Some of them will be partly corrected in the process of finding the exterior orientation (Geomatics, 2003).

2.3.2 Exterior orientation

The exterior orientation describes the location and orientation of the camera in the object coordinate system. It can be used to eliminate the geometric distortions in the photo due to the central perspective projection, altitude variations and earth curvature. The camera position and orientation at time of taking the photo can be reconstructed by fitting straight lines between several ground control points (GCP) and their accompanying image coordinates by crossing the principle point of the lens. This is usually done in a block adjustment using multiple adjacent overlapping photos to minimise

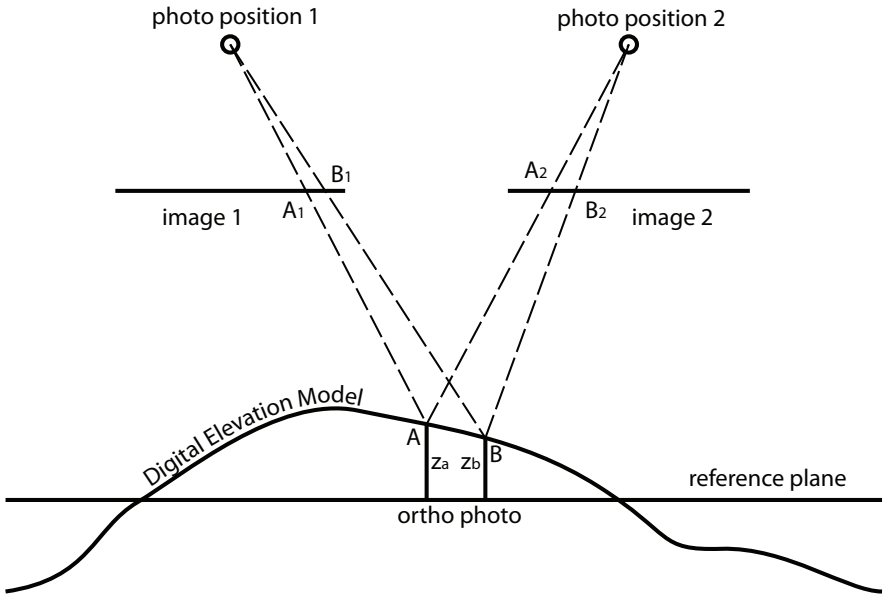

Figure 2.12: Geometry of two overlapping epipolar photos (stereo pair) for DEM extraction. Using matching points in both images ($A_1 \rightarrow A_2, B_1 \rightarrow B_2$ the corresponding elevation above a reference plane for those points (z_a, z_b) on the earth surface can be reconstructed using the exterior orientation of the cameras when acquiring the photos. See text for details.

relative errors between them. Using this model residuals for all GCPs can be calculated by computing the RMS-difference between the real coordinates of the GCPs and their coordinates predicted by the model. The overall RMS-value gives a good approximation of the expected accuracies for the DEM and the ortho-photos using these registered images. In the ideal case it should be near the image resolution or GCP accuracy. The collection of GCPs is described in Section 2.2.3. After finding the exterior orientation a DEM can be extracted using the height information hidden in the geometric distortions (see next Sec. 2.3.3) or an existing DEM can be used to deskew the images producing an ortho-photo (Sec. 2.3.4).

2.3.3 DEMs from stereo images

As adjacent aerial photos overlap by 60% (Fig. 2.10), it is assured that every area is at least seen by two photos from different view angles. Each image holds elevation information hidden in its geometric distortion, which can be revealed in three steps. First the image pairs have to be epipolar reprojected so that each row of one image corresponds to the same row in the other image. Such epipolar images can be used for stereoscopic views with the help of optical techniques which allow to see only one image with each eye. It will reveal a 3D view of the terrain. In the second step image correlation techniques are used to find matching points between the two images. It basically uses the same technique described in Section 2.6.3. Small windows around the corresponding pixels between the two images are correlated to find the highest cross-correlation peak, resulting in corresponding points with known coordinates in both images. By finding the point of intersection of the two rays from each camera related to the same point, the elevation can be calculated knowing the exterior orientation of the camera for each image (Fig. 2.12).

In a third step elevations from different stereo-pairs are combined and reprojected

in the desired map projection. During the second step a scoring depending on the quality of the fit between the matching image points is kept for each elevation value, so that in the last step the elevation with the best associated scoring can be used for the final DEM.

If the terrain is very mountainous and the angle between the stereo-pair of images is too high, the matching process can fail due to high perspective distortions of the matching kernels. In this case the matching algorithm can find wrong matches and therefore produce artefacts (like spurious peaks) in the final DEM. To reduce the problem, the match score can be used to remove all elevation points with a score below a certain threshold. Another problem is the presence of objects like houses, trees and pylons in the images, which may be appear quite differently from different view angles and lead to noise in the DEM. As this will be noise with a relative small wavelength, it can be mitigated by low-pass filtering at the expense of the spatial resolution.

2.3.4 Orthophotos

Ortho-photos are aerial or satellite images reprojected from the centric projection of the photograph to a geographic projection. For each image the view of the camera is simulated using its exterior orientation towards the DEM so that for every DEM pixel the corresponding pixel of one of the two available images can be assigned (Fig. 2.12). By projecting them on the reference plane the ortho-image is done. As the overlapping area of one image pair is relatively small, often many ortho-photos have to be joined by mosaicking. Because the colors between adjacent images , especially the brightness, can vary a lot, the image can be blended into each other or connected at unobtrusive break-lines. The final ortho-photo can be used to measure areas, be draped on a DEM for a 3D view or derive displacement fields by cross-correlation techniques (Sec. 2.6).

2.4 Aerial Lidar

In order to analyse a landslide a high resolution DEM (say, better than 2 m resolution) can substantially help to understand the geomorphology or be used for modelling purposes. Conventional techniques to derive DEMs are usually not well suited because they can not achieve such high resolution (interpolation of altitude-isolines from topographical maps, stereo-photos from aerial or spaceborne optical sensors, spaceborne Radar) or because of their low spatial coverage and low measurement density (traditional geodetic methods). If stereo-photogrammetry can potentially reach high resolution, one of its limitation is to not be able to reveal the earth surface below vegetation, which often covers significant parts of landslides. Since about 2000, airborne Lidar is more and more used to fill these needs, because it is able to deliver DEMs up to decimetre resolution and precision even in very steep terrains and highly vegetated areas. The procedure to obtain a DEM from Lidar can be divided in three parts: Acquisition, the point-cloud classification and gridding, which will be covered by the following sections.

2.4.1 Acquisition of aerial laser scan

Lidar is an active remote sensing method based on range measurements derived from the two-way travel time from emitted and then backscattered laser-pulses. In an aerial laser scan (ALS) this is done from a helicopter or plane flying at heights between

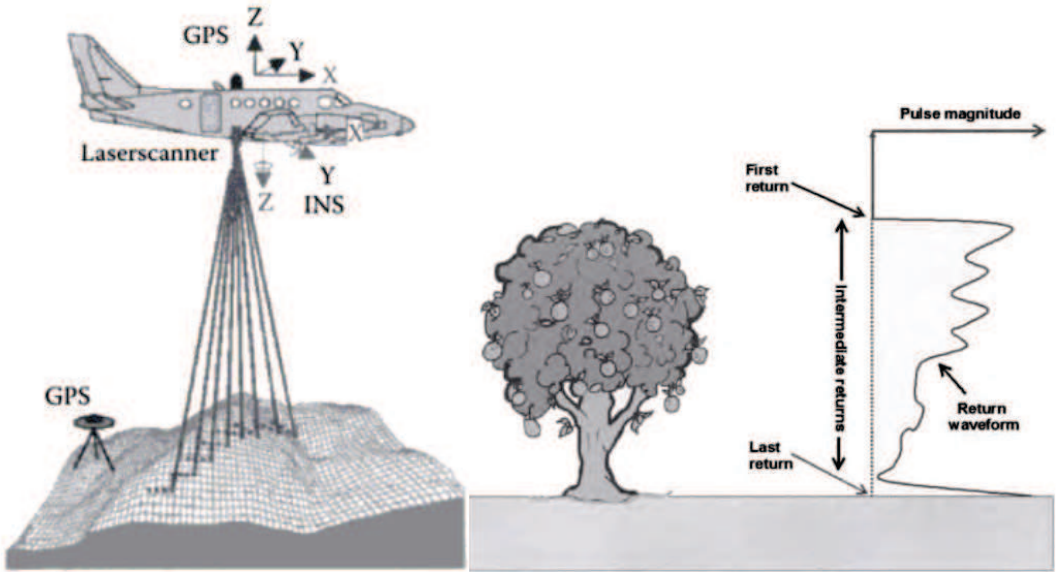

Figure 2.13: Aerial Lidar scan acquisition principle showing (a) the aircraft with the mounted Laserscanner, GPS and INS (Inertial Navigation Unit) and a GPS reference station on the ground. (Fig. from Weng and Quattrochi (2007)) and (b) the received full wave signal with its different maxima corresponding to different objects (like the tree and the ground) in its line of sight. (Fig. from Mather and Koch (2004)), see further details in Sec. 2.4.1.

2 000 m down to 100 m above the ground. In order to obtain the exact position from where the pulse was backscattered, the position and orientation (pitch, roll and yaw) of the plane need to be known. Therefore a GPS unit is measuring the absolute position of the aircraft with a sample frequency of 1-2 Hz by differential GPS (Sec. 2.2.2) with the help of a fixed ground station located not far (no more than a few km) from the studied area. Considering the speed of the aircraft and deviations from a linear flight path the error of positioning between two received GPS signals can be significant. To overcome this, an INS (Inertial Navigation System) with accelerometers and gyroscopes measures with a sample frequency of 100-400 Hz accelerations and rotations in 3D from which the exact flight path and look orientation can be reproduced. A typical aerial laser-scanner works with wavelengths in near infrared (NIR) with a pulses repetition frequency of 5-50 Hz and a pulse length of 10 ns (Weng and Quattrochi, 2007). Usually more than one single pulse is back-scattered from one emitted pulse depending on the wavelength of the laser and the scatter and absorption properties of the materials in the line of sight (Fig. 2.13b).

The waveform is evaluated for pulse maxima (on-the-flight or in post-processing) and the corresponding calculated point positions are kept resulting in a 3D point cloud. Some systems keep the first or last pulse only, some both or even intermediate pulses and others the full waveform for further analysis in post-processing. In the optimal case the last pulse represents the ground, but if the coverage of vegetation is to thick and the laser pulse can not pass, the last pulse is not the ground. Furthermore, multi-path problems at corner reflectors can lead to points below the actual earth surface. Therefore the obtained point-cloud has to be classified and can be filtered to derive the bare-earth model (see Sec. 2.4.2). The final density of points depends mainly on a trade off between the flight height, flight velocity, pulse repetition rate and acquisition time which is directly related to the costs. A typical acquisition by plane at a flight height of 1 000 m would result in point densities of about one point per square-meter.

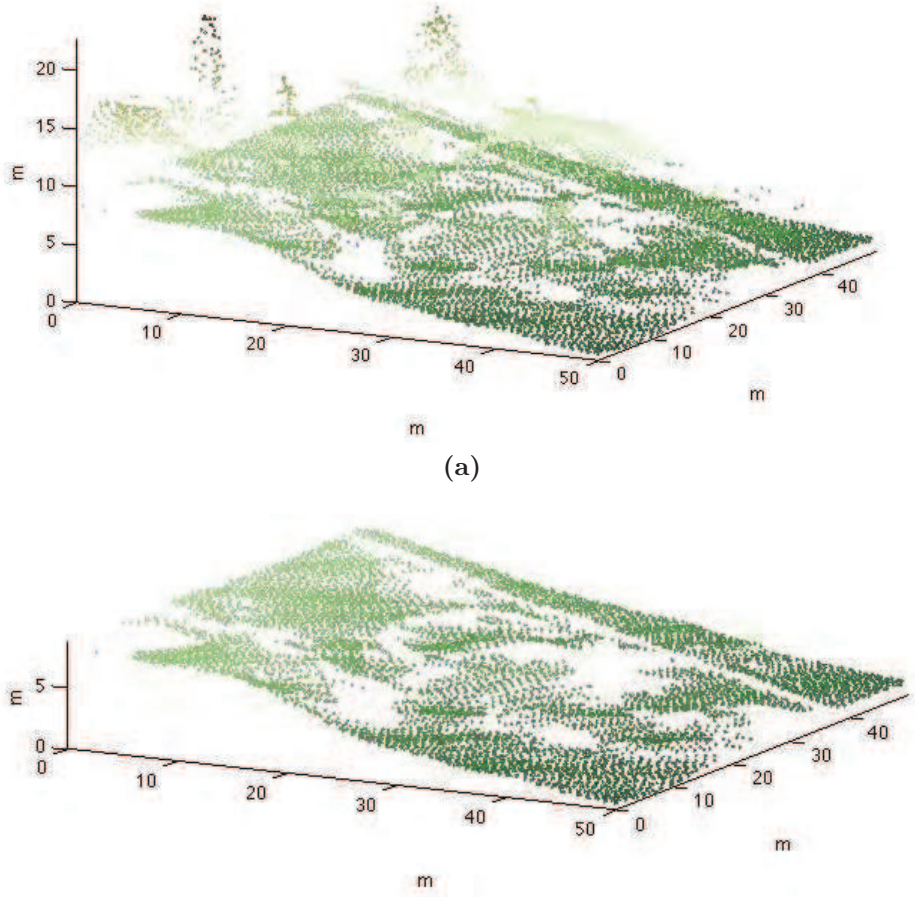

(a)

(b)

Figure 2.14: Example from a subset of the Lidar 2006 point-cloud showing the unfiltered (a) and filtered point-cloud (b). Whereas the unfiltered raw point-cloud also includes points resulting from reflections at houses and trees, the filtered point-cloud contains only the points classified as ground.

For this study helicopter flights were preferred, (1) Low flights (<1000 m) from plane are not feasible at the study site due to the alpine landscape, (2) higher densities are necessary to obtain a good coverage of the bare-earth even in higher vegetated areas and (3) parts of the study site contain very high slopes (the Harmalière headscarp, the cliff of the compacted alluvial layers) and can be better scanned from aside with a low flying helicopter equipped with a handheld laser-scanner.

2.4.2 Point-cloud classification

In order to obtain a bare-earth DEM, which will hold the relevant geomorphological informations of the landslides, every point in the point-cloud has to be classified (e.g. as ground, building, low/mid/high vegetation). Figure 2.14 shows a typical subset of the unfiltered and filtered Lidar 2006 point-cloud over the study area.

The aim of the point-cloud classification is to assign a classification tag for every point in the point cloud. This tag or classification byte indicates the nature of the material which reflected the laser-pulse and produced this point. Many papers have been published about the classification of airborne lidar scans. All classification methods make assumptions about the structure of bare-earth points in a local neigh-

bourhood, based on slope/height differences (Sithole and Vosselman, 2001; Roggero, 2001; Whitman et al., 2003; Vosselman, 2000), a buffer zone above a local horizontal plane (Wack and Wimmer, 2002; Zhang et al., 2003), a buffer zone near a parametric fitted surface (Axelsson, 2000; Elmqvist, 2002; Pfeifer et al., 2001; Sohn and Dowman, 2002; Wack and Wimmer, 2002) or by clustering/segmentation (Brovelli et al., 2002). Comparisons between those filter methods applied at different terrain types (e.g. urban planes, forested mountains) can be found in Sithole and Vosselman (2004) and Zhang and Whitman (2005). Furthermore Meng et al. (2009), by using a multi-directional ground filtering algorithm, could achieve better results on the same test-sites used in the comparison of Sithole and Vosselman (2004). Using a multi-scale curvature algorithm Evans and Hudak (2007) developed a filter especially for mountainous forested terrain. Most of these methods are working well in flat terrain but show difficulties in mountainous areas, especially if they have a dense vegetal cover, as it is the case in the study area of this work. In this study the "Hierarchical robust filtering" method (Pfeifer et al., 2001; Kraus and Pfeifer, 2001; Briese et al., 2002) is used as it shows relatively robust results in these kind of problematic terrain. It is implemented in the commercial software SCOP++[7].

As illustrated in Figure 2.15 first this algorithm thin out the point-cloud by choosing the lowest point in a coarse regular grid (Fig. 2.15a). Then a first approximation of a surface is computed (red line in Fig. 2.15b). After that a weight is assign to each point depending on the vertical distance to the derived surface. Points below the surface are weighted higher than those above. The surface is then recomputed using a linear prediction (similar to kriging) taking into account the different weights. It means the surface is magnetized by the low points (black line in Fig. 2.15b). This procedure is iterated until the surface does not change anymore between two iterations or it exceeds a certain number of iteration steps. After that all points of the original point-cloud are classified due to their vertical distance to the interpolated surface (Fig. 2.15c). Points within a predefined threshold are accepted as bare earth (green points in Fig. 2.15c and subreffig:robustfiltd). Using only these bare earth points a new surface is computed (green line in Fig. 2.15d) and the points are again iterative weighted due to their distance to the interpolated surface, until a final stable bare-earth surface is derived (black line in Fig. 2.15d). In this example only two hierarchical levels are used, but the procedure can be extended to any number of pyramidical subsets of the points derived by thinning them out towards a uniform spatial distribution. Also the example only distinct in ground points and non-ground points, but different classifications (e.g. low/mid/high vegetation) can be assign to the points due to their vertical distance to the final interpolated surface. Furthermore other spatial criteria can be used to recognise houses, power lines etc.

2.4.3 Gridding

In order to further process the classified non-uniform point-cloud for visualization, morphology analysis and cross-correlation, it needs to be gridded to a regular grid, because most of these methods are based on matrices. To derive a regular grid from an irregular point-cloud the height of each regular point has to be estimated by an interpolation function based on all points or a local subset of points. Commonly used methods for DEM generation include linear, cubic, polynomial, spline and kriging

[7]SCOP++ is a Geo-modelling software by inpho (`www.inpho.de`) co-developed with the Institute of Photogrammetry and Remote Sensing of the Technical University Vienna

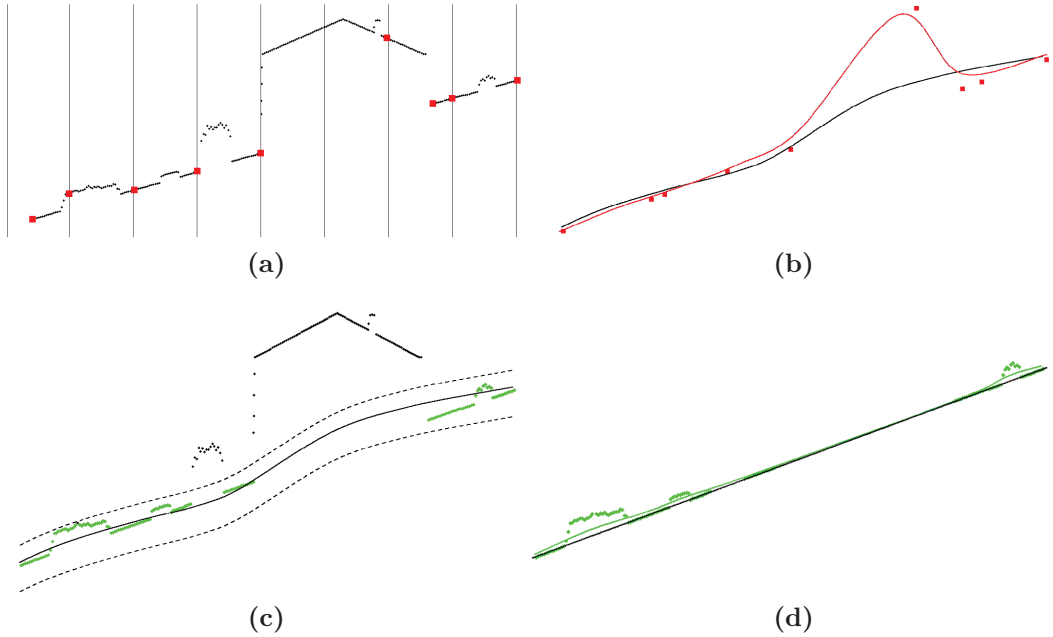

Figure 2.15: Sequence of the hierarchic robust interpolation (a) Creation of a data pyramid, small points: original data, thick points: data pyramid (lowest point in a regular 5m interval). (b) DEM generation in the coarse level by robust interpolation, the remaining point on the house is eliminated with an asymmetric and shifted weight function. The surface in the first (red line) and last iteration (black line) is shown. (c) Coarse DEM with a tolerance band, all original points within the tolerance band are accepted. (d) DEM generation in the fine level by robust interpolation using an asymmetric and shifted weight function. Again, the first (red line) and the last iteration (black line) is shown. (Figure from Briese et al. (2002))

interpolations and derivatives of those. Sometimes triangulated irregular networks (TIN) are also used prior to gridding algorithms, which would be equivalent to a trilinear interpolation method based on the 3 nearest neighbours. TINs are especially useful for DEMs with high variability of complexity or terrains which can not be well represented in a 2D view (like vertical cliffs). It is the fundamental basis of almost every 3D-visualisation of surfaces.

The simplest case of an interpolation function would deliver just the value of the nearest neighbor (NN in Fig. 2.16). If the grid spacing is near the average point-cloud spacing or lower, this can lead to substantial bias in the resulting DEM, because if several points are falling in the borders of one pixel, only the nearest point from the center of that pixel is representing the whole pixel value. Considering some "noise" in the point-cloud (acquisition accuracy, miss-classification), the nearest-neighbour interpolation would adopting the noise in the final DEM. By using the average of all neighbours (AN) inside the pixel, the noise would be smoothed out (Fig. 2.16).

This method is also useful to access other statistical properties of the point cloud on a pixel basis, for example the point density (also per class) or the minimum, maximum and deviation of the height or intensity/reflectivity. Pixels which do not cover any point are defined as NaN (Not a Number) and will turn up as data-holes, which raises problems in further processes like the computing of slope, aspect and shaded relief or cross-correlation techniques. Therefore this kind of gridding is only useful to obtain coarse rasters (relative to the point-cloud density), for example to obtain overviews of Lidar point-clouds and their density variations, in order to determine a feasible resolution for a finer gridding.

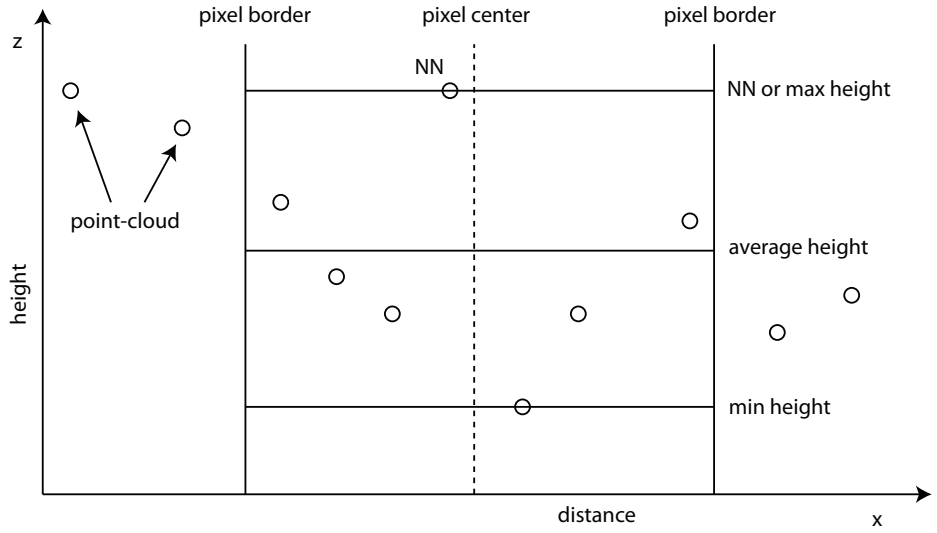

Figure 2.16: Sketch of defining the height value of a pixel (or grid-cell) in a regular grid (DEM) using different properties (min, max, average) of the point-cloud inside the pixel borders. The point NN is the nearest neighbour of the pixel center. Using the NN-interpolation would only use one point to assign the height for the whole pixel, which is not representative for the terrain height in this case. The min and max can be used for example to extract the vegetation height. (See Sec. 2.4.3 for details)

Such finer gridding can be done using other interpolation methods, like linear, cubic, spline or kriging. As an example, problems and solutions using spline interpolation for Lidar data can be found in Mitasova et al. (2005).

This study is using the Gridfit-method for all gridding operations of point-clouds, except in cases of building coarse rasters using the all neighbours-method. Gridfit uses a modified ridge estimator to generate a smooth surface which approximates the scattered data. The gridfit-method is written by John D'Errico (Matlab[8]-code released in version 2.0 on 23.05.2006) as contribution to the open code-sharing website Matlab Central[9] (no publication available). It is specifically adopted to handle highly heterogenous scattered and huge datasets. It overcomes artefacts seen in the spline-interpolation (Fig. 2.17) with close points of large differences and when extrapolating at the borders of grids. Further more it re-scales data with highly un-isotrop densities before interpolation, which reduces for example directional bias of the topography due to the scan-direction from the acquisition. It also handles huge datasets by tiling it in overlapping sub-grids and calculate them separately. The Gridfit-function allows powerful control about the smoothness, the internal interpolation function, the regulariser character, the iterative solver, the tile-size of the sub-grids and their overlapping area. In this study Gridfit is always used with its default parameters. Further details can be obtained from the in-function help of that function.

In order to compare different gridding methods, Figure 2.17 shows an example of a Lidar profile through a small ridge with steep slopes. A random small subset of points were chosen to interpolate the surfaces (at every meter). The deviation between the interpolated surface and the original point cloud reveals some weak points of the methods. The nearest neighbour interpolation introduce strong edgy artifacts in slopes and the linear interpolation underestimates edges (i.e. at distance 25 m in Fig. 2.17).

[8]Matlab is a technical computing software by Mathworks - `mathworks.com`

[9]Matlab Central is an open file exchange platform operated by Mathworks - `mathworks.com/matlabcentral`

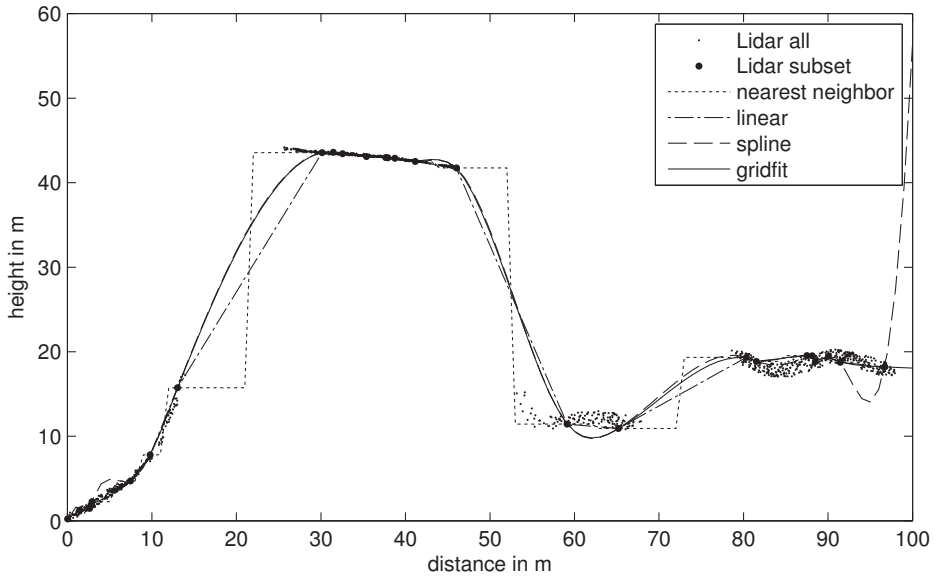

Figure 2.17: Comparison of interpolation methods on a Lidar point-cloud profile of a small ridge with steep cliffs. Small dots representing all points within a swath of 2 m along the profile. Big dots are a randomly chosen subset (1 out of 50) of all points. The for different lines showing the interpolated height at every meter by using only the subset of points. The misalignment of the different methods compared to the original point-cloud illustrate the problems arising from interpolating heterogenous point-clouds.

On the other hand they are very fast. The spline interpolation, which basically fits local polynomial functions to the points by keeping the transition "smooth" between them, can introduce artefacts at close points with relative big height differences (i.e. at distance 5 m in Fig 2.17) and at the borders of the gridded area (i.e. at distance $>$ 90 m). Such artefacts can be minimised by smoothing-parameters of the spline methods.

2.5 Digital Elevation Model analysis

Visualisations of DEM derivatives like slope, aspect, shaded relief, drainage system and roughness can help to interpret landslides (Glenn et al., 2006; Corsini et al., 2007). Furthermore they can be used in addition to other spatial data (e.g. optical images, landuse map) for semi-automatic or automatic detection and classification of landslide bodies (McKean and Roering, 2004; Van den Eeckhaut et al., 2007) or for susceptibility-analysis using among others morphological properties (Greco et al., 2007; Ercanoglu, 2005). They can be derived from several sources at various resolutions, e.g., aerial stereo-photos (>1 m, see Sec. 2.3), Lidar (>0.1 m., see Sec. 2.4), Radar (30-90 m, SRTM), spaceborne satellite images (20 m, Spot).

The following sections present the basics of the quantitative measurements derived from DEM used in this study (slope, aspect, shaded relief, drainage system and roughness). For all following operations it is assumed the DEM is available in a raster format, a matrix of uniformly sampled elevation values derived, e.g., by gridding (see sec. 2.4.3).

2.5.1 Slope and aspect

The slope is the amount of inclination of the terrain surface to the horizontal and the aspect describes in which direction the slope faces. In order to derive the slope and aspect on a pixel basis in a DEM, first the gradients in x- and y-direction are calculated by

$$\nabla x = \frac{\delta z}{\delta x}, \nabla y = \frac{\delta z}{\delta y} \tag{2.1}$$

. From these gradients the slope and aspect can be computed by transforming the cartesian coordinates ∇x and ∇y into polar coordinates θ and slp.

$$slp = \sqrt{\nabla x^2 + \nabla y^2} \tag{2.2}$$

$$\theta = \begin{cases} \tan^{-1} \frac{\nabla y}{\nabla x} & \text{if } \nabla x > 0 \\ \tan^{-1} \frac{\nabla y}{\nabla x} + \pi & \text{if } \nabla x < 0 \text{ and } \nabla y \geq 0 \\ \tan^{-1} \frac{\nabla y}{\nabla x} - \pi & \text{if } \nabla x < 0 \text{ and } \nabla y < 0 \\ \frac{\pi}{2} & \text{if } \nabla x = 0 \text{ and } \nabla y > 0 \\ -\frac{\pi}{2} & \text{if } \nabla x = 0 \text{ and } \nabla y < 0 \\ 0 & \text{if } \nabla x = 0 \text{ and } \nabla y = 0 \end{cases} \tag{2.3}$$

slp is the slope defined as the "absolute" gradient, sometimes expressed in percentage through multiplication by 100. Often, instead of the slope, the slope angle α is used derived by

$$\alpha = \tan^{-1} slp \tag{2.4}$$

α is always in the interval $(0, \frac{\pi}{2})$ or $(0, 90°)$. To obtain the aspect β in a geographical sense (0 to north and increasing clockwise) it is necessary to correct θ by

$$\beta = -(\theta + \frac{\pi}{2}) \tag{2.5}$$

In order to analyse pre- and post-failure morphology of a landslide, slope and aspect maps can help to understand the fundamental morphological properties of a terrain. In the pre-failure analysis the slope angle often contributes as one of the main factors influencing the susceptibility of landslides. In post-failure analysis it may help to distinguish between different morphologies inside a landslide.

Figure 2.18b shows a slope map of a landslide which partly reflects the differences of the landslide blocks indicated in Figure 2.18a, where the Upper Block (UB) near the headscarp of the 1937 Landslide shows higher slopes (25°-45°) than the Body (B) (10°-25°). The slope map of the head area of the Harmalière landslide (part of the study area of this work) is another example (Fig. 2.20a) that reveals the scarps as red strips (steep slopes of 20°-30°) inside the overall blue map (gentle slopes of 0°-15°). The aspect (also called orientation) is sometimes useful to reveal preferential failure orientations (i.e. due to faults or layering of the involved material) or to highlight back-tilted blocks of a landslide, which are orientated in the opposite direction to the general slope (e.g. red lineaments inside the green in the south-west quarter of Fig. 2.20b).

Figure 2.19 shows a terrain representation using slope and aspect at the same time to analyse joint-sets related to rockslides. Here the terrain is colour-coded in the HSV (hue, saturation, value) colour-scheme by assigning the aspect to the hue and the slope to the saturation in order to highlight surfaces with similar 3D-orientations in one view. Slope and aspect maps are also substantial for the shaded relief (Sec. 2.5.2), drainage network (Sec. 2.5.3) and roughness (2.5.4) computation.

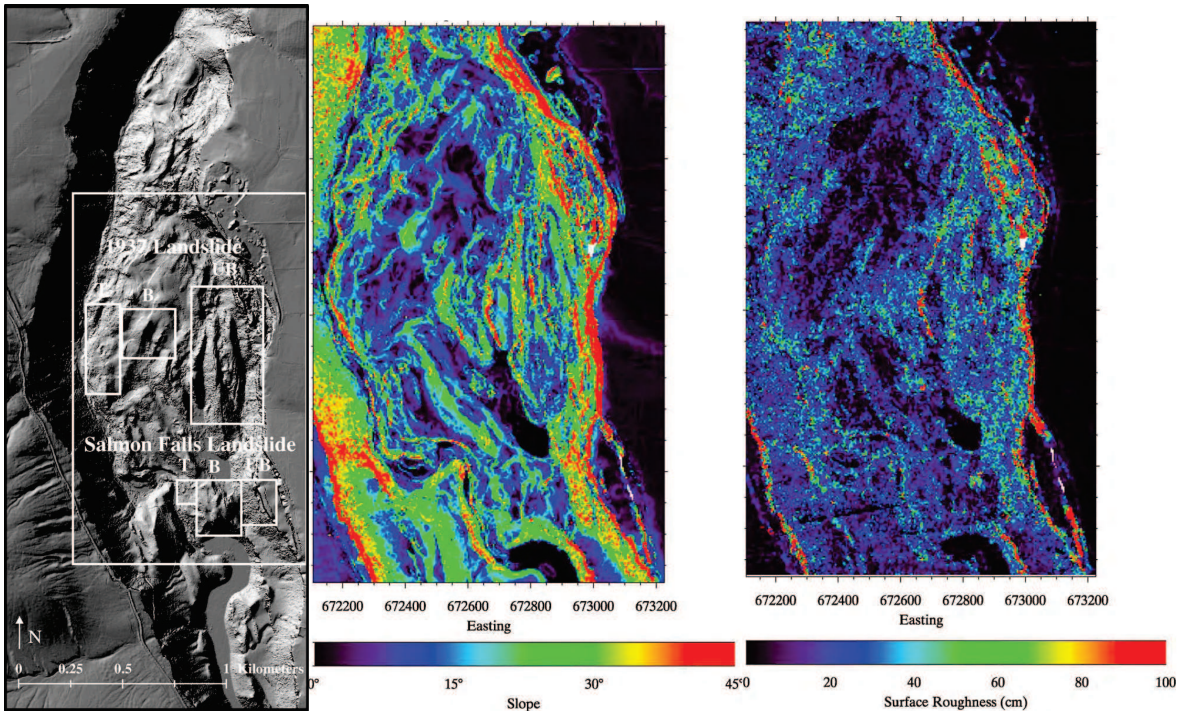

Figure 2.18: Shaded relief (a), Slope angle map (b) and roughness map (c) of the Salomon Falls landslide and the 1938 landslide in the Sinking Canyon area, southern Idaho, USA, from Glenn et al. (2006). The white outer box in (a) shows the area of (b) and (c). UB=Upper Block, B=Body, T=Toe. The displayed roughness is the average RMS-deviation over length scales from approximately 1 m to 5 m.

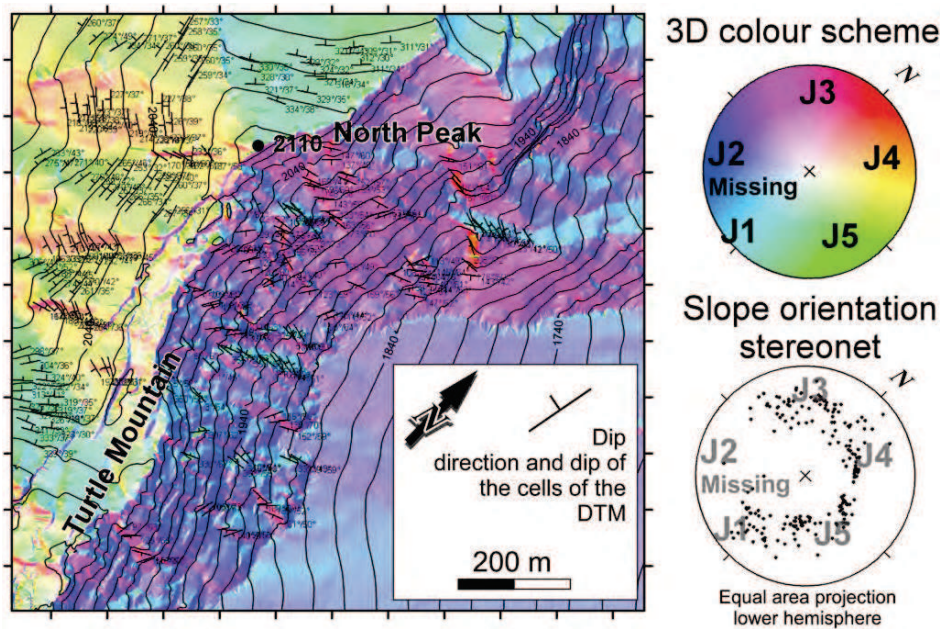

Figure 2.19: Interpretation of the relief of the rockslide scar at Turtle Mountain using COLTOP-3D. The upper stereo-net o the right indicates the color scheme of the map based on the pole of the surface orientation. The lower stereo-net corresponds to the displayed measures of the left map. (from Jaboyedoff et al. (2009))

2.5.2 Shaded relief

A shaded relief is a representation of a DEM imitating the illumination from a simulated sun shining from a predefined azimuth direction ω and zenith ϕ above the horizon. In every pixel a greytone is calculated depending on the slope angle α and aspect β relative to the sun direction. It exists several ways to calculate a shaded relief (or hill-shade) trying to find a realistic, aesthetic and representative depiction of the terrain, for instance taking into account a certain degree of diffusion in the atmosphere, different reflecting properties of the ground or a general slope orientation to locally adjust the sunlight direction. For this study a relatively simple algorithm from ESRI[10] is used given by

$$greytone^* = \cos\phi\cos\alpha + \sin\phi\sin\alpha\cos(\omega - \beta) \tag{2.6}$$

$$greytone = \begin{cases} 0 & \text{if } greytone^* \leq 0 \\ greytone^* & \text{if } greytone^* > 0 \end{cases} \tag{2.7}$$

The resulting *greytone* is in the interval $(0, 1)$ and the whole matrix can be enhanced by adjusting image properties like contrast and brightness. Figure 2.20 shows different shaded reliefs of the same head area of the Harmalière landslide using different lightning directions. It illustrates the importance of the lighting direction for geomorphological interpretation. In this example some scarps are badly seen in some of the images due to their relative orientation towards the lightning direction. Therefore a geomorphological interpretation should always be based on more than one shaded relief map using different lightning.

A shaded relief map of a landslide DEM (e.g. Fig. 2.18a or Fig. 2.5) is a powerful tool to visualise the morphology of a landslide and it uncovers landslide features which are not even visible during field investigations, especially when derived from filtered laser scans in vegetated areas. It is often the basis of geomorphological interpretations (accompanied with aerial photo interpretation and evaluation in the field).

2.5.3 Drainage system

The Drainage system of a DEM represents the theoretical accumulation of water in stream channels resulting from equally distributed rainfall. It is often assumed that only surface flow occurs with no consideration about the kind of surface, so that there is only a dependence on the topography. In order to extract the stream channels of an DTM (digital terrain model), for each pixel the upslope area has to be computed for each pixel, which is the sum of the whole area which would theoretically drain through that pixel. A general problem in all the methods are sinks (or pits). It refers to regions in the DEM which are completely surrounded by higher elevations. It could come from inaccurate DEMs, lakes or subsurface drainage systems. To overcome that, the DEM has to be "filled" by a procedure which raises such a region to the next adjacent saddle point before calculating flow-directions.

In order to calculate flow directions for each grid-cell of the DEM, the first and easiest approach is to assign the flow from each pixel to one of its eight neighbors (D8-method) which was introduced by O'callaghan and Mark (1984) and is widely used in GIS applications. One disadvantage of this method is the discretisation of the flow only in derivatives of 45° (Fig. 2.21A).

[10]ESRI is a software company for GIS, the algorithm is taken from the online help of their ArcGIS software package `http://edndoc.esri.com/arcobjects/9.2/net/shared/geoprocessing/`

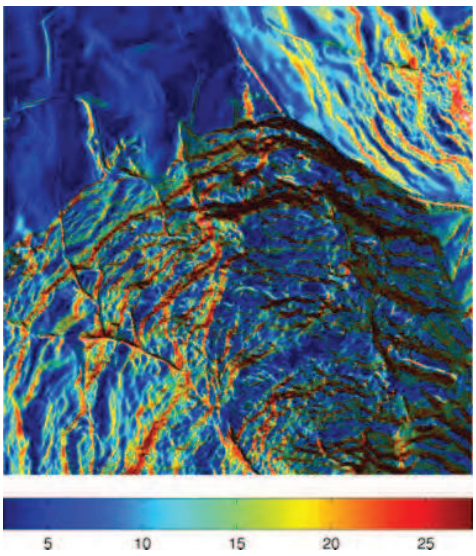

(a) slope in °

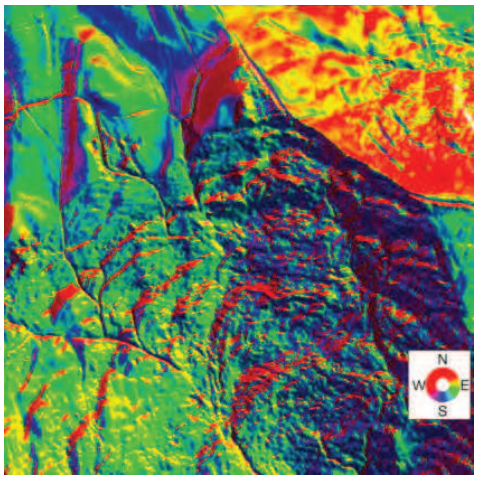

(b) aspect

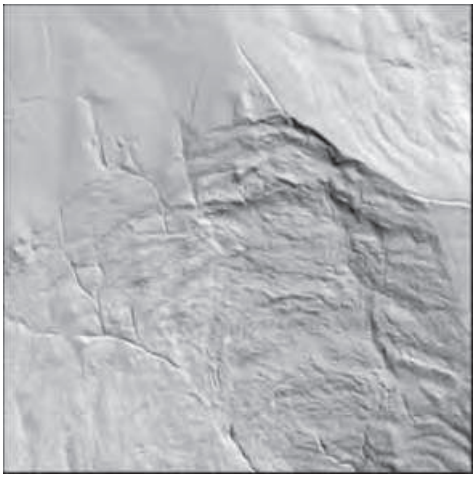

(c) azimuth NE, zenith 45°

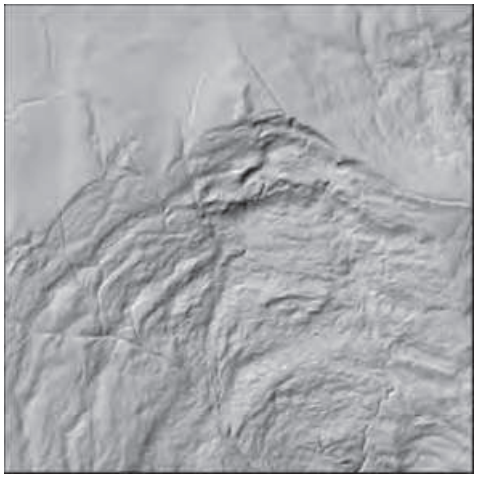

(d) azimuth NW, zenith 45°

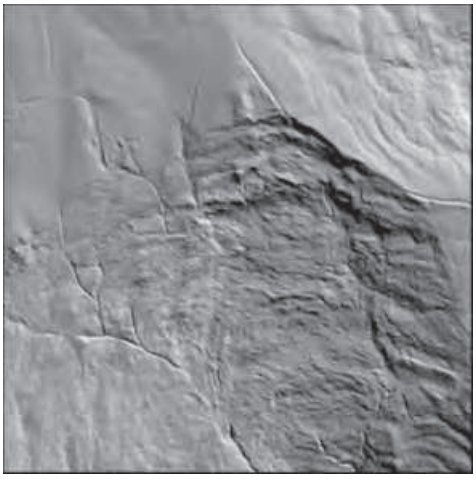

(e) azimuth NE, zenith 30°

(f) azimuth NE, zenith 60°

Figure 2.20: Some morphological derivatives at the head area of the Harmalière landslide from the Lidar-DEM 2006. Slope (a) and aspect (b) are draped on a shaded relief, follwed by different shaded reliefs using different azimuth and zenith angles for the sun. (c) tends to highlight NW - SE scarp directions. (d) tends to highlight NE - SW scarp directions. (e) is missing details in steep slopes facing SW because they are too dark, but shows good contrast for minor undulations on the NW plateau. (f) shows more structure in the steep dark slopes facing SW, but is too bright on the rest of the image and therefore is lacking of showing the details.

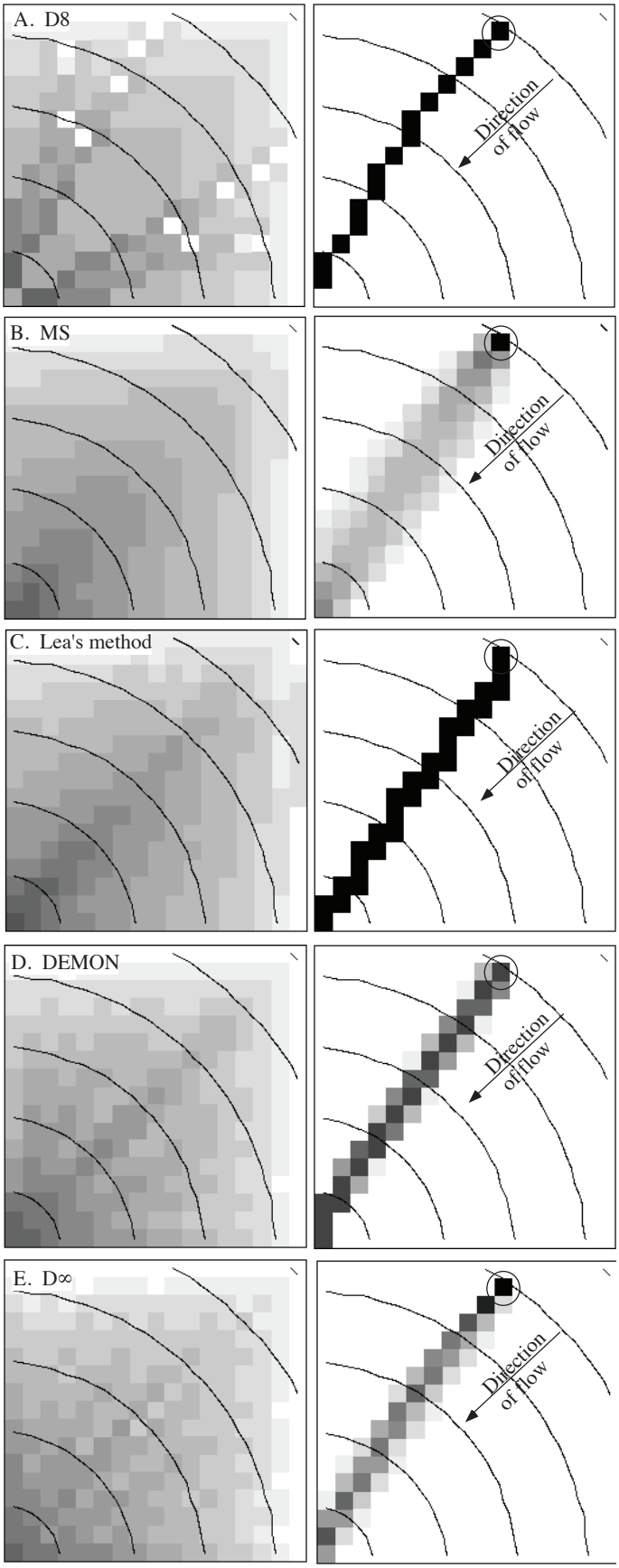

Figure 2.21: Comparison of different methods to compute flow on a DEM grid for an inward cone (black thin lines represent elevation contour lines). Left panel: Upslope area in grayscale (higher values are more dark). Right panel: Influence map from the circled pixel as origin (darker = more water is passing that pixel when the flow starts at the origin). A. D8 method, B. MS method (Quinn et al., 1991), C. Lea's Method (Lea, 1992), D. DEMON (Costa-Cabral and Burges, 1994), E. D∞ method.

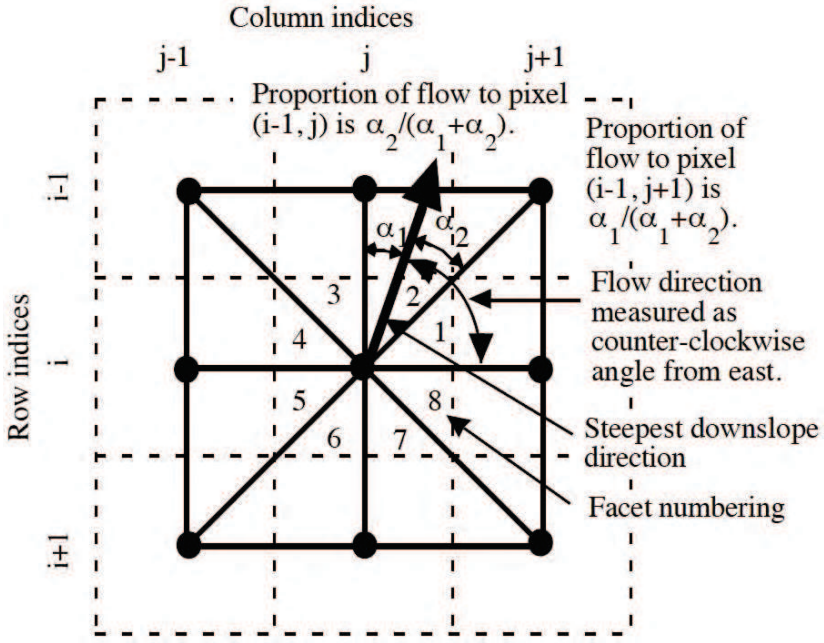

Figure 2.22: The geometry of an DEM-pixel with its 8 neighbors and 8 triangular facets showing the parameters for calculating flow direction and the proportions of flow to the two pixels defining the edges of the steepest downslope facet. (Figure from Tarboton (1997))

To overcome that Freeman (1991); Quinn et al. (1991) proposed a multi-flow approach by dividing the flow to all lower neighboring pixel depending on the slope. The drawback here is that the flow is dispersed over all neighboring pixels with lower elevation and leads to an uncontrollable spreading with distance (Fig. 2.21B). Lea (1992) introduced a flow based on an associated aspect for each pixel with the advantage to assign a flow direction continuously in the interval $(0, 2\pi)$. It avoids a flow influenced by the grid itself and do not add dispersion (Fig. 2.21C). It was extended and implemented in a toolset named DEMON[11] by Costa-Cabral and Burges (1994) which includes dispersion on neighbouring pixels without uncontrolled spreading (Fig. 2.21D). The problem in these methods is that only a single plane is specified in each pixel to determine the aspect and with that the flow direction. This can lead in inconsistent or counter intuitive flow-paths as shown by Tarboton (1997) for example at saddle points. He introduced a new technique (D∞) to overcome this problems (Fig. 2.21E) by calculating 8 triangular facets in a 3x3 window centered on the pixel and computing the flow direction on the facet with the steepest downward slope (see Fig. 2.22). The proportions of the flow given to the two pixels, defining the edges of that facet, depend on the angles between the flow direction and the directions to that pixels (Fig. 2.22).

To calculate the upslope-area from the flow-directions Tarboton (1997) use a recursive-method from Mark (1988). The upslope-area of each pixel is computed as the sum of its own area and the area of upslope neighboring pixel that drain some fraction into it. This procedure is called recursively beginning on the outlet pixel of interest. It calls itself for all pixels that contribute to the upslope area at that outlet. Further details can be read in Tarboton (1997).

A drainage basin (or watershed) is the extend of all pixels contributing to the flow of a particular pixel (called the dependence map of that pixel). This pixel is called the

`spatial_analyst_tools/how_hillshade_works.htm`

[11] DEMON: Digital elevation model networks

outlet of the watershed. Usually an outlet is chosen just before a drainage is flowing into a body of water of the next higher order, like a bigger river, a lake, an ocean or just the limit of the DEM. The drainage basin can be automatically mapped for a certain outlet by using the recursive approach for the upslope-area described above resulting in a matrix where every pixel with a value higher than zero is part of the drainage basin. Sometimes it can be tricky to choose the right outlet pixels to calculate the watershed if the drainage in question is flowing into a lake, which is the case of the Avignonet and Harmalière area. The outlet into the lake can then be found by first calculating the upslope-area from the outlet of that lake. Then defining the border pixels of that lake by its lake-level. And finally choosing all border-pixels that have an upslope-area above a predefined threshold to derive the outlets of significant contributors to the lake. This procedure allows to identify automatically the outlet of the Harmalière and the multiple outlets of the Avignonet watershed.

The knowledge of the drainage network can help to estimate surface runoff contributions to the hydrological system of a landslide. Using auto-extracted drainage networks from high-resolution DEMs could also help identifying preferential flows inside the landslides and may allow conclusions to be drawn about their influence on heterogenous landslide activity. However, runoff models from DEMs are only focusing on surface flow and do not take into account, e.g., seepage and evapotranspiration involved in the hydrological balance of the landslide. Preferential orientations of derived stream channels may also allow speculations about lineaments of material or structural weaknesses of the ground and subsurface.

2.5.4 Roughness

Another derivative of a DEM is the surface roughness, which characterises the degree of elevation variation across a given area, usually along elevation profiles. Although it is a visually intuitive parameter in a shaded relief, it is not easy to quantify it. Many ways to quantify it have been proposed in the literature. A good summary and suggestions about roughness-parameters are given by Shepard et al. (2001). The main roughness-parameters are the rms-height, the rms-deviation or slope, the Hurst-exponent and the breakpoint-scales, if possible associated with their uncertainty. Except for the rms-height, they are 1D-parameters along profiles and cannot be easily adapted in 2D.

To avoid bias from the overall slope of a profile or 2D-matrix, it is necessary to detrend the DEM data before further analysis (Shepard et al., 2001). This processing can be done by subtracting the linear fit in a least square sense from the data. For all equations presented below, it is assumed that the data have been detrended before, so that the mean height is zero and the linear fit is horizontal.

The **rms-height** ξ or standard deviation is defined by

$$\xi = \left[\frac{1}{n-1} \sum_{i=1}^{n} z(x_i)^2 \right]^{1/2}, \tag{2.8}$$

with n being the number of points of the profile and $z(x_i)$ the height at point x_i.

The **rms-deviation** or Allan-deviation ν is defined for a given lag, step or scale, Δx by

$$\nu(\Delta x) = \left\{ \frac{1}{n} \sum_{i=1}^{n} \left[z(x_i) - z(x_i + \Delta x) \right]^2 \right\}^{1/2}. \tag{2.9}$$

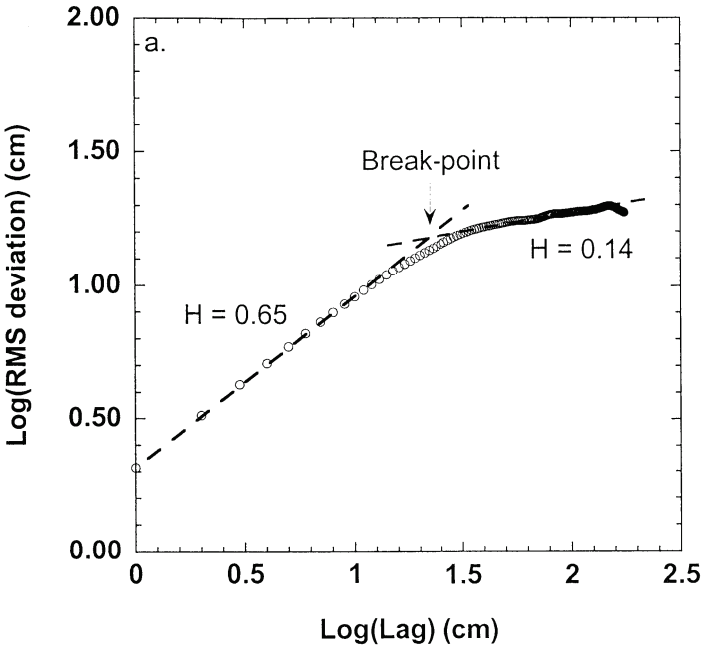

Figure 2.23: Deviogram (rms-deviation versus lag) of a typical profile (from a surface of eroded, silty salt) showing a Hurst-exponent from the smallest scale up to a breakpoint where the Hurst-exponent rapidly changes to a different value. (Figure from Shepard et al. (2001))

This roughness definition is used in Figure 2.18cc which shows a roughness map of two landslides for wavelengths between 1 and 5 m. It can be seen that the most active parts show higher roughness with the highest values near the headscarp in the East. When compared to the slope-map (Fig. 2.18cb), the roughness is positively correlated with the slope-angle, i.e. the steeper the terrain the higher the roughness.

The **rms-slope**, s_{rms}, is the rms-deviation divided by the lag, Δx,

$$s_{rms} = \frac{\nu(\Delta x)}{\Delta x}. \tag{2.10}$$

It is often given as an angle, θ_{rms}:

$$\theta_{rms} = \tan^{-1} s_{rms}. \tag{2.11}$$

For profiles (1D-geometry) this gives only the slope-deviation in the direction of the profile. When extending it for the 2D-case of a DEM, assuming a Gaussian-distributed set of slope surfaces, the roughness-value would be higher by a factor $\sqrt{2}$(Shepard et al., 2001).

The **Hurst-exponent** is derived from a deviogram, which is a plot of the rms-deviation ν versus the lag Δx in a log-log scale (Fig. 2.23). It usually follows a power-law from lower scales and "breaks over" in a different power law. The Hurst-exponents are the slopes of those two power-laws, while the break-point is the intersection of the two lines. The used lag-sizes should be limited to less than 10% of the overall profile length in order to be representative (Shepard et al., 2001).

A last roughness parameter reported in the literature is the **standard deviation of the curvature** (Corsini et al., 2008). The curvature in 2D is the maximum radius of a sphere, which touches the pixel and do not intersect any neighbouring pixel. This parameter can be extended by considering not the direct neighbour pixel, but the pixel in a certain distance (lag) around the target pixel. The curvature is a standard

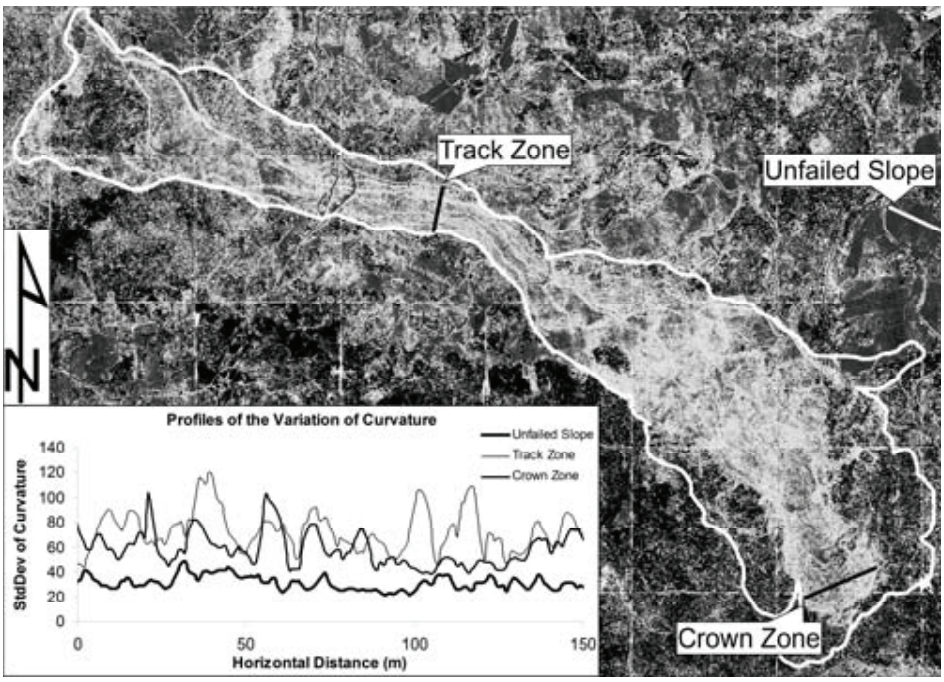

Figure 2.24: Map of standard deviations of the curvature derived from a 0.5 m LiDAR dataset of 2007 at Trafoi Landslide, South Tyrol, Italy. The entire area of reactivation is outlined. The main scarp in the crown and the area characterised by earth flows is clearly distinguishable. Three profiles illustrate the changing curvature in the surface of unfailed slope, the crown and the track zones of the landslide. (Figure from Corsini et al. (2008))

morphometric derivative of DEMs in GIS (Geographical Information System)[12]. Figure 2.24 shows a map of this standard deviation for a zone encompassing a reactivated landslide, which illustrate the potential of the parameter to differentiate between active and non-active landslide bodies.

As the roughness is usually anisotropic, a way to extend the roughness from 1D-profiles to 2D-DEMs is to compute the roughness at pixel scale along small profiles with two perpendicular directions, i.e. North-South and East-West or along and perpendicular to the slope. The latter case is further elaborated in Section 3.2.7.

2.6 Displacements from multi-temporal images

Comparison of images or DEMs acquired at different times over a landslide can give information about the displacements that occurred between the different dates. This analysis can be done visually by an expert to spot some evolutions, but also by automatic image analysis to derive more quantitative results (e.g. a surface velocity map, Fig. 2.1). In this section we focus on the sub-pixel correlation technique, which has been applied on our studied area. In order to measure changes between two images or DEMs, a first requirement is that the displacement need to be high enough with respect to the ground resolution of the images. By using sub-pixel correlation techniques, a rule of thumb is that measurable displacements can be approximately as low as one tenth of the image resolution, depending on its quality. Second, the matching kernel (i.e. the small pixel window around the feature to track) need to be unique in its neighbourhood to avoid false-matching. Unsuitable cases would be a flat area in

[12]The curvature can e.g. calculated in Grass-Gis (an open source GIS - `grass.itc.it`) with the function r.param.scale.

a DEM or a waterbody in an aerial photo. Third, the matching kernel need to stay identifiable between the images, e.g., a stable block of a transitional landslide can be tracked, but a rotational landslide which collapsed into a fast mudflow can not, due to the chaotic change of the matrix. Moreover, if the movement of the kernel is affected by significant rotational (in the horizontal plane) or scale variations, more advanced tracking techniques are needed.

In this Section will be described the basic techniques for image cross-correlation (Sec. 2.6.1) and the displacement extraction principle using searching windows (Sec. 2.6.2), which can be similarly used with optical images, DEMs or derivatives (e.g. slope maps, filtered images, etc.). Finally Sections 2.6.3 and 2.6.4 outline the specific problems when applying these methods to aerial photos and DEMs derived by aerial laser scans (ALS).

2.6.1 Image cross-correlation

Given two signals s_1 and s_2, which could be elevation, shaded relief, slope or radiometric values, it is possible to compute by a measure expressing how much they are related to each other, that is their similarity. An usual way to do it is to compute the covariance, which is defined as

$$\mathrm{cov}(s_1, s_2) = \overline{(s_1 s_2)} - \bar{s}_1 \bar{s}_2, \tag{2.12}$$

with the overline symbolizing the average operator. The covariance is high if s_1 and s_2 similar and small if not.

To standardise the covariance in an interval $(-1, 1)$, with 0 for uncorrelated, 1 for completely correlated and -1 for completely inverse correlated, the covariance can be divided by the product of the standard deviations of the two signals. This is called the correlation-coefficient, ρ_{12}, given by

$$\rho_{12} = \frac{\mathrm{cov}(s_1, s_2)}{\sigma_1 \sigma_2}. \tag{2.13}$$

The cross-correlation (or cross-covariance), $(s_1 \star s_2)$, is the sliding dot product of the two non-complex signals s_1 and s_2, given by

$$(s_1 \star s_2)(\Delta x) = \sum_x s_1(x) s_2(\Delta x + x). \tag{2.14}$$

It is basically the covariance computed for every shift Δx of the signal s_2 relative to signal s_1. Δx at the maximum of the cross-correlation function $(s_1 \star s_2)$ is then the best estimated shift between these signals, assuming their are similar enough. This principle can be extended for 2D-signals (or images) by

$$(s_1 \star s_2)(\Delta x, \Delta y) = \sum_{x,y} s_1(x, y) s_2(\Delta x + x, \Delta y + y) \tag{2.15}$$

in order to get the shift in Δx and Δy at the maximum of the correlation-matrix $(s_1 \star s_2)$.

The processing of the 2D-cross-correlation is rather time-consuming. To speed up the computing the cross-correlation can be computed with the help of the Discrete Fourier Transformation (DFT). The DFT, $S(u, v)$, for two-dimensional non-complex signals, $s(x, y)$, of size $M \times N$ is given by

$$S(u, v) = \mathcal{F}s = \frac{1}{MN} \sum_{x=0}^{M-1} \sum_{y=0}^{N-1} s(x, y) e^{-i2\pi(ux/M + vy/N)}. \tag{2.16}$$

This results in a matrix S of complex numbers with the same size $M \times N$. Simply said the amplitudes and phases of these complex numbers describe the sinusoidal components of the input signal s. The inverse discrete Fourier transformation (DFT) is given by

$$s(x,y) = \mathcal{F}^{-1}S = \frac{1}{MN}\sum_{x=0}^{M-1}\sum_{y=0}^{N-1} S(u,v)e^{i2\pi(ux/M+vy/N)}. \tag{2.17}$$

The circular convolution theorem states that multiplication in the frequency-domain (or Fourier-space) is the same as the convolution in the spatial domain. Convolution is the same as cross-correlation, but with an transposed second signal (compare with eq. 2.15). It is given by

$$(s_1 * s_2)(\Delta x, \Delta y) = \sum_{x,y} s_1(x,y)s_2(\Delta x - x, \Delta y - y) \tag{2.18}$$

This leads to the cross-correlation theorem, which states that the cross-correlation can be expressed in the Fourier-space as the multiplication of the Fourier-transforms with one of them conjugated (*):

$$(s_1 \star s_2) = \mathcal{F}^{-1}\big(\mathcal{F}(s_1)^*\, \mathcal{F}(s_2)\big). \tag{2.19}$$

This speeds up the computation and allows to use the DFT-registration algorithm of Guizar-Sicairos et al. (2008) to obtain the shifts also with sub-pixel accuracy. Sub-pixel shifts can be derived by up-sampling the original images with a sampling rate of the desired accuracy. This would result in large memory usage and computation time. It can be avoided by obtaining a maximum peak in the correlation-matrix using the original resolution and then only producing an up-sampled correlation-matrix around this first estimate (Guizar-Sicairos et al., 2008) by using the Fourier-transforms of the signals. This is more accurate than to only up-sampling the first correlation matrix, because the whole information of the original images is directly used (Guizar-Sicairos et al., 2008).

One drawback by using the DFT for cross-correlation is that the DFT produces always circular convolution. To overcome that, sequences have to be zero-padded so that circular wrap-around always wraps over zeros to avoid mis-matching. Another problem using the DFT is the not normalised cross-correlation matrix, because the normalised form of the cross-correlation does not have a simple frequency domain expression (Lewis, 1995). It has no influence when finding the best shifts by choosing the maximum correlation-coefficient, but does not allow to compare this correlation-coefficient with those obtained from other correlation matrices. This could be overcome using precomputing integrals of the image and image^2 over the search window (Lewis, 1995), but is not implemented in the procedures of this study.

2.6.2 Displacement extraction

In order to derive a displacement map, every pixel in the reference image (usually chosen to be the older image) is assessed in a loop. Figure 2.25 illustrates such a neighbourhood around one pixel. First, the reference kernel and the search kernel are extracted from the reference image and the search image (the image with displacements relative to the reference image). The reference kernel is than zero-padded to match the size of the search kernel and the sub-pixel displacement (dx, dy) is obtained finding

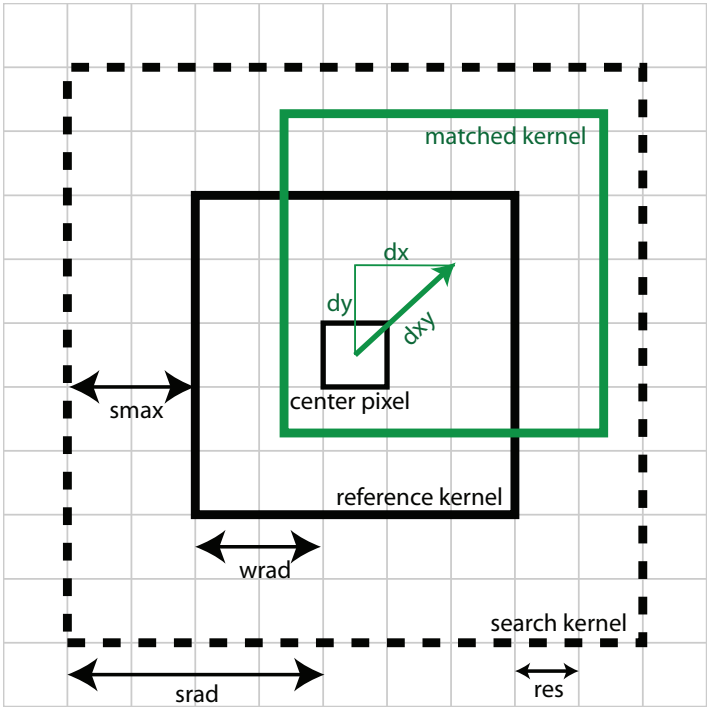

Figure 2.25: Geometry of the image displacement detection at a single point. The reference kernel extracted with the window radius (wrad) around the center pixel from the reference image is used to search for the best fit inside the search kernel extracted from the search image with the search kernel radius (srad) around the center pixel. The displacement in East-West (dx) and North-South (dy) direction is derived from the DFT sub-pixel image registration (see text for details). The maximum displacement (in dx, dy) detectable is limited by the search radius smax ($= srad - wrad$).

the maximum value in the correlation-matrix of the DFT-registration algorithm (see Sec. 2.6.1).

This procedure works best with a small search radius as the chance of finding false matches is limited. In order to obtain large displacements without introducing false matches a pyramidical approach is applied. Therefore, the original image is resampled with a coarse resolution and a first estimate of displacements are obtained. Then these displacements are used to define the initial center pixel of the search kernel when obtaining the displacements from the high resolution images. The number of intermediate levels can be adapted to the complexity and the a priori knowledge of the landslide's displacements.

2.6.3 Displacements from Aerial photos

Special problems arise when using multi-temporal images for displacement extraction acquired by mobile platforms (i.e., satellites, planes, helicopters or drones). The aerial images processing steps usually include the co-registration of multiple images acquired at one time to obtain ortho-photo mosaics at every time-step. For more accurate displacement detections, the multiple ortho-photos need also to be co-registered, to minimize errors not compensated during the ortho-photo processing. Or better, all photos of all time-steps are co-registered in one model to avoid decrease of detail due to multiple interpolation steps as introduced by (Leprince, 2008) and implemented in the software Cosi-Corr[13]. In this study the accuracy of the obtained ortho-photos were

[13] `http://www.tectonics.caltech.edu/slip_history/spot_coseis/index.html`

not high enough (up to tenth of meters) to obtain displacements with respect to the expected order of magnitude (meters).

One difficulty in the registration steps arises from the use of recently obtained ground control points for the registration of old aerial photos as they could have moved meanwhile. This can be avoided by only using GCPs outside of the landslides, which leads on the other hand to lower accuracies inside the landslides. This is even more challenging with old photos due to incomplete camera calibration reports and the overall lower technical precision of the equipment. Another problem is the landcover changes between different time-steps, e.g. the agricultural fields due to their changing seasonal cultivation status can completely change in brightness on aerial photos. Therefore different image filters could be used to homogenise the colours, but maintain structural shapes, e.g. an absolute gradient filter.

2.6.4 Displacements from aerial Lidar DEMs

When applying the subpixel image correlation technique to get displacements from multiple laser scans, several factors can influence the quality of the correlation process. First of all the number of points used to grid the area of the reference and search kernel effect the qualities of the DEMs (Fig. 2.26(a)(b)). If the number of points is not high enough to significantly represent the terrain in both DEMs at that location, the kernels will correlate at a somehow random displacement. The number of points is mainly determined by the Lidar acquisition velocity and repetition near that area, but is also decreased by filtering out some point classes (e.g. buildings, vegetation). If the (normalised) DEMs of both kernels are relatively flat, the correlation will be very high, but insignificant. To have a more robust correlation the variance of the normalised DEM need to be high. In flat areas this can be achieved by not only using the bare earth model, but including other classes like high vegetation and buildings. The drawback is that especially trees can appeal quite different in two DEMs, due to their growing in time or to different scan angles.

Another problem arises when using gridded DEMs resampled at too high resolutions, especially in flat terrain. The Figures 2.26(c)-(h) show the shaded relief of a flat field of the 2006 and 2009 Lidar scans gridded at resolutions of 1 m, 0.5 m and 0.25 m. As (c) and (d) seem to be quite similar and therefore are expected to give a correct match. The grids (e)-(h) exhibit linear undulation artifacts coming from systematic height bias between overlapping parts of different flight-paths during the acquisition. If these lineaments are orientated in similar directions in both DEMs, positive amplifications in the convolution during the correlation-process at certain displacements can lead to false matching.

To overcome some of these drawbacks, several parameters determining the quality of the correlation matrix are kept for every derived displacement, for instance the number of original points used to grid the DEM in each kernel, error of the DFT-registration process, variance of the reference kernel and different parameters describing the quality of the correlation-matrix. For DEMs, once the horizontal displacement (dx, dy) is successfully extracted, the vertical displacement can be derived using the difference between the average elevation of the point-clouds inside the matched kernel and the reference kernel (Fig. 2.25). Due to the sub-pixel precision of the horizontal displacement, this can not be achieved using the already gridded kernels, as the grid at the matched kernel is not directly computed during the DFT-registration.

In this study a specific strategy for a reliable displacement extraction from multiple Lidar DEMs has been developed and is detailed in Section 4.2.

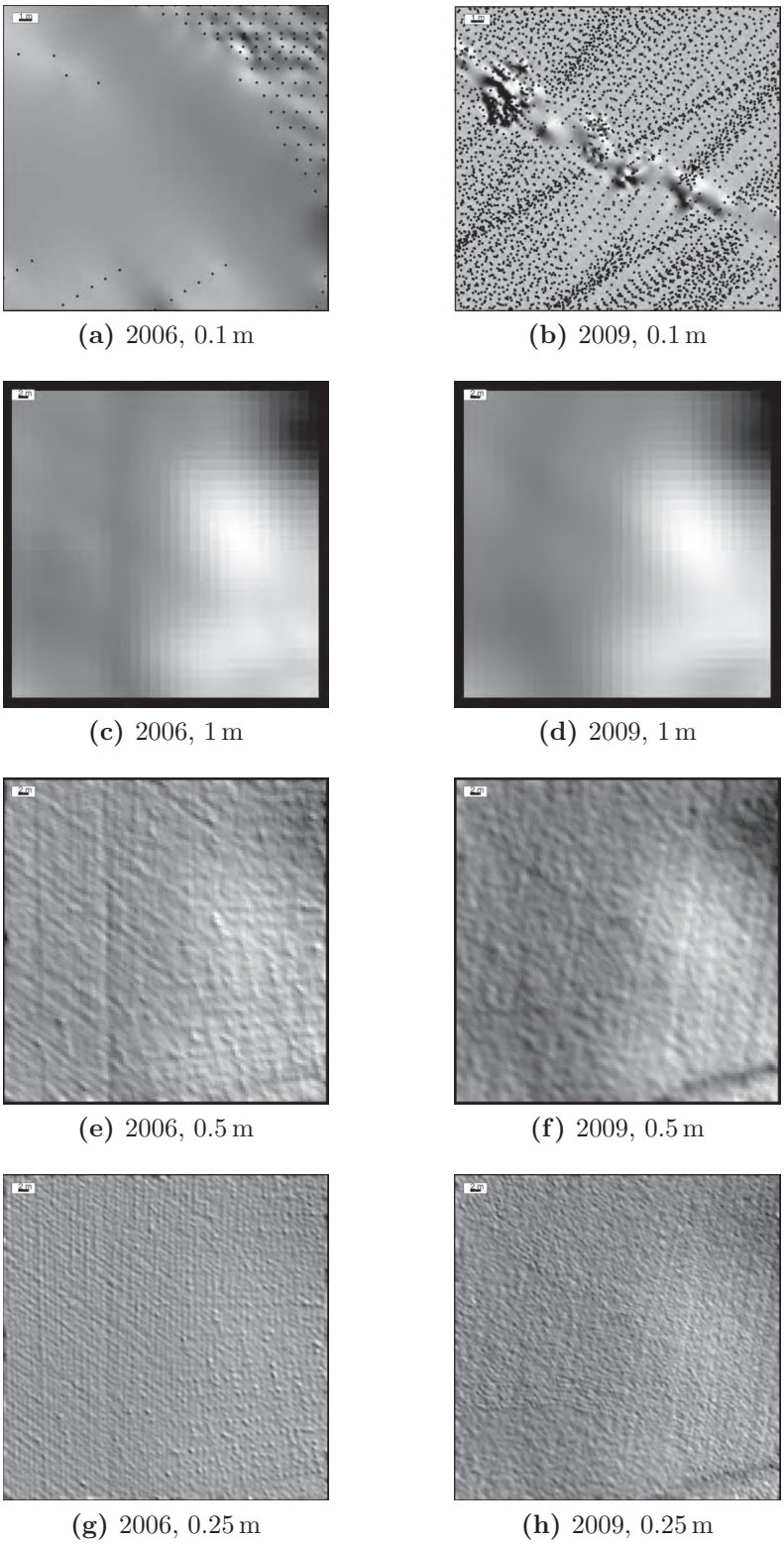

(a) 2006, 0.1 m **(b)** 2009, 0.1 m

(c) 2006, 1 m **(d)** 2009, 1 m

(e) 2006, 0.5 m **(f)** 2009, 0.5 m

(g) 2006, 0.25 m **(h)** 2009, 0.25 m

Figure 2.26: Shaded relief Lidar grid samples illustrating gridding artifacts which are problematic in the displacement extraction process. The acquisition year and grid resolution is given under each subfigure.
(a) and (b) representing the same location in the two Lidar sets of 2006 and 2009 with different point cloud densities (black dots), resulting in different gridded DEMs.
Subfigure (c) to (h) are illustrating the influence of different grid resolutions on the smoothness of the DEMs on a flat field. At higher resolutions linear undulations are visible due to different bias between swath-paths of the Lidar acquisition.

2.7 Spaceborne SAR interferometry

As illustrated in Section 2.1.2, SAR interferometry can be used to derive velocities of slow moving landslides by different approaches. This section focuses only on the data and the methods selected for the Trièves landslides application. That is ERS-1 and ERS-2 satellite images acquired by a Synthetic Aperture Radar (SAR) from 1992 to 2008 in full resolution stripmap mode and processed through a Permanent Scatterer time-series approach. The spatial extent of the selected images is about 100 x 100 km, which is more than necessary to cover the study area. The images cover the whole Trièves area but also its surrounding area including Grenoble city (see Figure 2.27). However, as the processing chain is starting from the raw data (Level 0) to keep control on all the images parameters, it is, in practice, easier to get the default raw data size that corresponds to the full swath of the instrument (100 km). Furthermore, the study could benefit from the presence of the Grenoble urban area as a test-site for the standard processing chain. The raw ERS radar data have a poor kilometric spatial resolution, but the SAR instrument acquired the data in such a way that, through the processing step called focalisation, the image resolution can be dramatically improved to about 20 m x 5 m on flat terrain. The data acquisition, geometry, and SAR processing are further explained in Section 2.7.1.

Deriving information about the ground displacement from SAR images is not a straightforward process. It can be done by combining amplitude and phase information of two SAR images acquired at different time, and also orbital and topography data. This is called satellite differential SAR interferometry (InSAR), whose principles are given in Section 2.7.2. However, although conventional InSAR analysis can potentially achieve centimetric to millimetric accuracy of displacement measurement, this approach can be severely limited under certain conditions. For instance, in the case of rural and vegetated area, not all the pixels can be used because of the rapid temporal

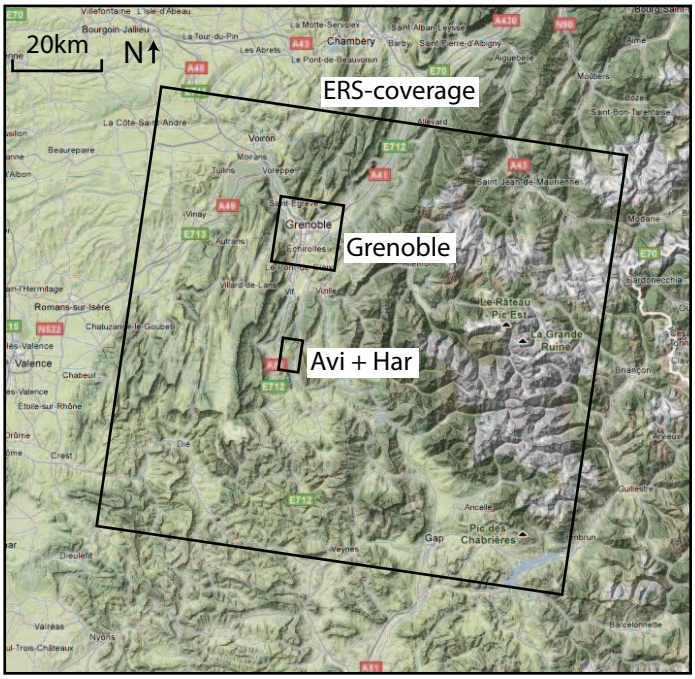

Figure 2.27: Image extent (about 100 x 100 km) of the ERS1/2 SAR images (descending track number 65), the sub-frame of the Grenoble study case and the subframe used for the analysis of the Avignonet and Harmalière landslide (Avi + Har).

decorrelation of the signal (as fast as a few days for C-band ERS data), that can affect a significant amount of the pixels making their measurements not reliable. Other problems can arise from an insufficient temporal sampling with respect to the ground deformation rate. This is because InSAR measurement of one pixel is not absolute, but relative to the other pixels, and also is only known modulo half the wavelength (see Sec. 2.7.2), that is 2.8 cm for ERS data. In practice, if during 35 days (the typical time interval between two successive ERS images) the finite displacement of one pixel with respect to the closest reliable pixels exceeds 2.8 cm, there will be an ambiguity of the measurement.

To overcome these limitations, which both occur in the study area, a time-series approach rather than single pairs of images analysis is needed. As explained in Section 2.7.2 the Permanent Scatterers (PS) approach has been chosen and is implemented through the Gamma software[14] processing chain. A short introduction to the Permanent Scatterers concept is given in Section 2.7.3. The number of points with displacement information in the final PS result is a subset of pixels from the SAR images and its density depends on the availability of permanent scatterers in the target area. The standard Gamma Interferometric Point Target Analysis (IPTA) processing is illustrated on the Grenoble subsidence case (Sec. 2.7.4) using the same dataset. The Grenoble case has been used as a test-case to master and adjust the procedure for this set of SAR-images. It is an "easy case", because of its urban environment, which offer a good density of PS, and because the subsidence phenomena show globally a low deformation rate (a few mm/year across the city). In Chapter 4.3, results from the application to the more difficult case of the Avignonet and Harmalière landslides are shown, and advanced methods are also proposed and applied to improve the results. Further details about SAR and Insar processing can be obtained, among others, from Simons and Rosen (2007); Hein (2004); Franceschetti and Lanari (1999), about PS-analysis from Simons and Rosen (2007); Kampes (2005); Usai (2001) and about their applications on landslides from Colesanti and Wasowski (2006); Fruneau et al. (1996). Studies using the IPTA module of the Gamma-software are given by Strozzi et al. (2005); Wegmüller et al. (2004); Werner et al. (2003).

2.7.1 Synthetic Aperture Radar (SAR) images

In order to understand the results, their significance and the applicability of the SAR-based methods, some basic principles and terms about SAR imagery need to be explained, setting the focus on the ERS SAR instruments and their operability in mountainous terrain. The similar SAR instruments on board the two ERS satellites have been operational from 1992 - 2000 on ERS-1 and 1995-2011 on ERS-2.

Both satellite followed a sun-synchronous near-circular polar orbit with an inclination of 98° (with respect to the equatorial plane) at an altitude of about 780 km a repeat cycle of 35 days (for almost all its lifetime, except a few months with a repeat time of 3 days and 168 days that are excluded from the dataset). Consequently, as the Earth rotates under its orbit, each satellite flights half of its cycle either roughly (with an deviation angle of about 10°) from North to South (descending pass) or from South to North (ascending pass) during an image acquisition. Because the SAR instrument is right-looking (with respect to the flight direction, see acquisition geometry in Figure 2.28a), the looking direction is respectively westwards for descending orbits and east-

[14]Gamma is a SAR processing software by Gamma Remote Sensing `http://www.gamma-rs.ch/`

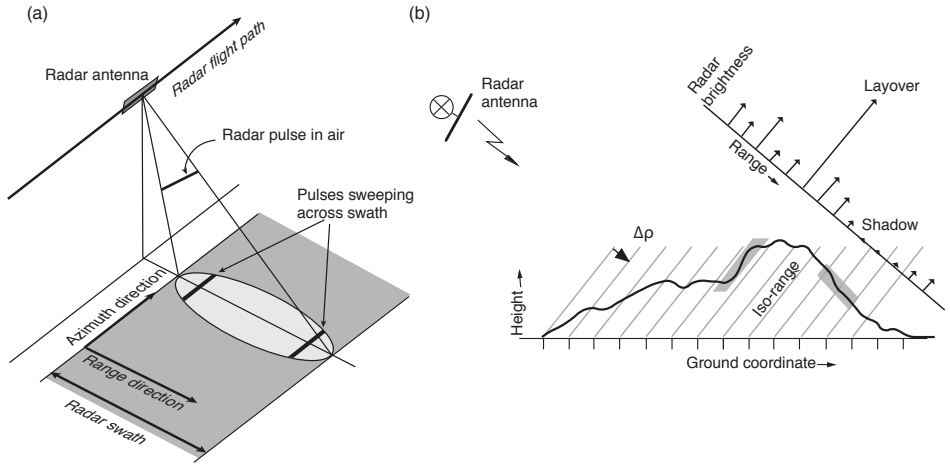

Figure 2.28: Real aperture acquisition geometry. (a) Typical imaging scenario for a SAR system. The platform carrying the SAR instrument flights along azimuth direction. The radar antenna points to the right-side covering an ellipsoidal footprint in the range direction with one pulse. With multiple pulses emitted and received along the track, the full swath is recorded. (b) The pulse of length $\Delta\rho$ emitted by the Radar antenna is backscattered from the terrain. After image formation, the radar return is resolved into an image in range-azimuth coordinates. The profile is shortened at slopes towards the antenna and extended at slopes away from the antenna. Too steep slopes towards the antenna produce layover (multiple returns at the same time from different locations) and too steep slopes away from the antenna produce shadow (out of the line of sight and therefore no return). Figure from Simons and Rosen (2007, p.393).

wards for ascending orbits. In this study, it is focused on the descending data as this archive was more important than the ascending archive.

The Radar antenna, mounted on the satellite, is moving along the satellite flight track (called azimuth direction)sending pulses in the direction perpendicular to the flight path and looking to the right (called range direction). The angle from the vector normal to the earth surface and the incident ray is the incidence angle, which is for ERS-1/2 between 20° at near range and 26° at far range (23° at mid swath). Each emitted pulse is sweeping across the swath illuminating an ellipsoidal footprint from which the baclscattered signal is recorded on board (Fig. 2.28a). The received return signal is correlated with the sent signal, and intensity (brightness) and phase is stored sorted by arrival time. Figure 2.28b illustrates the effect of foreshortening, layover and shadow due to the acquisition geometry. Gentle slopes of the terrain in range direction (lower than the incident angle) will lead into foreshortening in the SAR image, which results in brighter pixels with spatial shortening at slopes towards the antenna and darker pixels with spatial stretching at slopes away from the antenna respectively. If a slope towards the antenna exceeds the incidence angle, multiple returns are received at the same time, resulting in layover with very bright and spatial distorted areas. If a slope away from the antenna exceeds the incidence angle, it can not be reached by the pulse and therefore gives no return, resulting in dark shadow in the SAR image.

To achieve a resolution in range of 8 m (that corresponds to a cell resolution of 20 m on flat terrain for ERS taking into account the 23° incidence angle), the length ($\Delta\rho$) of an emitted pulse (Fig. 2.28b), should be about 60 ns. As it is technically difficult to emit the necessary energy for a proper return in such a short time, a longer frequency-modulated signal (chirp) is used and lasts 37 μs. The higher temporal resolution, and therefore higher resolution in range, is then achieved by demodulation of the return signal. The synthetic derived "compressed" pulse length (e.g. 64 ns at ERS-1), leads

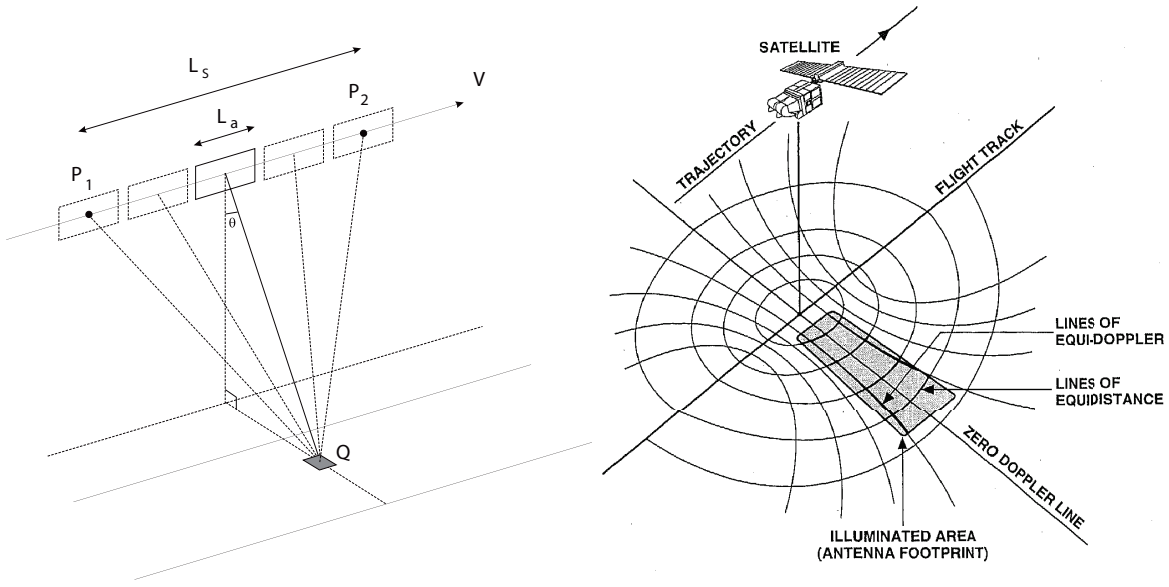

(a) **(b)**

Figure 2.29: The Doppler effect in SAR processing. (a) The Doppler-history of the point Q is obtained by receiving the return from different angles in azimuth direction during the flight-over of the satellite. (b) The footprint of the antenna at one pulse. Lines of equidistance connect terrain-points which have the same distance to the satellite. Lines of equi-Doppler connect terrain-points showing the same Doppler-effect, meaning they have the same velocity relative to the satellite. Figure from Usai (2001, p.10)

to the range resolution of 20 m.

With the ERS-satellite velocity of 7.5 km/s and a pulse repetition frequency (PRF) of about 1.7 kHz, a pulse is emitted approximately every 4 m resulting in widely overlapping footprints. This implies on the other hand, that a point on the ground is "seen" by multiple pulses (several hundreds) resulting in blurring along the azimuth direction in the raw data. As the pulses are received from different angles at one point on the ground (Fig. 2.29a), the relative velocity between the antenna and that point varies during the flyover. This leads to different frequency-shifts of the returned pulses due to the Doppler effect (Fig. 2.29a). The Doppler-effect also slightly changes in range direction due to the different distances from the flight path. Finally, every point on the ground has its unique Doppler-history (Doppler-frequency vs. time). Figure 2.29b illustrates the lines of equal Doppler-frequencies on the ground relative to the satellite position. The Doppler-history is then used to separate and stack the pixels at one location from the raw data, which synthetical increases the sharpness in azimuth direction.

The processing of the raw-SAR data by compression (or focalisation) in range and azimuth direction, results in the SLC image (Single Look Complex), which represents a spatial image with complex numbers in each pixel, holding the intensity and phase information of the corresponding location on the earth surface (ground resolution-cell).

Due to the different pixel dimensions in azimuth (4 m) and range (20 m), the SLC is five times elongated in azimuth direction. In order to compute a nearly equally scaled image and minimise the high frequency brightness variation (called speckle), the SLC image can be resampled by averaging each 5 pixels in azimuth, into an image called 5x1 multi-look image (MLI) (see e.g. Fig. 2.34 and Fig. 4.29). Sometimes smaller MLIs are calculated averaging in azimuth and range by 10:2, 15:3 etc., to further smoothing

the images. In the case of a descending orbit (westward look) the image need to be flipped in E-W-direction for a "natural" representation, because the first arrival (near range) is returned from the East-most ground, but is stored in the first (left-most) column of the image.

2.7.2 Interferometric SAR (Insar)

The obtained phase in each pixel of an SLC image (see previous section) is related to the distance between the sensor and the corresponding ground resolution-cell. Considering that the emitted electromagnetic wave on its two-way travel from the antenna and the ground has covered a large but integer number of oscillations. Assuming a second measurement with similar conditions except a slightly longer distance along the travel path (the range change being smaller than the wavelength λ), the pulse will have to travel slightly more, resulting in an additional fraction of the next oscillation. The phase difference between the two signals ϕ is then directly related to a change of the distance along range (between the antenna and the terrain) Δr by

$$\phi = \frac{4\pi}{\lambda}\Delta r \tag{2.20}$$

The wavelength λ is 5.6 cm for ERS-1/2. The image representation of the phase differences calculated for each pixel of two SAR images is called interferogram. Since the phase differences can only be measured in the interval $[0, 2\pi]$, the interferogram is characterised by patterns of fringes (as seen in the upper left in Fig. 2.36). Each fringe is representing one phase cycle (Fig. 2.30), which is after Eqn. 2.20 the half of the wavelength λ (2.8 cm in the case of ERS-1/2).

Starting from 2 single look complex (SLC) images, the following steps are necessary to obtain displacements from InSAR:

- Precise co-registration of the two SLC images. It can be done in four steps: (1) rough offset estimate, (2) precise offset estimate, (3) deformation model using using polynomial estimation, (4) resampling of one image in the geometry of the other.
- Complex multiplication of the two SLC coregistered images and generation of the interferogram
- Correction of the interferogram for different distortions due to the slant radar geometry, topography (need a DEM and orbital data) and correction from atmospheric effects (if necessary and possible)
- phase unwrapping (see Fig. 2.30) to transfer interferometric patterns into displacements

The Co-registration is starts by using a rough estimate of matching the two SLCs. To estimate the rough offsets in azimuth and range direction between the two images, either tie-points in both images are used or precise orbits[15] by determining the positions of the satellite using the start and end time of the images. In order to derive phase differences the SLCs need to be superimposed at a sub-pixel level near an accuracy of

[15]Post-processed precise orbit calculations for ERS-1/2 and Envisat are among others available from the Department of Earth Observation and Space Systems of the TU-Delft, Netherlands - `http://www.deos.tudelft.nl/ers/precorbs/orbits/`

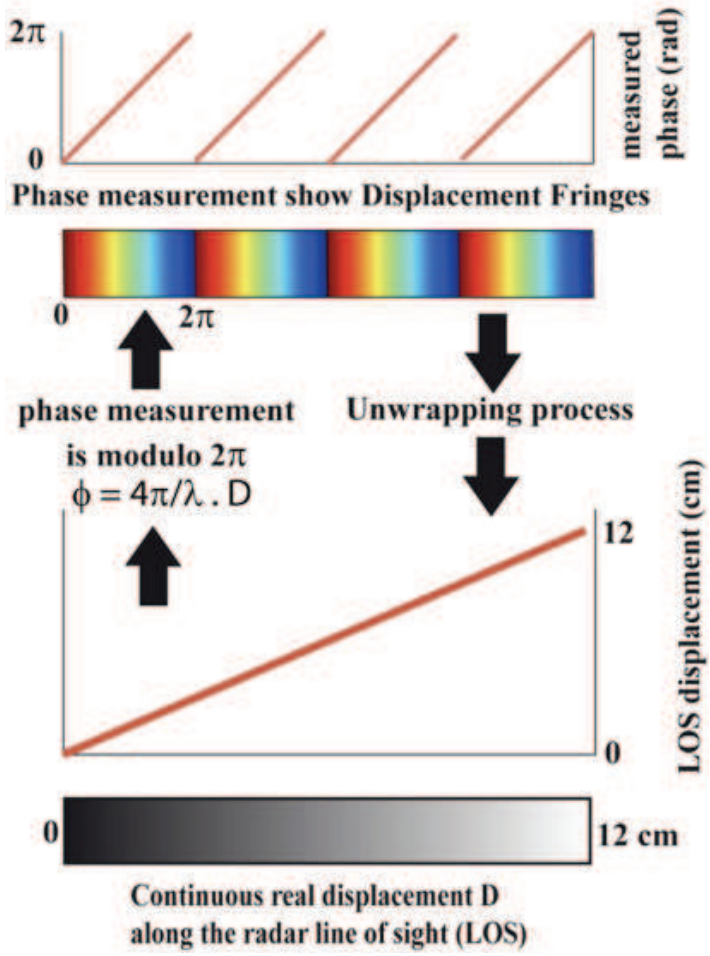

Figure 2.30: Principle of measuring and unwrapping an interferometric phase from/to a ground displacement in the Radar line of sight (LOS). E. Pathier (unpublished)

1/8th of a pixel (Geudtner, 1995). Therefore, first, a precise linear offset is calculated using cross-correlation (see Sec. 2.6) of the intensity images or a coherence based method. However, if the perpendicular baseline between the two images is near the critical baseline (1100 m for ERS (Usai, 2001)), the latter method will fail due to baseline-decorrelation (Wegmüller et al., 2003). After deriving the precise linear offset, a polynomial function is estimated using least-squares registration (Wegmüller et al., 2003). Finally the polynomial function is used to resample the co-registered SLC (slave) into the geometry of the reference SLC (master).

After the co-registration of the two SLCs each pair of corresponding pixels, contains the complex signals S_1 and S_2 which can be expressed as

$$S_1 = |S_1|e^{i\phi_1} \qquad S_2 = |S_2|e^{i\phi_2}, \tag{2.21}$$

S_1 and S_2 are then complex multiplied

$$I = S_1 S_2^* = |S_1||S_2|e^{i(\phi_1 - \phi_2)} = |I_0|e^{i\phi} \tag{2.22}$$

I corresponds to the complex interferometric pixel-value. The interferometric phase ($\phi = \phi_1 - \phi_2$) is the actual interferogram which is the sum of different contributions, one of them being the displacement between the two dates of acquisition (see Fig. 2.32).

If the satellite does not pass exactly at the same position during the two acquisition, which can be quantified by the perpendicular baseline between the two orbit passes (see

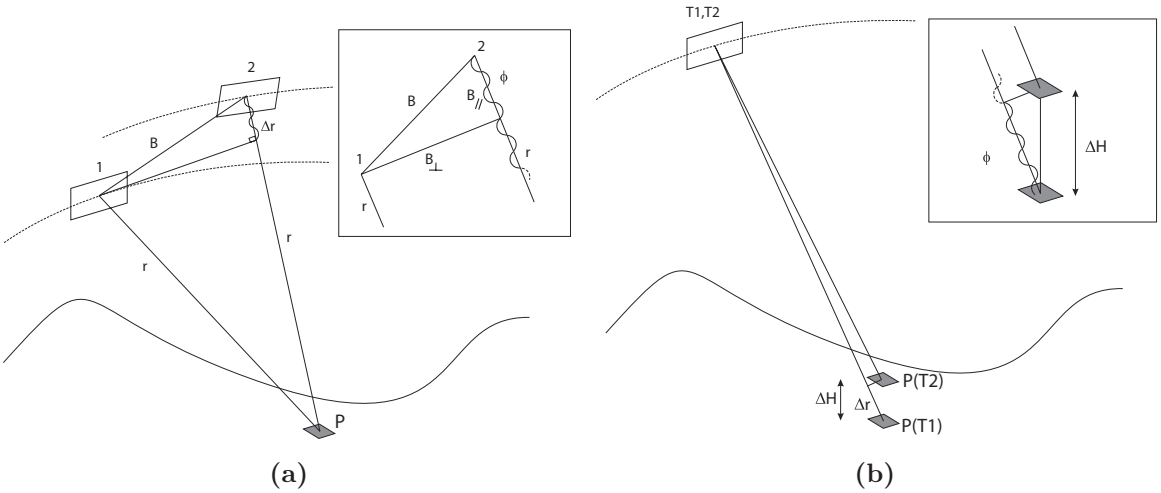

Figure 2.31: Interferometry of two SAR images to derive a DEM or ground displacements. (a) A point of the terrain P is seen by two images (1, 2), separated by the perpendicular baseline $B_\perp$, from slightly different angles, which causes a path difference Δr. As Δr is directly connect with the phase difference ϕ, relative elevations Δr can be determined using interferometric patterns. (b) The phase difference ϕ between two images acquired at different times (T1, T2) from the same position can used to obtain the share of the whole displacement ΔH in the line of sight (LOS)-direction Δr.Figures from Usai (2001, p.20, 22).

Fig. 2.31a), the interferogram contains phase variations only due to the topography ϕ_t. This effect can be used to extract a DEM from the interferogram using the known perpendicular baseline. On the other way around, this effect of the topography in the interferogram, due to non-zero baselines, can be modelled using an external DEM and precise orbits and then removed from the interferogram to form a so-called differential interferogram.

Figure 2.32 illustrates the remaining contributions to the interferogram phase, i.e. the actual displacements ϕ_d, the spatial variability of the atmosphere ϕ_a, the residual phase due to error on the orbits ϕ_o or error on the DEM and geometric and temporal phase decorrelation as well as noise (thermal noise affecting phase measurement, coregistration error).

The orbital (or flat earth) residual fringes can be modelled at 10 - 50 km-scale by a linear one-directional gradient throughout the image. If the deformation signal is of smaller extent, as it is the case for most of the landslide, this gradient can be estimated from the interferogram itself and then removed from the interferogram.

The atmospheric perturbation, due to change of atmospheric condition between the two acquisition dates, are more difficult to eliminate. Because atmospheric perturbation are correlated in space at kilometric scale, they are less critical for landslides with smaller extent. Some strategies can be applied to mitigate them for instance by modelling them using atmospheric models (Webley et al., 2002; Li et al., 2006). Besides, DEM errors can also affect differential interferograms. One way to detect them when having several interferograms is that DEM errors are proportional to the perpendicular baseline. Apart from other minor noises coming, e.g., from the SAR sending and receiving unit, or SLC misregistration, another important factor is the decorrelation (Fig. 2.32).

Decorrelation can have several origins. One is the already mentioned baseline-decorrelation. The higher the perpendicular baseline, the higher the decorrelation. The phase recorded in one pixel is the sum of the returns from several individual

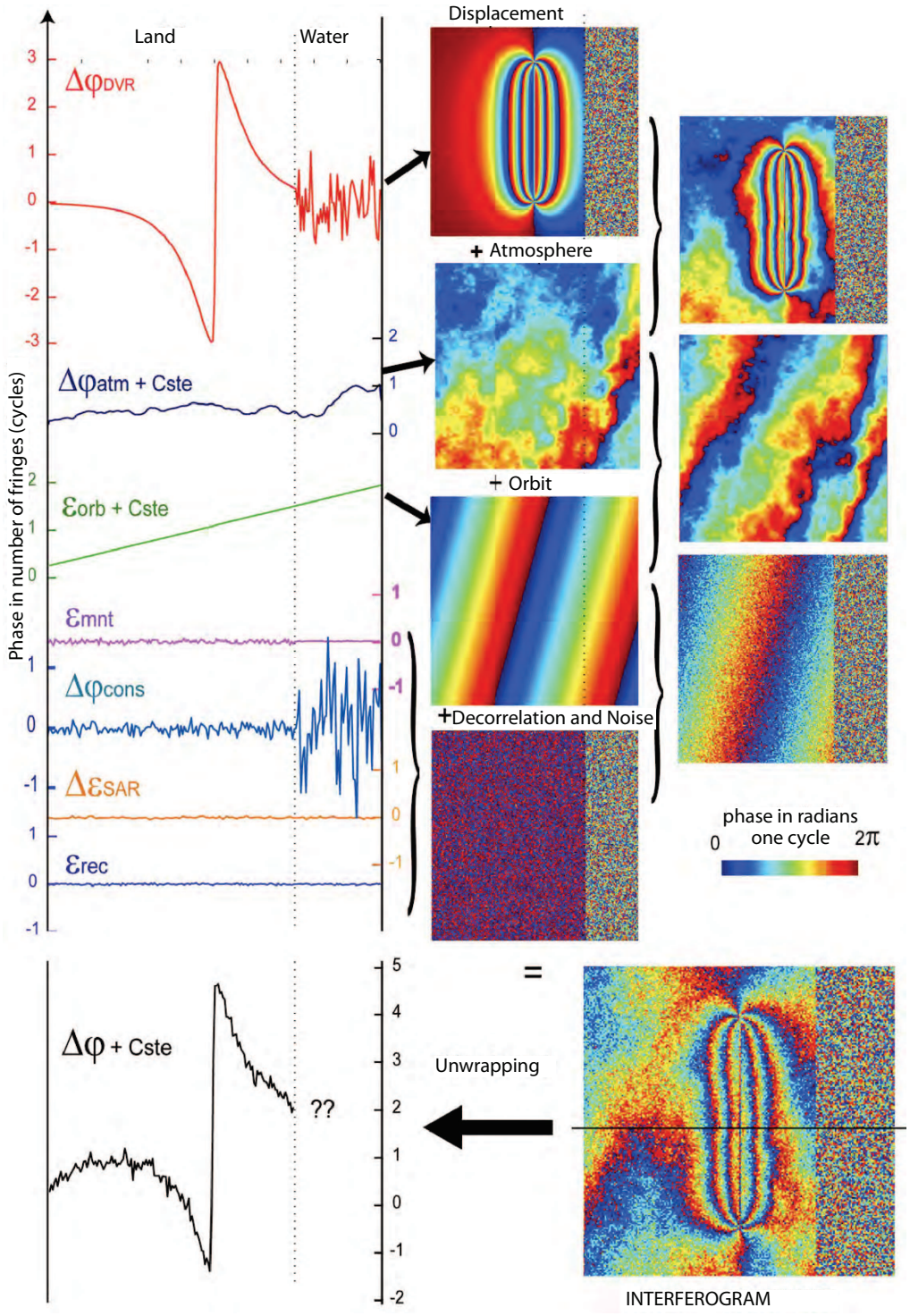

Figure 2.32: Contributions to phase of a differential interferogram, illustrated by the case of a simulated earthquake causing vertical ground deformation localised around a fault (top profile and image). The interferogram in the lower right corner can be seen as the sum of different contributions to the phase signal. DVR: ground displacement, Atm: atmospheric effects, EOrb: orbital error, Emnt: DEM error, Cons: temporal or geometric decorrelation, ESar: instrumental error, Erec: misregistration error. The transects on the left show the unambiguous unwrapped phase along an horizontal profile. The central column figures show the same signal but modulo 2pi (wrapped phase). The right column show examples of combinations of different contributions. Figure from Pathier (2003, p.71).

scatterer inside that corresponding ground resolution cell. If the local incidence angle slightly changes, the returns of the individual scatterer may changes, but also the way they are summing together that is the construction phase. When the phase has been measured exactly from the same point of view, when doing the phase difference the construction phase of each pixel cancel out, and only the phase change due to the displacement of the resolution-cell remains. However, when the image are taken from a even slighty different point of view the construction phases do not cancel out anymore introducing decorrelation noise. The theoretical critical baseline leading to a total decorrelation for ERS is 1100 m, but in practice this geometric decorrelation noise already starts to be significant from baselines above 300 m (Usai, 2001). Another big factor causing decorrelation is a change of the earth surface between two acquisition times (temporal decorrelation). A good example are water surfaces, since they are varying within seconds due to waves (even very small ones). But the major problem, especially with respect to the relatively small extents of homogeneous displacements on landslides, is coming from vegetation. The movement of leaves, the seasonal growing and dying of plants or agricultural activities, change the signature of the land surface quite rapidly, sometimes even between a Tandem-acquisition of ERS-1/2 within one day. This temporal decorrelation may not affect all the pixel of a given area. However, if one reliable pixel is surrounded by noisy pixel, it is impossible from a single interferogram to detect it. A method to overcome this problem by enabling the detection of permanent scatterers is explained in the following Section 2.7.3.

2.7.3 Persistent Scatterer Insar (PSI)

As described in the previous section, one of the major error sources in a single Insar image is spatial and temporal decorrelation. Figure 2.33 illustrates that problem. The sketch on the right shows a tree backscattering the Radar pulse from the satellite. All the leaves of that tree reflect the Radar signal and the satellite receives the sum of all scattering elements leading to a complex value in the final SAR-image pixel. Row (a) shows the complex plane of the pixel at two different times (T_1 and T_2). In this plot a dot is a complex value. The image intensity is the distance to the origin and the phase is the angle between the abscises axis and the line from the origine to the dot. Because all the different contributions are small and random, the final value is also of low intensity and contains a random phase. At T_2 the leaves (or water, grass, sand etc.) have naturally moved or the orbit of the satellite has slightly changed, which leads to an altered geometry of all sub-reflectors and therefore to a completely different phase and intensity value. This means the pixel is temporally decorrelated. If the neighbouring pixels are random as well the pixels are also spatial decorrelated.

In the case (b) the reflected signal contains random contributions as well, but also one or several dominant reflectors, which are consistent (also called persistent or permanent) over time and are relatively robust to small geometrical changes of the satellite orbit, which tends to be the case for punctual target and corner-reflector targets in opposition to extended targets. The corner reflectors are more often found at buildings, street or exposed hardrocks. Therefore the sum of all the single sub-reflectors contribution do not change much over time and the pixel shows temporal coherence.

The principle of Persistent Scatterers Interferometry (PSI) is to identify and only use the PS because they are the most reliable points for displacement measurements. It should be noted that the perfect isolated corner-reflector and the numerous randomly distributed small targets are two end-members and that in most of the cases pixel

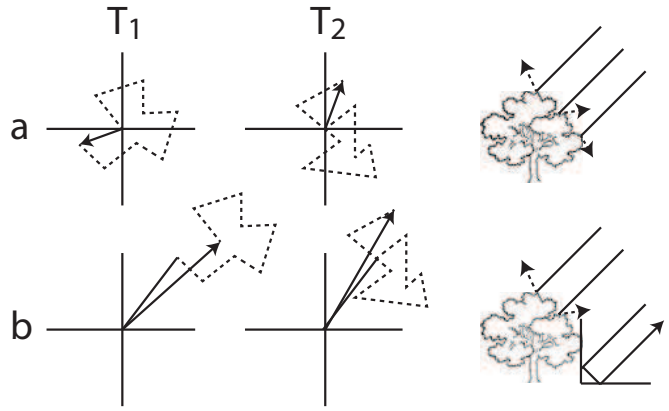

Figure 2.33: Principle of the contribution of a permanent scatterer to the complex SAR image pixel. Multiple scatterers contribute to a single complex SAR image pixel. Here they are represented in the complex plane (intensity=distance to the origin, phase=angle from the x-axis). The individual scatterers inside one pixel (dotted lines) sum together into the backscattered complex value (solid arrow) that will be measured by the SAR instrument. (a) the top row illustrates the case of a resolution cell without dominant scatterers (like a tree covered by leaves): left and central plots shows the same pixel from two different acquisitions at time T_1 and T_2 and affected by some temporal or geometrical decorrelation. The resulting intensity (length of the arrow) and phase (orientation of the arrow) of the overall pixel can be very different. (b) bottom row illustrates the same situation but including a permanent scatterer (solid line) that dominates the other distributed scatterers. The resulting intensity and phase of the overall pixel remains similar between the two acquisition because of the strong contribution of the dominant scatterer.

lie in between. Consequently threshold value has to be decided at some point in the processing.

How to know if a pixel corresponds to a permanent scatterer, as even if its phase is only a little affected by decorrelation it can also be significantly affected by atmospheric perturbations, orbital and DEM error? Another point is that the differential phase of an interferogram pixel has no absolute meaning, instead it has to be computed against a reference pixel.

The most used PS strategy has been designed by Ferretti et al. (2000). It consists of the analysis of phase differences between pairs of close pixels both in time and with respect to the perpendicular baseline. To perform this analysis all the SLC images are coregistred to one master image, then it is possible to get the interferometric phase with respect to the master date for each date with an associated perpendicular baseline value. The idea is that atmospheric and orbital error show slow variation across an interferogram, so that the difference of their phase contribution between a pair of close pixels is small. Consequently if the pixels of the pair correspond to permanent scatterers, their phase difference should mostly depend on their relative displacement and their difference in DEM errors. But without any further assumption it is still difficult to distinguish permanent scatterers from other pixels just based on their phase.

In order to correct the phase between two points from the DEM error the elevation difference between those points needs to be accurately determined. If the pixel pair had no relative displacement, this height difference can be extracted from the phases itself by using multiple images and finding a linear dependency between the differential phase and the perpendicular baseline per pixel. From that the height can be corrected and the DEM error contribution to the phase can be subtracted from the differential

phase.

On the other hand, if the pixel pair had no relative DEM error, how to know if the pixels are permanent scatterers? If the two pixels had completely independent and significant displacements, their phase difference evolution with time may not be distinguished from the one of a pair of non-permanent scatterers pixels having no relative displacement but just temporal decorrelation. At that point, it is necessary to restrict the identification of the permanent scatterers only to those that fulfilled an additional condition: there is a spatial correlation of the displacement between pairs of close pixels. For instance, in Ferretti et al. (2000) the selection is restricted to pairs of permanent scatterers for which relative displacement evolution is linear with time. In this case the relative displacement rate can be detected from the phase-values itself by using multiple images and finding a linear dependency between the differential phase and time per pair of pixel.

In practice relative DEM error and linear displacements can be present, which leads to the necessity of finding the height-correction and linear deformation rate at the same time, which is done by a 2D-linear regression analysis using the differential phases of a stack of co-registered SAR-images. In this thesis the processing follows mainly the IPTA-approach implemented in the Gamma-software[16]. This processing is outlined in more detail in the following section using the city Grenoble as a test case.

2.7.4 Subsidence in Grenoble as a test case

This section details the "standard" Gamma IPTA processing illustrated through the case study of the subsidence of the Grenoble city which is starting from the same dataset of raw images than for the landslides studied in Trièves.

2.7.4.1 From raw-data to SLCs

As a first step the 26 ERS1- and 124 ERS2-images covering 100 x 100 km (see Fig. 2.27) are processed into SLC (Single Look Complex) and MLI (Multi Look Image) using the MSP (Modular SAR Processor) module of the Gamma-Software. For that, the accuracy of the position and velocity (state vectors) of the satellites is increased by using precise orbits calculated by DEOS[17]. For the following 4 ERS1-images precise orbit files are not available: 01.08.1997, 10.10.1997, 19.03.1999 and 28.05.1999. During the processing missing lines and decorrelated lines are counted. Decorrelated lines are lines exceptional dissimilar to their neighbouring lines, indicating erroneous data. A full SLC image has a dimension of 4912 samples and 28075 lines in azimuth. About half of the images (ERS2) after Feb 2001 contain an increased amount of decorrelated lines (without missing lines). Before the only problematic image is the one of 13.06.1998 with 12269 missing lines, which is nearly half of the image. Figure 2.34 shows a detail of that erroneous image together with a successfully processed one. The problematic image is excluded from the data-base. Two images contain minor errors, the ERS2 image of 04.01.1997 is missing 232 lines and the ERS1 image of 14.04.1995 is missing 14 lines. Three images miss less than 10 lines and 8 images contain less than 30 decorrelated lines. All the images with these minor problems are kept in the data-base. All other images (before Feb 2001) do not show any errors.

[16]IPTA - Interferometric Point Target Analysis is the PSI module of the software Gamma by Gamma Remote Sensing AG - `www.gamma-rs.ch`

[17]DEOS - Delft Institute for Earth-Oriented Space Science - `http://www.deos.tudelft.nl/ers/precorbs/orbits/`

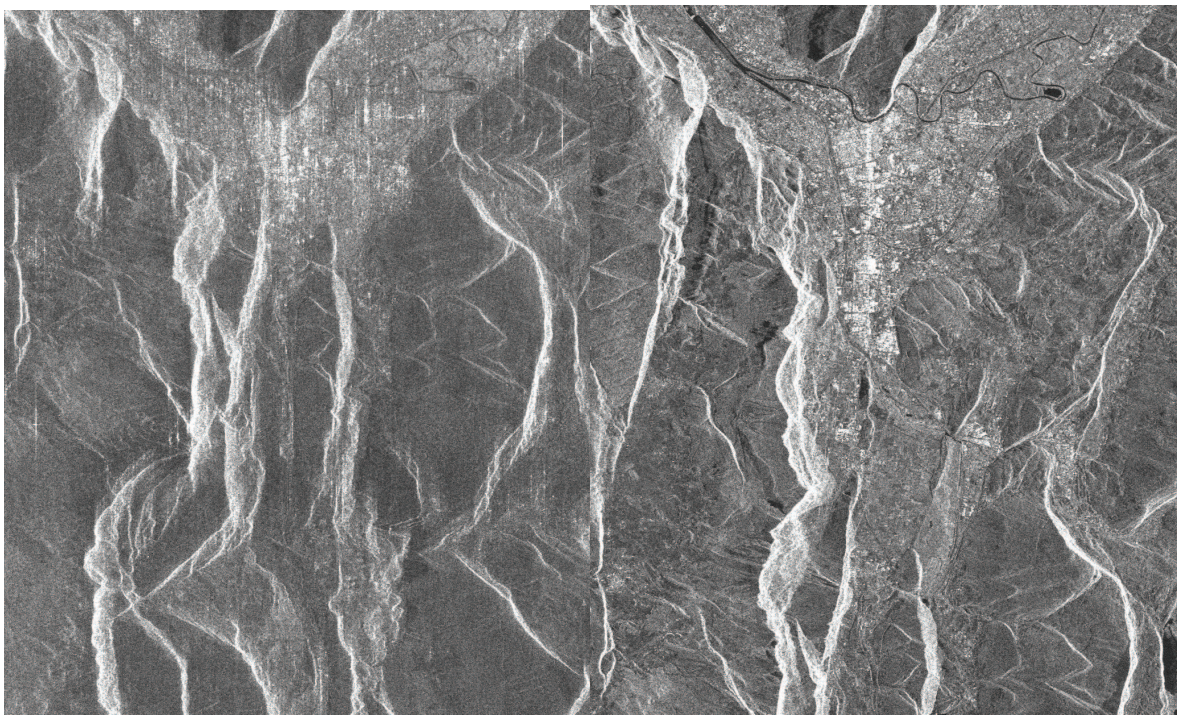

(a) MLI **(b)** MLI

Figure 2.34: Details of two ERS2-MLIs (1:5) showing Grenoble and the South of it. a) is from 13.06.1998 and is missing 12269 lines during the processing of the SLC, leading to a highly compressed representation in azimuth. b) is from one month later (18.07.1998) and was processed without errors.

In order to successfully calculate interferometric properties between images, the Doppler centroid needs to be similar. Figure 2.35 shows the first Doppler polynomial of all images. Due to instrument failures on the ERS2-satellite the ERS2 data after Feb 2000 are more difficult to use for interferometry especially within the standard Gamma approach. Therefore all images after Feb 2000 are removed from the data-base, leaving 65 images between 1992 and 2000 for further processing.

2.7.4.2 co-registration of SLCs

In order to calculate interferograms of SAR images, they need to be co-registered with sub-pixel accuracy. Therefore a master-image (MI) is chosen and all other images are recalculated (RSLC) to match the master. In order to minimize the differences between all images and the master-image, it should match certain criteria (from GAMMA-userguide):

1. The Doppler centroid of the MI is near the average Doppler centroid. As the Doppler frequency is nearly constant for all (leftover) images from the data-base, this is true for all images. But the Doppler-frequency is slightly different for ERS1 and ERS2 and the data-base contains more images from ERS2, so the MI should be an ERS2 image.

2. The orbit of the MI should be near the geometric center of the orbital tube spanned by all available SAR images. This is sufficiently accurate by choosing a MI with a perpendicular baseline near the average. The chosen MI is 46 m from that average.

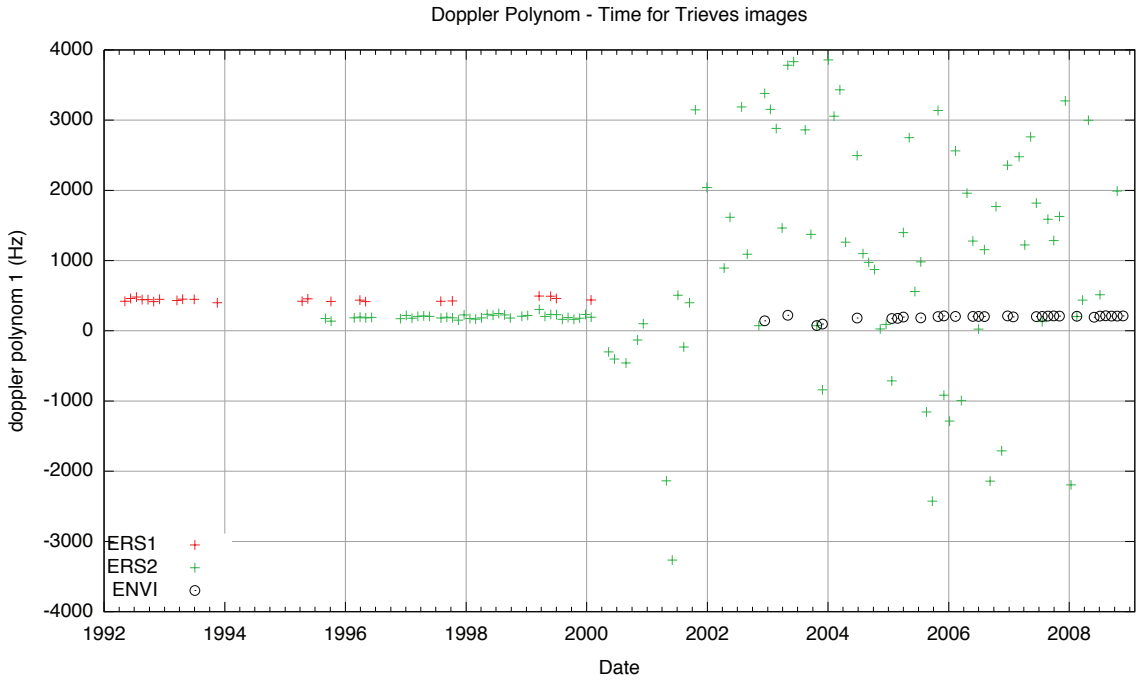

Figure 2.35: First Doppler polynomial of SAR database. Images with constant Doppler polynomial are available from ERS1 and ERS2 between 1992 and 2000. Due to instrument failure onboard of ERS2 in Feb 2000, the Doppler polynomial is highly variable since then. ENVIsat images are available since 2003 with Doppler frequencies near to ERS2. The Doppler Frequency between ERS1 and ERS2 differs by about 200 Hz.

3. The MI should be near the temporal average of all images, which is Feb 1996. The chosen MI is from one year after.

4. The MI should be based on precise orbit files and not reveal errors during the SLC-processing, which is true for the chosen MI.

5. The MI should not contain high atmospheric distortions. This is checked by calculating a single interferogram with the next temporal neighbor (08.02.1997 ERS2) and looking manually for suspicious pattern of fringes. Figure 2.36 shows that single interferogram. Only the valleys with higher building density show identifiable fringes. The fringes seem to be relatively monotonic and do not suggest the presence of higher atmospheric disturbances, however a proper judgement is impossible at that stage. But the presence of atmospheric distortions would be revealed in the further processing, which is not the case.

For the Grenoble area the master-image is cropped to an area of 800 pixel in range and 3400 lines in azimuth. The area includes some parts of the surrounding mountains in order to be able to proper co-register the DEM later on. The co-registration of the SLCs is done by first estimating the global shift using the orbital information of the images, refining the global shift by cross-correlation of the MLIs (1:1), building an offset model using small patches of the whole image and finally resample the SLC using that model. For the Grenoble area the offsets are obtained at 1024 equally distributed points (32x32 grid). The patch size is 64x128 pixel (oversampled by a factor of 2) and the correlation threshold is 7 (signal-noise ratio). In every image for about half of the points proper offsets are obtained (529 to 646 from 1024). The mean accuracy (standard deviation from model fit) is 0.04 pixel in range (0.03-0.06) and 0.08

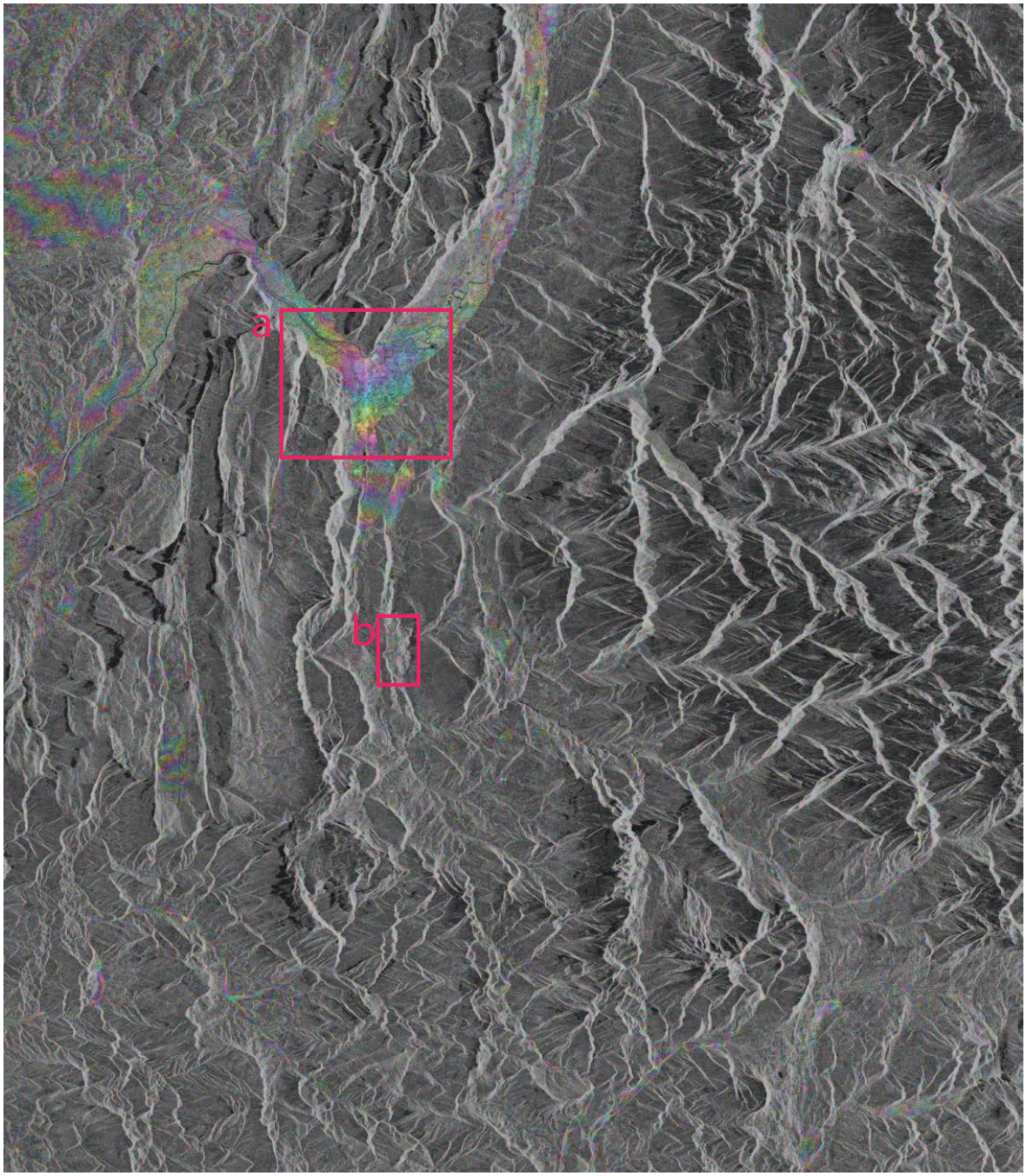

Figure 2.36: Single ERS2 interferogram using the images of 02.08.1997 and 15.03.1997 (colors). The greyscale background is the MLI (intensity). The extent is about 100x100km. Grenoble is in the center of the Y-shaped valley with good identifiable fringes due to the higher building density. (a) Excerpt for the Grenoble study case (b) Excerpt for the Avignonet and Harmalière landslide study

in azimuth (0.04-0.12), which is below 0.2 pixel as suggested by the software's user-guide. The co-registration of the image from 04.01.1997 failed (11 successful offsets from 1024 and accuracies above 10 pixel). This image is recalculated using only the 1:5 MLI and 12 from 35 offsets leading to an accuracy of 0.1 pixel in range and azimuth.

2.7.4.3 Co-registration of DEM

For the calculation of interferometric phases a DEM in SAR-geometry is needed. Therefore the IGN50-DEM (see App. A.4) was bi-linear oversampled to 20 m and converted from Lambert93 into geographical coordinates (map geometry). In order to derive pixel-accurate height information the DEM needs to be co-registered to the master-image similar to other SAR-images. First a simulated SAR-image based on the DEM is calculated and then co-registered to the master-image by establishing a lookup-table to convert coordinates from map-geometry into SAR-geometry. This lookup-table is then used to transfer the DEM from map-geometry into SAR-geometry.

2.7.4.4 Derive point candidates

For the IPTA processing suitable points of the images are obtained using two approaches. First by using spectral properties of single SLCs and second by stable intensities over time.

For each SLC a spectral correlation (cc) image and a mean/sigma ratio (msr) image is calculated and afterwards averaged. As point candidates all points are defined from those images (cc and msr) which show a spectral correlation higher than 0.35 and a mean/sigma ratio above 1.0. 33477 points match those criteria, which are about 1.2 % of all points.

For the second approach, all points which are stable over time (mean/sigma ratio of the intensity higher than 1.4) and showing 0.5 higher intensities as the image average are selected. Together with the points of the first approach, 46598 point candidates are obtained, which are about 1.7 % of all points.

2.7.4.5 Subsidence in Grenoble

From these point candidates a reference point near the Bastille in the North of Grenoble is chosen, because this area outcrops bedrock, which can assumed to be not effected by subsidence. From this reference point a linear regression analysis is calculated to all the other point candidates. The regression analysis searches for a height correction between two pixel and a linear displacement rate which best explains the phase values of the SAR-image stack. The search limits are chosen to be 30 m for the height correction (expected difference from the DEM due to heights of buildings) and 2 cm/a for the linear displacement rates (based on reported geodetic measurements).

The regression analysis results in unwrapped linear deformation rates in LOS (line of sight) for all 46598 points relative to the reference point (Fig. 2.37). The principles of the regression analysis are explained in Section 4.3.2. The obtained deformation rates are between 2 and -8 mm/a. In order to derived subsidence rates in a vertical direction, the value needs to be multiplied by about 1.09 due to the incidence angle of the ERS-satellites of 23° in average. In general the subsidence increases towards the center of the valley with some maxima along the Drac River in the west and along the highway in the south. The obtained subsidences rates has been used to investigate the possible relationship between subsidence, basin sedimentary deposits (thickness and subsurface lithology) and resonance periods. This work was used in two collaborative

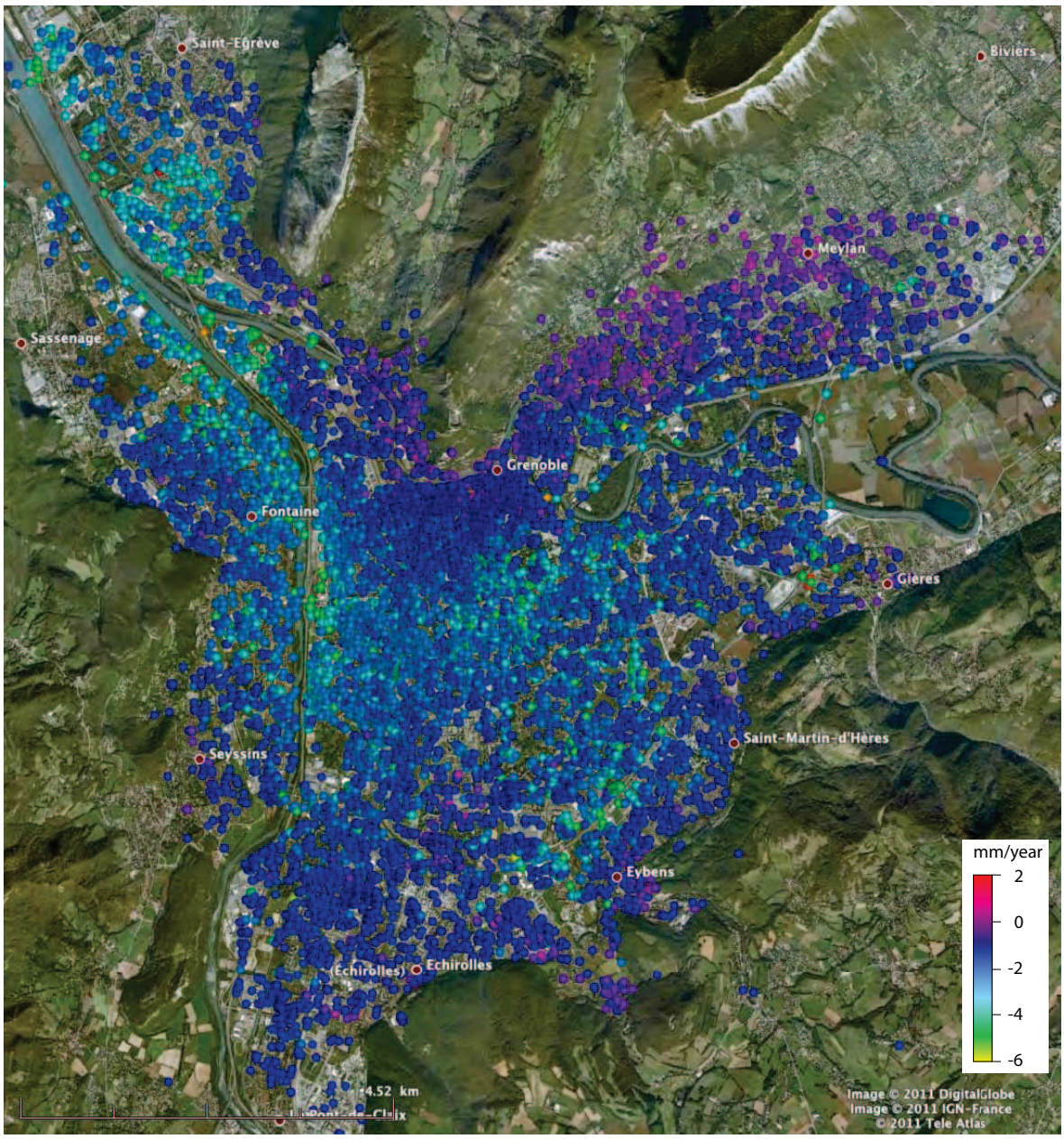

Figure 2.37: PSI deformation rate of Grenoble as processed by Gamma from ERS images between 1992-2000. The deformation rates are in LOS direction towards the satellite, so that negative values pointing into the ground.

communications ((Fruneau et al., 2010; Michel et al., 2010)). The abstracts of these are attached in Appendix

CHAPTER 3

Geomorphology and Geological Structure

This chapter is dedicated to the analysis of the geology and morphology at the present state using single-temporal data, whereas the next chapter 4 is all about the kinematics using multi-temporal data. The section 3.1 is an earlier longer version of a collaborative article later accepted from the journal "Geomorphology" in a shorten extent (Bievre et al. (2011)). It proposes a control of the activity of the Avignonet and Harmalière landslides by the morphology of the underlying substratum. My main contribution to this article is subsection 3.1.3 about the geomorpholgy and history of the two landslides. Second part of this chapter is section 3.2 about the analysis of the DTM, which results are also contribute to the general discussion about the kinematics at the end of the kinematics chapter.

3.1 Combined use of remote-sensing and ground geophysical techniques to investigate geological control on landslides (Trièves area, Western Alps, France)

3.1.1 Introduction

This paper presents a study combining remote sensing and seismic prospecting for investigating two clayey landslides (Avignonet and Harmalière) located in the Trièves area (Western Alps; Fig. 3.2).

Although affecting similar slopes made of similar clay layer under the same meteorological conditions, these two adjacent landslides exhibit, since the 1980s, major differences in morphology, displacement rate magnitudes and motion directions. These observations suggest the control of at least one additional internal factor on the landslide characteristics. Such control by lithological variations, hydrogeological drainage or structural features have been regularly depicted in clay slides (Bonci et al., 2004; Lapenna et al., 2005; Eilertsen et al., 2008; Bozzano et al., 2008). This study aims to explain the significant differences in geometry and kinematics observed between the landslides of Avignonet and Harmalière. Combination of geological mapping, airborne light detection and ranging (Lidar) data, aerial photographs, global positioning system

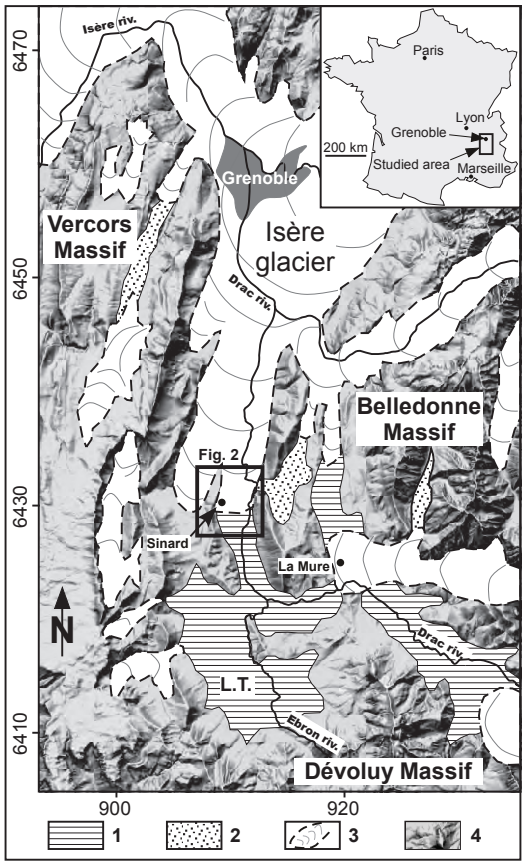

Figure 3.2: Location of the area and palaeogeographical map at the end of the Würm age (adapted from Monjuvent, 1973). Coordinates are kilometric and expressd in the French system Lambert-93. The black thick box shows the location of the study area and the extent of Fig. 2. 1: Laminated clay deposits in the Trièves area; 2: glaciofluvial deposits; 3: extension of the Isère Glacier at the end of the Würm age; 4: present-day topography; L.T.: lake Trièves.

(GPS) and seismic noise measurements allows characterizing the landslide morphology and the thickness of the soft layer down to the seismic substratum, providing a 3D view of the soft layer bottom. This reveals the palaeotopography upon which settled the clays and helps to assess the geological control on the two landslides behaviour.

In the last two decades, remote sensing techniques and geophysical prospecting methods have been increasingly used to image landslide structures at the surface and at depth, respectively. Remote sensing techniques, such as radar interferometry, high-resolution optical images correlation and multi-temporal laser scanning, allow the surface displacement field to be measured, which is a key parameter to understand the landslide mechanics (for a review, see Metternicht et al., 2005; Delacourt et al., 2007). In complement to conventional ground-based geodetic techniques and GPS surveys that provide only a limited number of discrete measurements, multi-temporal remote sensing imagery has the potential to measure nearly continuous displacement rate field over landslides (among others, Fruneau et al., 1996; Rott et al., 1999; Kimura and Yamaguchi, 2000; Squarzoni et al., 2003; Metternicht et al., 2005; Strozzi et al., 2005; Corsini et al., 2007). Nonetheless, performances of the remote sensing techniques strongly depend on the site conditions (slope steepness and orientation, vegetation, size, slide velocity) and on weather conditions. These techniques that can be borne on various platforms (space, aerial or ground) and combined together, can achieve decimetric to centimetric resolution and accuracy in favorable conditions (Delacourt et al., 2007). In the last few years, both airborne and ground Lidar techniques have been increasingly applied for mass movement studies, particularly in steep and rugged terrain (e.g. Thoma et al., 2005; Abellan et al., 2006; Corsini et al., 2007; Deparis et al., 2008; Oppikofer et al., 2008). Recently, airborne Lidar images were successfully used to map recent and historical landslides in gentle slope areas (Schulz, 2007; Van den

Eeckhaut et al., 2007). Major advantages of Lidar technique are the flexibility and the quickness of the acquisition as well as the relatively simple data processing, allowing multi-temporal Digital Elevation Models (DEM (digital elevation model)s) to be generated (McKean and Roering, 2004; Rosser et al., 2005; Thoma et al., 2005; Oppikofer et al., 2008).

In parallel, shallow geophysics has also considerably evolved with the emergence of 2D and 3D spatial imaging, allowing the study of the spatial and temporal variations inside landslides (for a recent review, see Jongmans and Garambois, 2007). Geophysical imaging has the major advantages to give continuous information on the studied body and to be non-invasive. However, resolution generally decreases with depth. Geophysical prospecting applied to landslides encompasses a large number of techniques: seismic reflection, seismic refraction, electrical resistivity tomography (ERT), seismic noise measurements, spontaneous potentials, electromagnetic, ground penetrating Radar (GPR) and gravimetry. Flexible and quick to deploy, these techniques have been applied on various types of landslides for slope varying from a few degrees (earth slide) to vertical (rock fall), with a penetration depth of the surveys ranging from 3 m to 400 m (Green et al., 2007; Heincke et al., 2006; Jongmans and Garambois, 2007).

Although remote sensing and geophysical techniques are complementary for landslide imaging purposes, they have been rarely associated. Roch et al. (2006) and Deparis et al. (2008) combined remote and ground imaging techniques for determining the geometry and the 3D fracture pattern of potentially unstable cliff sites. A dense digital surface model of the rock face was measured from laser scanning (Lidar) and/or photogrammetry, while the GPR performed on the cliff allowed the discontinuity pattern inside rock mass to be obtained. On low slope made of clay-rich sediments, Perrone et al. (2006) presented a joint analysis of synthetic aperture Radar (SAR) interferometry and ERT surveys for investigating and understanding complex ground deformation of different origin. Bruckl et al. (2006) utilized photogrammetric, GPS and seismic data to derive the kinematics of the Gradenbach deep-seated landslide (Austria) affecting crystalline rocks.

In the following, the geological setting of the study area is first assessed. Then, the use of Lidar data, aerial photos and GPS measurements will lead to better constrain the two landslides activity and extent as well as their kinematics. The easy-to-deploy and fast H/V prospecting will allow to estimate the soft layer thickness. The original combination and integration of these techniques will help to build a 3D view of the soft layer and assess a possible geological control on the landslides.

3.1.2 Geological structure and mapping

The Trièves area is located 40 km south of the city of Grenoble in the external French Alps (Fig. 3.2). This plateau region with a maximum altitude of 800 m above sea level (asl) corresponds to a large depression of about 300 km^2 drained by the Drac river and its tributaries. It is bordered, to the West and to the South by the Vercors and Dévoluy carbonate massifs, respectively. To the East, it is limited by the southern end of the crystalline Belledonne range (Fig. 3.2). This area is the main outcrop of quaternary glaciolacustrine clays. Many landslides affect this zone among which 15 % are supposed to be sliding (Lorier and Desvarreux, 2004). These slides might affect surfaces as large as 1 km^2. They can develop over several slip surfaces ranging from

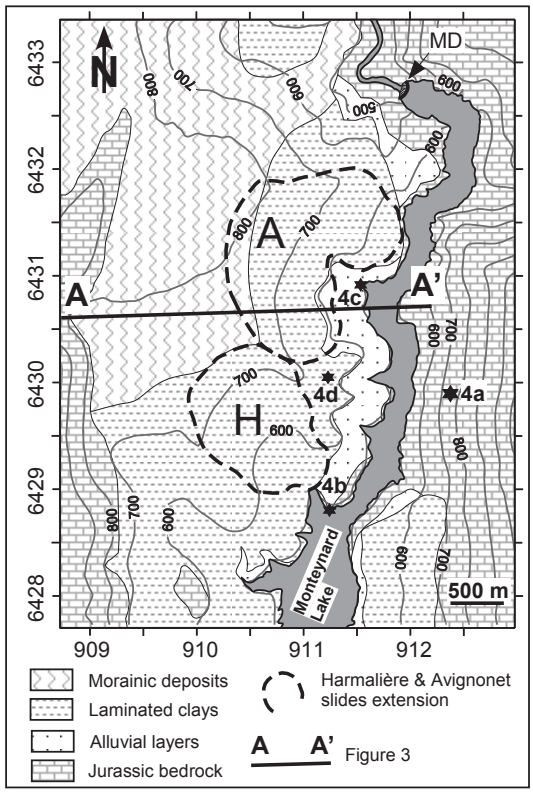

Figure 3.4: Geological map (location in Fig. 3.2) modified from Debelmas (1967) and Lambert and Monjuvent (1968). Screes and morainic colluvium have not been reported. Black stars refer to pictures in figure 3.6. Position of cross-section AA' of figure 3.5 is indicated. A: Avignonet landslide. H: Harmalière landslide. MD : Monteynard dam.

superficial (5 m to 15 m) to rather deep (down to 50 m; Blanchet, 1988; Jongmans et al., 2009). Slide velocities are generally low (a few cm/year) but can reach several m/year in certain places. In some cases, generally after a long wet period accompanied by quick snowmelt, the slides can evolve into a mudflow and velocities can reach several m/h. This lead to dramatic events in Harmalière in 1981 (Moulin and Robert, 2004) and in La-Salle-en-Beaumont in 1994 (Moulin and Chapeau, 2004). This important gravitational instability is mainly related to the Quaternary geological history of the region. It was controlled by several glacier fluctuations, which resulted in alternating deposition and erosion phases. The particular geometrical setting and the sediments recorded these major climatic fluctuations.

The substratum on which rely the quaternary formations is made of early Jurassic carbonate strata which were folded and faulted during the alpine orogenesis. Ancient glacial (Riss) and interglacial phases (Riss-Würm) carved the substratum and generated valleys partly filled with Riss-Würm alluvial deposits. This lead to an irregular shape of the basement prior to the last glacial phase (Würm; -80 to -12ky BP). During the last glacial maximum (LGM) extension (LGM, Würm period, -22 to -18 ky BP; Clark et al., 2009), the Isère glacier, coming from the North, blocked downstream the torrential flows from the Drac river and its tributaries, generating an ice-dammed lake (lake Trièves, Fig. 3.2; Monjuvent, 1973). This lake was progressively filled during thousands of years mainly by millimetric to decimetric rythmic alternations of clay and silt layers originating from nearby Mesozoic marls and crystalline massifs (Huff, 1974). These laminated clays rest either on carbonate or alluvial, locally cemented, compact layers from the interglacial Riss-Würm period. The irregular shape of the basement induces strong lateral thickness variations of the palaeolake infill, from 0 to more than 250 m (see Figs. 3.4 and 3.5; Monjuvent, 1973; Antoine et al., 1981).

The top of the clay is generally found at an elevation of about 750 m asl (Antoine et al., 1981). Morainic deposits which cap the clays are found as far as the south of

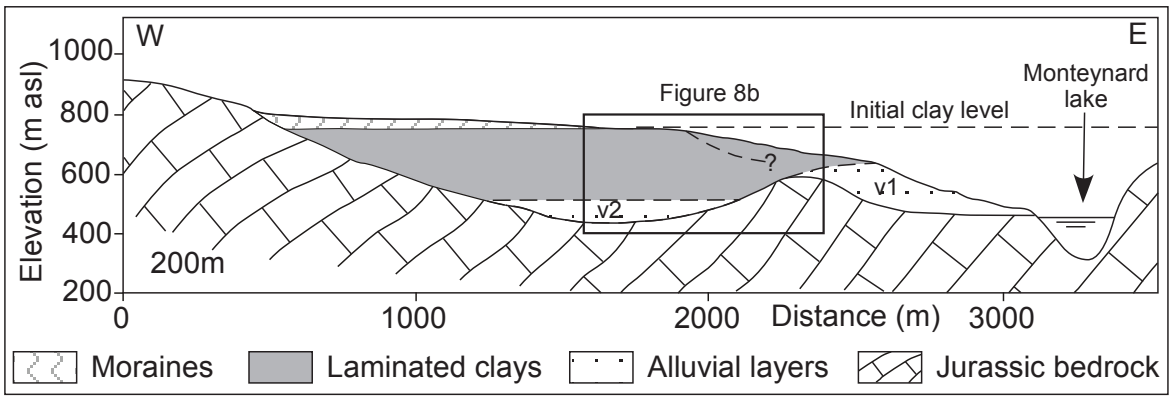

Figure 3.5: Geological cross section (location in Fig. 3.5). Screes and morainic colluvium have not been reported. v1: first palaeovalley ("Drac de Cros"). v2: second palaeovalley ("Drac de Sinard"). Initial level of laminated clays has been reported (750 m asl). Dashed line within clays depicts the lower limit of the Avignonet landslide, deduced from inclinometer data. See text for details.

the village of Sinard, indicating the southward limit of the würmian glacier extension (Figs. 3.2 and 3.4). Also, these moraines are not present in the downslope parts of landslides, where clays outcrop (Fig. 3.4). At the study site, their thickness evolves, around Sinard, from 50 m to the West to a few meters to the East. At the end of the LGM in Europe, the Isère glacier withdrew, allowing the rivers to cut deeply into the formations. This last erosion phase created the actual Drac river valley. This favoured the conditions for landslide development in the clay with a general Eastward motion in the study area (Fig. 3.4; Brocard et al., 2003; Jongmans et al., 2009).

The geological map and the cross-section of figures 3.4 and 3.5, respectively, show the geometrical arrangement of the geological formations in presence. Two palaeovalleys, labelled v1 and v2 on figure 3.5, depict previous interglacial incision phases. Palaeovalley v1 is the oldest one (Monjuvent, 1973; Brocard et al., 2003). Both palaeovalleys are filled with locally cemented alluvial layers. They have been recognized by field observations and, under the clay cover, by geophysical investigations conducted in the 1950s for the construction of the Monteynard dam (location in Fig. 3.4; Crosnier-Leconte et al., 1953; Monjuvent, 1973). In the study area (Fig. 3.2), these erosion and deposition phases resulted in an irregularly shaped substratum top (Fig. 3.5). The last erosion phase, at the end of the LGM, resulted in the actual Drac river valley. A general view from the opposite side of the lake is presented on figure 3.6a. Jurassic bedrock, quaternary alluvial layers and laminated clays are shown on outcroup pictures of figures 3.6b, 3.6c and 3.6d, respectively.

3.1.3 Landslide geomorphology and history

3.1.3.1 Techniques

In this part we will focus on the comparison between the Avignonet and Harmalière landslides. Three techniques have been used to analyze and compare the geomorphology and kinematics differences of these slides. To obtain a DEM for geomorphological interpretation a Lidar laser scan, covering the two landslides, was performed. Aerial photographs and GPS measurements were used to analyze the kinematics back to 1948.

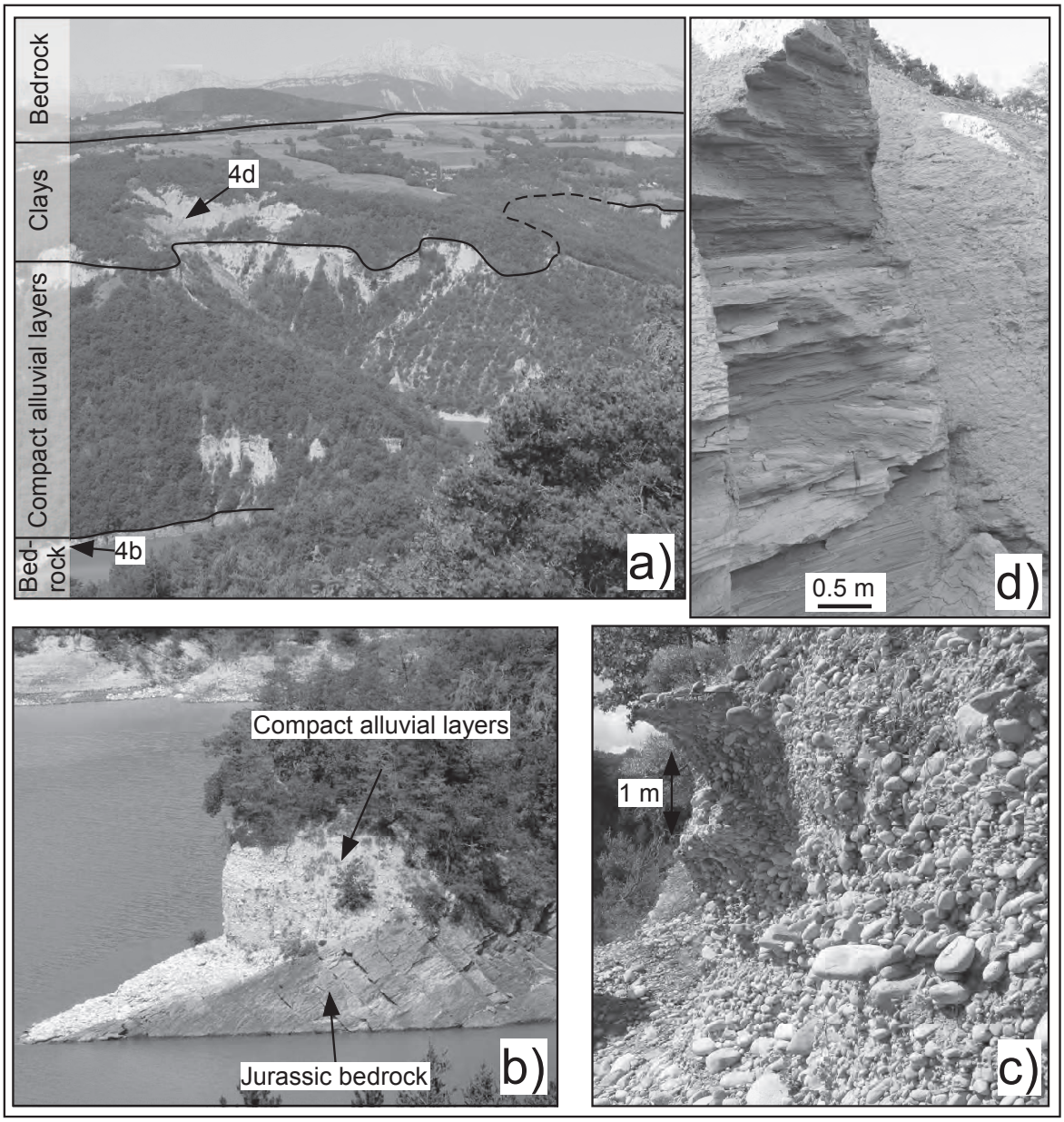

Figure 3.6: Outcrop pictures. **a)** General view of the Avignonet landslide from the opposite bank of lake Monteynard (picture taken from location 4a in Fig. 3.4); **b)** Jurassic bedrock overlain by compact, locally cemented alluvial layers constituted by hetermetric and heterogenic gravels. Present-day Drac river is at the forefront; **c)** Compact alluvial layers; **d)** laminated clays. Location of the pictures is detailed on Fig. 3.4

The Lidar scan was performed in November 2006 using the handheld airborne mapping system Helimap® (Vallet and Skaloud, 2004) mounted on a helicopter flying about 300 m above the terrain. The landscape is characterized by forest, agriculture and grassland. There are no artificial structures on Harmalière but a few small roads, 3 piles of an electric landline and 54 buildings on the Avignonet landslide. The time for the acquisition was chosen to be in November, so that the leaf coverage has already decreased and snowfall has not started yet. The system has recorded 36 million last pulses of the surface reflection resulting in an average of 6 points per m^2 with an accuracy of 10 cm in vertical and horizontal directions. In order to derive the bare earth model excluding trees and houses the point cloud was filtered and interpolated to a 2 m raster grid with the software SCOP++® (IPF, 2004) using the *robust interpolation* method (Briese et al., 2002). The number of points classified as ground reflections and therefore used for the griding of the DEM is 21 million, which is equivalent to an average of 3 points per m^2. The resulting shaded DEM is shown in figure 3.7.

Shaded representations with different light angles were used for geomorphologic interpretation.

GPS campaign measurements have been performed biannually (April and November) since 1995 by RTM (*Restauration des Terrains en Montagne*, a french public survey) at 25 points on the Avignonet landslide (Fig. 3.7), relatively to several reference points located on nearby stable bed-rock. The average standard deviation for all measured points is 6 mm. No GPS measurements have been done so far inside the Harmalière landslide, because of the quick surface evolution making benchmark installation difficult. Average horizontal velocity vectors are shown in figure 3.7. No clear temporal pattern of velocity changes emerges from the data certainly due to the low temporal sampling.

To analyze the kinematics further in the past, digital photogrammetric scans of aerial photographs from the *Institut Géographique National, France* (IGN) of the years 1948, 1956, 1978, 1985, 1993, 2001 and 2003 at scales between 1:20 000 and 1:30 000 covering the two landslides have been used. The photos were orthorectified with the software Geomatica® using the DEM BD-ALTI® from IGN with a resolution of 50 m (the Lidar DEM was not covering a large enough area to be used), the calibration certificates of the utilized cameras and 56 ground control points measured on the field with differential GPS. The ortho-photos have been analyzed to investigate the landslide activity through time. The mapping of the denuded area and of the headscarps was found to be useful indicators of landslide activity.

In the studied area, bare soil (mostly clays) can be observed in several places, over significantly large surface (from about 250 m^2 to more than 50000 m^2 in Harmalière). Where field observation has been done, it turns out that these bare soil surfaces result from erosion and weathering processes in relation to superficial landslide activities. In the following the term denuded area is used to refer to these surfaces. To quantify the spatial and temporal distribution of denuded area over the whole studied area, aerial photos have been used.

When comparing field observations at Harmalière and Avignonet landslides with ortho-photos, denuded area appears as very bright pixels in aerial photography compared to the surrounding forested or agricultural landscape except for some field crops, the river and some human constructions (road, buildings) that can also be bright (see Fig. 3.8, top).

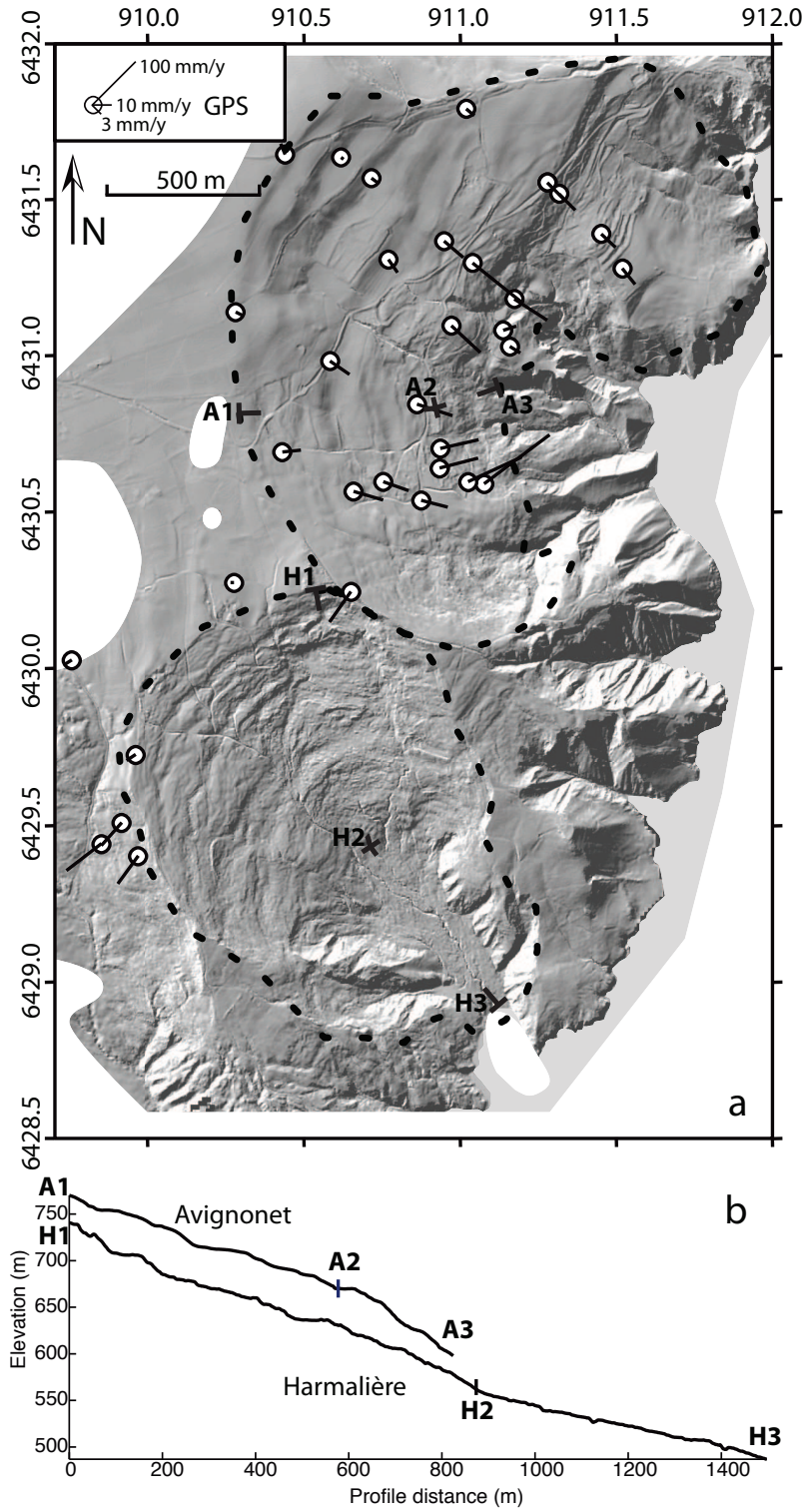

Figure 3.7: Lidar DEM and elevation profiles of the study area. **a)** Shaded Lidar DEM (light direction is from NW, horizontal resolution of 2 m) covering the Avignonet (North) and Harmalière (South) landslides. Dotted lines indicate the landslide limits. White areas indicate data holes in the Lidar coverage. The white circles show the position of the GPS points, and the thin straight lines represent the 11-years average horizontal velocity measured by GPS. A1-3 and H1-3 indicate the location of the elevation profiles. **b)** Elevation profiles through Avignonet and Harmalière with subdivisions in an upper and lower part. Profiles are 2 times vertically exaggerated.

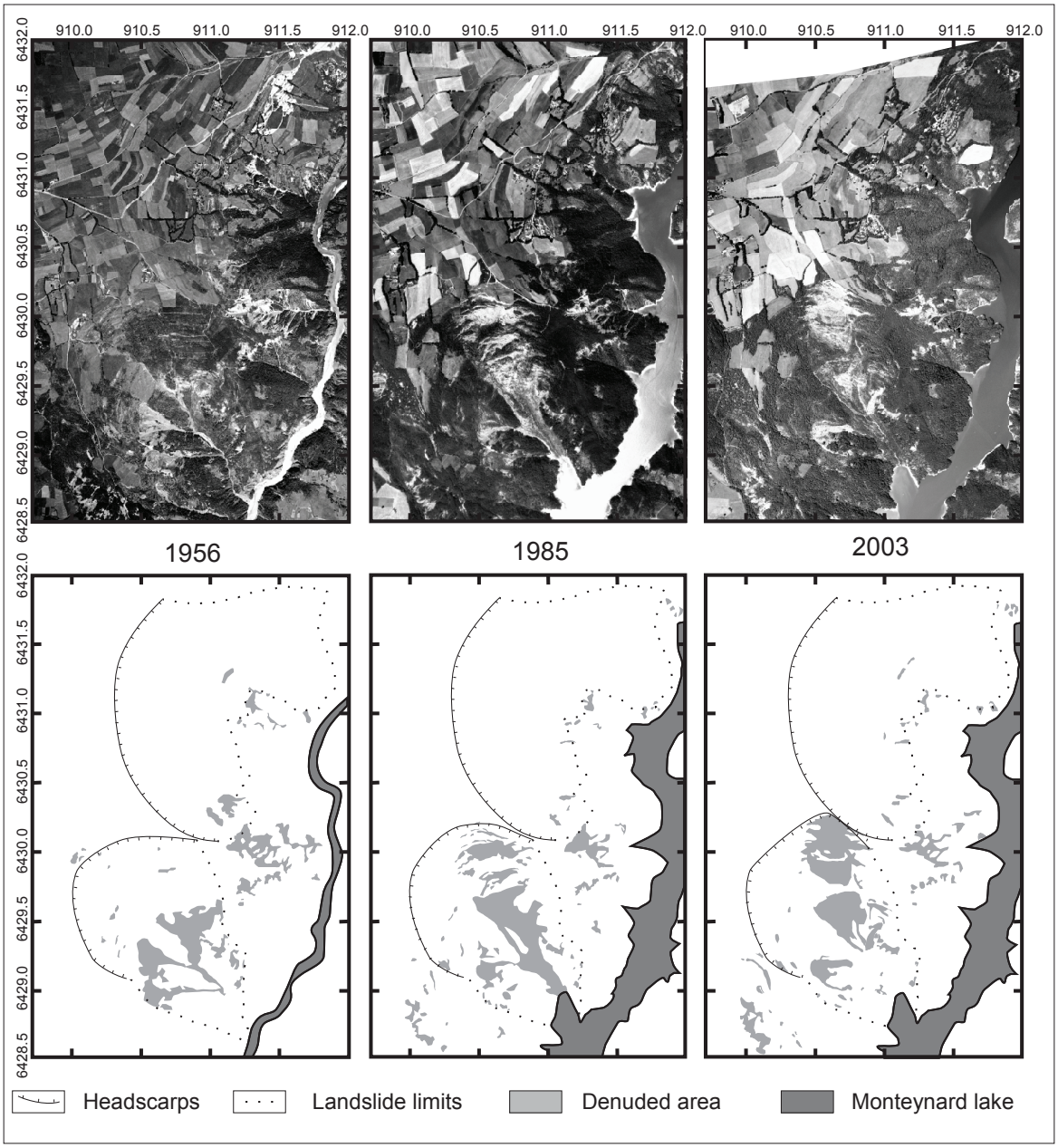

Figure 3.8: Top: Orthorectified aerial photos of the years 1956, 1985 and 2003. The scales of the original photos are 1:25 000, 1:30 000 and 1:25 000. Bottom: Interpretation of the corresponding aerial photo showing the denuded areas related to landslide activity. White areas are not covered by the images. In 1962 the Drac River was damed up creating the lake Monteynard shown in the photos from 1985 and 2003.

Consequently, for each ortho-photo, pixels have been classified as denuded area, using as reference the level of brightness of areas where bare soil has been observed in the field, and excluding the river (or the lac), bright fields, roads and buildings identifiable by their characteristic geometric shapes (see Fig. 3.8, bottom).

3.1.3.2 Analysis

Using the three sets of data, as described in the previous section, several features can be analyzed to highlight the difference in kinematics between the Avignonet and Harmalière landslides: the general orientation of the landslide, surface velocity, denuded area, headscarp evolution and surface roughness.

The clay area affected by sliding is larger on Avignonet (1.8 km^2) than on Harmalière (1.2 km^2). The headscarps of Harmalière and Avignonet mapped from the 1956 aerial photo (before the construction of the Monteynard Dam), show that the maximum distance between the headscarps and the Drac Valley is about 1.5 km in both cases. Both headscarps follow a curve that have a symetry axis oriented NNW-SSE, perpendicular to the Drac Valley, as it is expected in a homogeneous clay mass deeply cutted by a valley (see Fig. 3.8 on the bottom left). In Avignonet, the global sliding direction follows this axis as expressed by the fan-shape pattern of the GPS velocity vectors and of the slope directions of the main scarps. The 11-years average velocity vectors from GPS on the Avignonet landslide are oriented from N 70° E to N 130° E (Fig. 3.7), with a global N 100° E movement.

However, in Harmalière, according to the evolution of denuded area, the most active areas of the landslide develop along a NNW-SSE axis (Fig. 3.8) making a 30° angle with the Avignonet global sliding direction. The percentage of denuded surface is much larger in Harmalière than in Avignonet since the first photos in 1948 (13 % versus 5 % in 1948, 20 % versus 3 % in 1984 and 19 % versus 3 % in 2003). Only a very small active area in the south of Avignonet can be identified. The higher activity of Harmalière certainly goes back, at least, to the end of the 19th century: at that time, according to Moulin and Robert (2004), because of intense gully erosion occurring on the NW part of the Harmalière slide, a significant reforestation work has been implemented by the state authorities. Since the catastrophic Harmalière event in 1981, denuded area are more concentrated in the eastern part of the Harmalière landslide and has grown up-slope since then. Morphological changes due to the 1981 event can be seen in the 1985 sketch of figure 3.8 forming a NNW-SSE elongated body of denuded areas and also in figure 3.7 where, at the same place, a roughness contrast with the surroundin terrain can be noticed. The body itself can be divided into a steeper upstream part where erosion dominates and a smoother lower part corresponding to an accumulation zone, which has been conquered by trees again since the 1981 event (Fig. 3.8 on the right). It is noteworthy that the recent up-slope evolution is not directed straight to the NW, but has rotated clockwise to the N-NE toward the Avignonet landslide.

The main headscarp of Harmalière, which has developed since the catastrophic event of March 1981, has mainly regressed through several brutal events (biggest events were in 1988, 1996 and 2001; Moulin and Robert, 2004). This evolution is traceable from aerial photos analysis, providing a mean regression rate of about 10 m/year between 1981 and 2003. These values are in agreement with ground observations (Moulin and Robert, 2004). Since 2001, the headscarp regression has started to affect the southern limit of the Avignonet landslide. A GPS measurement on the crest between Harmalière and Avignonet indicates mass displacement towards the Southwest, which is consistent

with a faster regression of the Harmalière scarp toward the Northeast (Fig. 3.8) relative to Avignonet. To the North of Harmalière the limits with another landslide show a convexity toward the south (Fig. 3.7 and 3.8). On the Lidar DEM, in the northern part of Avignonet slide, the four uppermost major scarps (spaced by about one hundred of meter) seems to be cut by the northern limit. This suggests that the northern landslide has been the last to be the most active with respect to the Avignonet one.

Surface roughness is also an indicator for landslide activity (Glenn et al., 2006). Analysis of surface roughness from the shaded Lidar DEM (Fig. 3.7) shows differences between the Harmalière and Avignonet landslides in terms of wavelengths and amplitudes along the slope direction. In Harmalière, a characteristic small-scale roughness with wavelengths of 5-15 m and amplitudes of 0.5-5 m can be observed, as well as roughness at a larger scale with wavelengths of 80-200 m and amplitudes of 5-20 m. Two representative elevation profiles along the slope direction are shown in Fig. 3.7b. They are divided into an upper and a lower part according to the presence of significant changes of slope angle and roughness. On these profiles, the roughness has been estimated using the root-mean-square deviations as described by Shepard et al. (2001) with step-sizes of 10 m and 100 m along with the mean slope angles (see table 3.1) corresponding small-scale roughness and large-scale roughness at the wavelengths of 10 m and 100 m respectively.

	A1-A2 upper Avignonet	A2-A3 lower Avignonet	H1-H2 upper Harmalière	H2-H3 lower Harmalière
Profile length (m)	577	247	874	624
Mean slope angle (°)	9.8	16.3	11.6	6.9
RMS deviation (m) small scale (10 m)	1.1	1.6	1.6	1
RMS deviation (m) large scale (100 m)	4.4	4.4*	5.4	2

Table 3.1: Root-mean-square deviations from the elevation profiles seen in Figure 3.7b for 2 different wavelengths (step sizes) representing the roughness at different scales. See text for details. * This value is not reliable due to the short profile length.

In Avignonet the roughness is higher at the toe (1.6 m) than in the upper part (1.1 m) for the small-scale roughness, which can be explained by the higher activity down-slope, as suggested by the GPS, associated to a higher slope angle and may be a higher erosion rate. In Harmalière, the roughness is lower in the lower part than in the upper part for both wavelengths. Indeed, since 1981, Harmalière has shown intense activity in its upper part including collapsing at the headscarp and several minor scarps below, that are responsible in a higher large-scale roughness (5.4 m). In the lower part, it evolves into a more fluent mudslide (large-scale roughness at 2 m) related to the development of an accumulation zone which presents a lower slope angle. Similar large-scale roughness values are found for the upper parts of Avignonet and Harmalière. Assuming that features related to large-scale roughness are more robust through time that the small-scale one, this observation suggests that Avignonet and Harmalière have experienced similar landslide processes in the past. It must be stated that using roughness as an indicator of landslide activity can be biased by several factors that should be discussed. First of all the density of data points after filtering when building the DEM can influences the roughness. Data density decreased in forested

area because of the filtering and could lead into lower roughness. In figure 3.7, the constructed DEM is resampled at 2 m resolution: beside a few exceptions and after filtering the forest, the laser points were still dense enough to avoid smoothing effects due to interpolation. For instance, the south-western part of the Harmalière landslide, which is largely forested, show a higher small-scale roughness than the farming area of the Avignonet slide. On the other hand the effect of farming altering the surface roughness should also be considered. On a very small scale farming can decrease the surface roughness in a very short time, but also high scale roughness could be decreased by farming over decades. On the other hand if the activity of the landslide and with that the roughness is too high, the field will become abandoned and the roughness will be not further decreased. Therefore it can be said that farming amplifies the trend: smooth areas will be more smoothed and rough areas will stay rough above a certain threshold. If there are other causes to abandon a field then the landslide activity, the interpretation of roughness can be misleading. In the case of Harmalière, it can be observed from the aerial photos that a lot of fields become abandoned after being affected by the past 1981 events. Today farming is completely stopped on Harmalière. Also the active part in the south of Avignonet was partly farmland in the past and become abandoned recently.

Taking into account these limitations, the roughness comparison between the Avignonet and Harmalière slide still suggests a significant difference of the recent sliding activity: the Avignonet slide do not show major recent active movements in agreement with GPS data and aerial photographs analysis, in contrast to the Harmalière slide. Only some areas in the lower part and in the South of Avignonet exhibit small-scale roughness similar to Harmalière. This is consistent with the location of denuded area in the most recent aerial photos, which are correlated to a higher landslide activity.

Regarding slide velocity, values measured by GPS at the surface of the Avignonet landslide (Fig. 3.7) increase from less than 20 mm/year at the top to more than 130 mm/year in the most active parts at the toe. The aerial photos show no major signs of activity in Avignonet for the last 60 years with no significant evolution of the headscarp and very small denuded areas. In Harmalière no GPS measurements are available but, by tracking morphological features through different dates in the aerial photos, one can get a rough estimate of the average velocity of several meters per year for some parts of the main landslide body, which is significantly higher than in Avignonet.

Comparison of the two landslides by Lidar scan, GPS data and aerial photos has shown that the recent and former landslide kinematics are highly different for the two earth slides. Harmalière seems to be much more active than Avignonet, today and in the past 60 years. A major factor for this could be the underlying bedrock topography. This possible influence parameter is investigated in the following section.

3.1.4 Geophysical investigation

The objective of the geophysical investigation is to map the thickness of the soft layer over the two landslides. This thickness ranges from 0 to more than 250 m from the East to the West, respectively (Antoine et al., 1981). The site to be characterized encompasses a surface of 5 km^2. Geological investigations conducted in the 1950s for the study of the Monteynard dam (location in Fig. 3.4) were limited to the Avignonet

area. No information is available about the geological setting of the Harmalière area. Furthermore, geophysical campaigns which aimed to characterize the geological setting in the immediate vicinity of the dam were not published and only synthetic data are available. This poses the problem of the reliability of the established model of figure 3.5.

Recent works (Jongmans et al., 2009) have shown the existence of a strong shear wave (S-wave) velocity contrast (more than 3 on average) between the soft upper layers (clays and moraines; 250 m/s < Vs < 600 m/s) and the substratum made of compact cemented alluvial layers (Vs = 1250 m/s) and Jurassic limestone (Vs = 2000 m/s). With such characteristics, microtremor processing (H/V technique) has been proven to be one of the most robust and easy exploration tool for mapping the thickness of alluvial or lacustrine sediments (Ibs-von Seht and Wohlenberg, 1999; Delgado et al., 2000; Guéguen et al., 2007; Méric et al., 2007; Le Roux et al., 2008) including the Trièves area (Jongmans et al., 2009).

3.1.4.1 Method

The H/V technique is a single station method consisting in calculating the horizontal to vertical spectral ratios (H/V) of seismic noise records. For a single homogeneous soft horizontal layer (1D geometry) overlying the bedrock, the H/V curve exhibits a peak at a frequency f_{HV} that is the shear-wave resonance frequency f_0 of the soft layer (Bard, 1998). This theoretical resonance frequency is given by (Haskell, 1960):

$$f_0 = \frac{V_s}{4T} \tag{3.1}$$

where Vs is the soft layer S-wave velocity (in m/s) and T is the layer thickness (in m). The resonance frequency decreases with a decrease of Vs and an increase of thickness. If Vs is known, this equation allows the layer thickness to be determined. For a layered medium overlying a halfspace, the resonance frequency can be computed from the thickness and the dynamic characteristics of each soil layer (Haskell, 1960) and the total thickness of the soil layers can be deduced if the vertical velocity profile is known. When the seismic impedance contrast Z between the soft layer and the bedrock is high enough (Z > 4), the H/V peak was shown to result from a change in the ellipticity of the fundamental mode of the Rayleigh waves (Bonnefoy-Claudet et al., 2006). The corresponding ellipticity frequency f_{ell} is then equal to the resonance frequency f_0.

Measurements were made with a single three-component 5 s sensor giving a flat response between 0.2 and 50 Hz and connected to a light seismic acquisition system (Chatelain et al., 2000). Seismic noise was recorded during 15 minutes with a 200 Hz sampling frequency. Data were processed with the Sesarray package `www.geopsy.org` (Wathelet et al., 2004). Microtremor records were cut into 30 s time windows, for which Fourier spectra were computed and smoothed using the technique proposed by Konno and Ohmachi (1998). H/V spectral ratios were computed for all time windows and the mean H/V curve is given with standard deviations at each site.

The H/V method offers the advantages of being easy to deploy (one station-one people) and quick (about 10 sites per day), depending on field conditions. Limits are weather conditions, likely to influence the H/V curve (Koller et al., 2004), and the assumption of horizontally layered medium, which cannot be valid in case of strong lateral seismic contrasts (Uebayashi, 2003). In the study site conditions, the 5 km^2 area was covered within a two weeks delay by a single operator.

3.1.4.2 H/V data

H/V measurements were performed at 104 sites (Fig. 3.9) and were located with a GPS with a horizontal accuracy ranging from one to a few meters under forest.

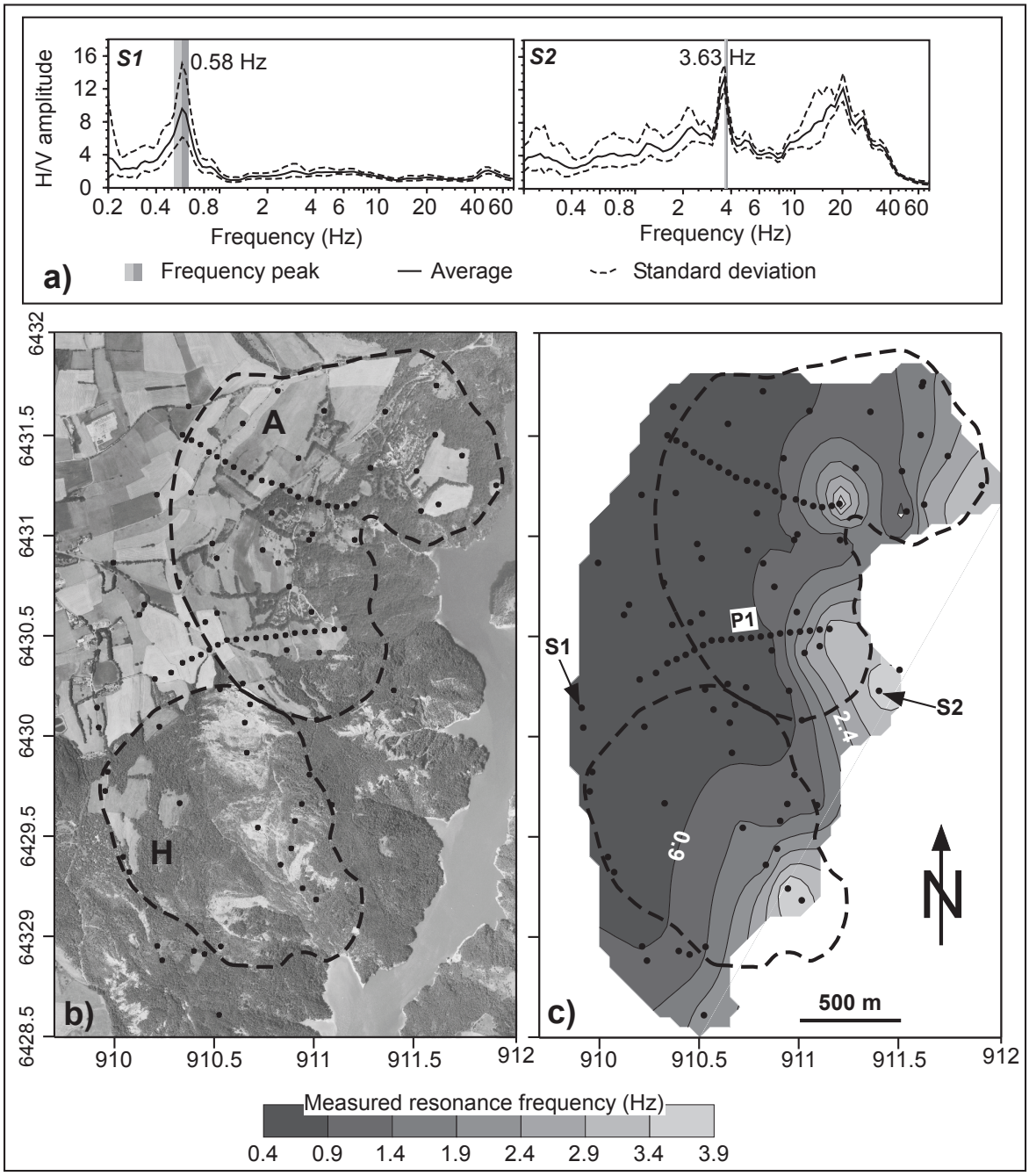

Figure 3.9: H/V measurements. **a)** H/V curves at points S1 and S2 (location on Fig. 3.9c). **b)** Location of the 104 measurement points with the landslides limits (dashed line); A: Avignonet landslide; H: Harmalière landslide. **c)** Resonance frequency map.

Elevation values were extracted from the Lidar DEM. H/V curves (spectral ratio versus frequency) at two sites (S1 and S2) are presented in figure 3.9a. Both curves exhibit a peak with amplitude over 8 at 0.58 Hz for S1 and at a 3.63 Hz for S2, corresponding to the resonance frequency of the site. At S2, a second peak appears at 20 Hz, which could correspond to the resonance of a superficial layer or to a higher resonance mode. The great majority of the 104 measured H/V curves fit the criteria proposed

in the SESAME guideline (Koller et al., 2004) for a 1D resonance phenomenon, with well-individualized peaks and H/V amplitudes greater than 2. For some measurements, located in the southeastern part of the Harmalière landslide (location in Fig. 3.9b), however, curves exhibit a plateau-like shape, suggesting 2D or 3D effects. This point will be discussed below.

The frequency field was gridded with a kriging algorithm (Kitanidis, 1997), using an exponential variogram model with a N-S anisotropy for the search radius. The gridded surface fits the experimental data with an absolute error of 3 %. The results are presented on figure 3.9c.

To the West, the frequency map (Fig. 3.9c) reveals a NNE-SSW 500 m wide elongated low-frequency zone, with values ranging from 0.4 to 1 Hz. To the East, frequencies increase rapidly with distance, from 1 to 4 Hz. This eastward evolution of the resonance frequency is consistent with the thinning of the clay layer and the corresponding rise of stiff layers shown in previous works (Fig. 3.5; Crosnier-Leconte et al., 1953; Lambert and Monjuvent, 1968; Blanchet, 1988; Jongmans et al., 2009). Applying equation 3.1 with a mean S-wave velocity of 600 m/s in the clay layer (Méneroud et al., 1995) yields a clay thickness between 375 m to the west and 37 m to the east. These thickness values are however approximate, owing to the vertical S-wave velocity variation in the clay layer. This results from the effects of compactness and landslide activity. The dynamic characteristics (P-wave and S-wave velocities, density) within the different layers (from top to bottom: morainic colluvium, moraine, disturbed clays, undisturbed clays, alluvium and bedrock) were obtained from previous seismic studies (Méneroud et al., 1995; Renalier et al., 2007; Jongmans et al., 2009) and are presented in table 3.2.

Table 3.2: Dynamic characteristics (compressional wave velocity Vp, shear wave velocity Vs and density) used for the calculation of the theoretical resonance frequency. See text for details.

Geological unit	*Thickness (m)*	*Vp (m/s)*	*Vs (m/s)*	*Density*
Morainic colluvium	5	500	250	1.9
Moraines	0-50	1850	150-450	2
Disturbed clays	0-45	1850	150-450	2
Unidisturbed clays	0-250	1850	600-650	2
Compact alluvium	0-100	2350	1250	2
Carbonate bedrock	Halfspace	3000	2000	2.6

Thickness values in the layers were estimated at each station from the available geophysical and geotechnical data (Monjuvent, 1973; Antoine et al., 1981; Blanchet, 1988; Lorier and Desvarreux, 2004; Jongmans et al., 2009). Then, the only free parameter left is the thickness of the undisturbed clay layer.

Preliminary theoretical sensitivity tests were conducted using the Sesarray package (Wathelet et al., 2004). They have shown that the clay thickness is the main parameter controlling the resonance frequency. Furthermore, these tests also showed that the impedance contrast, using the parameters of Table 3.2, between clays and cemented alluvial layers was sufficient enough to generate a peak corresponding to the resonance frequency. It implies that the measured frequency corresponds in each case to the base

of the clays. No change in the f_0 value has been found when passing the landslide headscarp (cf. Fig. 3.9c). Furthermore, within the slide, no high-frequency peak that could sign a shear plane has been recorded nor computed. These results support the use of resonance frequency measurements for determining the base of the clays. On an other hand, they indicate that this technique might not be suitable for detecting and mapping the slide itself (on the contrary of Méric et al., 2007). This could be due to an insufficient seismic impedance contrast between the disturbed clays and the undisturbed laminated clays (cf. Table 3.2).

The soft layer thickness was computed at each station by fitting the theoretical resonance frequency to the measured one using a trial and error method. The plot of computed thicknesses versus experimental resonance periods (inverse of the frequency) for the whole data set shows a good correlation (Fig. 3.10a), corroborating the determined velocities in the layers.

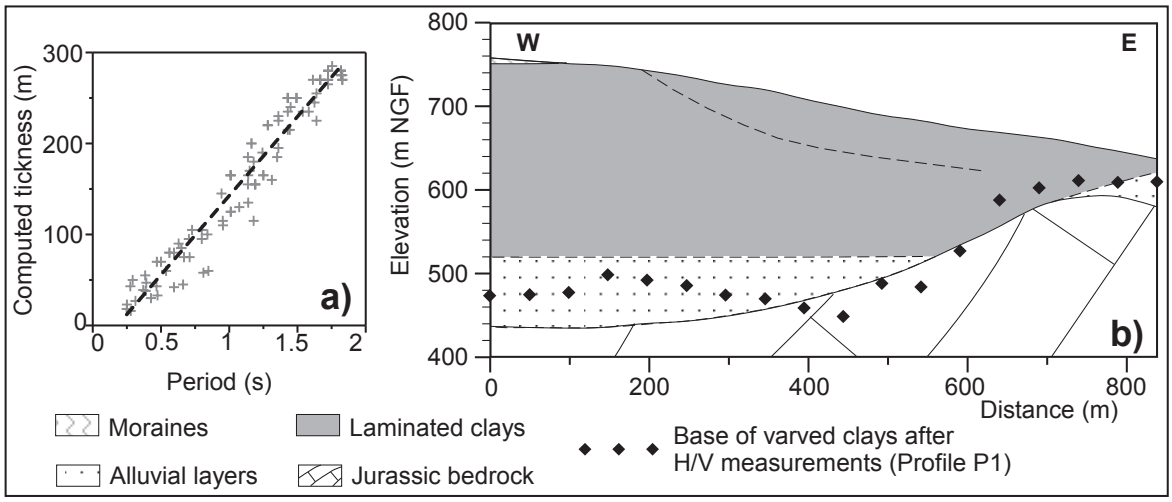

Figure 3.10: Frequency to thickness calibration for H/V profile P1 (location on Figs. 3.9b and 3.9c). **a)** Computed thickness as a function of the measured resonance period (inverse of the frequency) for the 104 stations. Linear regression (black dashed line) gives a determination coefficient r^2 equals to 0.95. **b)** Comparison of the geometry of the top of the Jurassic bedrock (Blanchet, 1988) and the bottom of the laminated clays after H/V measurements along profile P1 (location in Fig. 3.9c). Dashed line depicts the lower limit of the Avignonet landslide deduced from inclinometer data.

The H/V deduced geometry of the seismic bedrock top is compared to the section previously established from a long refraction profile conducted for the study of the Monteynard dam (profile P1, location in Fig. 3.9c; Blanchet, 1988) which depicts the top of the Jurassic bedrock. A general good agreement is observed between the two sections (Fig. 3.10b) in terms of relative way of the palaeotopography. Observed discrepancies range from a very few m to the East to some 40 m to the West. These disparities may come from strong changes in layer velocities which are not known. This also may come from the reference geological model, established from a refraction study and which reliability is not known. This prevents this H/V mapping from being exhaustive but allows the relative palaeotopography to be estimated and analyzed in terms of geometry. Errors may also arise from 2D and/or 3D effects as well as from varying cementation of the alluvial layers, as observed at outcrop. These points will be discussed further.

The thickness values obtained over the whole area were then kriged with an exponential variogram model to produce a map depicting the distribution of the thickness of the soft layer (moraines, morainic colluvium and clays) over the seismic substratum (alluvial compact layers and Jurassic bedrock; Fig. 3.11a).

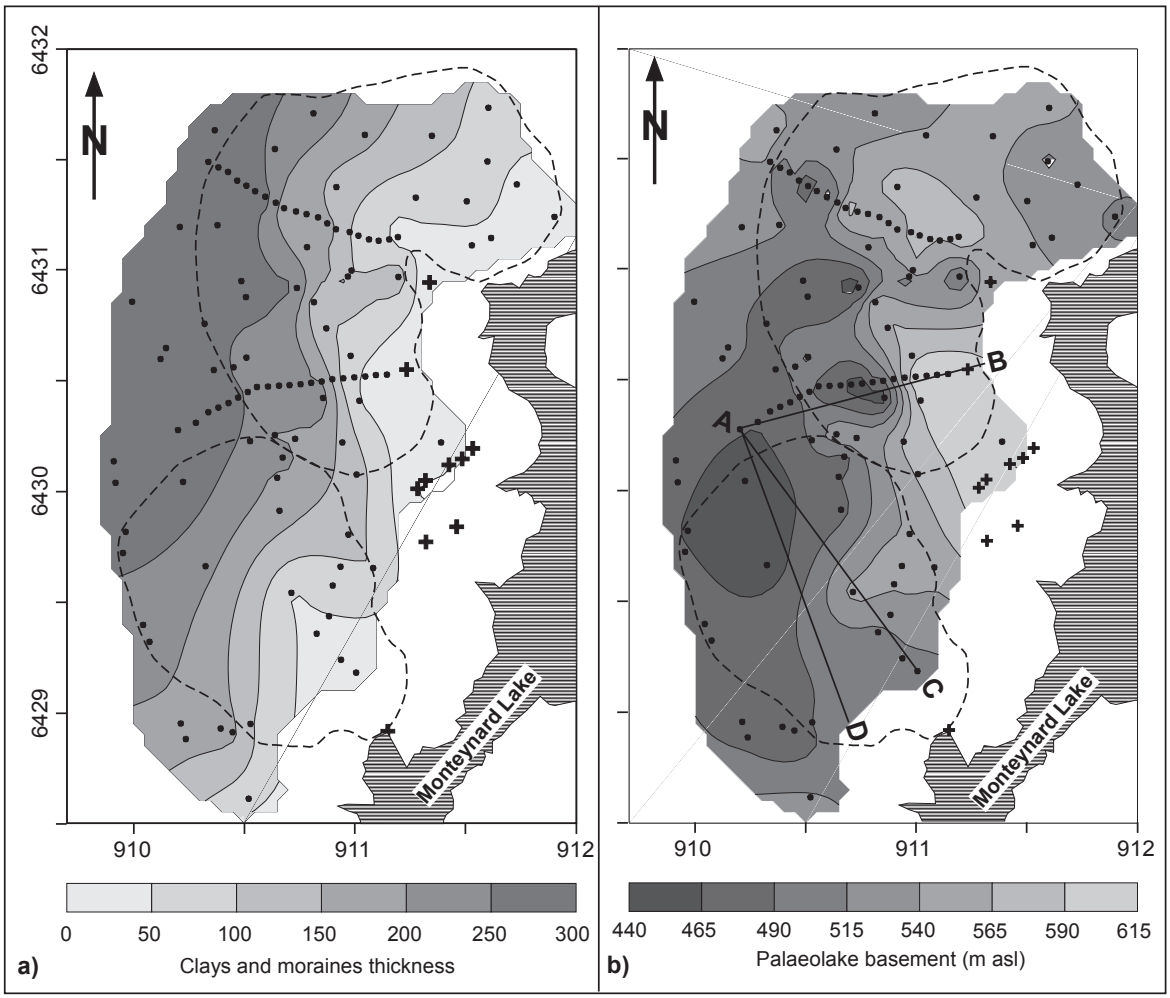

Figure 3.11: Soft layer thickness maps. **a)** Soft layer thickness map. The absolute error between computed and interpolated thicknesses is 5.29 %. **b)** Lake Trièves palaeotopography in the study area. The absolute error between computed and interpolated palaeotopography is 0.98 %. Dots refer to seismic measurements and crosses to field observations; dashed lines stand for Avignonet and Harmalière landslides limits.

Outcrops of stiff alluvium and carbonate bedrock (0 m of soft cover thickness) were added in order to better constrain the interpolation. The thickness map is in agreement with the frequency map of Figure 3.9, showing a significant westward increase of the clay thickness from 0 m on the valley flank to more than 300 m below the village of Sinard. These values are consistent with field observations and the outcropping of the alluvial layers to the East (Fig. 3.5). This is also consistent with previous estimations (Monjuvent, 1973; Antoine et al., 1981) that give a soft layer thickness from 0 to 300 m on the West (moraines and clays; see Table 3.2).

Thickness values were subtracted from elevation values given by the Lidar DEM at each measurement point. These points were again spatially interpolated using a kriging method with an exponential variogram model. The relief of the bottom of the clay layer is given in Figure 3.11b. The palaeotopography upon which clays have been

deposited is very irregular, with elevation variations of more than 150 m. The major feature is the presence of a depression striking NNE-SSW, which is bordered to the East by a N-S ridge culminating at an elevation of about 600 to 620 m (cross-section AB on Fig. 3.12).

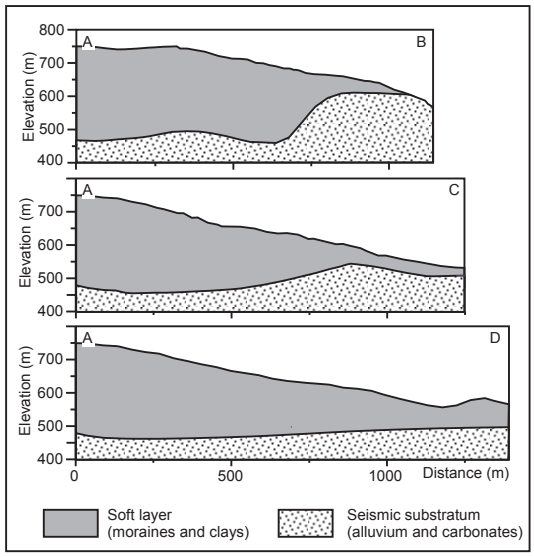

Figure 3.12: Cross-sections of the paleolake basement (location in Fig. 3.11b).

This depression probably coincides with palaeovalley v2 of the palaeodrac river, as suggested by the presence of alluvial outcrops along the lake (Figs. 3.4 and 3.5) and by previous works (Crosnier-Leconte et al., 1953; Monjuvent, 1973). The N-S ridge appearing to the east and shown on cross-section AB corresponds to the presence of carbonate bedrock irregularly covered with compact alluvial layers and sporadically outcropping along the lakeshore. To the South, this ridge disappears (cross-sections AC and AD; Fig. 3.12). In figure 3.11 are superimposed the limits of the landslides of Avignonet and Harmalière. Below the southern part of the Avignonet slide, on its eastern side, the ridge of compact layers continuously extends perpendicularly to the global slide motion and could act as a buttress. On the contrary, the Harmalière landslide clearly developed over the lower elevation zone (Fig. 3.11b) and its motion can be explained by its orientation which changes from N-S to NW-SE in the South.

3.1.5 Discussion

Geophysical investigation with ambient noise measurements allows to compute a frequency map (Fig. 3.9c) that can be turned into a soft sediments thickness map which is used to derive a paleotopography map (Fig. 3.11). Considering the thicknesses that have been computed, one may argue that 2D and/or 3D effects are present and that measured f_{HV} might be biased. The presence of non-1D cases is highlighted by strong lateral variations observed on the frequency map (Fig. 3.9a). Consequently, calibration based on the ellipticity of the fundamental mode of Rayleigh waves may be irrelevant and cannot provide the correct thickness for the soft layers. Some of these effects have been noticed on the signals located in the southeastern part of the Harmalière landslide (Fig. 3.9b) by plateau-like signals. By picking the frequency at the plateau cut-off, the resonance frequency tends to be overestimated (Guillier et al., 2006). Similar side effects have already been reported by studies conducted within small-apex valleys (Uebayashi, 2003; Koller et al., 2004; Guéguen et al., 2007; Le Roux

et al., 2008). This is illustrated on cross-section AC of figure 3.11. Between abscissa 800 and 850 m, a bulge of substratum is visible. It corresponds to a zone with pleatau-like H/V curves. This strong side effect tends to provide an overestimated measured f_{HV} and, thus, a lowered clay thickness. As a consequence, the observed bulge on cross-section AC is likely to result from side effects and not to represent a real structure.

Another problem arising from calibrations is the eventual presence of lateral Vs variations in the soft sediments. Vertical and W-E variations are known to be present within clays (Renalier et al., 2007; Jongmans et al., 2009) and were taken into account for the frequency to thickness computations. On an other hand, since the Würm glacier extension was limited to the village of Sinard (Figs. 3.2 and 3.4), the presence of such an ice-cap and of the 50 m thick moraines may influence the compactness and, then, the S-wave velocity of the clays across this boundary. Nevertheless, N-S velocity variations within the soft layer have not been reported hitherto and were not eventually integrated to this work.

As a consequence of these uncertainties, the soft layer thickness map computed from H/V data may contain more or less important error bars. These errors are estimated to a few meters to the East (were soft layer thickness is of a few tens of meters) to some 40 m to the West, were the soft layer reaches 300 m. These uncertainties do not question the reliability of the first order of observations since the aim of this work is to map the relative variations of the seismic substratum. The basement of the former Trièves lake on which were deposited the glaciolacustrine laminated clays is irregularly shaped and shows strong lateral variations. At most, this introduces an uncertainty in the exhaustive mapping of the clay thickness.

There is a N-S ridge to the East of the investigated area, culminating at about 620 m, which disappears to the south. Cross-sections AC and AD on figure 3.12 illustrate the progressive vanishing of this hard ridge marking a depression to the South at about 460 m, which continues toward the North-East and then runs along the west side of the ridge. This depression allowed the deposition of 300 m of clays and moraines over a seismic substratum located at an elevation less than 520 m asl. Over the ridge only a very few tens of meters of clay remain because of a lower thickness of sediment and of erosion. This analysis confirms previous works done by other geophysical methods on Avignonet (Crosnier-Leconte et al., 1953; Blanchet, 1988), and also extents consistently the knowledge of the palaeotopography to the south up to Harmalière. The new map also confirms the geological observations and interpretation inferring that several glacial and interglacial erosion phases, that took place during the Quaternary (Monjuvent, 1973; Brocard et al., 2003), created a palaeotopography marked by the incision of at least two paleovalleys of the Drac, called "Drac de Sinard" and "Drac de Cros", filled with alluvium and running below the laminated clay of the Sinard plateau, notably below Harmalière and Avignonet (Lambert and Monjuvent, 1968; Monjuvent, 1973). However, Lambert and Monjuvent (1968) and Monjuvent (1973) indicate that the top of the "Drac de Sinard" alluvium is at about 500-520 m asl in the Harmalière-Avignonet area, and that its bottom is at about 410 m asl, whereas our results show, west to the ridge, intermediate values ranging between 440 and 500 m asl. This could suggest that the method used is not sensible to the contrast between alluvial deposits and clay. Preliminary theoretical sensitivity tests revealed that the impendance contrast between the clays and the compact, cemented, alluvial layers was large enough to generate a resonance frequency peak. On an other hand, field observations, along with previous works (e.g. Monjuvent, 1973) indicate that these alluvial layers are only

locally cemented. Where they are not, their mechanical parameters, especially Vs, would dramatically decrease and approach values within clays (for Vs values within alluvial sediments, see for example, Pugin et al., 2009). In such cases, the measured resonance frequency and, consequently, the base of the soft layer, would correspond to the interface between the base of non-cemented alluvial layers and the top of cemented alluvial layers and/or the Jurassic bedrock. Here again, this aspect is pointless since the aim of this work is to map the seismic substratum. Furthermore, it could partly explain the important discrepancies between the computed thicknesses and the reference cross-section (Fig. 3.10).

The other palaeovalley, called "Drac de Cros", recognized by geophysics and geology (Crosnier-Leconte et al., 1953; Lambert and Monjuvent, 1968; Monjuvent, 1973) is supposed to run east to the ridge, below the North-Eastern part of the Avignonet landslide. The top of its alluvial deposits is expected to be at about 600 m asl. The location of this palaeovalley is not clear on our map. Geological observations suggest that this palaeovalley is narrower with steeper flanks than the "Drac de Sinard" one, which could explain the difficulty to see it. Here again, our estimations of the clay basement give a substratum at 530-560 m asl at the location of the expected "Drac de Cros", that is lower that geological estimate (600 m). This bias could again be explained by the fact that, the alluvial deposits are not always cemented (Monjuvent, 1973), leading to a localization of the basement that is intermediate between the top of the alluvial deposits and the top of the Jurassic bedrock. One can also notice a small East-West depression across the ridge in the middle of the Avignonet landslide that has not been reported before. However, because of the possible uncertainties of the map mentioned here before, we do not try to interpret it as a paleomorphological feature. In the following, we will retain only the robust features of our geophysical investigations, that are the N-S ridge and the depression related to the paleovalley of the "Drac de Sinard".

Beside the geophysical maps of soft layer thickness and of paleotopography, a comparison of the Harmalière and Avignonet landslides kinematics has been done based on GPS, aerial photo and Lidar DEM analysis. It turns out that two main differences between the two landslides are observed for the recent time: the orientation of the main sliding direction, and the level of sliding activity. Regarding the orientation it has been shown in section 3 that the Harmalière landslide is developing since 1948 along a NW-SE direction, which is significantly oblique with the expected NNW-SSE direction toward the Drac valley (before the lake filling) that can be observed, for instance, in Avignonet. The NW-SE axis also corresponds to the orientation of the "Drac de Sinard" paleovalley below the Harmalière slide, suggesting that the orientation of the Harmalière landslide might be controlled by the paleotopography. Regarding the level of sliding activity, a first observation is that the northern part of the Harmalière headscarp is moving to the North starting to erode the southern flank of the Avignonet slide. Secondly, GPS measurements and analysis of digital photographs, back to 1948, reveal that Harmalièreís main slide body is far more active than the Avignonet one: there are regression of the headscarp of several m per year being accompanied by rapid evolution of the denuded area (that are not observed on Avignonet since 60 years) and sliding velocity than can exceed 1 m/year, whereas, in Avignonet, the 11 years GPS data do not show velocity exceeding 15cm/year. These observations are consistent with the morphology of the landslides, especially the roughness, shown by the Lidar DEM which reflects more long-term activity. In Avignonet there is a gradient of displacement

from the uppermost sliding clays, showing displacements of about 1-2cm/year, up to the toe of the clay mass with 10-13cm/year where the clay thickness are less than a few tens of meters (around 30m). Downward, outcrops of alluvial layer or of Jurassic bedrock do not show sliding processes. On a W-E profile along the Avignonet slide, Jongmans et al. (2009) have observed a negative correlation between the sliding velocity and the Vs values of the first 5 m suggesting a downward increasing deformation state of this clay material. They also found evidence for a slip surface at about 40 m depth within the clay confirming previous hypothesis done from inclinometric data (Blanchet, 1988; Lorier and Desvarreux, 2004). When comparing these observations with the position of the ridge in the paleotopography, one can be inclined to think that, here also, there is a palaeotopographic control over the kinematics: the ridge of hard layers along the eastern part of the Avignonet landslide acts as a buttress that could mechanically prevent the slide from rapid evolution as observed in Harmalière (Fig. 3.7).

However, the hypothesis of a paleotopography control over the landslide kinematics has to be discussed taking into account a longer time interval than the last 60 years of observation on which it is based. This perspective arises several questions: is the present-day kinematics, in progress since at least 1948, representative of the long term evolution of the two landslides (i.e. over several thousands of years)? If the paleotopography controls the kinematics, what is its long term impact on the landslide morphology? One may argue that each landslide has its own evolution that consists in successive phases of slow movement (like in Avignonet today), followed by rapid events (like in Harmalière today). In this case, the present-day situation could have been the reverse at some periods in the past: an active Avignonet slide and a quiet Harmalière slide. Then, the supposed relationships between kinematics and paleotopography would be just a coincidence or negligible.

To address this issue, morphological parameters can be considered that may reflect the relative long term level of activity of the two landslides. The area of the Avignonet landslide is larger than in Harmalière. However, as noticed in section 2, the maximum distance to the Drac river is similar. This suggests a similar average speed of regression of the headscarps, if we do the reasonable hypothesis that erosion processes start at the same time for the two nearby landslides, when the Drac started to incise into the glaciolacustrine deposits.

Note that, in this discussion, we will not try to use absolute time to estimate incision or erosion rates, because the timing of the beginning of the Drac incision is still debated. Some authors favor a last Würm maximum at 50-40 Ka (Monjuvent, 1973; Nicoud et al., 2002) and others at 30-20 Ka coincident with the LGM (Brocard, 2003; Brocard et al., 2003). The volume of eroded clays can be also considered. As described in section 2, it can be assumed that, at the end of the last Würm maximum, the glacio-lacustrine clay material formed a flat plateau culminating at about 750 m asl on top of which were deposited an additional 50 m of moraines as far as the south of the village of Sinard (Figs. 3.2 and 3.4; Monjuvent, 1973; Antoine et al., 1981). The eroded volume of material can be calculated by subtracting the Lidar DEM from this 800 m asl surface over the area below which clay are present for each landslide. This gives about 436 million of m^3 for Avignonet and 340 million of m^3 for Harmalière (for comparison, during the 1981 main Harmalière mudflow, 250000 m^3 went into the lake (Blanchet, 1988) but more materials were mobilized that accumulated at the bottom

of the slide above the lake). If we divide theses values by the landslide area, it gives an average of 157 m of eroded clay material per m^2 for Avignonet and 195 m per m^2 for Harmalière, suggesting a higher average long-term activity for Harmalière. However, one cannot say if, for instance, these values correspond to very large events closely related in a short period of time (with the rest of the time a lower activity of the slide) or, in contrast, if they are representative of continuous evolution of the slides. The DEM morphology analysis has shown that there is a contrast in roughness between the two landslides that suggests (with the mapping of the evolution of the denuded area) that the Harmalière slide is more active than the Avignonet one. However it can be observed within the Harmalière slide that a short term event like the 1981 mudflow and its subsequent events can change the small-scale roughness and vegetation cover of the slopes: the 1981 active body shows a visible roughness contrast with the surrounding areas of the slide. Regarding the Harmalière headscarp regression over the Avignonet slide, it seems to reflect only a recent evolution because it does not significantly modify the regular headscarp curve of the Avignonet slide. Furthermore, the observed speed of the Harmalière's headscarp regression since 1981, at about 10m/year, is not sustainable over the long term. In brief, all these morphological criteria do not seem very reliable for reflecting significant differences in kinematics of the long term (thousands of years) evolution of the slides.

Physical mechanisms responsible of the laminated clays instability, has also to be taken into account in the analysis. It has been shown by several authors that, for the Trièves laminated clays, natural slope become instable when exceeding 6 to 8° (Antoine et al., 1981, 1991; Giraud et al., 1991). According to Antoine et al. (1981), three main types of sliding are frequently observed: **1)** sliding of the vegetative cover (thickness less than 0.5 m) over the clays; **2)** creeping of a whole top clay layer (thickness 0-6 m) associated with localized and superficial mudflow; **3)** sliding of mass of clay over a slip surface (thickness up to 50 m), than can evolve into a mudflow like in Harmalire in 1981 with velocities that can reach several m/h.

According to these processes, the palaeotopography should have an effect onto landslide activity when the clays thickness is lower than 50 m except if the material of the substratum has a significant impact on the hydrogeological conditions, for instance by draining water and influencing the water table. In Avignonet, analysis of piezometric data done so far, do not provide evidence of such an effect. Considering **1)** the present day topographic profile along the main slope direction of the Avignonet slide, **2)** the position of the ridge at about 700 m west to the Drac valley with a highest point at about 620m and **3)** the initial level surface, at around 800m asl, in which the Drac started to incise, one can say that the possible effects of the palaeotopography on the landslide activity did not start at the beginning of the slide's life and may be relatively recent in the slide histories. That could explain why there is no clear evidence of long term difference of activities between the two landslides. When the deep slip surfaces started to reach the clay basement, the development of new deeper slip surface has been influenced because the basement prevents them to go deeper, as it has been expected if no ridge were present. This certainly causes a slowing of their evolution. In Avignonet, Blanchet (1988) and Jongmans et al. (2009) proposed several hypotheses about the geometry of a deep slip surface at about 50m identified from inclinometric data. These geometries are influenced by the basement in their lowest part, suggesting that the Avignonet landslide activity may have been recently slow down by the

palaeotopography. The fact that the GPS velocities are the highest in the lowest part near the ridge is interpreted as being due to more intensive superficial creep at the toe of the slide. In the Harmalière slide, no inclinometric data are available. However, applying similar reasoning, one can say that the situation where the deep slip surfaces reach the clay basement has not started on the NW-SE profiles along which the slide is developing (Fig. 3.11). If, instead, we consider an E-W profile in the middle of the Harmalière slide, the situation looks more similar to the Avignonet case. This could explain why the Harmalière slide is developing along an NW-SE direction and why it has recently shown a highest activity than in Avignonet.

Consequently, we propose that paleotopography is a significant controlling factor of the Harmalière and Avignonet landslide evolutions, acting as a mechanical buttress against the development of slip surfaces in the clays. Paleotopography may also have another impact (not investigated in this study), that is an influence on the drainage condition of the two landslides because paleotopography is responsible of large permeability heterogeneities due to the presence of alluvial deposits in the paleovalleys.

3.1.6 Conclusion

The two adjacent landslides of Avignonet and Harmalière have been studied following an original multidisciplinary approach based on geodetic (GPS, digital photographs), remote sensing (Lidar), and ground geophysics (ambient noise measurements). The aim was to understand the differential kinematics, motion directions and morphology that characterize these landslides located in the same geotechnical setting.

GPS measurements and digital photographs reveal that the difference in kinematics between the two earthslides can be tracked back to 60 years ago at least. The Avignonet slide is mainly directed towards the East (N 100° E) while Harmalière is mainly oriented towards SE. The Lidar scan map illustrates this differential motion and morphology between the two slides and highlights that the Harmalière slide is still presently much more active than the Avignonet one.

A ground geophysical prospecting based on ambient noise measurements allowed to record the resonance frequencies at different locations. These measured resonance frequencies where turned into soft sediments thicknesses. Finally, a map depicting the base of the clays was computed. It indicates that the basement is very irregularly shaped with strong lateral E-W variations over 150 m. This map confirms previous field and geophysical observations that revealed a westward thickening of the clays. This map also reveals the presence of a N-S ridge of hard sediments (Jurassic bedrock and/or compact alluvial layers) on the eastern side of the Avignonet landslide. This ridge disappears when approaching the Harmalière landslide and makes place to what can be interpreted like a NW-SE oriented palaeovalley of the river Drac. It is proposed that the ridge could act as a butress which could mechanically prevent the Avignonet landslide from evolving as fast as the Harmalière one. Furthermore the NW-SE palaeovalley located under the Harmalière landslide corresponds to the motion direction of the slide. It is then finally proposed that the slides different behaviours are partly controlled by the palaeotopographic setting of lake Trièves.

This approach reveals to be a quick and relatively low-cost way to characterize the geomorphological setting of this sedimentary basin over an important area of $5\,km^2$ by building a geometrical framework for lanslide characterization within fine-grained soft-sediments.

3.2 DTM analysis

This section presents the results of the Lidar-DTM generation, the extraction of quantitative morphological parameters and its interpretation concerning activity and history of the two landslides. It is divided in the acquisition (Sec. 3.2.1), the DTM generation (Sec. 3.2.2), the geomorphological interpretation of the shaded relief map (Sec. 3.2.4), the slope characterization (Sec. 3.2.3), the drainage network (Sec. 3.2.6) and the roughness (Sec. 3.2.7). The focus is on showing differences between the two landslides, Avignonet and Harmalière, in order to explain their different behavior in the past and hazard potential for the future. The limits of the methods are discussed in Section 3.2.8. Some aspects presented in this chapter are also included in the general discussion of the landslide evolutions at the end of the next chapter (Sec. 4.4).

3.2.1 Lidar Acqusition

The area of the two landslides was scanned in 2006 and 2009 by Helimap[1] using a handheld helicopter based system described and evaluated in Vallet and Skaloud (2004). The reported accuracy is 10 cm in horizontal and 14 cm in vertical direction. The delivered unfiltered point-clouds contain $36 \cdot 10^6$ points for 2006 and $26 \cdot 10^6$ points for 2009 using the last pulse only. Further details about the datasets are given in Appendix A.2 and A.3. Acquisitions took place in November (2006) and April (2009) in order to avoid dense canopies and snow coverage. Figure 3.13 shows the point-cloud densities for both acquisitions before and after the non-ground filtering. The 2006 acquisition is more inhomogenous due to unstable weather conditions at the acquisition date resulting in inconsistent flight paths. The density map of the 2009 acquisition is more homogeneous with a higher point density at the headscarp of Harmalière (yellow-red area in the center of Figure 3.13b). A higher resolution was asked for this area exhibiting the highest landslide activity. For both scans a minimum density of about 4-6 pts/m^2 could be achieved.

In order to illustrate some properties of the scan concerning vegetation, Figure 3.14 shows a zoomed view on the headscarp of Harmalière. The aerial photo (a) shows 3 major vegetation zones: agricultural fields (yellow-brown colour), forest (dark green colour) and bare-earth outcrops of clay (white-grey colour). The unfiltered shaded relief map (b) of the same area exhibit distinctive morphological features for the areas, including the head-scarp of Harmalière with the downward slope to the South, as well as the forested areas with their bumpy anisotropic morphology. The reflectivity map (c) shows the average strength of the backscattered laser-signal of all points of the scan. It seems to be positively correlated with the vegetation density. This can be explained by the wavelength in the NIR-spectrum (near infra-red) of the operating laser, which is more reflective at vegetation relative to dry and wet soils. Additionally the maximum height difference was computed between all Lidar-points within each 2 m by 2 m grid-cell (d). Assuming that at least one point in each cell was reflected at the ground surface and one at the top of the vegetation, this parameter could be used to discriminate the areas. The distribution map (Fig. 3.14d) shows that the maximum vegetation height is lower in the agricultural field and bare-earth areas ($<$ 0.6 cm) and higher in forested areas. These results suggest that both, reflectivity and

[1] Helimap System SA is a Swiss mapping company - `helimap.ch`

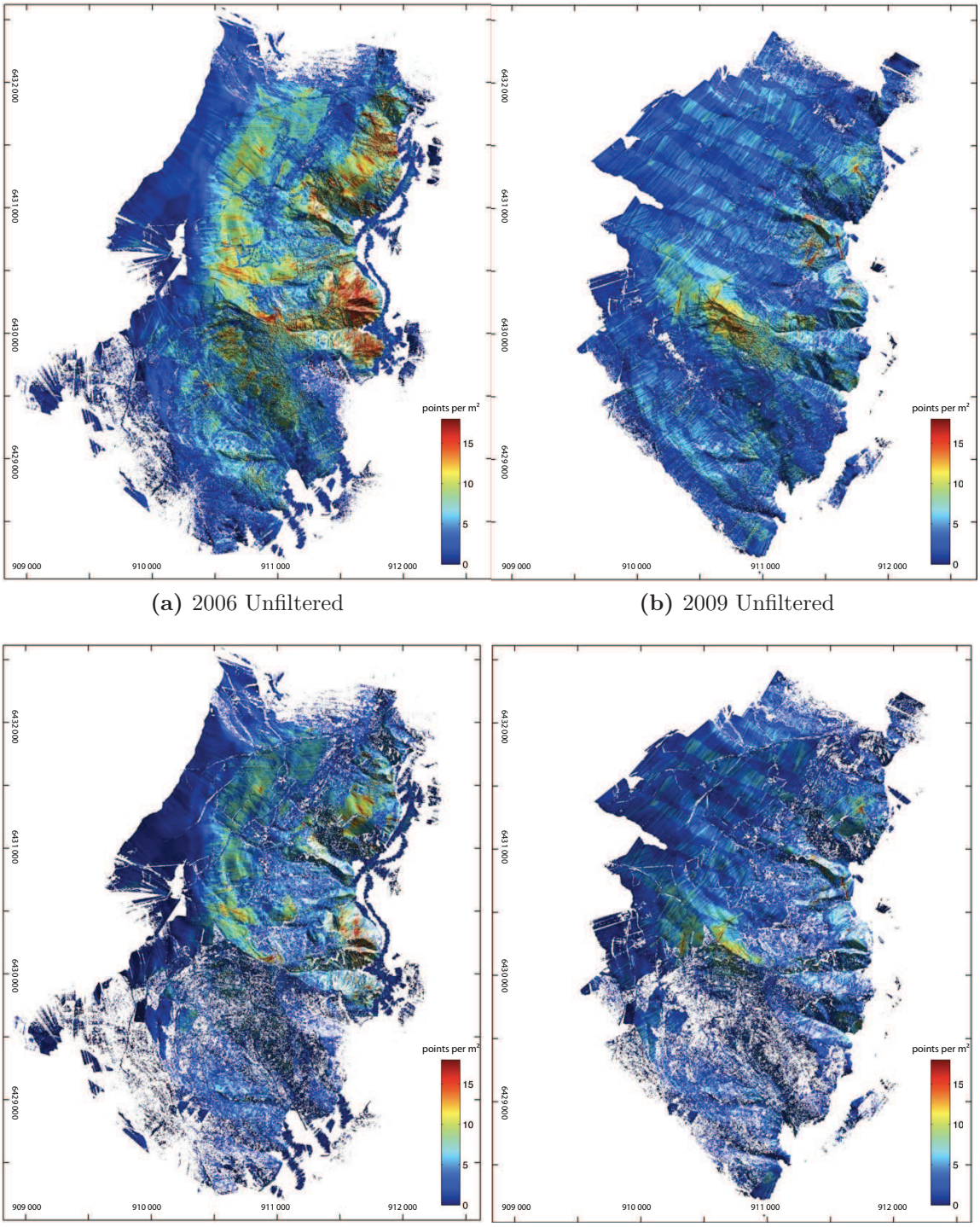

(a) 2006 Unfiltered **(b)** 2009 Unfiltered

(c) 2006 Filtered **(d)** 2009 Filtered

Figure 3.13: Densities of the point-clouds before for the two Lidar acquisitions of Nov 2006 (a and c) and Apr 2009 (b and d), draped on the shaded relief. (a) and (b): raw data (last pulse). (c) and (d): data filtered to remove the non-ground reflections generated by the vegetation. The raster resolution is 2 m and voids (white) are areas without any point. Coordinates in Lambert93.

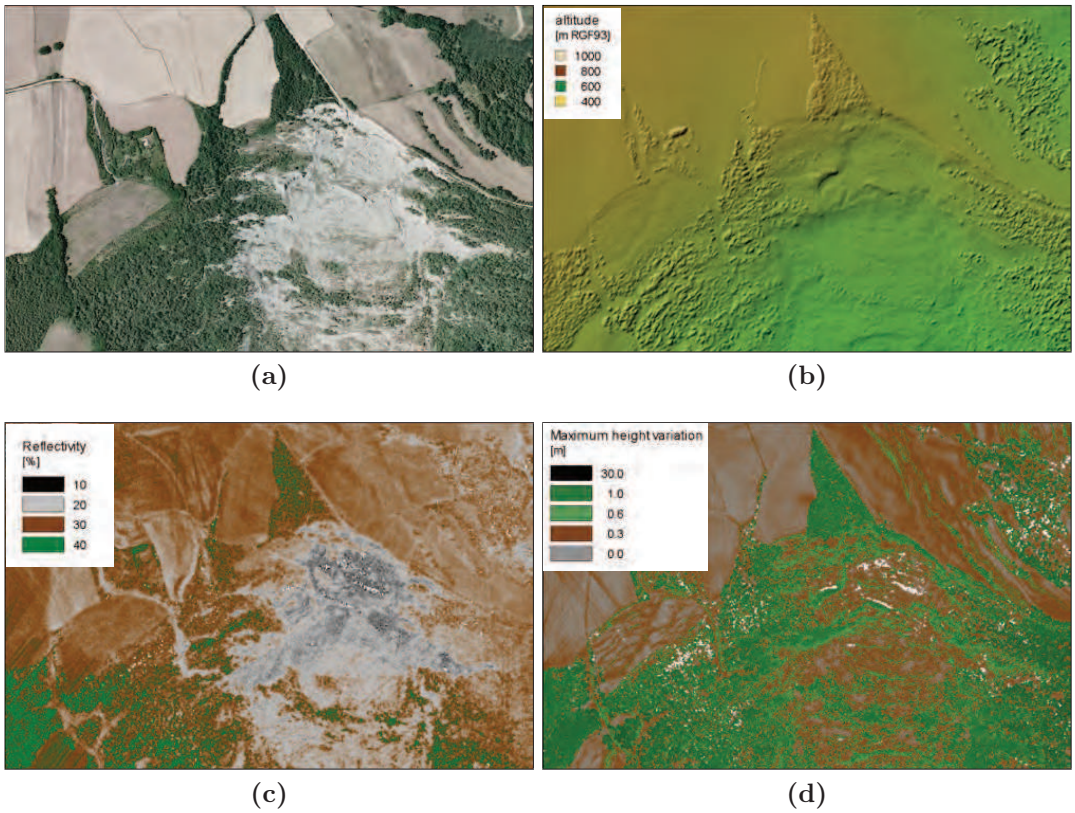

Figure 3.14: Vegetation zoning from the aerial photo and on the lidar scan on a region of 900x600 m at the Harmalière headscarp (a) on an aerial photo, (b) the unfiltered shade DEM with elevations, (c) the reflectivity and (d) the maximum height difference between all points per 2mx2m grid cell as representative of the vegetation height.

maximum height difference could then be used to make a simple classification leading to a land-use map, but this issue is not further investigated.

3.2.2 Bare-earth DEM generation

In order to derive a DEM for further morphological analysis the Lidar-data is filtered with the objective to remove the effect of the vegetation and buildings. This is done by classifying and filtering the Lidar point-cloud using the "Hierarchical robust filtering" of the software SCOP++ (see Sec. 2.4.2). At this step the original point-cloud was reduced to 21 Mpoints (58 %) for 2006 and to 18 Mpoints (67 %) for 2009. The average density for both scans is therefore about 3 pts/m^2. The comparison of the point cloud densities before and after the filtering (Figure 3.13) shows that the decrease is more significant at the Harmalière landslide in the South, as it is more vegetated than the northern Avignonet landslide. At Harmalière in 2006 the point distribution remains mainly homogeneous with an average point density of about 2.3 pts/m^2. On the contrary, the 2009 acquisition at Harmalière shows larger areas without points due to the lower point-density before filtering. Notably, a too low point-density before the filtering is problematic for the filtering step itself, because the algorithm needs to fit a surface through the bare-earth points in order to sort out the vegetation-points. If there are no or very few reflections from the bare-earth, the algorithm fails. The 2006-acquisition can be seen as the lower edge of the minimum point-densities necessary for a proper filtering in highly vegetated areas. This should be kept in mind especially for

	Test area 1	Test area 2
Morphology	mountainous	minor slope
Landuse	dense forest	suburban
Area	100x100 m	100x100 m
Min. difference	-3.21 m	-2.41 m
Max. difference	2.82 m	1.01 m
Mean difference	-0.85 m	-0.34 m
Standard deviation	0.70 m	0.37 m

Table 3.3: Characterisation and statistical values for two test-areas from the Lidar dataset. Differences are given between gridded DEMs derived from automatic and manual filtered point clouds of 2006. The manual obtained DEM is considered to be of better quality and serves as the reference DEM.

the DEM-displacement calculations in Section 4.2.

In order to evaluate the quality of the filtering, two test-areas of 100 x 100 m in difficult terrain (rugged surface, highly vegetated, buildings) are filtered manually using a 3D-Viewer for point clouds with advanced point selection tools (Point Cloud Mapper (PCM) developed at ITC (Netherlands)). The manual obtained DEM is considered to be of better quality and serves as the reference DEM. Figure 3.15 shows a part of the unfiltered (a) and filtered (b) DEM with the location of the two test-areas. The aerial photos of the two areas are shown in Figure 3.15(c and d). Test-area 1 is situated in dense forest with steep slopes ($> 25°$) including a drainage channel, while the second test-area is located in a village on just a gentle slope ($< 10°$) including some houses and trees. The manual filtered point-cloud and the automatic filtered point-cloud are gridded (2x2 m) and the difference between them are shown in Figure 3.15(e and f). Some characteristics of the two test-areas and statistics of the difference two test-areas are presented in Table 3.3.

The automatic filtering seems to throw out too much points of the bare-earth as the DEM is too low in average (-0.85 m). The maximal errors are about ± 3 m and the standard deviation of 0.70 m shows a quite high variation. The second test-area is located in a village on just a minor slope ($< 10°$) including some houses and trees. The results from the automatic filtering are better than for test-area 1, but still below the reference in average (-0.34 m). The standard deviation of 0.37 m indicates that the maximal errors of -2.41 m and 1.01 m are mainly outliers. The DEM difference maps of the two areas (Fig. 3.15(e and f)) show that the main difficulties are connected with lineaments, the drainage channel in test-area 1 and tree/bush-chains in test-area 2. This could be due to the detection of too less bare-earth points under dense vegetation, which gives less stable support for the interpolated surface over which points are considered as vegetation. Isolated houses or trees are filtered with less errors. It should be pointed out that the two test-areas are "worst-case" scenarios, because in other areas with a more smooth surface, less vegetation and no buildings the interpolated surface, which is the base of the classification, can be fitted more robust to the real bare-earth surface. The overall quality of the filtering appears to be better, but nevertheless it shows the major difficulties of automatic point cloud classification.

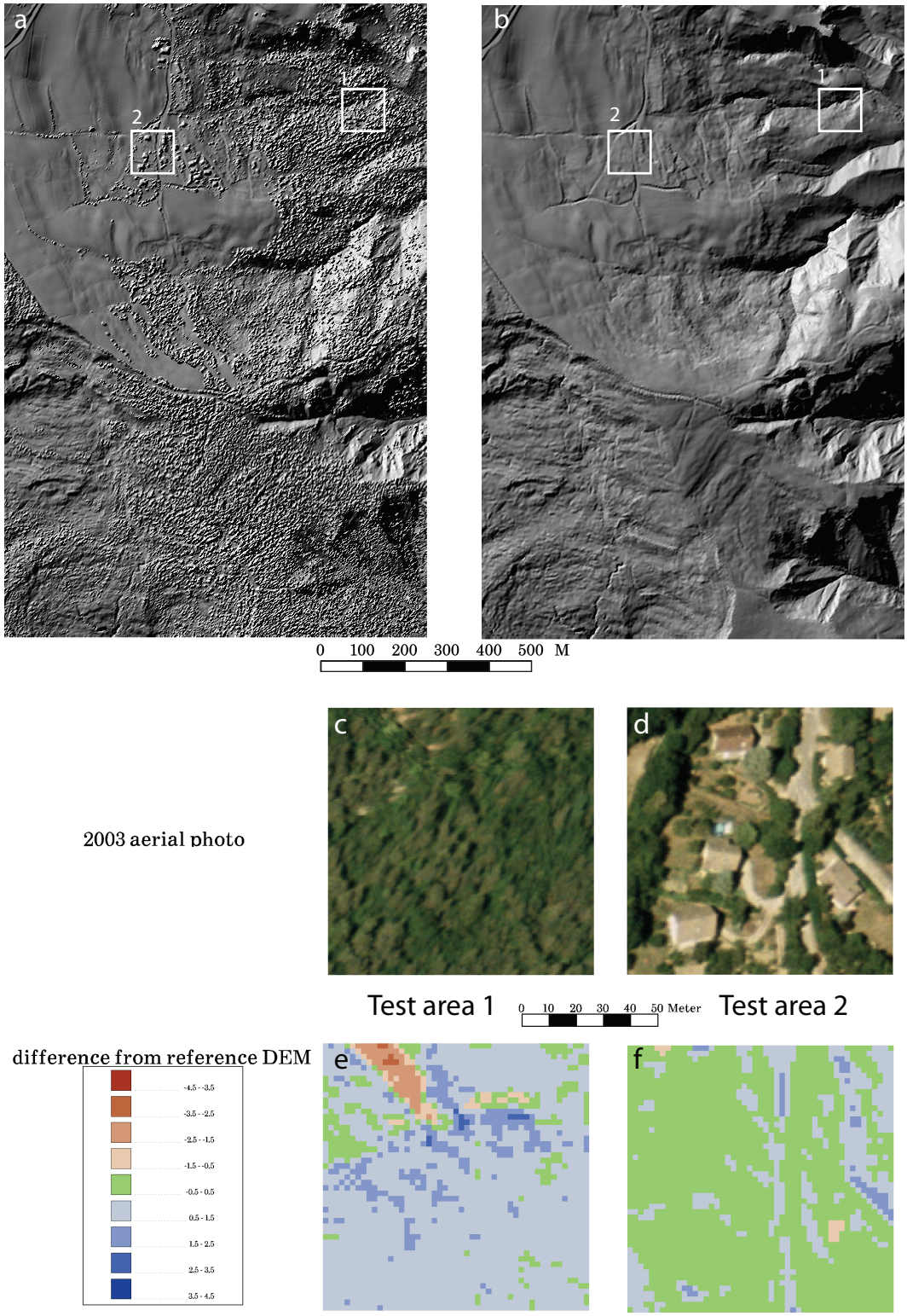

Figure 3.15: Evaluation of the filter quality for the two 100 x 100 m test-areas by comparing the automatic and manual filtered DEMs. (a and b) Example of the shaded relief from the unfiltered (a) and filtered (b) DEM with the location of the two test-areas. Aerial photos (c and d) and difference between manual and automatic filtered DEMs (e and f) of the two test-areas. The automatic filtering is done with the software SCOP++ (see Sec. 2.4.2). Manual filtering is done using the cloud editing software Point Cloud Mapper (PCM) from ITC (Netherlands) (including a 3D-Viewer with advanced point selection tools).

After filtering, the point-cloud is gridded to a raster with a resolution of 2 m using the "gridfit"-algorithm (see Sec. 2.4.3). The final grid was then cropped to the core area of the Lidar scans in order to avoid large extrapolated areas at the borders which would not represent the actual landscape. This DTM is used for the following morphological analysis.

Because the covered area is too small to include the whole watershed for the calculation of the surface drainage system (Sec. 3.2.6), it was extended using the IGN DEM with a source resolution of 50 m. Details about this dataset are given in Section A.4. The two datasets are merged by converting the IGN DEM raster into a point-cloud, sorting-out all points which are already covered by the Lidar DEM and re-gridding the joined point-cloud of both datasets with the 2 m resolution. Due to the different resolutions of the source, small artefacts can be seen at the transition between the Lidar DEM and IGN DEM. This is especially true at the western lake-shore (seen in Fig. 3.22), where the lake level is given by the IGN DEM, while the west lake-shore topography is defined by the Lidar DEM. As the lake-level is slightly lower in the Lidar-DEM, the west lake-shore is a little lower than the rest of the lake. Overall this artefact is expected to have no major influence in the following analysis.

3.2.3 Slope angle and aspect

In order to characterise the slope of the two landslides, maps showing the slope-angle and aspect are generated from the 2 m-Lidar-DEM as described in Section 2.5.1. The map of slope-angles is shown in Figure 3.16 and reveals some fundamental characteristics of the morphology. The map allows for distinguishing four major zones: (1) the upper plateau in the NW (dark-blue) with slope angles less than 3°, (2) the sliding areas of the Avignonet and Harmalière landslide exhibiting major and minor scarps with angles about 20-25° (green-yellow) and flat zones in between with angles below 10° (blue), (3) the area of steep terrain in the East with slope-angles above 25° up to 40° (yellow-red) and (4) the flat toe of the Harmalière landslide in the SE with gentle slope below 10°.

The sliding zones of the Avignonet and Harmalière landslide exhibit similar slope angles. However, the slope-angles between scarps and blocks at the Avignonet landslide are more clearly separated and smooth than at the Harmalière landslide, where the ground surface is more disturbed with numerous close minor scarps. The NW of the Avignonet landslide exhibits a flat area (blue colour) spreading relatively far to the East, which is not connected to the lake, contrary to the toe of Harmalière.

Figure 3.17 shows the slope aspect map of the area. Slopes of the Avignonet and Harmalière landslides are oriented SE to NE (green-yellow-orange colours) and SW to NE (blue-green-yellow colours) respectively. It results that the half moon shaped Avignonet landslide is generally oriented to the East while the U-shaped Harmalière landslide moves to the South-east. Furthermore, the Harmalière landslide exhibits numerous local counter-slopes dipping to the NW (purple colour), which are just locally observed in Avignonet. To the NW of the headscarp of, one can also observe three channel-like N-S lineaments with Westward aspects, which are in opposite to the general dipping of the plateau towards the East.

In order to further compare the slope characteristics of the Avignonet and Harmalière landslides, two representative profiles are extracted along the general direction of movement and shown in Figure 3.18. Their locations are shown in Figure 3.18a and the raw extracted elevations are presented in Figure 3.18b without exaggeration. To outline the differences in Figure 3.18c the two profiles are aligned at their headscarps

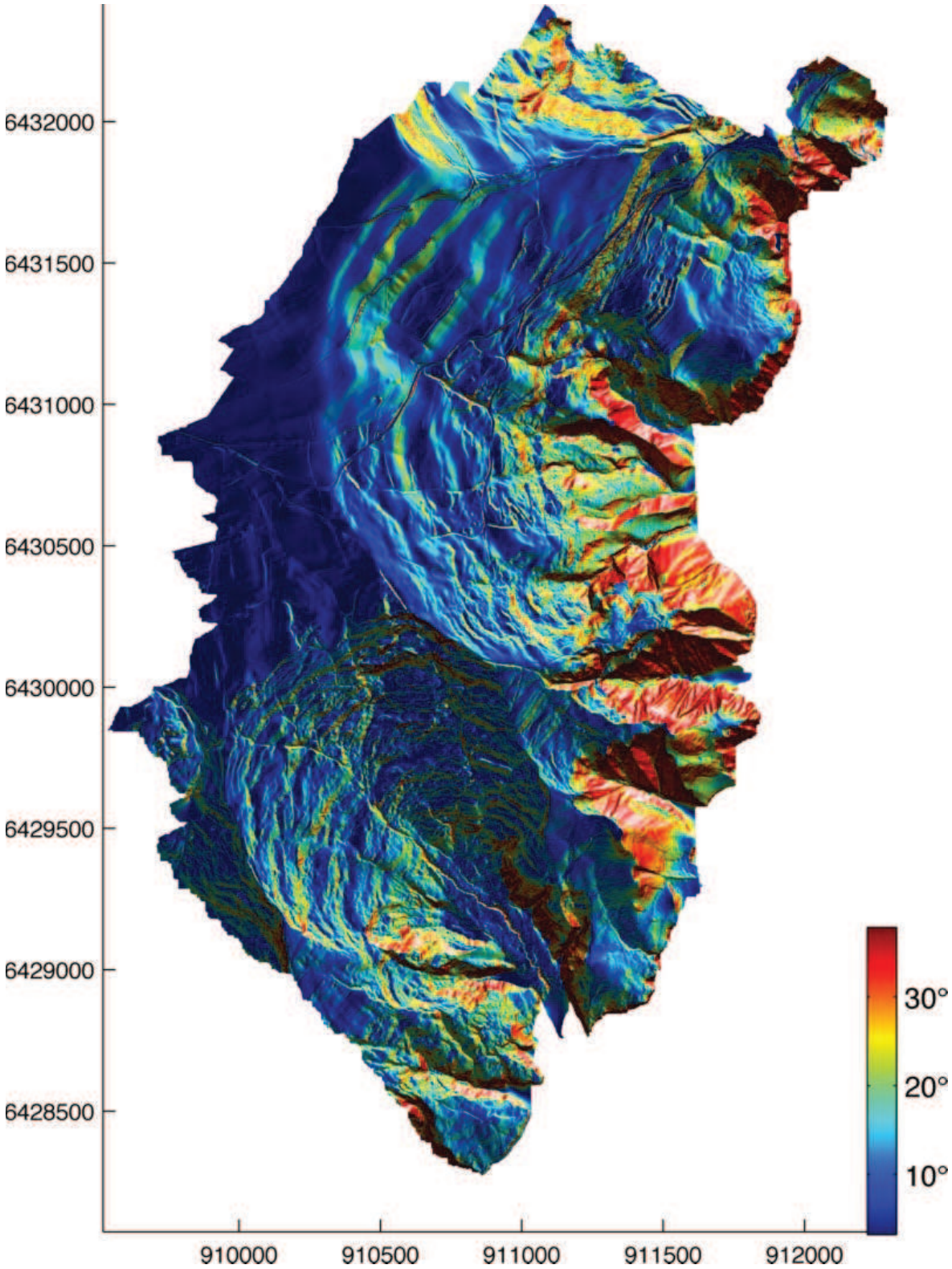

Figure 3.16: Slope-angles of the Lidar 2006 DTM draped on the shaded relief map.

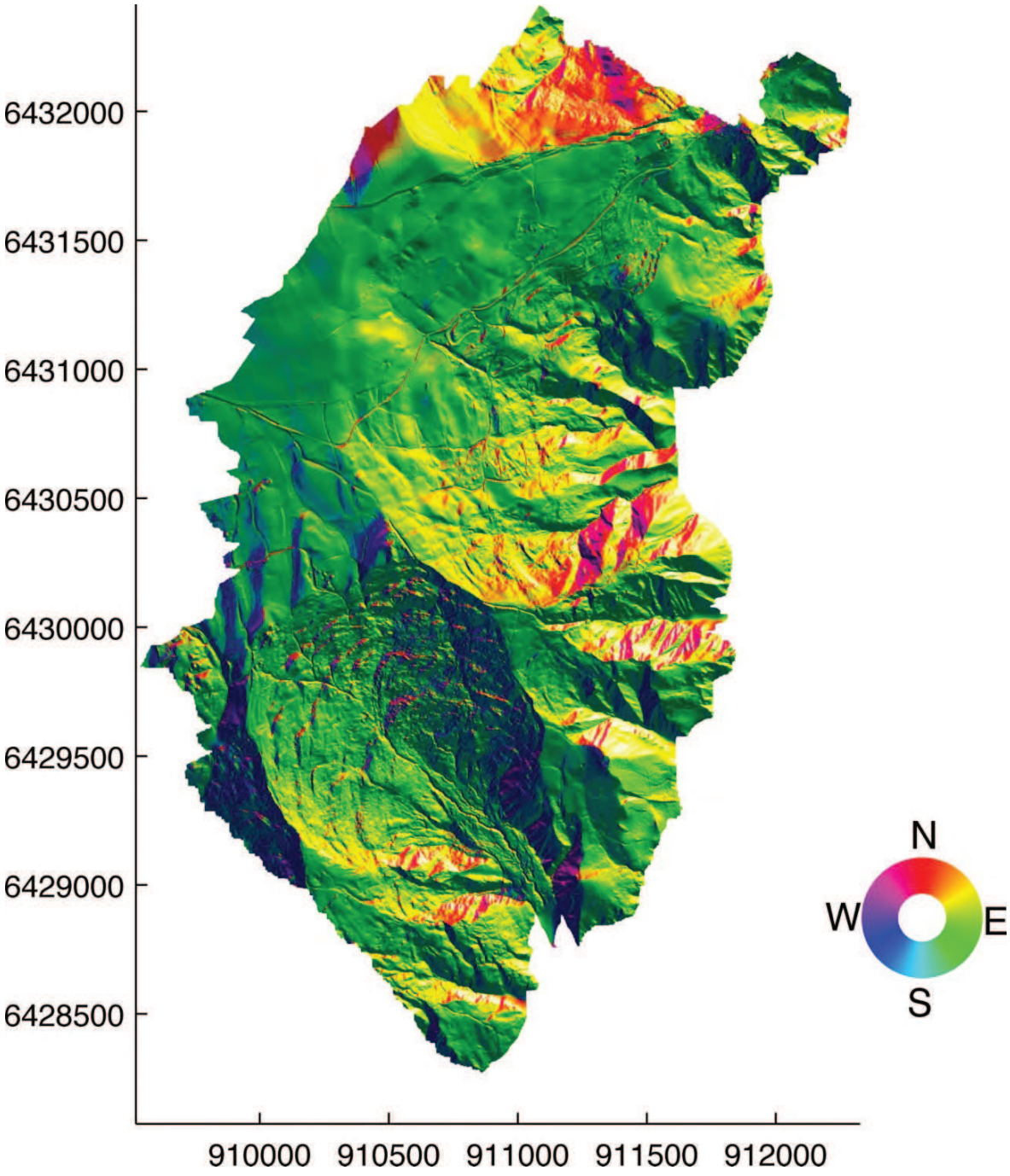

Figure 3.17: Aspect of the Lidar 2006 DTM draped on the shaded relief map.

and the vertical scale is exaggerated by a factor 2. It can be observed: (1) the total lengths of the moving zones are different, about 900 m at the Avignonet landslide vs. 1500 m at the Harmalière landslide, (2) the slope at the Harmalière landslide can be divided in 2 parts, the upper depletion-zone with its major and minor scarps (zone 2 concerning the slope-angles) and the lower more flatter accumulation-zone (zone 4 concerning the slope-angles), (3) Avignonet only shows the depletion zone, but do not have a flat accumulation zone, (4) the depletion zone is more convex at Avignonet and more concave at Harmalière, (5) the height of the depletion zone is similar for both landslides (about 175 m).

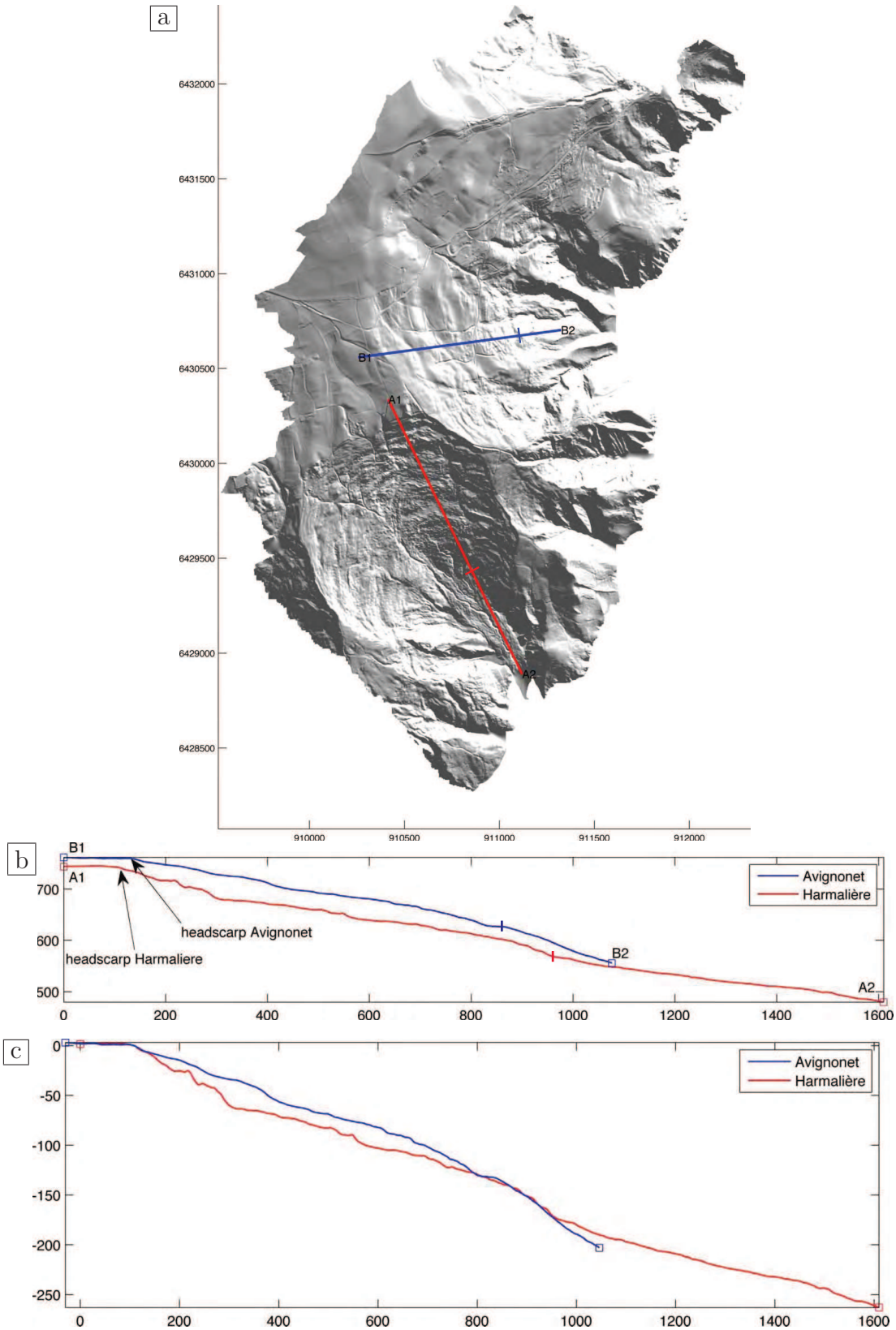

Figure 3.18: Longitudinal topographical profiles through the Avignonet and Harmalière landslides. (a) Location of the profiles on the 2006 Lidar DEM with a marker dividing them in an upper and lower part. (b) Extracted raw profiles with the upper/lower mark. (c) Profiles aligned at the top of the headscarp (2 times vertical exaggerated).

3.2.4 Shaded relief

Shaded relief maps are produced for morphological interpretation and the geolocated visualisation of other datasets. The shading is realised using the ESRI-algorithm (see Sec. 2.5.2). As morphological lineaments parallel to the illuminating directions are poorly seen, steep slopes towards or away from that direction can result in overall too dark or too light areas. Consequently, four different illuminating directions (NE, NW, SE, SW) are used for the morphological interpretation. The zenith is always 45° above the horizon. Shaded relief maps with colour-coded elevation are presented from the NE direction for the two Lidar acquisitions in Figure 3.19. The morphology of the two landslides is well evidenced, including the headscarps of the two landslides, major and minor scarps at different scales, bumpy earth-flow areas, drainage flow-paths, roads etc.. The major outcome of this process is the clear view on the bare-earth morphology in vegetated areas, which is hidden in the aerial photos and even difficult to access in the field. Secondly the comparison between the 2006 and 2009 datasets show no observable difference. Therefore the analysis of the slope, aspect, drainage system and roughness is only made with the DEM of 2006. Detailed quantitative differences between the two datasets are assessed in Section 4.2 using image correlation techniques.

Figure 3.20 shows the shaded relief map of 2006 with colour-coded slope aspects. The combination of these two maps exhibit the structures of the landslides in full detail, which can not be seen in aerial photos (e.g. Fig. A.7).

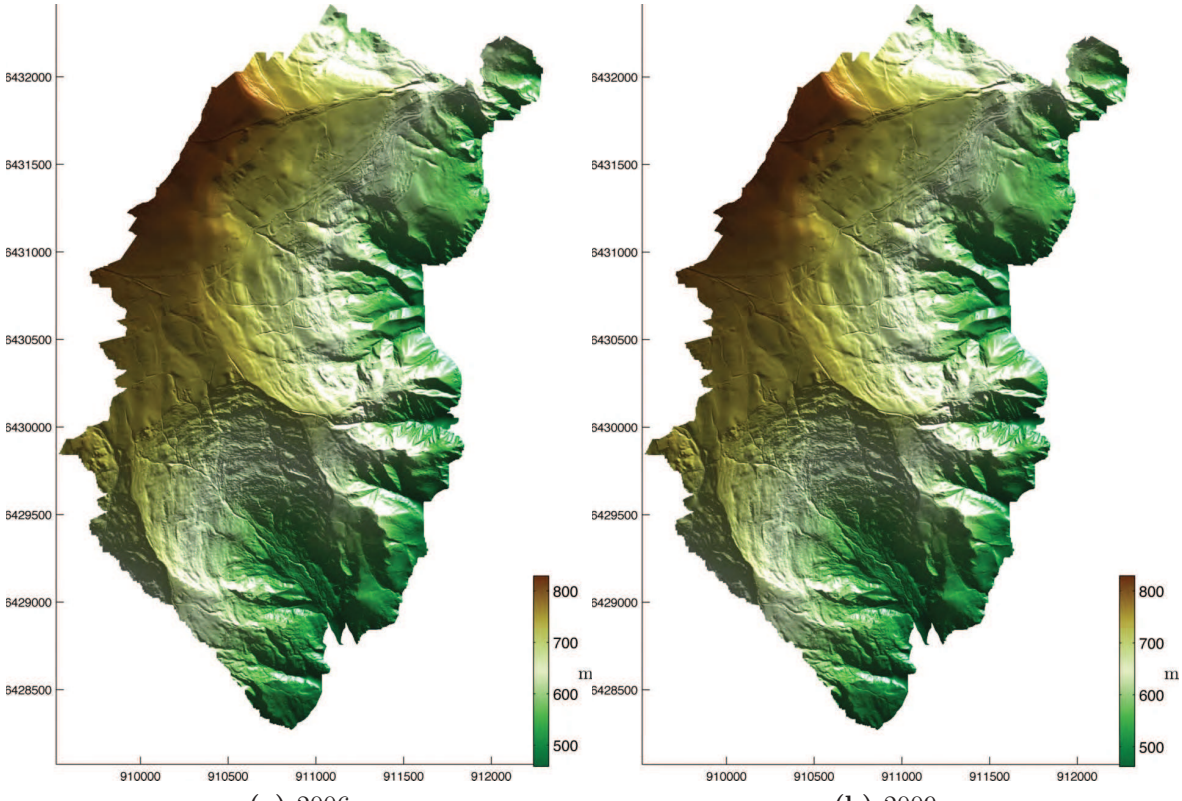

(a) 2006 **(b)** 2009

Figure 3.19: Shaded Lidar DTMs of 2006 and 2009 with color-coded elevations. Illumination from NE and 45° above the horizon. The morphology of the bare-earth is clearly visible, but no differences can qualitatively obtained between the two dates.

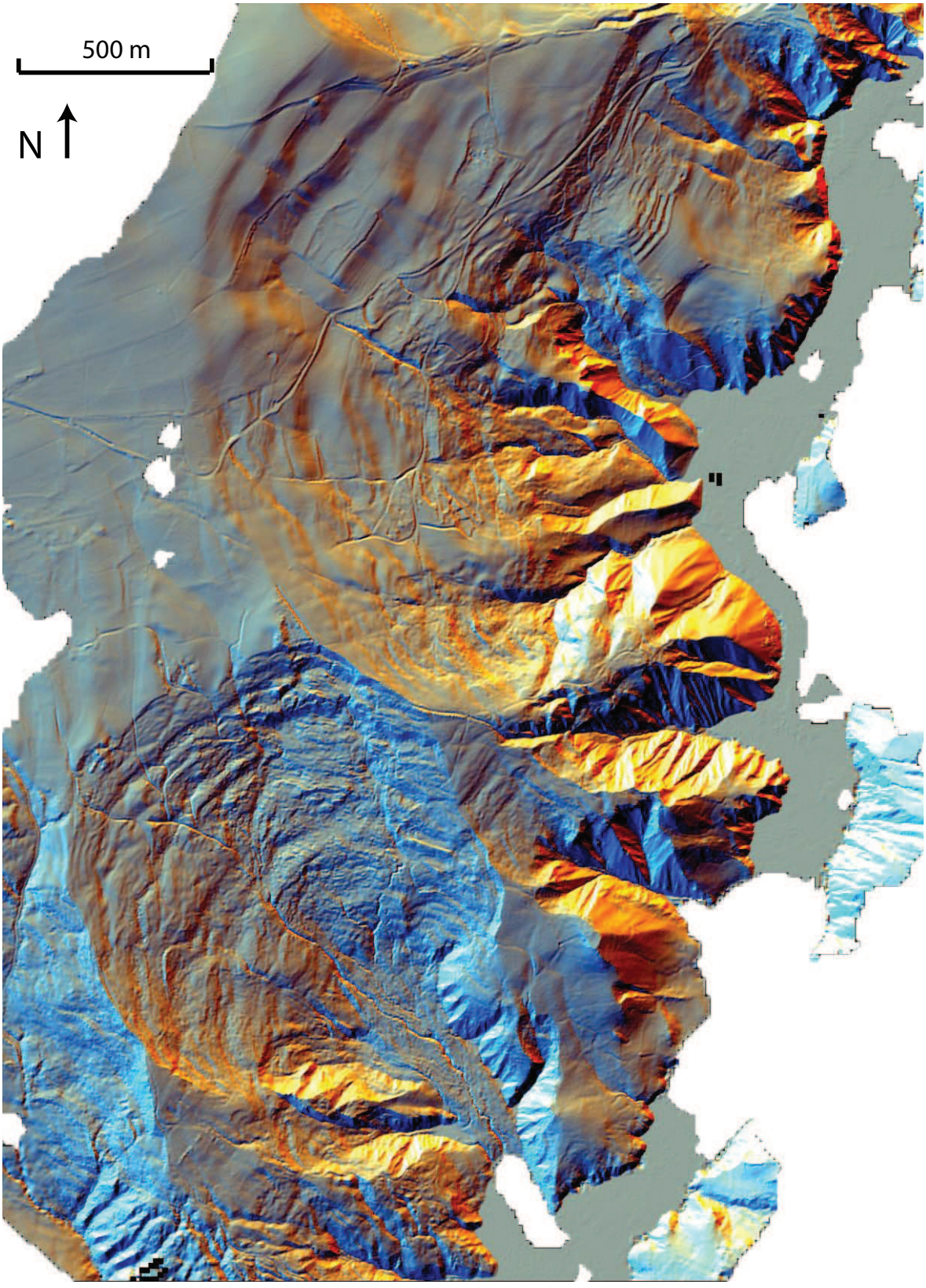

Figure 3.20: Shaded bare-earth Lidar DEM with colour-coded slope aspect. Data-holes in white. Lake Monteynard in grey in the East.

3.2.5 Geomorphological map

Figure 3.21 shows a qualitative basic geomorphological map derived from the interpretation of the shaded relief maps and some field observations. The morphological features are classified in major and minor scarps, screes and areas of mud-flow. The map shows that, in case of the Harmalière landslide, the upper limit corresponds to a succession of scarps drawing an U-shape opening towards SE. It is also characterised by a central zone, orientated more N-S and about 400 m wide, which corresponds to a large movement leading into a mudflow about half-way to the lake (corresponds to the upper and lower part of the profile in Fig. 3.18). The eastern flank of that sliding channel shows some linear scarps in opposite to the curved scarps everywhere else. The eastern side of the mudslide is bordered by a cliff with scree-slopes of higher angles suggesting the absence of clays. Near the confluence of the mudslide into the lake two small valley join from west and east, while the western one exhibits landslide morphology.

In the case of the Avignonet landslide, the upper limit is much more continues and the concavity is orientated towards the East, perpendicular to the lake. Also, the Avignonet landslide does not show an accumulation zone of the landslide materials, instead the lower limit is characterised by a continuous cliff with scree-slopes. The scarps appear to be increasingly small-structured towards the toe of the landslide and towards the South. The northern limit is defined by the next adjacent landslide retreating into the Avignonet landslide.

Except the most southern part of Avignonet, the surface of Harmalière seems to be more rough at small scales than the relatively smooth scarps of Avignonet. Therefore the roughness is quantitatively assessed in Section 3.2.7.

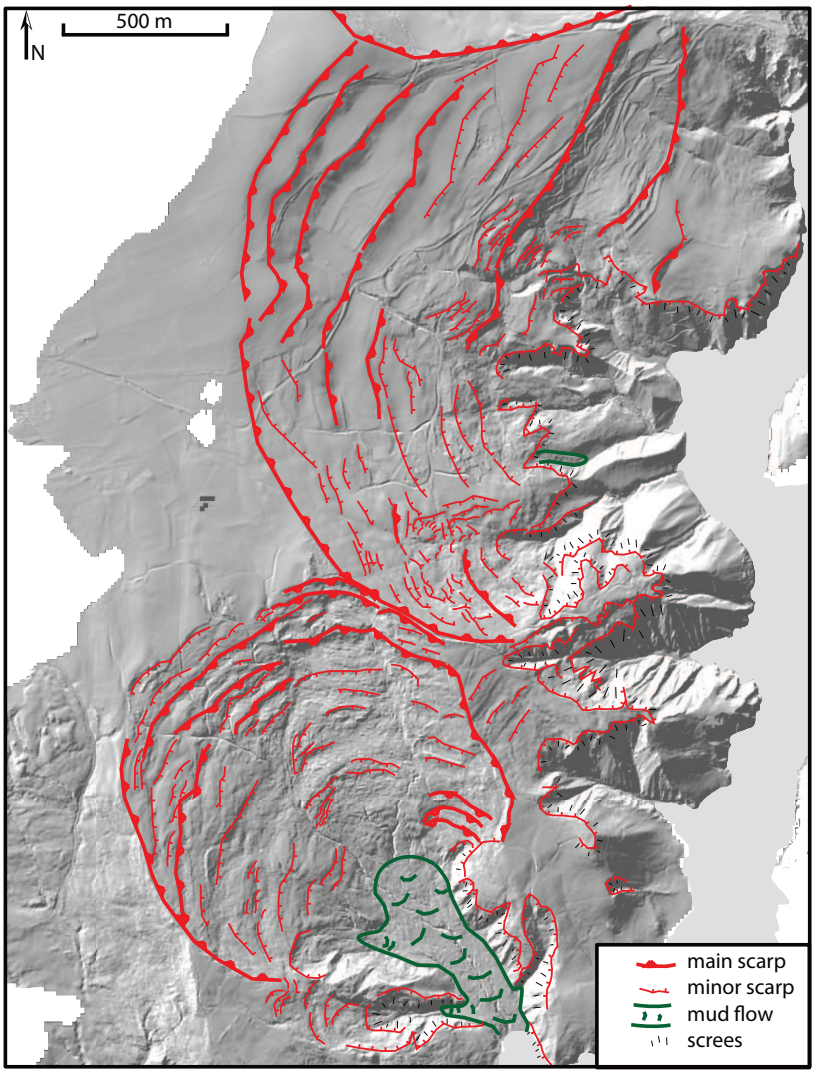

Figure 3.21: Geomorphological map interpreted from the shaded Lidar DEM and field-observation.

3.2.6 Drainage system

The accumulated rainfall has usually a major influence on the activity of landslides. The drainage network is then computed from the DEM to determine the catchment characteristics of both landslides. The processing is described in Section 2.5.3. The Lidar-DEM was extended using the 50 m-IGN DEM (see Section 3.2.2). Figure 3.22 shows the drainage-system of Avignonet and Harmalière draped on a shaded relief map. The colour-intensity reflects the log of the upslope-area. The Harmalière and Avignonet watersheds are coloured in green and red, respectively, while the adjacent watersheds are in blue.

The most important watersheds of the plateau are draining to the North and the South. The flows are in directions parallel to the morphology determined by the Jurassic limestone. The rainfall on the plateau is preferentially directed towards SSE or NNE. This drainage network is only partly captured by the Avignonet landslide, whose watershed (red) covers an area of 2.0 km^2 (only 25 % larger than the landslide itself), with a drainage system generally oriented perpendicular to the lake. On the contrary the watershed of the Harmalière landslide (green) is smaller with 1.7 km^2 (70 % larger than the landslide itself), but has a geometry elongated parallel to the adjacent flows

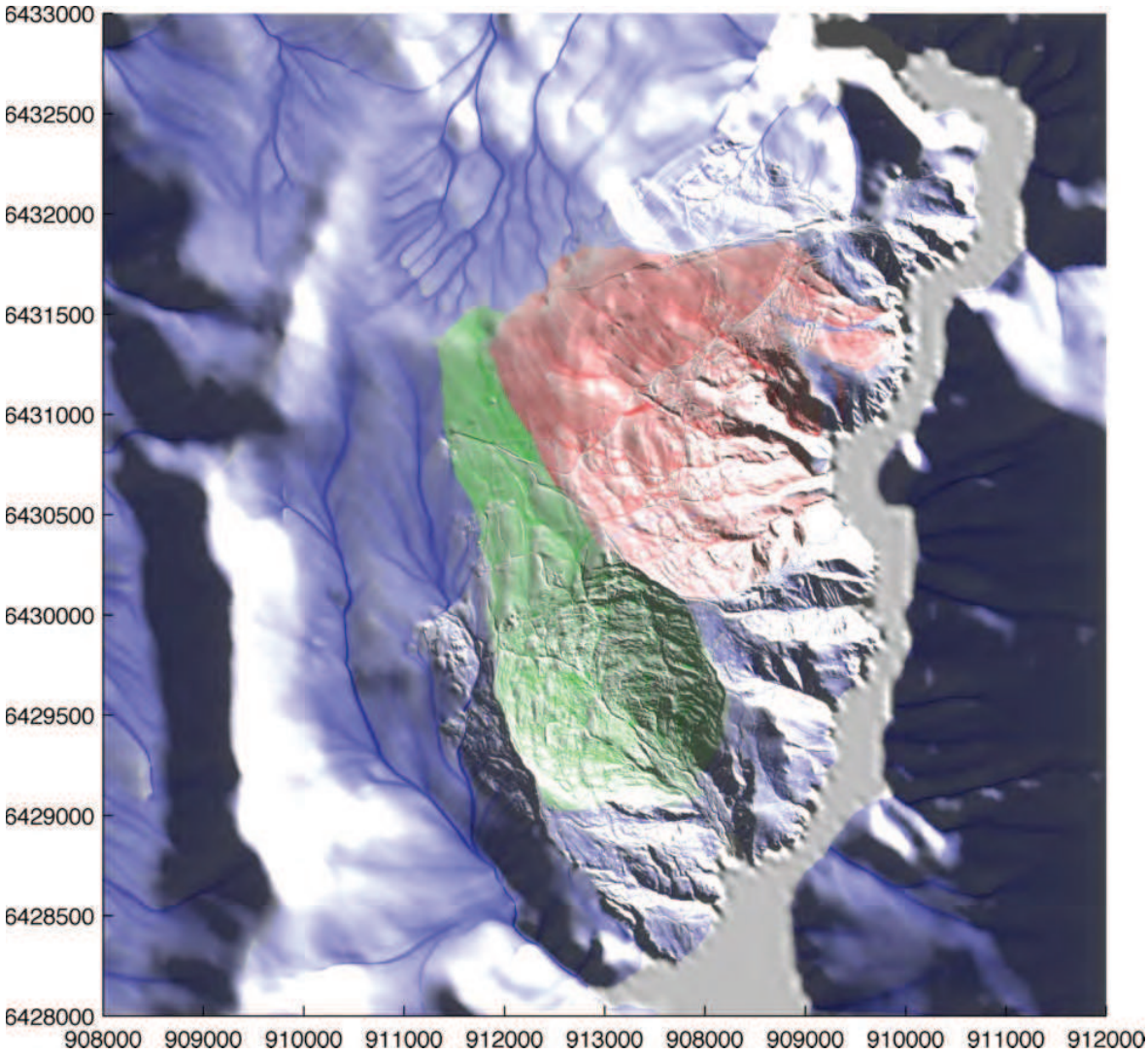

Figure 3.22: Drainage system of the Avignonet and Harmalière watersheds. Derived using the upslope area computation after Tarboton (1997) and colouring the watersheds of Avignonet (red) and Harmalière (green). All other watersheds are blue. The colour intensity reflects log of the upslope-area.

of the plateau.

On a smaller scale, due to the roads crossing the Avignonet landslides, the automatic drainage is partly not representing the natural flow. Bridges (or water-tubes) below the roads are not considered in the flow calculation and therefore the water is often kept on the hill-side of the road for long distances until it can cross the road. This does not seem to have any influence on the overall watersheds, but should be considered when using such maps as input for landslide modelling.

If the morphology at different times would be more drastically changed, the capturing of adjacent drainage basins could massively influence the activity of a landslide. Drainage maps can help to detect such risks by identifying larger streams of neighbouring watersheds near the headscarp of a landslide, which could be captured by further sliding events. At the Harmalière and Avignonet landslide there is no evidence for that in the near future.

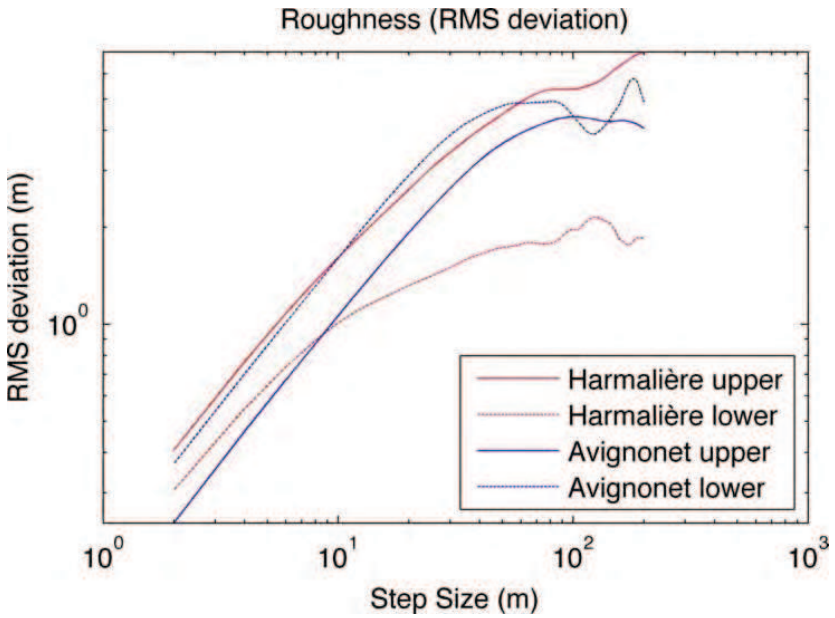

Figure 3.23: Deviogram (RMS-deviation) of two representative profiles from Harmalière and Avignonet. The location and height-profiles are shown in Figure 3.18 and 3.7.

3.2.7 Roughness

If not mentioned differently, in the following "roughness" will refer to the RMS-deviation along a profile as defined in Sec. 2.5.4. In order to highlight the differences between Avignonet and Harmalière the roughness is already discussed in Section 3.1.3.2. There, the roughness is computed along two representative profiles at Avignonet and Harmalière, which are subdivided in an upper and lower part. The location and height-profiles are shown in Figure 3.7 and with higher detail in Figure 3.18. Along these four sub-profiles the roughness is calculated with lags (= step size, wavelength or scale) of 2 – 200 m, shown in Figure 3.23. All curves following a general upwards trend, which comes from the naturally larger height-differences when comparing points with larger distances from each other. That means that the roughness is only directly comparable when using the same step-size. The range of step-size is limited to the sample resolution at the lower end and the profile-length at the higher end. Step-sizes near the profile-length are not statistically significant, which leads to the irregular characteristics at higher step-sizes. For the discussion in the journal-paper the roughnesses at step-size 10 m for small-scale and 100 m for large-scale are extracted and listed together with the profile-length and average slope angles in Table 3.1. The main statements are here that Avignonet is "more rough" in the lower part than in the upper part whereas in Harmalière it is the opposite and the large-scale roughness is similar in all sub-profiles but the lower part of Harmalière. The relation between roughness and short-term and long-term evolution of the landslides based on those profiles is further analysed and discussed in the paper (Sec. 3.1.3.2 and 3.1.5).

In order to analyze the spatial distribution of the roughness, it is calculated at profiles every 10 m covering the whole area at small-scale (SSc) and large-scale (LSc). The calculation is based on the 2006-Lidar DTM with a resolution of 2 m. At each location the average slope-orientation is taken from its vicinity (SSc: 20x20 m, LSc: 200x200 m). Then two height-profiles of the same length (SSc: 20 m, LSc: 200 m) are extracted, one along the downhill direction (UD = up-down) and another perpendicular

to the first one, parallel to the slope (LR = left-right) each with a resolution of 2 m. After that the roughness (RMS-deviation) is calculated at the profiles with the a step-size of 2 m at small-scale and 20 m at large-scale. The results of those four maps are presented in Figure 3.24.

The idea is to reveal areas of higher roughness in general, but also to divide roughness due to landslides and roughness due to gullying (erosion). Therefore it is assumed that terrain affected by landslides is showing higher UD-roughness due to the major and minor-scarps and terrain mainly affected by erosion is showing higher LR-roughness due to the absence of scarps and drainage paths in downhill direction. Figure 3.24a) and (b) show the small-scale roughness in UD- and LR-direction. The UD-roughness is low at the plateau (dark blue) and higher in Harmalière, the lower part of Avignonet and the terrain E of Avignonet and Harmalière along the lake. The LR-roughness is low everywhere but the terrain along the lake. In order to distinct between the landslide- and erosion-milieu the difference of the UD- and LR-roughness (directional roughness) is shown in (c) and reveals yellow-red areas with predominant UD-roughness and blue areas with predominant LR-roughness (green shows balanced areas). The intensity of the colors is varied by the sum of both roughnesses to hide areas with a low insignificant roughness in either direction. At a first glance this map can be divided in three parts, (1) the plateau and upper part of Avignonet with low roughness, (2) Harmalière and lower parts of Avignonet with UD-dominated roughness and (3) the terrain below the Avignonet landslide and E of Harmalière along the lake with LR-dominated roughness. The directional roughness seems to be a good indicator for landslide activity. By looking more in detail, several parts of Harmalière and regions along the lake reveal more balanced (green) directional roughness and are not easily dividable.

The same maps are presented for the large-scale roughness (20 m) in the lower row (d-f). These maps are less noisy due to the averaging effect of the large profiles (200 m) relative to the grid-spacing of 10 m. Overall the large-scale maps show the same trend as the small-scale maps with some differences. The elevated UD-roughness in (e) includes larger areas of the upper part of Avignonet in opposite to the small-scale case. This seems to match the lower activity in the upper part of Avignonet which leads to undulated morphology with longer wavelengths and therefore shows only up at larger scale. In addition, the directional roughness (f) shows LR-dominated (blue) areas along the ridges between the landslides (N Avignonet, between Avignonet and Harmalière, SW-Harmalière). This is most likely due to the determination of the profile directions, which are depended on the slope-direction. As the slope-direction is in the large-scale case the average of an area of 200x200 m, the slope-orientations of both sides of a ridge annihilate each other leading to an averaged orientation along the ridges, which causes a rotation of the profile directions at those points and finally an inversion of the directional roughness. To minimize this effect the size of the area to determine the average slope could be reduced, or better, the orientation of the profiles should not be determined by the omni-directional orientation ($0-360°$) but the linear-orientation ($0-180°$), which would be more stable during the averaging.

Conclusively the directional roughness seems to be a good parameter to classify morphology, especially for the localization of landslides, but larger test-areas would be needed to test this. Further investigation in this direction could include the use

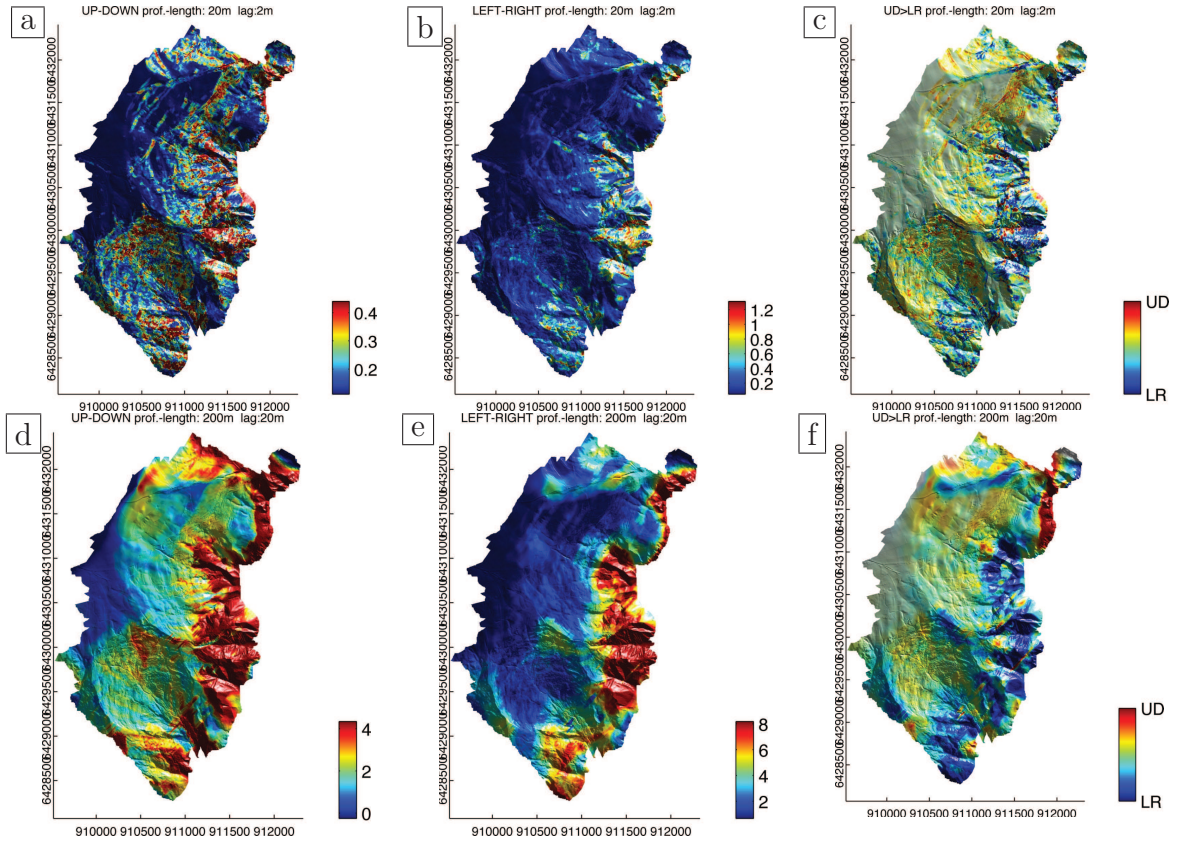

Figure 3.24: Small-scale (a-c) and large-scale (d-f) directional roughness calculated at locations equally distributed at every 10 m. The roughness is shown in downhill direction (a, d) and parallel to the slope (b, e). c and f present the difference between the downhill (UD) and slope-parallel (LR) roughnesses, meaning red areas are more rough downhill than slope-parallel and vice versa. The intensity of the colours in c, f is the sum of the downhill and slope-parallel roughness (general roughness) in order to highlight areas with higher roughness (independent of the direction). The roughness is computed as RMS-deviation. For small-scales the profile length is 20 m and the lag is 2 m. For large-scales the profile-length is 200 m and the lag is 20 m. See Section 3.2.7 for details. The colour-bars do not represent the whole spectrum of values. They are limited to the a representative range of values to highlight the spatial differences.

of different roughness definitions to calculate the directional roughness or combining roughnesses of different scales.

In order to support the findings from the roughness of the single profiles of Harmalière and Avignonet used for the journal-paper, histograms of the UD-roughness of Avignonet and Harmalière are compared in Figure 3.25. At small-scale (left histograms) in Avignonet the majority of roughness-values are lower with a peak at 0.05 m than in Harmalière, where the maximum is at 0.25 m. Interestingly this does not apply for the large-scale case (right histograms), where the peak is at 0.2 m for Avignonet as well as Harmalière. This supports the statement that Harmalière is "more rough" than Avignonet at small-scale, but not that differently shaped at large-scale.

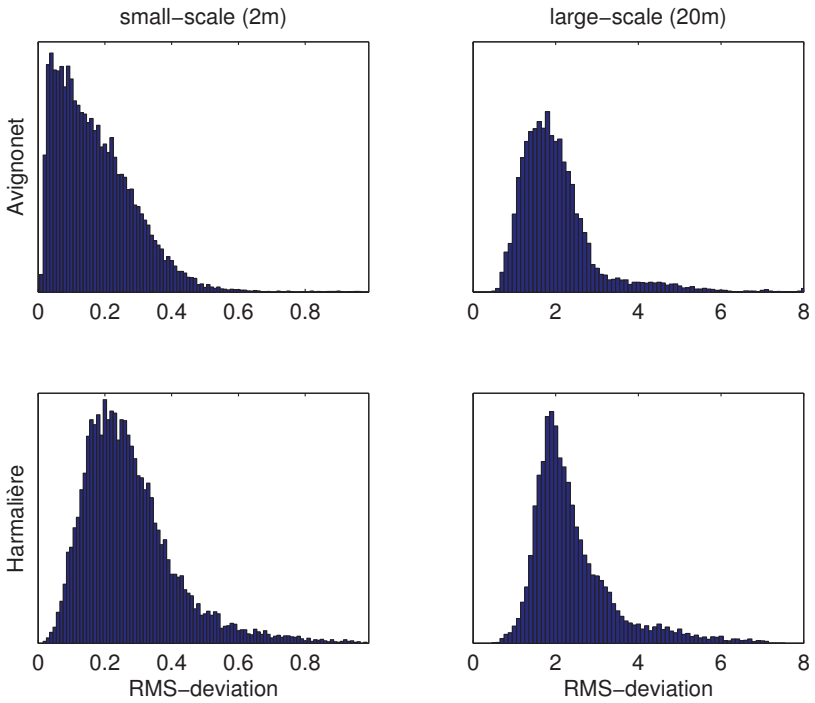

Figure 3.25: Small-scale and Large-scale roughness histograms of downhill profiles at Harmalière and Avignonet. See Figure 3.24 and Section 3.2.7 for details.

3.2.8 Conclusions and recommondations

The following conclusions can be drawn from the results of the DTM-analysis:

1. As the point-cloud density should be simply near or higher than the desired resolution of the final DTM, for a proper filtering of the vegetation a minimum point-density of 5 pts/m^2 is recommended depending on the vegetation density. The loss of points during the filtering is about 20 % in low-vegetated areas and up to 50 % in higher vegetated areas. As the acquisition from a helicopter is more inhomogenous than e.g. from a plane, the average point cloud density should be chosen higher than theoretically needed to have a good coverage in all areas.

2. Automatic filtering of vegetation works sufficient also in mountainous areas, but decreases the accuracy due to classification difficulties between bare earth and low vegetation, especially near scarps and cliffs.

3. In addition to field-mapping, slope, aspect and shaded relief maps are essential in developing a geomorphological map, especially in forested and hardly accessible areas.

4. The computation of drainage networks is a quick tool to assess the superficial hydrological system and watershed of a landslide. In case of the presence of man-made structures, special attention is necessary concerning sub-terrain flows (bridges, tubes). Using DTMs of lower resolution can minimise such problems.

5. Roughness, especially directional roughness, can be a good indicator for landslide activity and is able to distinguish between gullying and landsliding milieu. It needs to be refined and tested at larger areas and different kind of landslides.

6. All the DEM-derivatives could be useful for an automatic classification of landslides, especially the directional roughness, slope-angles and slope-aspects. However, the scale dependancy should be further investigated.

Some results of the DEM analysis (like slope angles, slope aspects and drainage system) are used as supporting arguments for the interpretation of the short- and long-term evolution of the Avignonet and Harmalière landslide in Section 4.4.

CHAPTER 4

Kinematics

This chapter deals with the extraction of information using multi-temporal data. At first, the results of the computation of DEMs and ortho-rectified images from aerial photos are presented and discussed in section 4.1, starting with a short excursion into the quality of the measured ground control points. After that, the displacements extracted from the Lidar-sets are presented and discussed in section 4.2, which is the main subject of the thesis. The third section 4.3 covers the outcomes from the Insar analysis starting with the test case of Grenoble identifying subduction velocities, followed by the focus on the Avignonet and Harmalière landslides. At last the kinematic informations from all three methods are summarized and discussed in section 4.4, including the short- and longterm evolution of the landslides, influencing factors and implications for the future development.

4.1 Aerial Photogrammetry

Aerial photos of different years are available to evaluate the evolution of the Avignonet and Harmalière landslides. As these are raw photos, they need to be ortho-rectified using the interior and exterior orientation of the camera in order to be comparable to other georeferenced data-sets. Also the stereo properties of the photo-sets are used to generate DEMs. For the exterior orientation, ground control points are measured in the area with differential GPS in order to determine geographical coordinates of identifiable features in the photos. The absolute accuracy of the resulting ortho-photos can not be better than the ground control point accuracy. Section 4.1.1 goes into the details of the GCP accuracy including some advice for future GPS campaigns . Section 4.1.2 shows the results of the DEM generation from the photos and the comparison of those relative to the Lidar DEM. The computed ortho-photos are compared with focus on the landslide activity and potential influence factors in Section 4.1.3. Finally the shortcomings of the method and its implications for future works are discussed in Section 4.1.4.

4.1.1 Ground control point accuracy

The ground control points (GCPs) are measured using a differential GPS from Ashtech. Solutions from the raw data are computed with “Ashtech Solutions”. The method is described in Section 2.2.3 and Figure 2.9 illustrates the GPS-network which is used

to calculate the coordinates of the GCPs. The accuracy of the derived GCP-locations depends on the reference stations used to calculate the solution. To estimate the influence of the used reference stations, different solutions are compared using an increased amount of reference stations. Figure 4.1 gives an overview of these solutions. Focussing on the chart (a) in that figure, it can be observed that (1) using differential GPS increases the accuracy at least one magnitude by comparing the raw positions with the solutions using reference stations (column 2, 3). This is why differential GPS is used in the first place. (2) The vertical precision (c) is about 5 times lower than the horizontal (a). But this seems to be true even when using the local permanent GPS-station (3rd column). (3) Even when reaching decimetric average accuracy (3rd column in (a) and (c)), outliers can still be erroneous by 2 m (3rd column in (b) and (d)). (4) Calculating the same solution with and without precise orbit files (POF), which is not shown in the figure here, the accuracy increased only by about 14 %.

Overall it should be stated that this accuracy assess only gives an idea of the increase in accuracy using different reference stations. Due to missing direct measurements of precisely known positions or repeated measurements of the same points (e.g. on different days) the absolute accuracy is inaccessible. It should be part of every GPS campaign in order to assess the accuracy. Also greater attention should be given to the local reference station (here REF1). It should have a more than usual good free view to the sky as it needs not to see only as much satellites as possible, but also the exact same satellites as the rover station is seeing during its measurement. During the calculation it took out that even permanent GPS stations far away (>100 km) are still good to increase accuracy of the absolute coordinates and should be included in the solutions. If the local reference station is fine, one permanent station with precisely known coordinates seems to be enough. On the other hand precise orbit files (POF) do not increase the accuracy a lot and can be ignored when looking for decimetric precision.

4.1.2 DEMs from stereo photos

In order to quantify the removal of material through time, 2 DEMs are calculated from the overlapping aerial photos of 1970 and 2003 for the headscarp area of Harmalière. The date 2003 is chosen, because it is the nearest available photo-set for the comparison with the Lidar data of 2006. The photo-set of 1970 reveals the best quality concerning resolution, sharpness and contrast before the collapse of Harmalière in 1981. The DEMs of the aerial photos are computed using the software Geomatica Orthoengine in version 10.1.3. Figure 4.2 (top) shows the shaded relief representations of the three DEMs. The Lidar DEM is the vegetation-filtered DTM of section 3.2.2. Besides the vegetation the shaded DEM of 2003 (b) does not show morphological differences to the Lidar DTM of 2006 (a). In contrast, the 1970 DEM shows some major artifacts of the processing and the absolute quality is questionable. However, it shows the still existent landslide body in place before the collapse of 1981 along the main mud-slide channel at Harmalière. Interestingly, the left and right flanks of that channel are already foreshadowed as vague linears in the DEM of 1970. The artifacts are due to false-matching between the stereo pairs, which leads to positive and negative peaks in the DEM. The difference between the 2003 DEM and the 2006 Lidar DTM (d) is dominated by the appearance of vegetation (blue). This is unavoidable due to the principle of stereo-photogrammetry which always includes the vegetation. In areas without vegetation the difference is below 0.5 m (light green). The difference between the 1970 DEM and the 2006 Lidar DTM (e) shows the huge loss of material from the headscarp all the way down to the

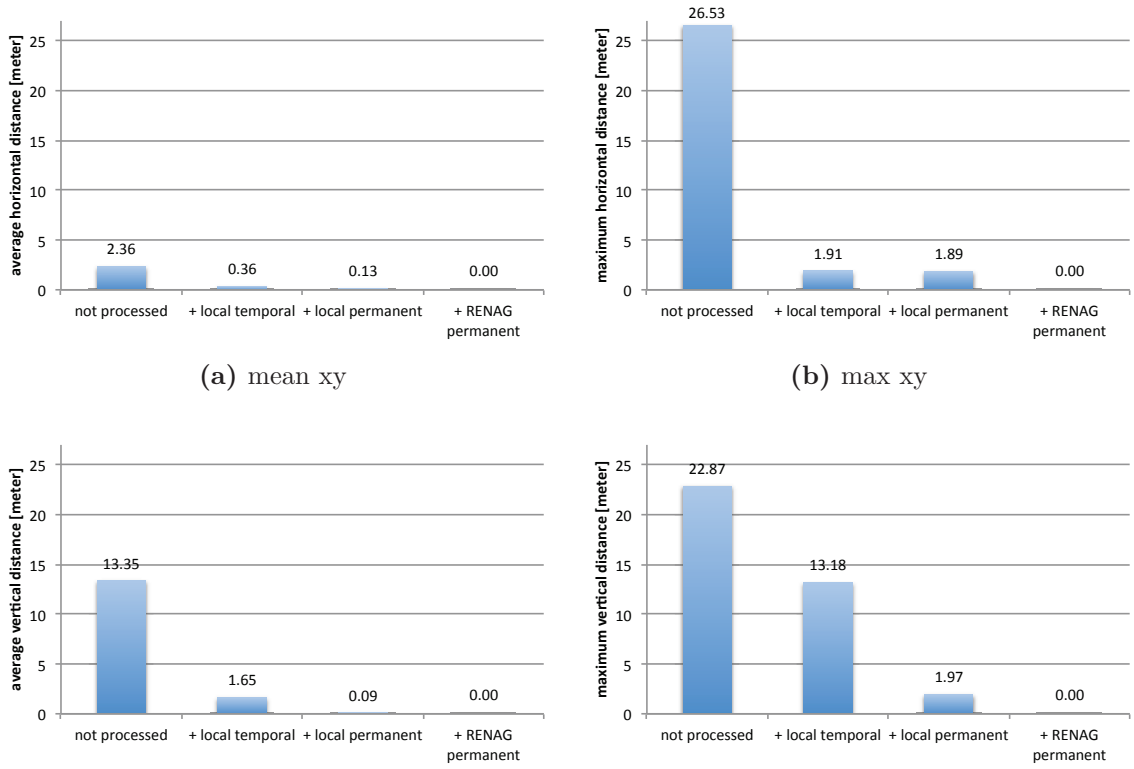

(a) mean xy **(b)** max xy

(c) mean z **(d)** max z

Figure 4.1: Ground control point accuracies of different differential GPS solutions. Each chart contains 4 columns. The 4th column represents the solution using all available GPS-reference stations and is considered to be the best. The charts show the distance relative to this "best" solution. So it is always zero for the best solution itself in the 4th column. The 1st column represents the raw positions without being processed. The 2nd column is the solution if only the local temporal reference station (REF1) is used which was installed 8 hours parallel to the GCP measurements. The 3rd column shows the solution using in addition a local permanent GPS-station (CREF) and precise orbit files (POF). For the 4th case another local permanent station and a permanent station from the RENAG-network are added to the solution. See Section 2.2.3 for details.
The comparison is divided in horizontal (xy) and vertical (z) directions. The left charts (a, c) show the average distance of the GCP-positions from the "best" position. The right charts (b, d) show the maximum distance, which is in fact the worst case of all GCPs. The charts are discussed in greater detail in Section 4.1.1.

south along the main mudslide channel. But, beside the small artifacts for example seen in the lower left corner as small cones in (c) and as red dots in (e), an even larger systematic error appears. The ridge at the top of the figure (e) should be more or less the same between 1970 and 2006 but shows positive difference up to 30 m. The cause for this huge error could not be identified, but is probably due to a wrong (or imperfect) calibration report or an insufficient set of GCPs. Due to those gross errors a reliable mass-balance can not be calculated.

Figure 4.2 shows the extracted DEMs and their difference to the Lidar 2006 DEM

4.1.3 Ortho-photo comparison

All photo sets from 1948 up to 2003 are orthorectified using the IGN50-DEM (A.4) with its relative low resolution of 50 m. Full page prints of the ortho-photos can be found in the appendix in Section A.1. A summary of the landslide activity in the

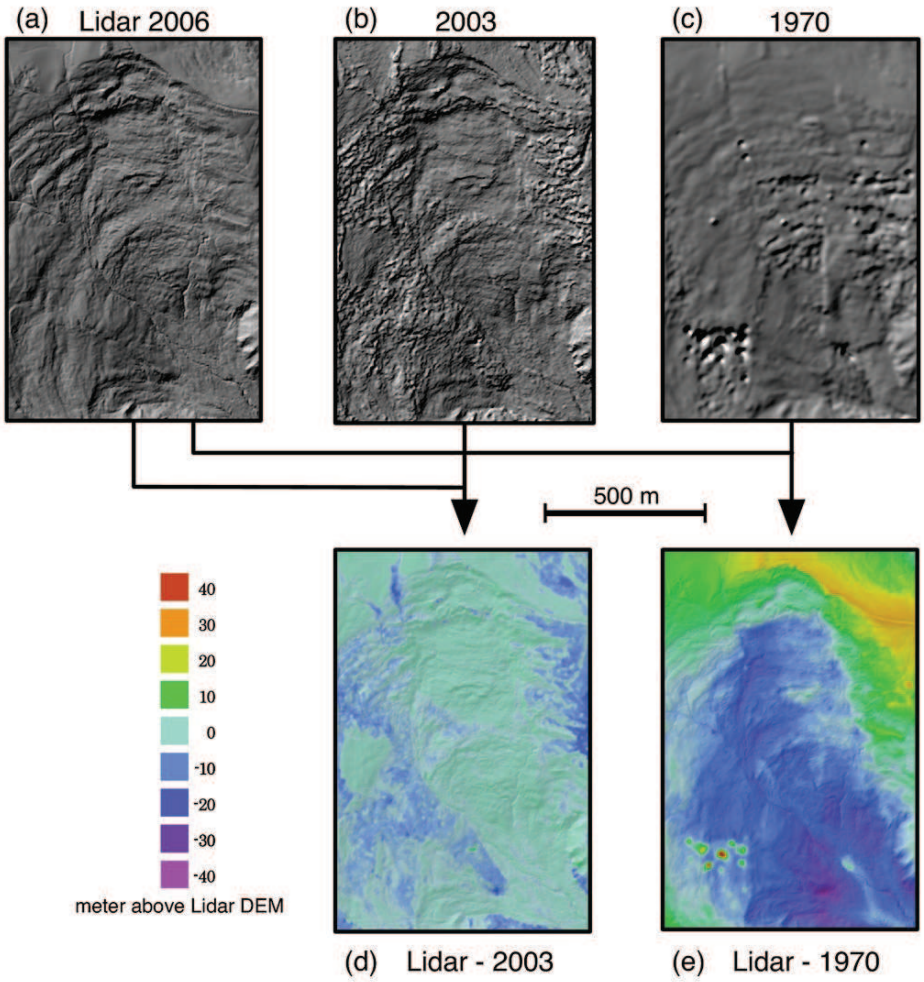

Figure 4.2: Shaded relief maps of the headscarp from Harmalière derived from (a) the Lidar (2006) as reference, (b) aerial photos of 2003 and (c) aerial photos of 1970. Below the differences between the Lidar DTM and the DEMs of the aerial photos, (d) for 2003 and (e) for 1970. Negative values in the differences should be related to loss of material and positive values to accumulation of material.

last decades is already given in Section 3.1.3 including Figure 3.8, which quantifies landslide parts of higher activity based on the classification of denuded areas in the ortho-photos. The main statement here is the higher activity of Harmalière in contrast to Avignonet in the last decades. Harmalière shows activity in 13 - 20 % of its area on all photos from 1948 to 2003 and Avignonet only about 3 %. Additionally the ortho-photos are qualitatively analyzed with regard to landslide activity and landuse change and the main observations from every photo are listed in Table 4.1. The findings will be included in the discussion about the landslide kinematics at the end of this chapter in section 4.4. A direct extraction of displacements using cross-correlation techniques could not be done due to insufficient accuracies of the computed ortho-photos. The numerous reasons are presented and discussed in the following section.

4.1.4 Discussion

Aerial photos with stereo-coverage are processed to obtain DEMs and Ortho-photos for the years 1948, 1956, 1970, 1978, 1985, 2001 and 2003. The DEM from 2003 is fairly accurate, but DEMs from older photos contain major errors and are only use-

between	landslide activity	landuse change
1948 - 1956	activity in lower Harmalière	urbanizing in N Avignonet
1956 - 1970	increased activity in S Avignonet	deforested channel in Harmalière filling of Monteynard lake
1970 - 1978	activated scarps in upper Harmalière increased activity in S Harmalière	urbanizing in S Avignonet
1978 - 1985	major event in 1981 at Harmalière	further urbanizing in S Avignonet
1985 - 2001	Harmalière headscarp reaches Avignonet continues activity in Harmalière	
2001 - 2003	two small landslides E and W of the main lower Harmalière flowpath	

Table 4.1: Summary of observations derived from the aerial ortho-photos between 1948 and 2003.

ful for a coarse qualitative analysis. Ortho-photos are produced using a DEM with 50 m resolution. The final resolution of the photos is about 0.5 m as its best, but the positional accuracy varies by several meters and therefore is inadequate for direct displacement measurements. In order to obtain an overview about the activity over the last decades and environmental changes like land-use change or constructions the described method of deriving ortho-photos using a general DEM is fast and sufficient. Also photos without a proper calibration-report are treatable at this level accuracy. Landslide features like scarps, larger cracks and exposed soils can be mapped from the ortho-photos or with the help of manual stereo-views using stereoscopes or equivalent computer-software. However, the initial objective of extracting displacements directly from the ortho-photos using cross-correlation techniques could not be reached, because the positional errors are too large of the derived ortho-photos in relation to the expected displacements. The following problems are identified in the processing chain and improvement strategies are proposed for each:

1. Missing or incomplete calibration reports leading to higher inaccuracies due to distortions of the images coming from the camera and lens construction. This problem is amplified by the fact, that older photos usually contain higher distortions, due to more imprecise manufacturing techniques in the past, and are more often missing proper calibration reports. A strategy to derive satisfying calibration parameters could be to use photos of the same acquisition-flight (using the same camera and lens) which cover stable areas. By using a high-resolution DEM of that area and a well distributed set of control points (coming from a recent georeferenced ortho-photo or GPS measurements in the field) the calibration parameters could be estimated. This would also deliver a good estimation of the expected accuracy in the target region.

2. At the step of the DEM generation from the stereo-photos, accurate ground control points (GCPs) are needed. The distribution of those ground control points should include points from the whole elevation range inside the images. This is challenging in the region of Avignonet and Harmalière, because the majority of areas below the plateau are potentially unstable and stable points on the bedrock near the lake are hard to identify on the photos due to the filling of the Monteynard lake and followed lake-level fluctuations. However, by starting the computation of DEMs and ortho-photos with the most recent ones and continuing

step by step to the next older ones, additional or different GCPs can be extracted from a set of photos and used in the next older set. This would not need to measure recent GCPs in the field which are recognizable on older photos, but would add the positional error of every step in between.

3. It should be highlighted that sharing a DEM or GCPs between different dates inside potentially unstable areas is necessary to avoid, as otherwise the displacements would be already computationally eliminated or amplified in the ortho-rectification process. However, tie-points between the individual photos of the stereo-pair from one date should cover the whole area and especially the unstable areas. As one can see, this already exposes a methodical weakness, because of the lack of a direct positional control inside the unstable areas in the past.

4. Another unavoidable shortcoming is the presence of vegetation in the photos. First simply because of the highly changed texture when looking from different angles on trees. This leads to mis-matching of corresponding points in the stereo-pairs and therefore to errors in the DEM and causes mis-matching again in the displacement extraction from the ortho-photos. And secondly, even if the match in the stereo-pairs is correct, the measured height will be the top of the vegetation (or buildings) and lead to high distortions at that point during the ortho-photo generation. This could be minimized by filtering the DEM from small peaks or should at least be masked out in the final map of displacements as those points will be inaccurate. This problem only applies if the displacements to be measured are at the same scale or shorter than the height of such obstacles (up to 10 m for trees and houses), which is the case in the actual study area.

5. The next issue when extracting displacements from aerial photos are the change of textures due to seasons and landuse change. For example some agricultural fields are completely changing colors (or brightness) due to changing cultivation (e.g. type of crop, state of harvesting). Therefore it would be more suitable to use derivatives of the images instead of the original ortho-photos. This could be for example the absolute gradient of brightness, which would highlight the edges of objects and be more independent of the actual colors. Or even more consequently the shapes could be extracted as abstract vectorized objects and the changes analyzed between the objects extracted from different dates.

A good starting point for further improvements of displacement extractions could be the software Cosi-Corr[1] and the related paper (Ayoub et al., 2009) which deals with displacement extractions from aerial photos.

[1] `http://www.tectonics.caltech.edu/slip_history/spot_coseis/index.html`

4.2 Lidar DTM comparison

In opposite to Section 3.2 which describes the static view of the DTM, this section is all about the information extracted from two DTMs of different dates. In Section 4.2.1 a basic comparison is done by looking at the height differences between the DTMs. This already gives an overview of the overall activity of the landslides and the most active regions. But it can not determine block movements, especially if they are parallel to the slope showing only minimal height differences. Therefore the two DTMs are accessed by cross-correlation techniques to extract surface movements. For that, first some parameters are determined by some statistical tests in section 4.2.2 before calculating the displacements on the whole area and focussing on key-regions of the landslides in section 4.2.3. Finally the advantages and limitations of the method are discussed in section 4.2.4.

4.2.1 Height difference

In order to calculate the height differences, the Lidar DTMs of 2006 and 2009 with a resolution of 2 m (from Sec. 3.2.2, see Fig. 3.19) are limited to their overlapping area and then the older one is subtracted from the younger, so that loss of material will give negative results (blue) and accumulation of material will be positive (red). The map of the height difference is given in Figure 4.3. From that difference map the following observations can be made:

1. There is no significant vertical offset between the two Lidar datasets. The difference is basically everywhere about zero.

2. There seems to be a dependency of the slope orientation. N-facing slopes are a few decimeter lower than S-facing slopes. It seems to be due to a small global offset in N-S direction and will be better determined in the next section using cross-correlation techniques.

3. Some higher positive and negative artifacts are shown along the borders of the data coming from interpolation effects of low density areas and different lake levels of the artificial Monteynard lake at the times of acquisition.

4. Three larger movements in Harmalière (a, b, c) and one in Avignonet (d) characterized by pairs of adjacent blue (material loss) and red (material accumulation) spots. The maximum height differences are no more than about 2 m.

5. A larger spot of negative difference appears on the plateau at the coordinates N 6430700 E 910200 due to the data-hole in the 2006-Lidar dataset at this area, which can be seen in the point-density map on Figure 3.13.

6. There are some small areas with high differences along the steep cliff, which is the E limit of the compacted alluvial layers. It could be due to real loss of material (for the blue parts), filtering difficulties of vegetation along the edges or shadow-effects from the measurements.

Conclusively, the interesting outcome of the map are the non-zeros areas inside the landslides. These spots (a-d) are shown at larger scale in Figure 4.4 together with representative cross-sections parallel to the slope.

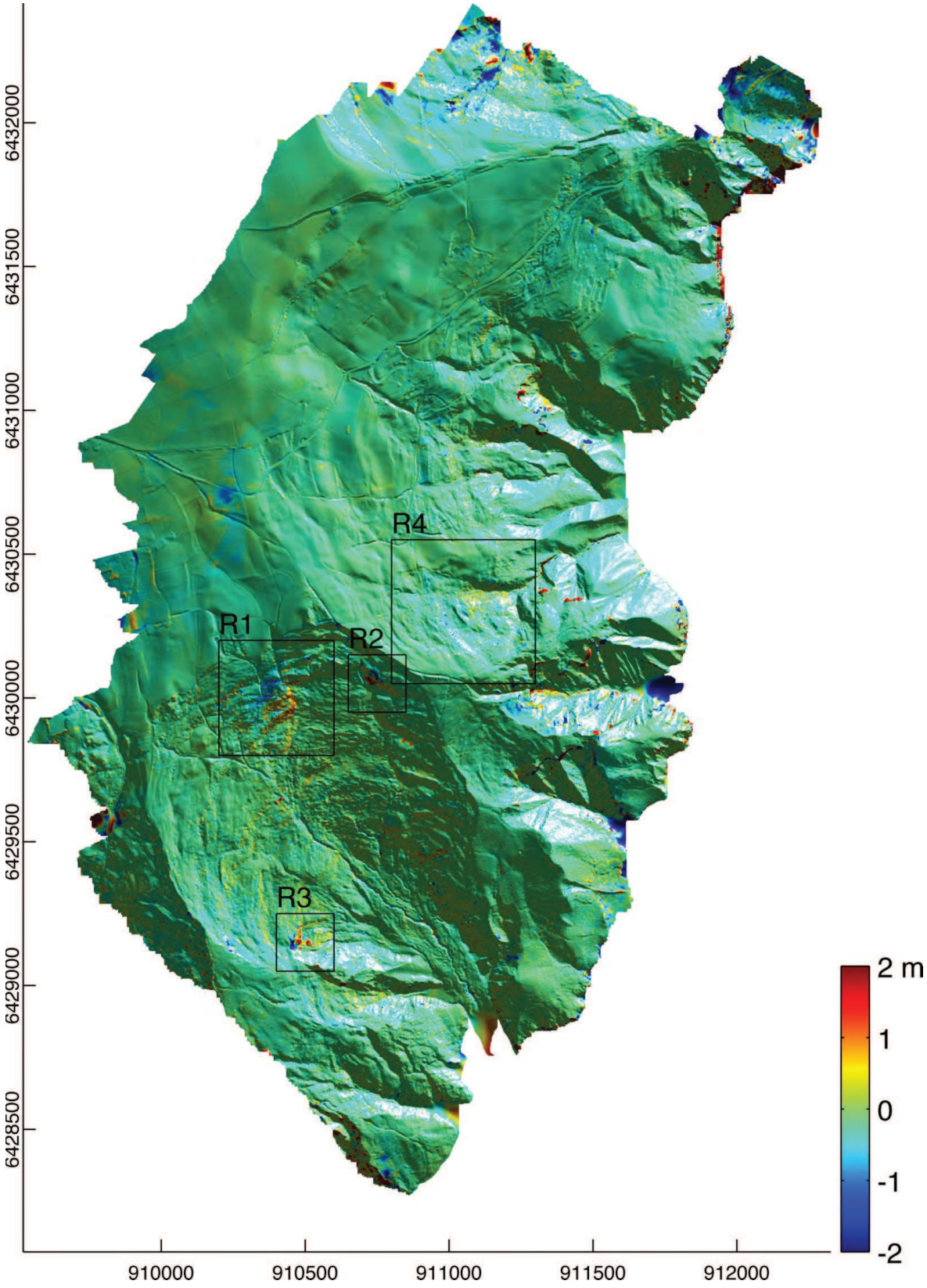

Figure 4.3: Height difference between the 2006 and 2009 Lidar DEM

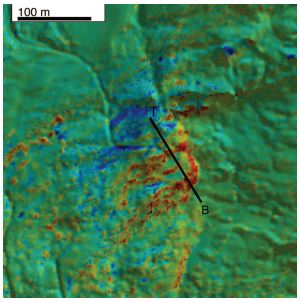

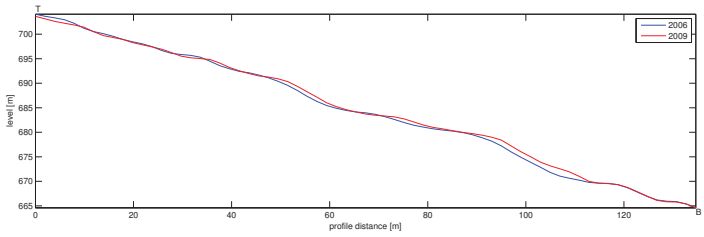

(a) R1

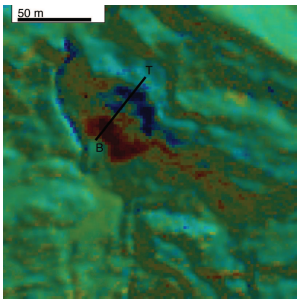

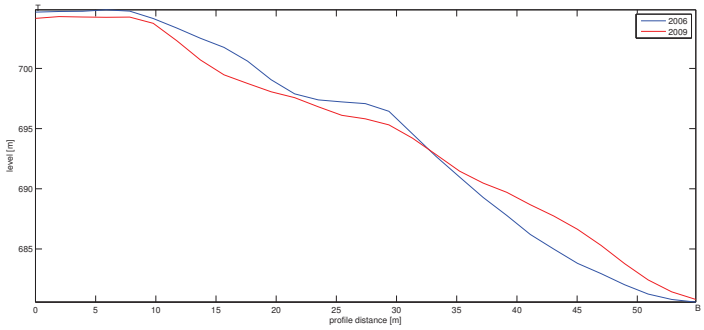

(b) R2

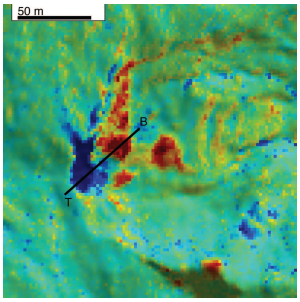

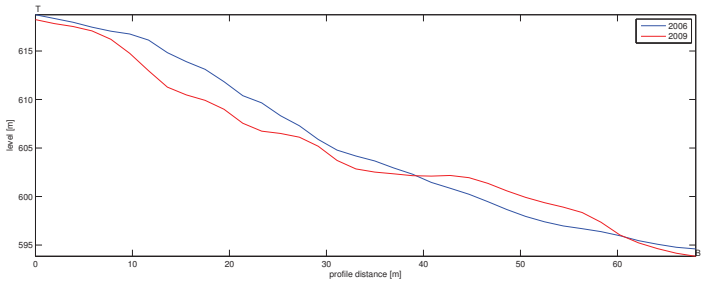

(c) R3

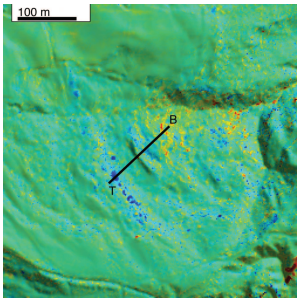

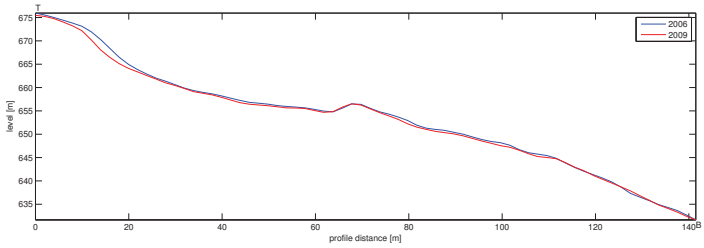

(d) R4

Figure 4.4: Height difference between the 2006 and 2009 Lidar DEM at the zoomed region indicated in Fig. 4.3 and a representative profile for each region parallel to the slope from the top (T) to the bottom (B).

R1 contains the largest sign of activity of both landslides affecting an area of about 100x150 m in the upper part of Harmalière near the headscarp. It is characterized by an upper part of material deficit and a lower part of material accumulation. The profiles from both DEMs are very similar suggesting an almost horizontal block movement of about 2 m in SE direction. This makes that area most suitable to be analyzed by cross-correlation techniques of the next section, which will give a better spatial characterization of the movement of that block.

R2 contains a small area of about 40x40 m inside Harmalière near the headscarp. It shows a spatially narrowed upper area of material loss with an adjacent slightly larger area of deposition downslope. The profiles of both DEMs are very different and therefore can not be mainly related to a block movement. A simple collapse of a part from a scarp with its directly deposition below seems more likely. The transportation distance is about 30 m.

R3 in the SW of Harmalière is situated at the headscarp of a sub-slide inside Harmalière facing E. This sub-slide is about 500 m long before reaching the main track of Harmalière and about 100 m wide. The dissimilarity between the profiles of the DEMs suggests also a fail at the edge of this scarp with a direct deposition at the scarps foot. However, the N-S elongated shapes of the blue and red spots indicate multiple smaller events along the headscarp of this sub-slide.

R4 is the only area in the Avignonet landslide showing some major height differences. It is situated in the S of Avignonet half way between headscarp and toe facing towards NE. It shows loss of material along a scarp of 150 m length (blue at "T") and gain of material near the drainage channel 150 m downwards the scarp (red at "B"). In the middle of the profile, parallel to the scarp is a little ridge of 3 m height. Unlike the former cases (a)-(c), the flow of material here is not obvious. Either the material of the scarp is transported and spread superficially towards the drainage channel or there is an underlying block-movement which can not be seen as height differences. The small ridge could be a highly eroded back-tilted block like the ones near the most active Harmalière headscarp.

As the height-difference is a quite limited tool to assess the full kinematics of the landslides from DEMs, further details about movement directions in the 3D-space are obtained by cross-correlation techniques described in the following section.

4.2.2 Parameter tests for Lidar displacements

The quality or even the ability of getting displacements from multi-temporal DTMs by feature-matching techniques depends highly on several parameters like grid resolution, kernel size, search area, point density, terrain type etc.. In order to choose the best parameters and estimate the accuracies of the results, a few tests are made and described in the following sections before coming to the results of the whole study site. First, the meaning of point-overlapping is defined and examined together with the influence of the grid resolution on the quality of results in section 4.2.2.1. At next the dependency on kernel size and search distance is assessed in section 4.2.2.2 followed by a view on sub-pixel precisions in relation to upscaling factors in section 4.2.2.3. At last the dependency on terrain types and in the computation included point cloud classes are explored in section 4.2.2.4.

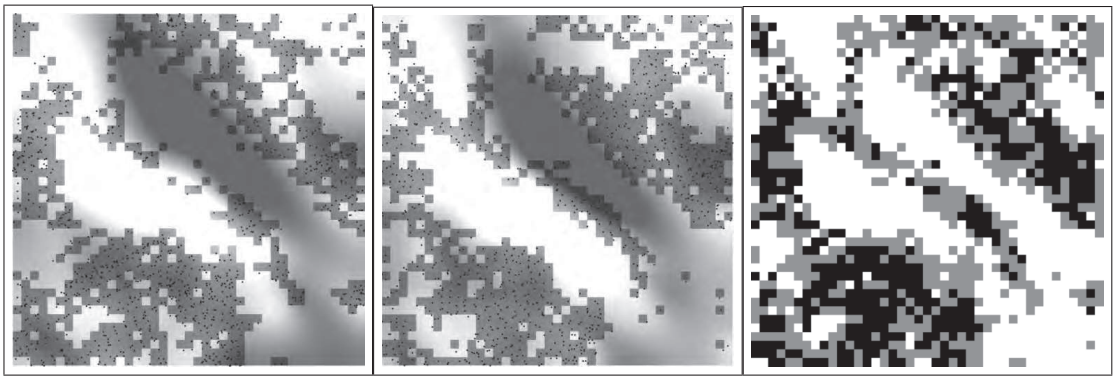

(a) 2006 **(b)** 2009 **(c)** overlap

Figure 4.5: Example of calculating the point overlap. (a) and (b) represent two small areas of 20x20 m from the two Lidar sets. The small black dots show the locations of the available points from the Lidar-point cloud. The shading shows the interpolated surface through this points on a regular grid with 0.5 m resolution. At the grey pixels the kernel is well defined, the white areas are only interpolated. (c) represents the overlay of (a) and (b), showing the pixels which are well defined in both kernels in black, pixels which are only well-defined in one of the kernels in grey and pixels which are only interpolated in both kernels in white. The actual point overlapping is the percentage of black in the whole grid, here 24 %.

4.2.2.1 Testing point-overlapping and grid resolution

Before the calculation of the cross-correlation between two kernels, they need to be gridded from points of both datasets. The matching quality decreases necessarily if the two kernels are not well defined by the points from which are they interpolated. To describe the quality of a match regarding this problem, the point-overlapping is computed, which depends on the point distribution and grid resolution. The point-overlapping is the number of pixels well defined in both kernels at the same location in relation to all pixels of the kernel. "Well defined" means that the area of a pixel contains a point from the original Lidar-point cloud. Figure 4.5 shows an example for the calculation of the point-overlapping. As mentioned before, the point-overlapping depends not only on the point-distribution, but also on the grid resolution. A higher resolution result in a lower chance that pixels are well-defined in the same location in both kernels. In order to test how the point-overlapping decreases with higher resolutions and if this has an influence on the displacement detection quality, displacement by cross-correlation is computed at 32 locations with known displacements from GPS-measurements (see dataset A.5). 5 GPS-locations are outside the Lidar-coverage and not used. As the GPS-dataset ends in 2006, the average annual velocity is used and multiplied by the timespan between the Lidar-sets (2.4 years) to derive GPS-displacements comparable to the displacements derived from the Lidar-sets. This assumes a constant movement of the landslides. The influence on the resolution test here is certainly very low, because the majority of the GPS-displacements is below the general Lidar-accuracy (≈10 cm). The influence of the grid resolution on the point-overlapping and displacement error is shown in Figure 4.6. The test reveals that the determination of the displacements is better with higher resolutions, but is getting worse again with too high resolutions below 0.4 m pixel size (Fig. 4.6a). Also the point-overlapping decreases rapidly at pixel sizes below 0.8 m and becomes lower than 10 % at pixel size below 0.2 m (Fig. 4.6b). Both figures suggest to choose a grid resolution around 0.5 m for best results.

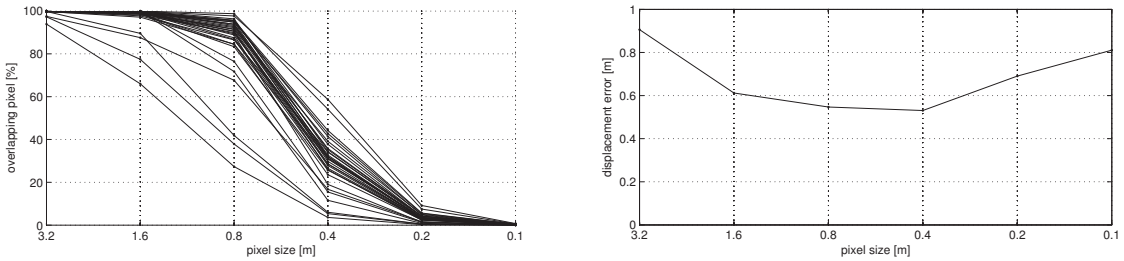

(a) **(b)**

Figure 4.6: Test of the influence of grid resolution on the accuracy of displacements using GPS-displacements as reference (see dataset A.5). 32 averaged GPS displacements inside the Lidar-coverage are used. (a) Point overlap at the 32 GPS-locations with kernel sizes of 65x65 m. Up to a resolution of 0.8 m the majority of locations show a good point-overlapping with more than 80 %. At a resolution of 0.4 m the overlap is still between 20 and 60 %. Higher resolutions lead to point-overlapping below 10 %. (b) Average displacement error (relative to the GPS-displacements) using cross-correlation with 64x64 m kernel, 6.4 m search radius and 10 times subpixel precision. The displacement error decreases with resolutions up to 0.4 m and increases again when using finer resolutions.

4.2.2.2 Kernel size and maximum search distance

This test is supposed to clarify the choice of kernel size and maximum search distance. The advantage of smaller kernel sizes are faster computation and better representation of variabilities of the displacement vectors, but larger kernels are less prone to mismatches. Similarly short maximum search distances result in faster computation and less mismatches, but the search distance need to cover the expected displacements of the landslide. If the expected displacements are very high, a pyramidical approach with higher search distances at lower resolutions in a first step and an iterative "focussing" at higher resolution with shorter distances can help to avoid mismatches. Figure 4.7 shows the mismatching error for 32 locations as a function of kernel size and maximum search distance. The displacement errors are obtained using the GPS-displacements at these locations as reference, which is already described in the previous test.

As expected, larger kernels and shorter search distances lead to smaller mismatching errors. On top of that it seems to exist a minimum kernel size per search distance above which a further increase of the kernel size does not lead to higher matching quality, e.g. 21 m kernel size for search distances of 5 and 10 m (no lower values to the right of those values in the figure). As the figure only shows an average dependency, the kernel size should be chosen a bit larger to be safe. The visual inspection of the shaded DTMs from the Lidar-sets suggest that a search distance of 5 m should be enough for the whole area. As a conclusion of this test the kernel size for this search distance should be not smaller than 21 m. The test was done with grid resolutions of 0.5 m. When using other resolutions, the kernel size should be scaled by the same factor, to keep about the same grid-size (here 41x41 pixel).

4.2.2.3 Upscaling and subpixel precision

In order to derive displacements with a higher precision than the grid resolution (i.e. 0.5 m) the peak in the cross-correlation matrix need to be defined with sub-pixel precision. This is achieved by upscaling the cross-correlation matrix by the factor "usfac" before obtaining the maximum peak for the best fit. For test purposes the correlation was done using the same Lidar-set as reference and search target, which means the

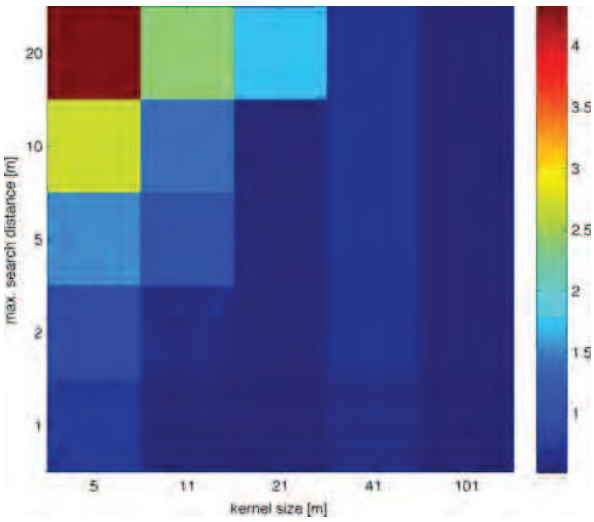

Figure 4.7: Average mismatch in meter of displacements using different kernel size and maximum search distance with cross-correlation at 32 locations of GPS-points (Sec. A.5). The grid resolution is 0.5 m. Small kernel sizes lead to higher mismatches especially in combination with high search distances. For every maximum search distance exists a minimum kernel size above which the quality does not further increase.

displacement should always be zero. If the difference between the computed peak-position and the center (= no displacement) is more than 0.5 pixel, then the upscaling has not gained any increase in precision. Figure 4.8 shows the horizontal displacement mismatch using cubic- and spline-interpolation of the cross-correlation matrix with different upscaling-factors. As there is almost no difference between the interpolation methods (left column vs. right column), only one column is described here. 66 locations in an area of 1x2 km in the center part of the area covered by the Lidar-data are used with kernel sizes of 10x10 pixel and search radii of 2 pixel. The matching starts with no upscaling (usfac = 1) at a grid resolution of 0.5 m (first row). All obtained displacements are zero. A mismatch would show up at 1 or even higher, as without upscaling there is no subpixel precision. For the next higher upscaling-factor (usfac = 2, 2nd row) the used grid resolution is 1 m in order to look for the same absolute precision of 0.5 m as in the first case and not having the problem of insufficient point-cloud densities when using higher grid resolutions. Almost all obtained displacements are correct at zero, only in one case a false mismatch leads to an error of 0.5 pixel, which is the limit of accuracy gain. For upscaling-factors of 5 and 10 the majority of results is still below 0.5 pixel, meaning a gain of information. For higher upscaling-factors (last row) in most cases the mismatch is higher than 0.5 pixel and there fore worse than without upscaling and not useful. It should be mentioned that for the real case of matching two different Lidar-sets the mis-match will be worse, so that a factor of 10 can be seen as the upper limit for useful upscaling.

The conclusion of this test is, that there is no use in upscaling factors higher than 10 and the interpolation method (bicubic or spline) has no influence.

4.2.2.4 Terrain type and classification classes

Another question for the correlation process is which classification classes of the point cloud should be used. Table 4.2 shows the number of points per class for the two Lidar sets. The main classes are ground and low, medium and high vegetation. The class buildings plays a minor role looking at the counts, but could be important in villages

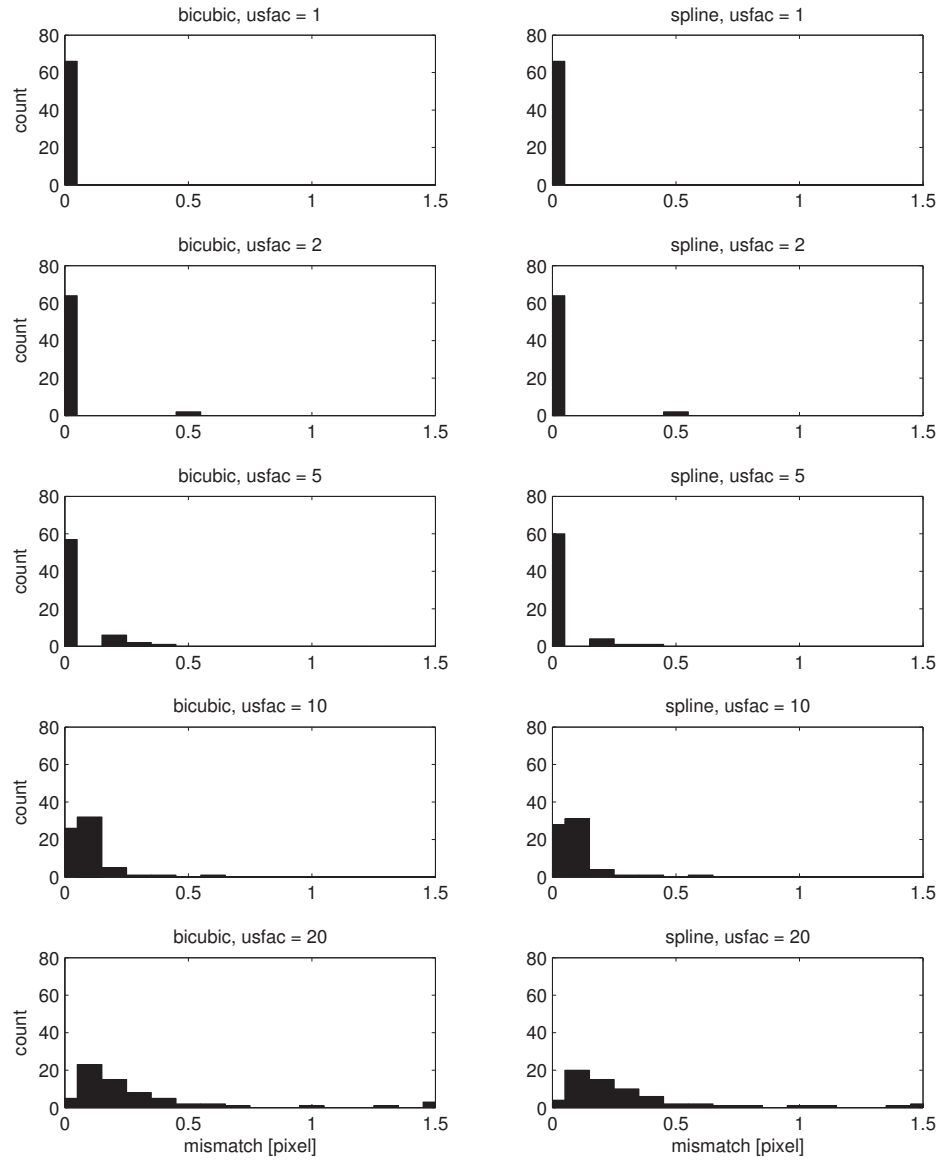

Figure 4.8: Test of sub-pixel precision with the ideal case of two identical Lidar-sets at 66 locations with kernel sizes is of 10x10 pixel and search radii is 2 pixel. The grid resolution varies with the upscaling factor usfac starting at 0.5 m. The histograms showing the number of obtained displacements per mis-match distance. A mismatch of more than half a pixel means no gain of precision against no upscaling. At usfac = 10 the majority of displacements is still below 0.5 pixel, meaning a gain of precision. At usfac = 20 the accuracy of displacements are mainly worse than 0.5 pixel, meaning no gain of precision.

class	las id	2006	2009
point sum		36.15M	26.21M
		=100 %	=100 %
unclassified	1	0.002 %	0.003 %
ground	2	58 %	67 %
low vegetation	3	23 %	11 %
medium vegetation	4	7 %	7 %
high vegetation	5	12 %	13 %
building	6	0.2 %	0.6 %
low point (noise)	7	0.6 %	0.6 %

Table 4.2: Overall number of points and percentage per class of the classified Lidar point clouds from 2006 and 2009. "las id" is the class identification number of the standard file format "LAS1.2".

because they do not change as much as vegetation over time. The question of classes depends on the terrain type. Four types should be considered:

T1 active landslide parts with rough terrain and minor vegetation (e.g. near the headscarp of Harmalière),

T2 agricultural areas with smooth surfaces and minor vegetation (e.g. the upper parts of Avignonet and the plateau),

T3 forested terrain (e.g. the low areas of Avignonet),

T4 villages (e.g. the Mas d'Avignonet in the S of the Avignonet landslide or the camp-site in the northern part of Avignonet).

For each terrain type the displacement method is tested at 16 locations using different sets of classes. The points are equally distributed in each terrain (Fig. 4.9a), but at T4 the points are centered on houses. In general the advantage of using more classes is a higher point-cloud density and more trackable terrain-features. The disadvantages are vegetation changes over time and distortions due to changed scan-angles between the two Lidar-sets. The following combinations of classes are tested (in brackets the las ids of Table 4.2):

C1 [2] ground only to avoid distortions from vegetation,

C2 [2 3] ground and low vegetation in case the low vegetation class includes essential parts of the ground,

C3 [2 5] ground and high vegetation to have larger trackable features without the underlying noise of lower vegetation,

C4 [2 3 4 5 6] all classes including buildings,

C5 [2 6] ground and buildings only for the villages (T4) to have more stable trackable objects without the noise of vegetation.

Figure 4.9a shows a map with the test-areas for each terrain type. As there are no control displacements available at all terrain types, a different approach is used to analyze the quality of the derived displacements. The locations at each terrain type are

chosen close together assuming minimal displacement changes between them. Then the standard deviation of the 16 derived displacements is computed for each terrain-class combination. Feasible displacements would be more or less in one direction and therefore would result in a low standard deviation, whereas mismatch errors are expected to be unidirectional and therefore would lead to higher standard deviations. The inclusion of a variable amount of classes influences the point density in both Lidar-sets and therefore the point-overlap percentage for each displacement extraction. The link between terrain type, class-set and point-overlap is shown in Figure 4.9b. Surprisingly at T1 there is a big difference between the point-overlap using C1 or C2. That means many points in this rough terrain are classified as "low vegetation", either because of real low vegetation or just because of the rough terrain causing the procedure to classify slightly elevated points from small scarps as vegetation. At T2 in smooth terrain without much vegetation the differences between the class-sets are insignificant. In the forest at T3 the overlapping without the high vegetation (trees) is quiet low, because the canopy of the trees is hiding the ground from the laser. In the village at T4 the increase of overlapping when including buildings is surprisingly low. This could be due to miss-classification of buildings as medium or high vegetation, especially if there are trees and houses close by.

Figure 4.9c shows the standard deviation of the derived displacements for each set of 16 points. Some observations can be made from that graph: (1) The error in smooth terrain is about one third higher than in the other terrain types. This is expected due to the nature of correlation. (2) Except for the smooth terrain, the inclusion of the low vegetation class increases the quality of displacements, certainly due to the point density increase without heavily altering the morphology. (3) Using C3 (ground + high vegetation) the quality is everywhere decreasing or equal compared to C1. (4) Using all classes (C4) brings only some advantage in the village, probably due to the fact, that many building-points are miss-classified as high vegetation. (5) The building class (C5) should only have an effect in the village, as in all other terrains it should be the same as using the ground class (C1) only. The forested terrain however shows a major error when using C5. After looking into the details it took out this is due to some building-points in one of the Lidar-sets resulting in a very high mismatch at one location. So again, the problem seems to be the miss-classification between building and high vegetation. Also the high error for C5 at T4 in the village supports this assumption. Miss-classified building-points would highly alter the shape of buildings when only using the remaining building-points. But also shadow effects due to the line of sight during the laser-scan could have a major influence of the shape of buildings after gridding.

In conclusion the best choice seems to be C2 (ground + low vegetation) in all but the smooth terrain T2, where C1 (only ground) is slightly better.

4.2.3 Lidar-displacement results

4.2.3.1 Global shift

As conclusion from all previous tests the following parameters are chosen for the computation of the displacements:

- grid resolution 0.5 m
- kernel-size 20.5x20.5 m = 41x41 pixel

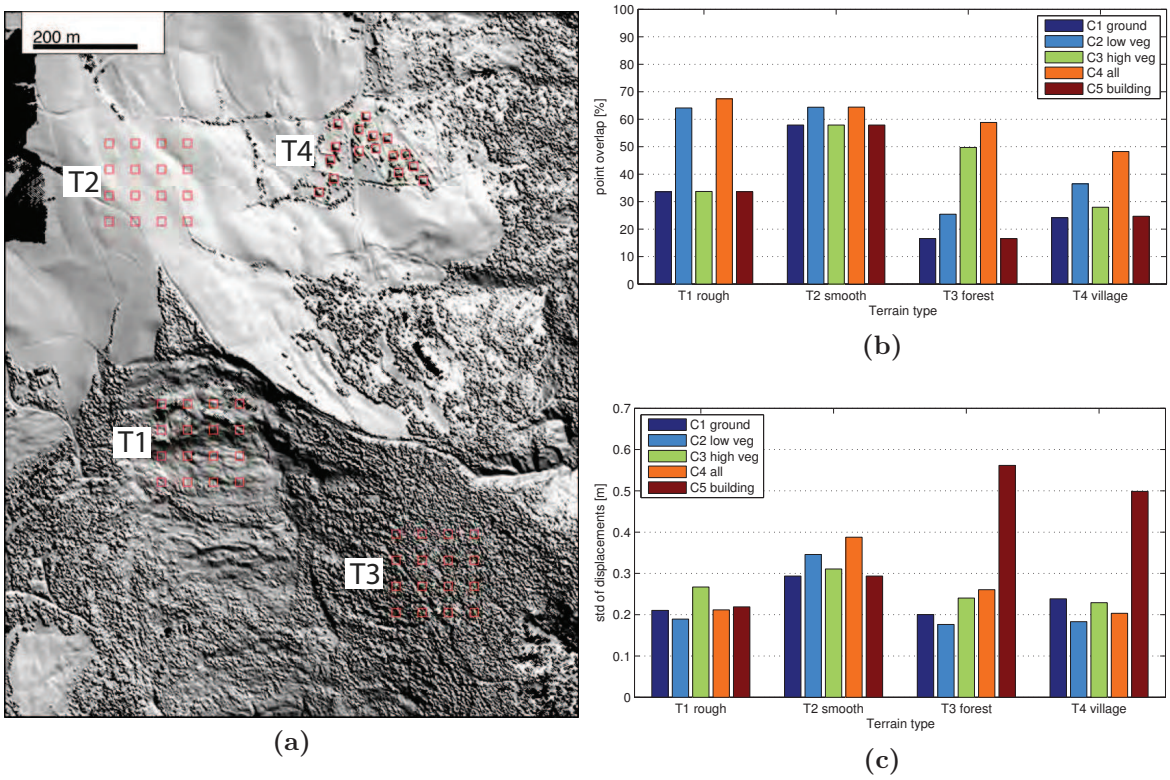

Figure 4.9: Test of influence of included point-cloud classes on the quality of extracted displacements at different terrain types. The displacements are calculated at 16 points per terrain type at resolution 0.5 m, kernel size 41 m and search distance 5 m. For a detailed description of the terrain types and class-sets see the text. (a) Shaded relief map of the DEM (using all classes) showing the tested locations at the different terrain types. (b) Average point-overlap per terrain type and class-set. (c) Standard deviation of displacements per terrain type and class-set.

- maximum search radius 5 m = 10 pixel
- upscaling factor of 10 for the cross-correlation matrix (bicubic interpolation)
- the resulting resolution for the derived displacements is therefore 0.05 m
- used point classes are ground + low vegetation
- point-overlapping is calculated at 2 m grid-resolution

In a first attempt, displacements are calculated at points in a regular grid with 10 m spacing covering the whole Lidar-set in order to look for a global shift between the two data-sets and identify problematic areas. The absolute horizontal displacements are shown in Figure 4.10a. The yellow-red areas inside Harmalière seem to be plausible, also the S and E of Avignonet contain larger homogeneous areas. In the contrary the upper parts and especially the plateau show major irregular patterns, most likely due to erroneous displacements. In order to obtain a global shift, if there is any, a two-dimensional histogram of the E-W (dx) and N-S (dy) directions is computed. Displacements from mismatches are assumed to be random and real landslide displacements are also multi-directional due to the different slope angles. In the case of no global shift the most often displacement would be at dx= 0 m, dy= 0 m. The global shift can be obtained by finding dx and dy at the highest peak in the 2D-histogram, which is shown in Fig. 4.10b. It can be seen that the peak is near the center of the

diagram. Figure 4.10c shows a zoomed 10-times upscaled spline-interpolated version of that peak, revealing the presence of two close-by peaks. The highest is at dx= −0.07 m and dy= −0.27 m which is assumed to be the global shift between the two Lidar-sets. The accompanying vertical shift is obtained from the histogram of the vertical components of all displacements within a radius of 0.05 m around that horizontal global shift (Fig. 4.10d). The highest peak here is at -0.15 m. The sense of those values for the global shift from the 2006 to the 2009 Lidar-set is towards SSW and downwards. This shift is already incorporated in Figure 4.10a. All following results are corrected by that shift.

Another interesting aspect of the displacement distribution in Figure 4.10b is the presence of displacements covering the whole possible range of 5 m in all directions, which is the maximum search distance. Those outliers are assumed to be the mismatches, mainly occurring on the plateau W of Avignonet. Furthermore, the shape of the displacements-cloud has two condensed indentations, one elongated towards SE (dx= 2, dy= −3) and another more indistinct one towards ENE. They can be explained by the slope direction at the main moving blocks seen on the displacement map (Fig. 4.10a). The higher displacements towards SE would correlate with the SE facing slope of the block in the NW of Harmalière and the higher displacements towards ENE would correlate with slope direction at the moving parts in the SW of Harmalière and the S of Avignonet.

4.2.3.2 Quality filtering of displacements

Even if all parameters chosen carefully taking into account the previous tests, the obtained displacements will always include wrong displacements due to mismatching. For example in Figure 4.10a it can be seen that the displacements on the (most probable stable) plateau in the NW are very chaotic (not only in absolute displacements as seen in the Figure, but also in direction). In order to detect possible mis-matches the following quality measurements are obtained in parallel to the displacement computation:

sharp

Describes the sharpness of the match, or rather the sharpness of the peak in the correlation matrix (CCM). This is defined by the difference between the correlation coefficient (CC) at the peak and the maximum CC on a circle with radius 2 pixel around the peak divided by the radius of 2 pixel. This gives the worst sharpness of the peak of all directions. If “sharp” is high, then the peak is sharp and if it is low, the peak is blurred. In the regular case of using an upscaled CCM , “sharp” is derived from the upscaled CCM using a radius of 2 times the upscaling factor, so that the sharpness is comparable between the upscaled and non-upscaled CCM.

stddz

Describes the change of morphology of the matched kernel. It is defined by the standard deviation of the height differences between the matched kernels. Because of subpixel precision, the reference kernel is re-gridded using the original point cloud shifted by the computed horizontal displacement. This is the same principle used for deriving the vertical component, which is the average height difference between the matched kernels. If “stddz” is near zero, the morphology of the kernel has not changed except for the overall displacement and if “stddz” is high, the morphology has changed irregular.

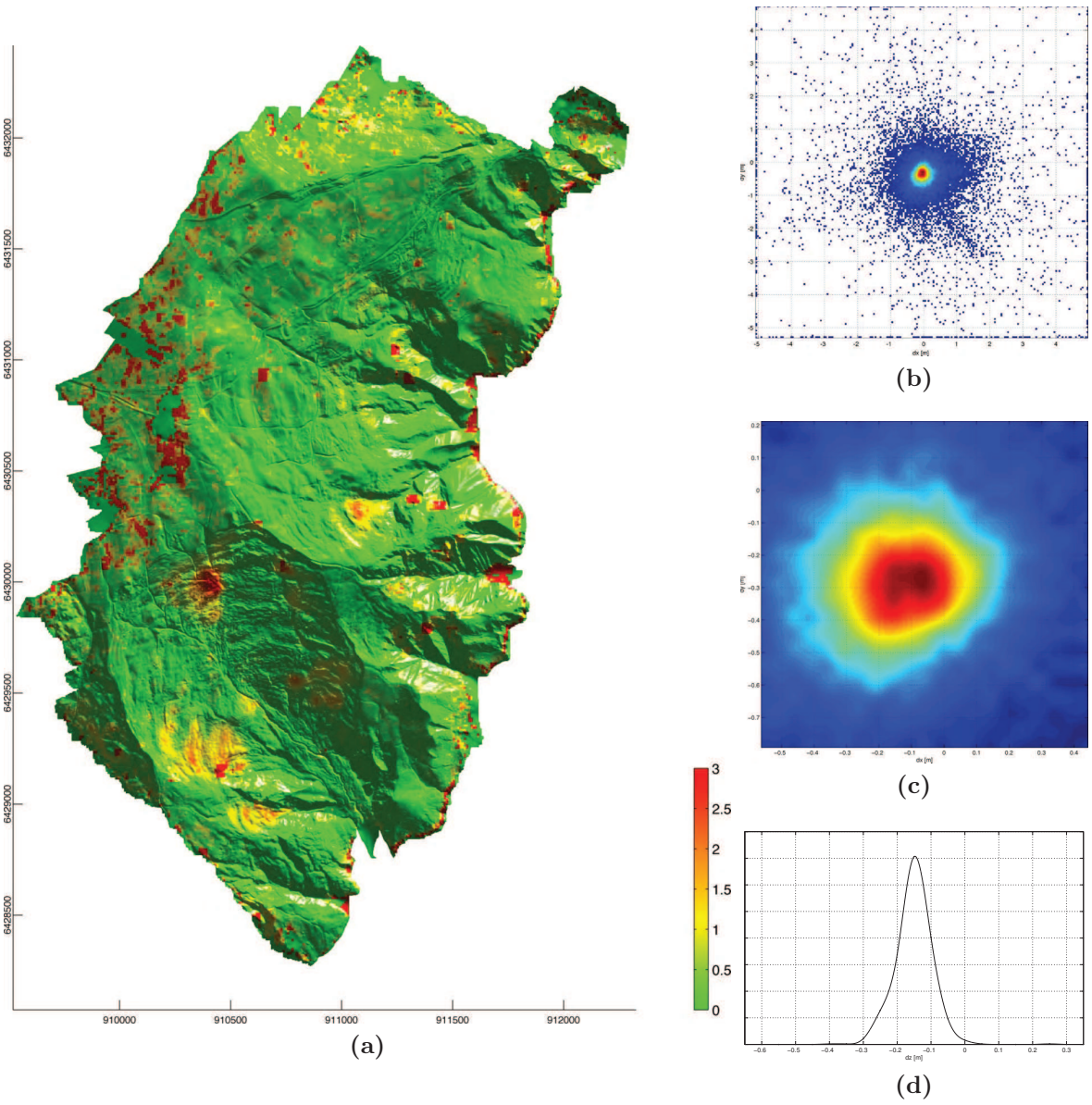

Figure 4.10: Global shift between the 2006 and 2009 Lidar-sets. (a) Map of absolute horizontal displacements in [m] between the two Lidar-sets derived at every 10 m using 0.5 m grid resolution, 41x41 m kernel-size, 5 m maximum search distance and cross-correlation matrix upscaling by 10. The result includes a global shift of about -0.07 m in x, -0.27 m in y and -0.15 m in z in the sense that the 2009-Lidar is shifted SSW and downwards. (b) 2D-histogram of all displacements in x- and y-direction without the correction of the global shift showing the most frequent combination at the red peak near 0, 0. (c) 10-times upsampled peak of (b) revealing 2 close peaks. The highest is at dx=-0.07 and dy=-0.27. This is assumed to be the global shift. (d) Histogram of the vertical component using only solutions within a horizontal displacement of 0.05 m of the global shift. The peak is at dz=-0.15 m and is assumed to be the vertical global shift. Coordinates are in meter in Lambert93.

ccmax
: is the maximum correlation-coefficient of the correlation-matrix indicating the matching quality between the kernel. It is somehow the same as "stddz" but less useful because of the normalization of the cross-correlation. It can be near one (perfect match) even if the difference between the matched kernels is high.

ell
: describes the ellipticity of the peak in the CCM. As "sharp" is the worst sharpness of all directions, "ell" is the ratio between the best and worst sharpness using the minimal CC of the circle around the peak as described for "sharp". In case of a perfectly circular peak, "ell" is one. For increased ellipticity, "ell" will be higher.

pol
: is the point-overlapping as described in Section 4.2.2.1. It is the percentage kernel-area covered by points from both Lidar-sets. Low values are due to low point densities and/or uneven point distribution. High values stand for well defined kernels by the underlying point-clouds.

In order to sort-out displacement measurements of bad quality using these quality measures, the most common problems for mismatching need to be understood. The following list describes each type of problem and how this problem can be identified using the quality measures.

P1 A low density of points will lead to smooth interpolated kernels, which can show good correlation without meaning. In this case "pol" will be low and all other measures are insignificant.

P2 Even with an average high point density the points can be distributed very irregular inside the kernel area and lead to dissimilar kernels. This will also show off in a low "pol" and all other measures will be insignificant.

P3 An insignificant morphology inside the kernel. The extreme example would be a flat kernel which perfectly matches everywhere in the equally flat search area, but the result has no meaning. In this case "sharp" will be low as well as "stddz". The other measures are insignificant.

P4 An invariant morphology in one direction, like a linear scarp, can lead to mismatch in that direction. In this case "sharp" must be low too (in the direction of the linear). "stddz" should be slightly higher as there is some variable morphology involved. "ell" must be high indicating the un-isotropic matching quality. If the ellipticity is high enough, the displacement perpendicular to the linear could still be significant, e.g. the scarp movement down the general slope could be extracted even if the movements to the sides remain unknown.

P5 A chaotic change in morphology between the two Lidar-sets. This could either be due to a too small search distance or because the morphology is heavily altered (erosion, irregular mass-movement, vegetation change, earthworks or new/removed buildings if the relevant classes are included). In both cases the kernel would just match the most similar morphology even if it is very different. In this case "stddz" will be high and "ccmax" will be lowered. The other measure are insignificant. As this case has a relevant geomorphological meaning it should be distinguished from the other more technical problems and identified in the displacement results.

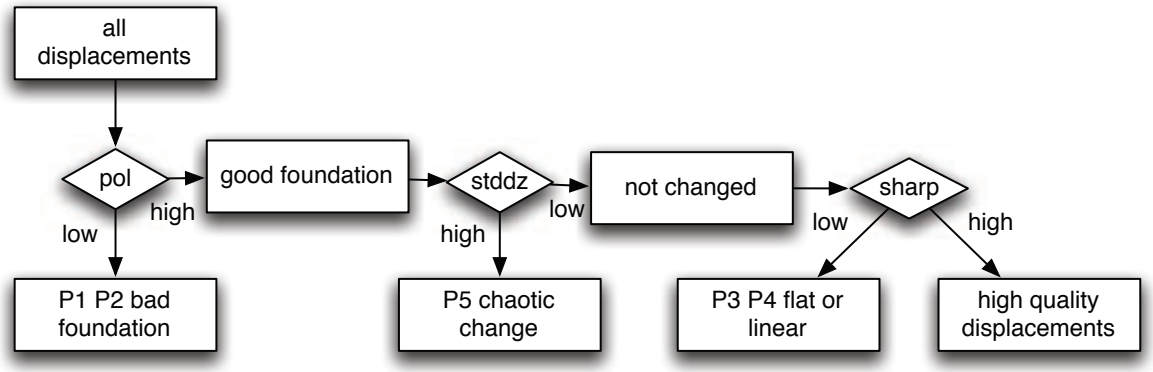

Figure 4.11: Flow-chart of the filter-strategy to sort-out mis-matched displacements derived from the Lidar-data. "pol" is the point-overlapping, "stddz" the standard deviation of height difference after the matching the kernels and "sharp" is the sharpness of the peak of the cross-correlation matrix. P1-5 are the different problematic cases which lead to mis-matched displacements. See Section 4.2.3.2 for a detailed description.

Figure 4.11 shows the resulting strategy to filter the derived displacements by quality. As there is no need to separate P1 from P2, those cases can be identified by a low "pol". After sorting those out, a high "stddz" can be used to identify P5, the areas of chaotic change. And finally P3 and P4, i.e. the fuzzy matches, can be identified by a low "sharp". In this study the possibility of deriving one-directional displacements as described for P4 will be neglected.

In order to find the exact thresholds for the quality-filtering, the preliminary results (displacements at every 10 m over the whole area) are analyzed. The histogram of "pol" in Figure 4.12b reveals the majority of displacements are well founded on well distributed points (at the used resolution of 0.5 m). Furthermore the map of the point-overlapping from all derived displacements in Figure 4.12a shows that those problematic areas are at the borders of the Lidar-coverage and some smaller parts in Harmalière due to the partially low point-cloud density of the Lidar-set from 2009 (Fig. 3.13). As it is not easy to separate the problem of mis-matching due to a lack of point-overlapping a relatively conservative threshold of 80 % is chosen in order to exclude the areas of low point-cloud density at the borders without "loosing" larger areas in Harmalière.

To find the reasonable thresholds for "stddz" and "sharp", four different groups of displacements are chosen, which exhibit the different problematic cases. Then histograms of the quality-measures are shown for each group in order to determine the thresholds. The displacement groups are:

Q1 (slow) Rough terrain with small displacements near the headscarp of Harmalière, assumed to be the best conditions for displacement detection. Only displacements below 0.2 m are considered. (count: 371 displacements)

Q2 (fast) Rough terrain with larger displacements near the headscarp of Harmalière inside a larger moving block.These are more problematic conditions as the movement is not completely rigid, but should not be sorted out by the quality-filtering. Only displacements larger than 1 m are considered.(count: 244 displacements)

Q3 (chaotic) Rough terrain with chaotic change of morphology near the headscarp of Harmalière. This location is R2 from Figure 4.4 and there already described as an irregular movement. Only displacements larger than 1 m are considered. These displacements are meant to represent Problem P5. (count: 28 displacements)

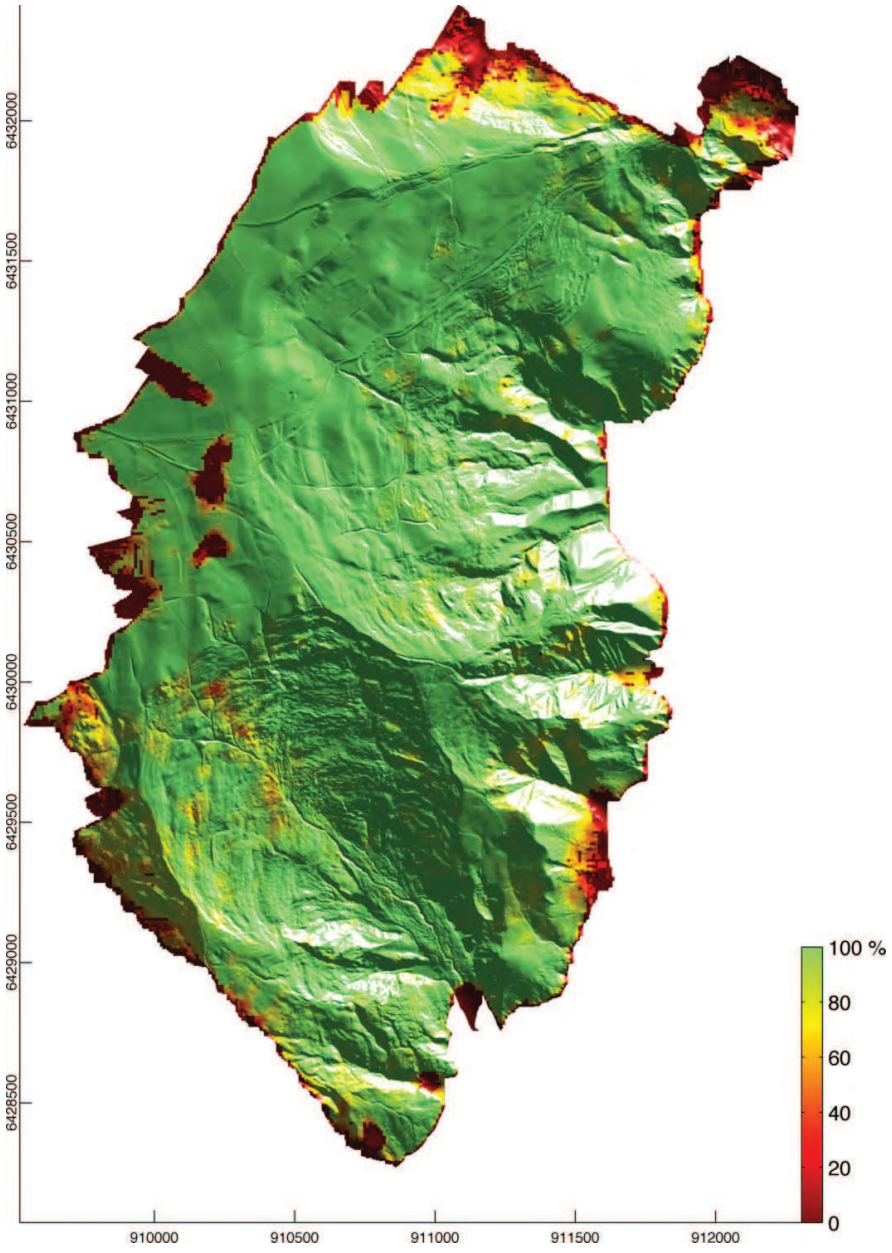

(a)

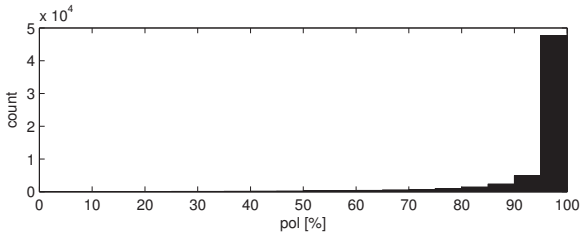

(b)

Figure 4.12: Threshold determination for quality filtering of point-overlapping. The displacements are derived using 0.5 m grid-resolution, kernel size of 20.5x20.5 m (41x41 pixel) and search distance of 5 m (10 pixel). Point-overlapping is defined in Section 4.2.2.1. (a) Map of point-overlapping ("pol") from displacement extraction draped on the shaded Lidar-DTM. The color-axis is restricted to higher "pol"s for better visualization. (b) Histogram of "pol" showing the whole range values. (c) Horizontal displacements (dxy) versus "pol" showing the probability of mis-matching (overexposed large dxy) at decreased "pol". Coordinates are in meter in Lambert93.

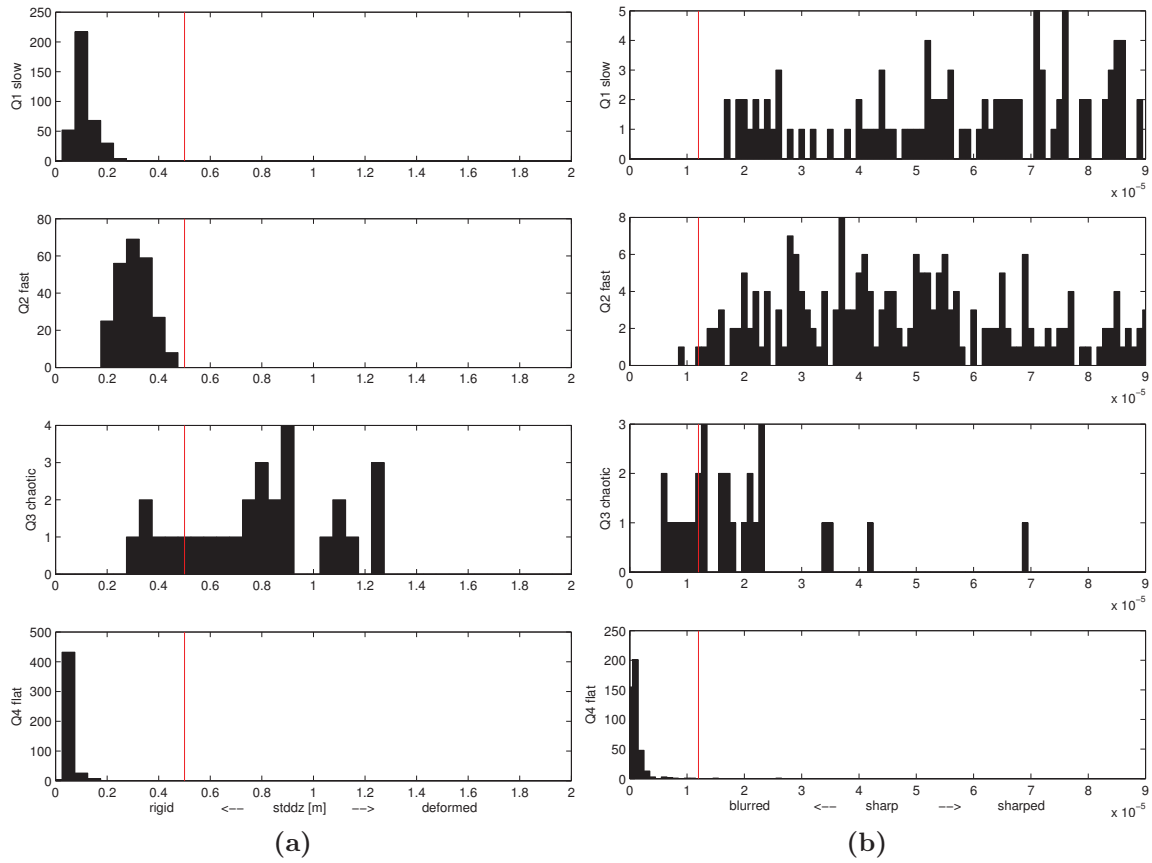

Figure 4.13: Histograms of stddz and sharp of example-displacements in order to determine thresholds for the quality-filtering.

Q4 (flat) Smooth terrain at the plateau W of Avignonet. Only displacements larger than 1 m are considered. These displacements are meant to represent Problem P3 (and therefore also P4). (count: 469 displacements)

Figure 4.13a shows the "stddz"-histogram for each displacement group. According to the flow-chart (Fig. 4.11) at this step P5 needs to be detected, therefore the threshold for "stddz" should separate Q1 and Q2 from Q3. Because Q2 and Q3 are overlapping between approx. 0.3 - 0.5 m, a perfect threshold is not possible. The threshold is set in favorite of Q2 at 0.5 m, meaning all displacements of Q2 are kept, allowing some displacements from Q3 to "slip through". The two reasons for this decision are due to the weak representation of the Problem P5 by the displacement-group Q3. First, the quantity of displacements in Q3 are very low (28) compared to Q2 (244), and second, the kernel size of the displacement detection is relatively large compared to the area of chaotic movement and therefore always includes "rigid" parts from nearby leading to lower "stddz". So the true displacements representing P5 are assumed to be at higher "stddz"s. Finally Figure 4.13b shows the "sharp"-histogram for each displacement group. The next step is to sort-out mis-matches due to flat areas (P3, P4) which are represented by displacement-group Q4. As Q3 is already sorted out, a threshold need to be determined to separate Q1 and Q2 from Q4. The threshold is chosen quite conservative at $1.2 \cdot 10^{-5}$ in order to avoid more mis-matched displacement at the cost of a few good results in fast moving areas.

The final result of horizontal displacements after the quality filtering is shown in Figure 4.14. There are still problematic displacements on the plateau, but beside of

that some active spots can be observed in Harmalière and at least one in Avignonet (red spots). They will be assessed in more detail in the next section. Also some chaotic deformations could be classified (blue spots), two in Harmalière, several ones along the lake and some at the cliff of the alluvial layers E and SE of Avignonet.

The following two sections will focus in more detail on the spatial distribution of horizontal displacement vectors and the vertical component along profiles at the Harmalière and Avignonet landslides.

4.2.3.3 Displacement vectors at Harmalière

Figure 4.15 shows the vector-field of the final displacements at the Harmalière landslide. For visual purposes the original spacing was reduced from 5 m to 20 m. The length of the displacements are highly exaggerated as the displacements are very small in relation to the map extend. The scale of the displacement vector is shown in the upper left corner. This is the absolute displacement between the two dates f the Lidar-campaigns, which is 2 years and 5 months. The annual value can therefore be calculated by division with 2.4. The scale of the map can be seen from the Lambert93-coordinates at the map-frame, which are in meters. Displacements exposing a high difference of the matched kernels (stddz > 0.5 m) are shown as blue dots. Displacement results with a too low point-overlapping (pol < 80 %) or insignificant morphology (sharp $< 0.8 \cdot 10^{-5}$) are shown as red dots. The purpose of this distinction is that red indicates a lack of extractable information, which is a technical problem, but blue shows regions with chaotic displacements (e.g. superficial mass-transport), which is an information coming from the terrain.

From 95 % of the whole Harmalière landslide area displacements could be extracted, 1 % was classified as chaotic displacements and 4 % were untreatable. About 34 % of the area show minor displacements below 0.2 m, which is about the accuracy of the method. 73 % are still below half a meter displacement and only 8 % are above 1 m. These higher movements are distributed in five smaller blocks.

Block at Z1 The largest displacements are seen at Z1 in Figure 4.15. This block is about 100 m away from the NW-headscarp of Harmalière and moved perpendicular to the headscarp towards SE. Figure 4.19 gives a more detailed view of that block with displacement-vectors at every 10 m. The dimension of that block is about 200x200 m and seems to be a few degrees rotated counter-clockwise. The vertical components of the movement can be seen in the cross-sections in Figure 4.20. The profile P1 parallel to the slope is shown in (a). The uppermost diagram shows the non-exaggerated height profile with the movement vectors in the cross-section plane. The profile was computed every 2 m, but only a few vectors are shown for better visualization. Interestingly the vectors of the upper half of the block pointing slightly downwards into the ground and in the second part slightly upwards. This could indicate a rotational block. The second diagram reveals the full resolution of the derived absolute horizontal displacements. It can be subdivided in 4 parts. The first 10 m do not show any movement. The next 80 m are moved by about 0.5 - 1 m. Then the displacements going up 2.5 m with a peak movement of 3 m for about 120 m. Then the fast movement stops abruptly and decreases to a fairly constant level of about 0.25 m. The 3 diagrams below illustrate the dependency of some quality measures on the displacement and terrain. The cross-correlation coefficient of the best fit (ccmax) decreases at the positions of highest change in displacements. The standard deviation of the height difference (stddz) is very similar (in an inverse sense) to ccmax, but a better measure, because of the

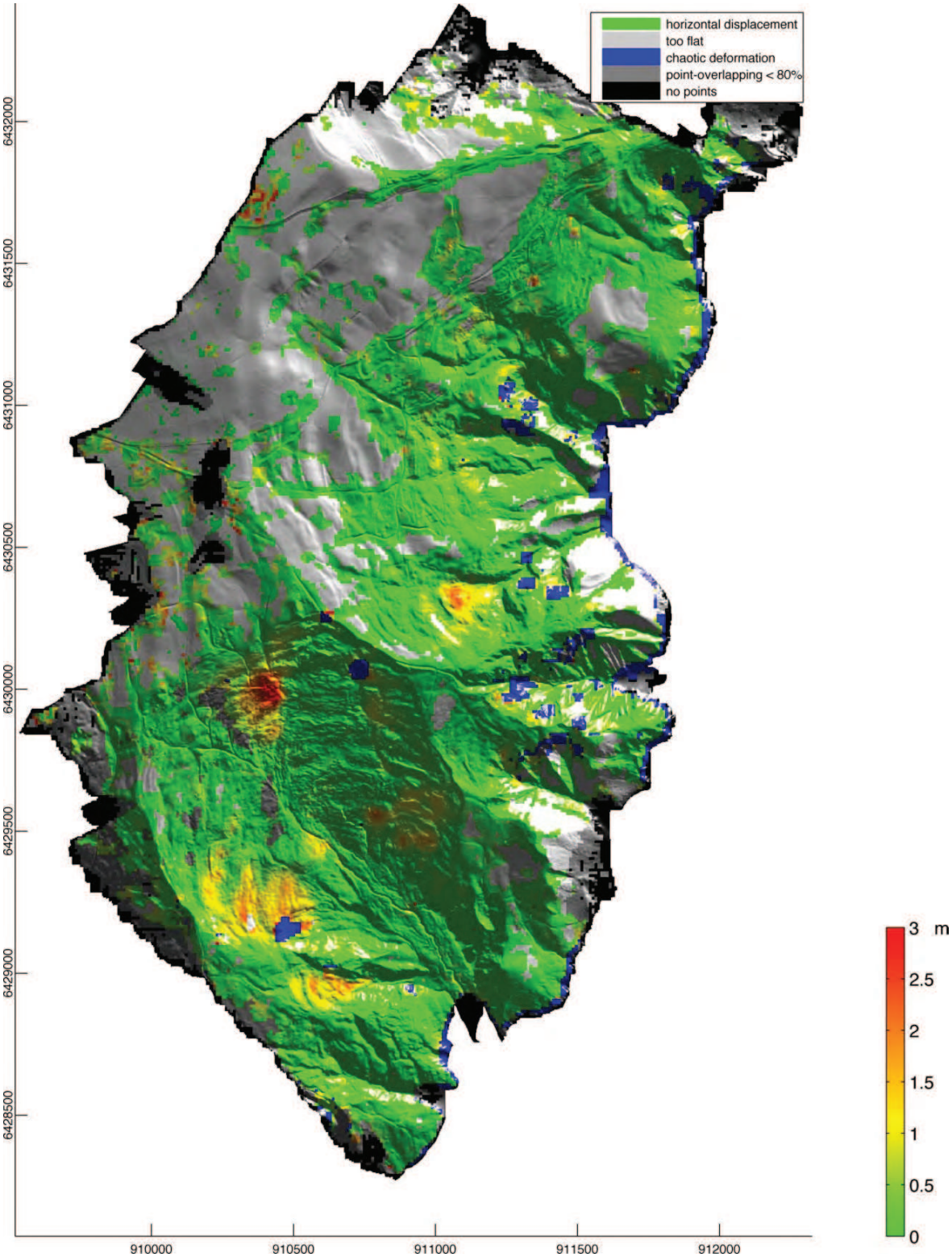

Figure 4.14: Map of horizontal displacements (at 10 m spacing) of the whole area after quality-filtering, draped on the shaded Lidar-DTM. Chaotic deformation (in blue) describes areas, where the morphology has changed too much for proper displacement extraction. Areas with insufficient point distributions of the two Lidar-sets are marked as grey. Black areas are data-holes in either one of the Lidar-sets. Coordinates are in meter in Lambert93.

independency of the search area. ccmax is always near one, depend on the correlation-coefficients in the whole search area, due to the normalization of the cross-correlation. So in later examples only stddz will be shown. As narrower the transition between different displacements as higher will be stddz, because the non-uniform distortion inside the kernel window (40x40 m) will increase the height differences. So the two peaks in the stddz-diagram are caused by the transition zone into (at 100 m) and back from (at 240 m) the fast moving block. The second peak of stddz goes up to 0.5 m which is the threshold to classify the displacement as chaotic. As this is at the border of the highest displacements of the whole Lidar-coverage, it can be assumed the threshold will not accidentally overtopped anywhere and is well chosen. The last diagram, the ellipticity (ell) of the cross-correlation matrix, is mainly related to the scarps. At a scarp the similarity is higher in scarp-direction than parallel to the slope, leading to an elongated cross-correlation matrix. The diagonally cross-section (level) in (b) shows that the moving block is slightly elevated by 3-5 m. From the corresponding displacement-diagram (dxy) it can be seen that the transition of displacements between the moving block and the surroundings is more smooth.

Block at P5 Another large area of co-directional displacements is located in the SW of Harmalière at the profile P5 in Figure 4.15. The extend is about 400x300 m and the displacements are directed towards east. In opposite to Block 1, the displacements are not as parallel, but pointing towards the outlet at P5B of a small sub-basin, favoring the presence of superficial movements (like a mudflow) prior to a larger rigid block. A look to the cross-section in Figure 4.18a supports this assumption, as the displacement-vectors are just following the slope. For a rotational block they should look more like at Block 1, pointing downwards in the upper part and upwards in the lower part. A translational block would require parallel displacements independent of the slope direction. The displacement diagram suggests a division in two parts, a smaller upper part from 25 m to 75 m and a larger part from 150 m downwards with smoothly decreasing displacements towards the bottom.

Block at P6 Just south of Block 2, along the profile P6 in Figure 4.15, seems to be a similar formation as in the previous case but smaller. This 300x100 m small valley directed towards E is separated from the main Harmalière landslide by the bulge in the north and is therefore not even necessarily part of Harmalière. The joining directions of the displacement-vectors pointing to the outlet of the small valley at P6B and the elongated shape of the slide, suggest again a more superficial mudslide as displacement mechanism. The cross-section in Figure 4.18 supports this by the parallel direction of the displacement-vectors to the slope. In addition, at the toe, the vectors pointing upwards, which could be related to a build-up of material. The dxy-diagram shows fluctuating displacements at the first 100 m, which is reflected also by the increased stddz. The next 100 m are characterized by an increase of displacements from 1 m to 2 m in 3 steps. After a fast transition towards displacements of 0.5 m the movement nearly stops towards the very end.

Block at P7 This Block is the area of fastest movements on the E-side of Harmalière. It is an area of about 200x200 m stretching from the headscarp to the main mudslide-channel of Harmalière. The cross-section in Figure 4.16a reveals displacement vectors facing mostly horizontal and parallel, suggesting the presence of translational blocks. The dxy-diagram shows variable displacements, with 0.5 m at the head, about 1 m

in the middle part and two peaks reaching almost 1.5 m. The fastest movements at the toe are related to the highest slope angle and the increased stddz at this point describes a quite turbulent movement before an almost complete stopping inside the main mudslide.

Block at P8 This block at the NE-border of Harmalière is about 150x100 m large and is with displacements of 0.5-1 m the slowest of all blocks described in Harmalière. The displacement-vectors in the cross-section in Figure 4.16b show displacements parallel to the slope in the upper half and almost horizontal displacements in the lower half. This suggests superficial movements in the upper part and translational blocks in the lower part. The upward pointing vectors at the very end are at displacements about 0.2 m and are therefore not very reliably. The dxy-diagram shows almost no movement, even about 50 m downward the headscarp. Then parallel to an increasing slope-angle the displacement goes up to 0.6 m at 80 m and after a short decrease smoothly up to nearly 1 m at the steepest point. At the end at 250 m, inside the main mudslide-channel, the displacement decreases fast down to 0.3 m.

Another interesting area is the chaotic movement at profile P2. It is already identified as an irregular "falling" block from the height difference profile (R2 in Fig. 4.4) and used for the determination of the stddz threshold to classify displacements as chaotic. Figure 4.17 gives a detailed view to the quality measures (ccmax, stddz, ell) as an representative example for such locations of chaotic displacements. The cross-section (level) shows the regular displacement vectors in black and in blue the ones which are classified as chaotic displacement due to their overtopping of stddz above 0.5 m (red line in the stddz-diagram). At those blue points, it was possible to find a best fit inside the maximum search distance (5 m), as all horizontal displacements (dxy) are below that search distance, but this best fit contains such a different morphology from the origin, that it is not even likely to be the same. A further discussion about the advantages and disadvantages of the displacement extraction method and the significance of the quality measures can be found in Section 4.2.4.

Finally the cross-section P9 shows the displacements along the main mudslide-zone of Harmalière from the headscarp (P9T) down to the lake (P9B). The vector-field in Figure 4.15 does not show any movement inside these zone, which is surprising and not expected when looking at the geomorphology map (Fig. 3.21). The more detailed cross-section in Figure 4.16c shows displacements (dxy) between 0.2-0.4 m. The displacement-vectors in the cross-section (level) pointing upwards in the upper half of the profile, but due to the low displacements of about 0.2 m, this is not reliable. An explanation could be, as we include the "low-vegetaion"-class, a growth of low vegetation, which raises the elevation and not altering the morphology very much. The peaks of horizontal displacement at 850 m, 1100 m and after 1300 m are occurring at the points where the profile crosses the incised stream. Together with the displacements there also going in irregular directions, it could be just erosion effects of the stream on its banks, which is than "tracked" as displacement.

4.2.3.4 Displacement vectors at Avignonet

Figure 4.21 shows the vector-field of horizontal displacements at the Avignonet landslide. The displacements are displayed with a spacing of 30 m and it should be highlighted, that the length of the displacement vectors are about 4 times longer relative to the ones on Harmalière (Fig. 4.15). This is due to the overall lesser activity of Avignonet and the smaller scale of display. The Lambert93-coordinates at the border

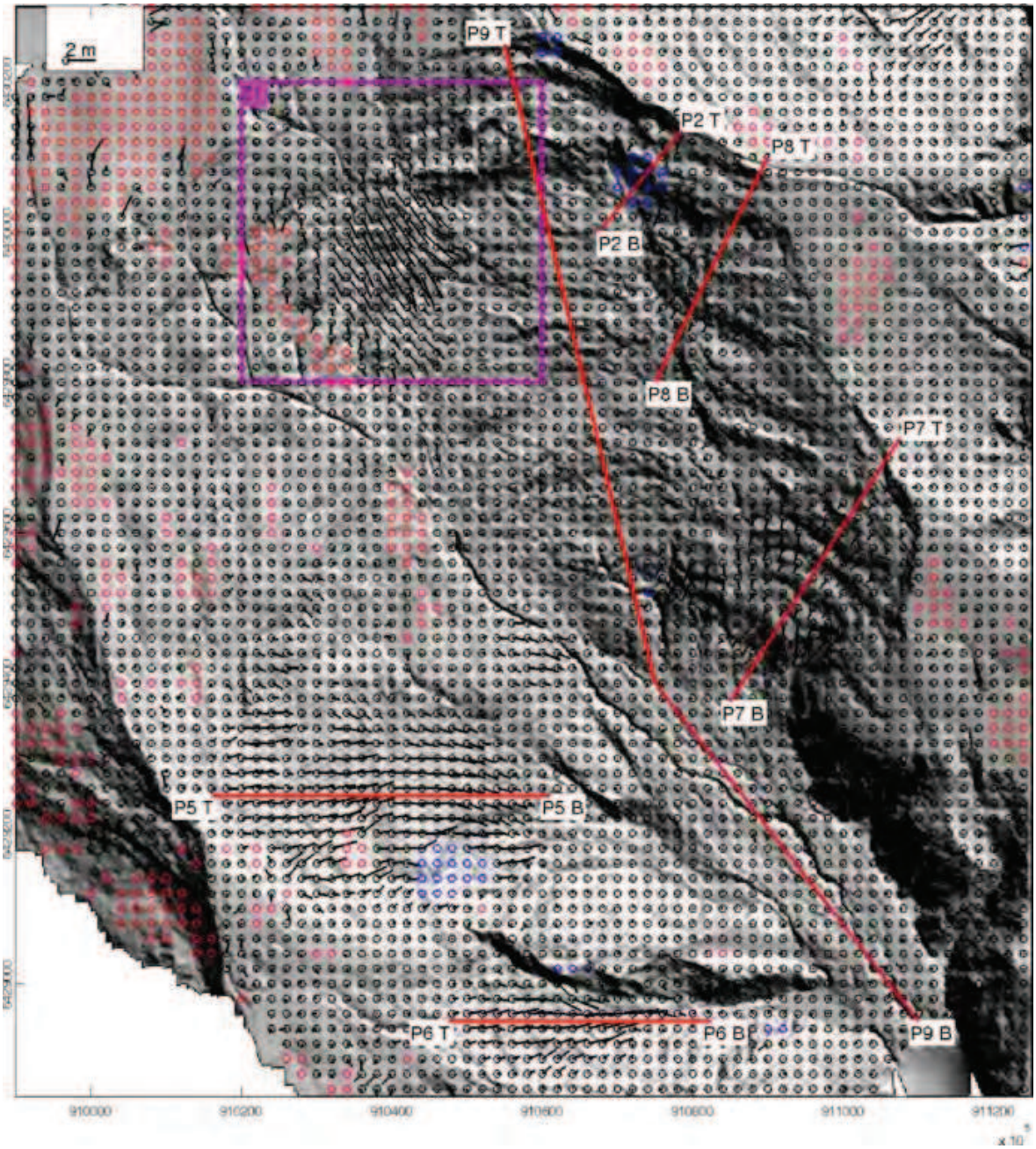

Figure 4.15: Map of horizontal displacements (at 20 m spacing) of the Harmalière landslide after quality-filtering. The displacement vectors are draped on the shaded Lidar-DTM. Blue dots are points with chaotic displacements (stddz > 0.5 m) and therefore no meaningful displacement. Areas with insufficient point distributions (pol < 80 %) or to smooth morphology (sharp < 0.8) are marked as red dots. The region Z1 is shown in higher detail in Figure 4.19. The red-lines are Profiles, which are shown on the following figures. "P" for profile, "T" and "B" for top and bottom, "L" and "R" for left and right when looking uphill. Coordinates are in meter in Lambert93.

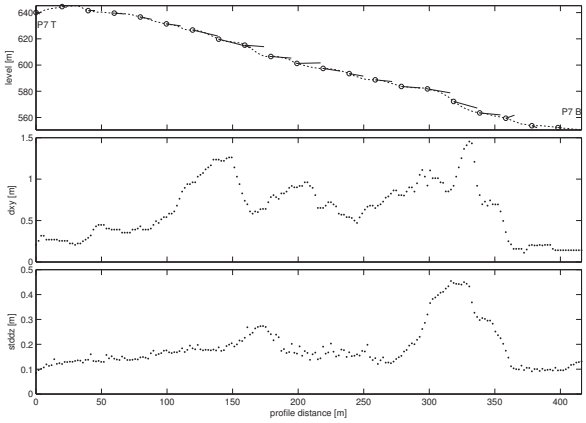

(a) P7

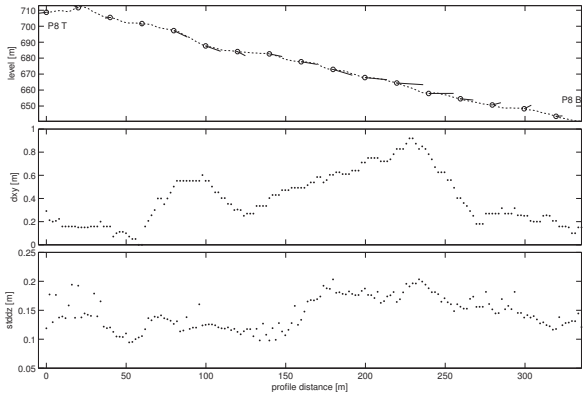

(b) P8

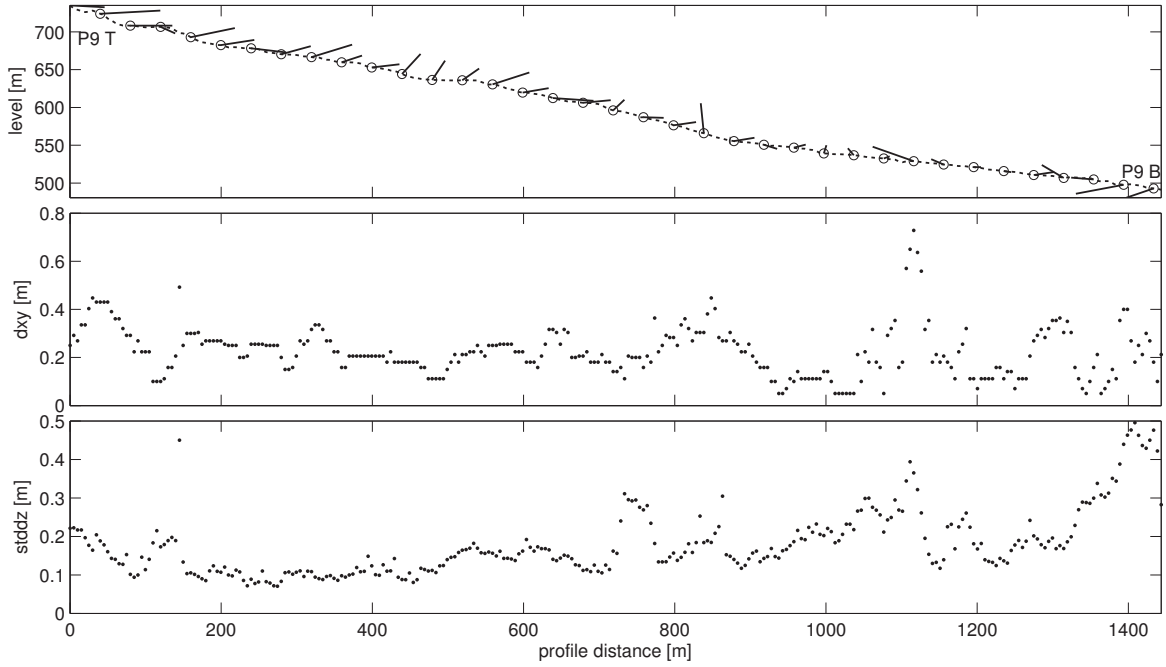

(c) P9

Figure 4.16: Profiles P7 and P8 at the E border of the Harmalière landslide and P9 along the main mudflow channel. Locations are shown in Figure 4.15 on the left page. Note the different scales of the displacement vectors due to different ranges of dxy.

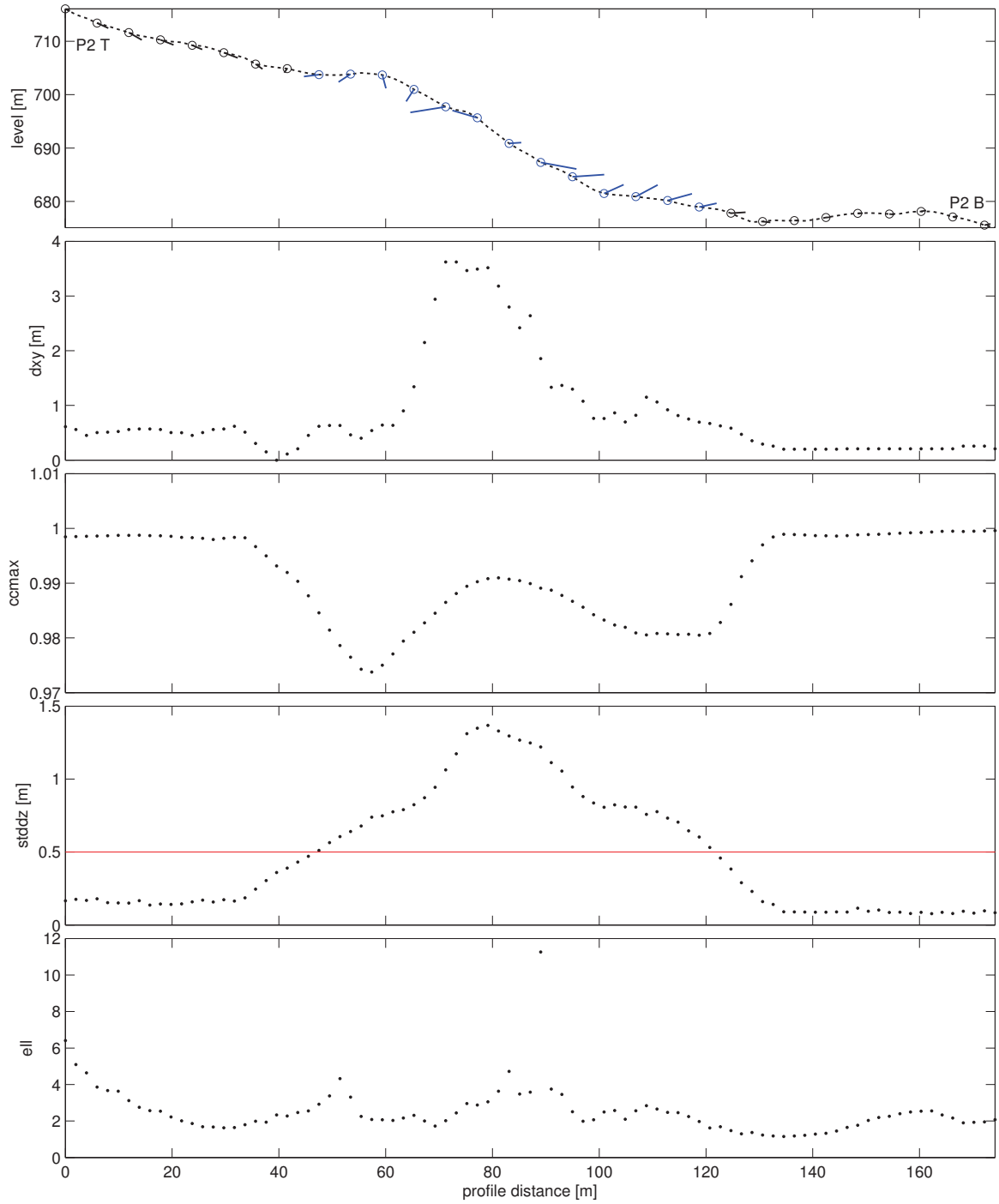

Figure 4.17: Profile P2 at the headscarp of Harmalière showing the variability of quality measures at a location with chaotic displacements. Locations are shown in Figure 4.15. Profile is from top (P2 T) to bottom (P2 B) along the slope direction.

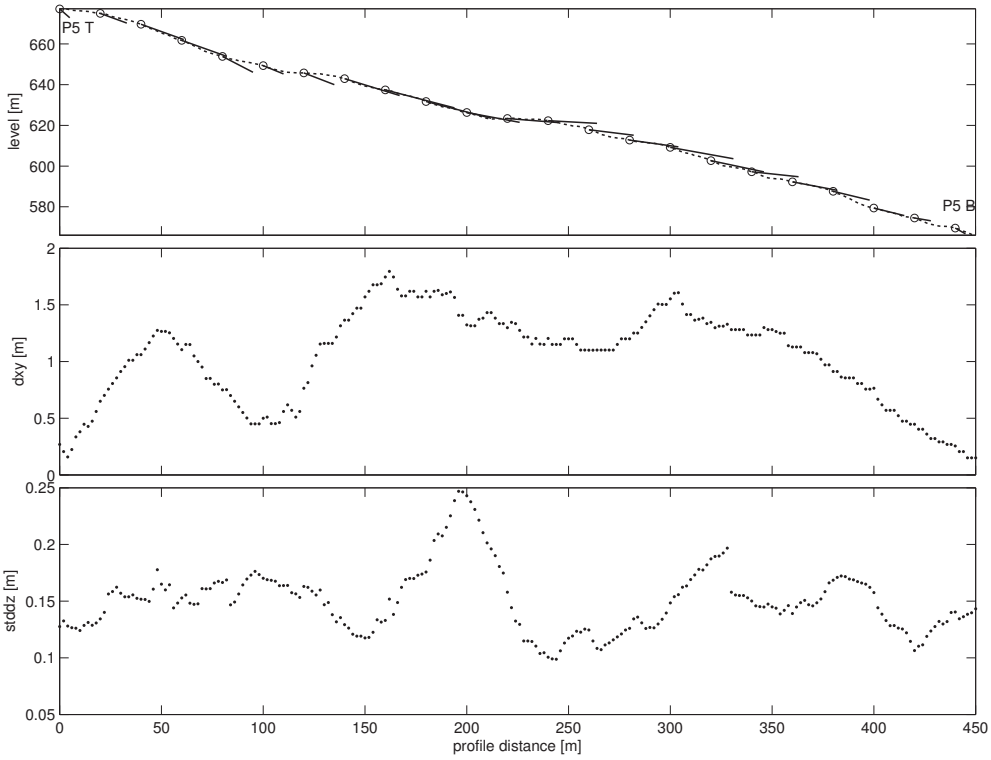

(a) P5

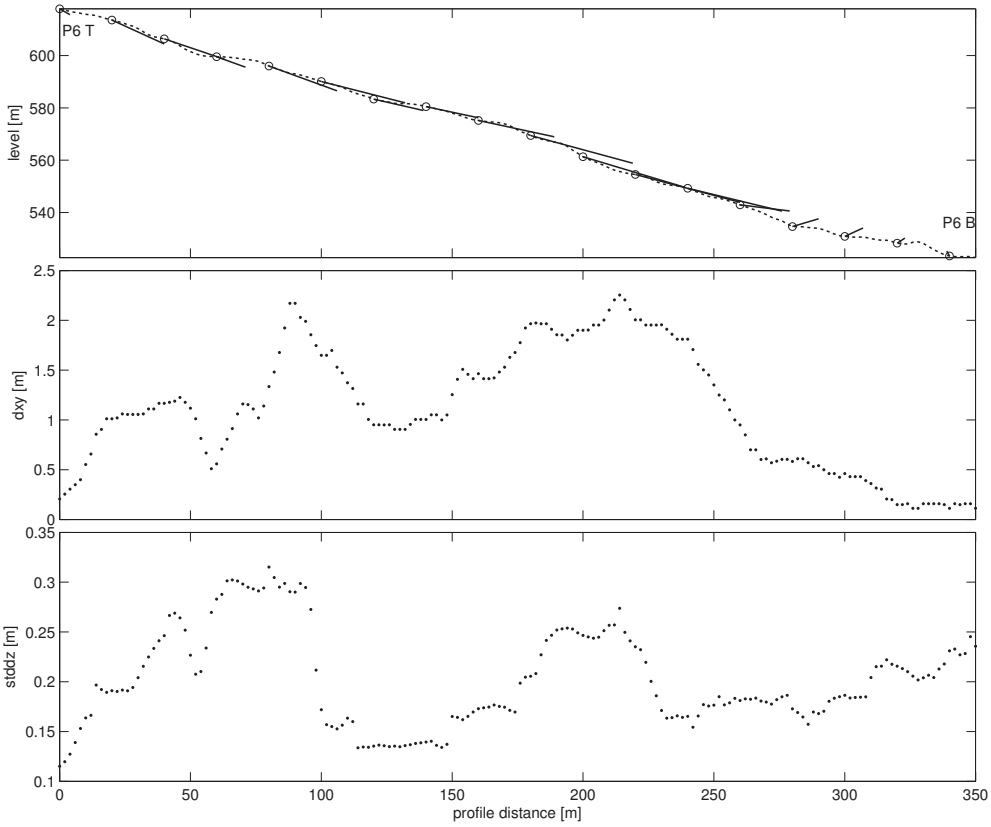

(b) P6

Figure 4.18: Profiles P5 and P6 in the SW of Harmalière showing displacements at active regions. Locations are shown in Figure 4.15. Profile are from top (P5,6 T) to bottom (P5,6 B) along the slope direction.

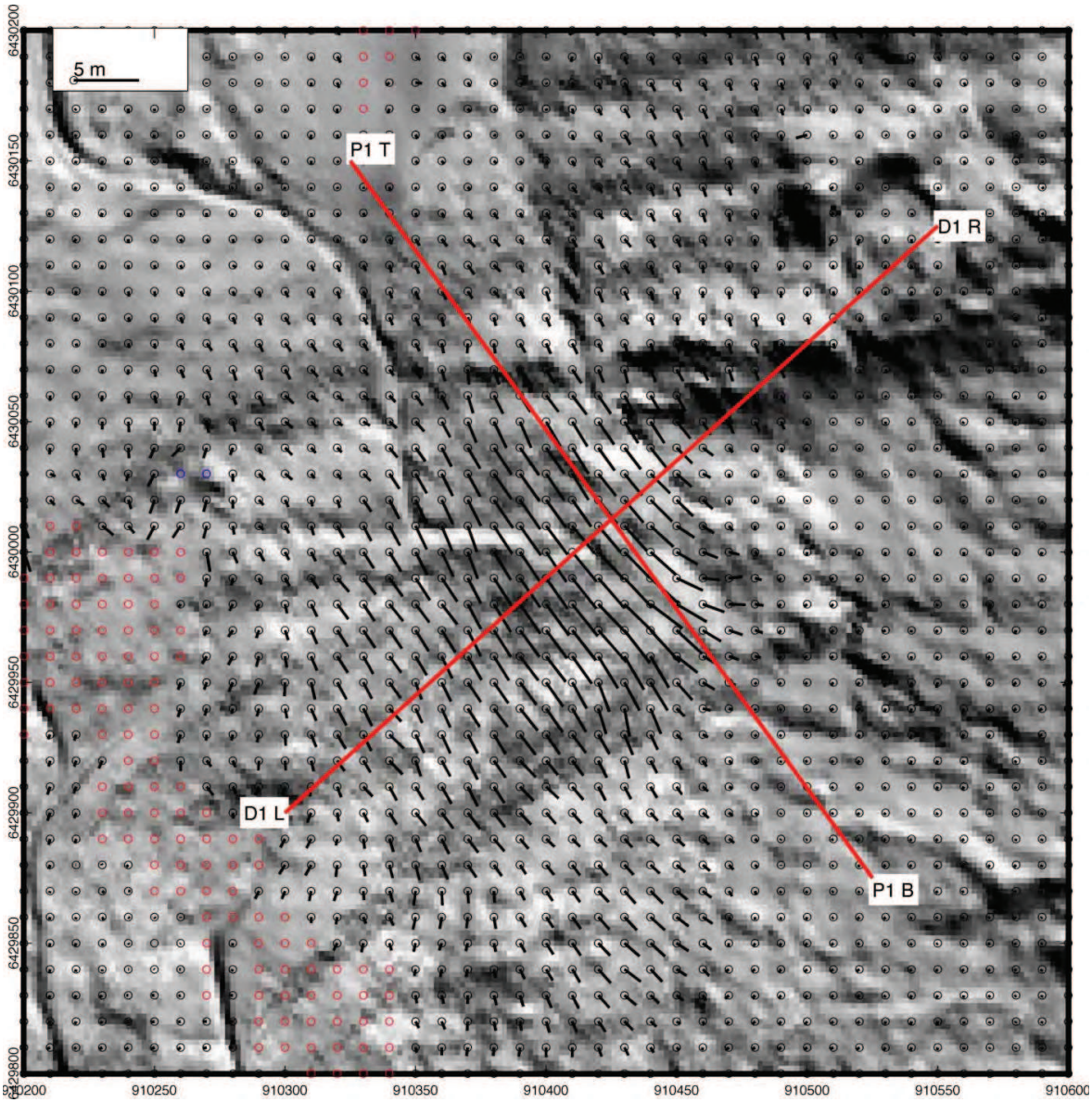

Figure 4.19: Zoom on horizontal displacements at the most active part of the Harmalière landslide near the N-headscarp. The location is shown as Z1 in Figure 4.15 The red lines are the locations of the profiles on the right page (Fig. 4.20). Coordinates are in meter in Lambert93.

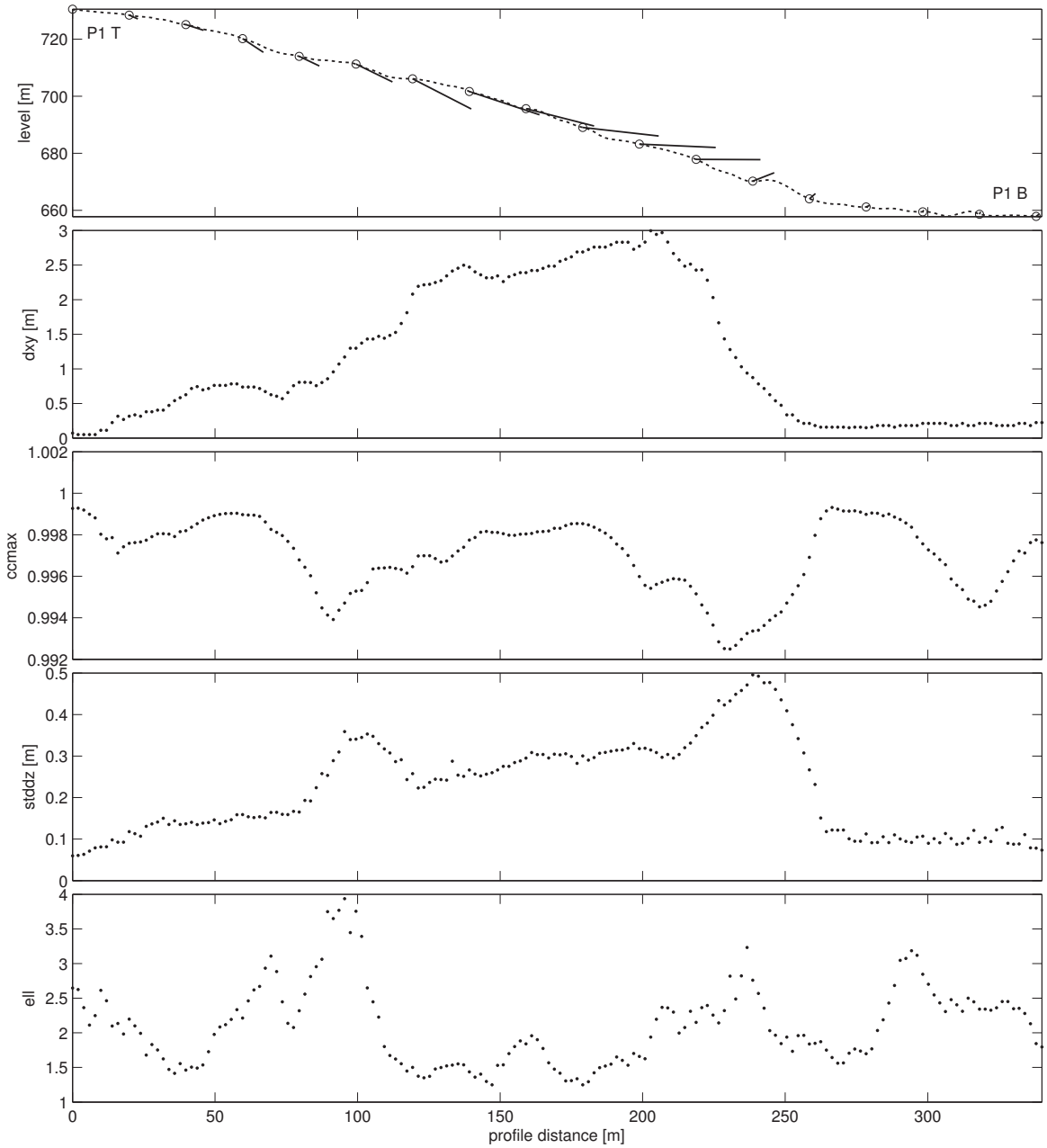

(a) P1

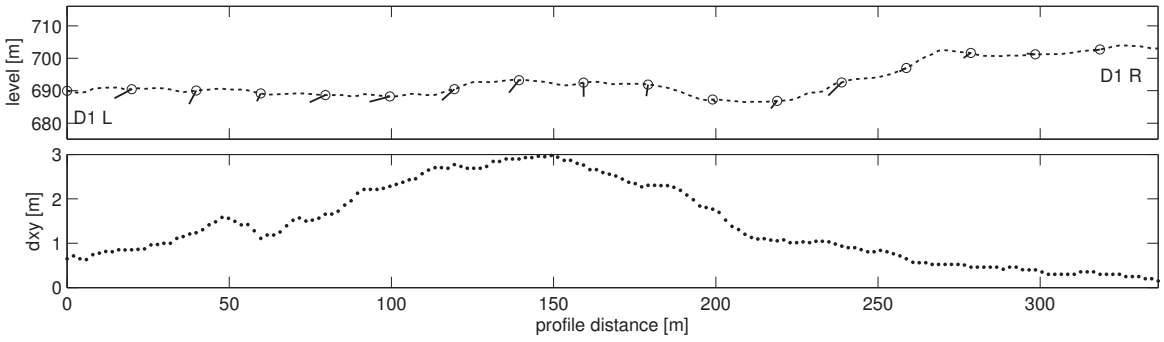

(b) D1

Figure 4.20: Profiles P1 (top-down) and D1 (diagonally). Locations are shown in Figure 4.19 on the left page. (a) Profile from top to bottom along the slope direction. (b) Profile from left to right looking uphill.

are meters. Due to the smaller displacements and therefore the more smooth morphology, amplified by the smoothening due to farming, the quality of the displacements at Avignonet are much less than in Harmalière. As seen in the displacement map, the upper part of Avignonet is for the major part too smooth (red dots) to derive reliable displacement-vectors. Therefore the analysis is concentrated in the lower and more active part of Avignonet. In order to evaluate the displacement vectors, the GPS-measurements (see data-set A.5) are plotted side-by-side in green, highlighted with grey circles and annotated with the point-ID. Unfortunately the data-sets are not directly comparable as the GPS-displacements are only available until 2006 and the Lidar-sets are from 2006 and 2009, so the GPS-vectors are projected displacements over the time between the Lidar-campaigns (averaged annual displacements multiplied by $2.4 = 2$ years and 5 months). However, the GPS-measurements indicate mainly continues displacements and are therefore suitable as reference. Besides the overall noise of the displacement-vectors, three areas with continues patterns can be recognized and will be described more detailed. These three active parts are grouped and directed towards 3 channel like outlets towards the lake.

Active part in the south of Avignonet In the south of the Avignonet landslide, along the profiles P4 and D4 in Figure 4.21, a block of about 300x200 m shows movements towards NE, leading into a narrow outlet. The cross-section in Figure 4.22 two minor scarps. At the upper scarp (50-80 m) the displacement vectors are unreliable (red) due to a low point-overlapping (pol) as the other cause for red vectors of a high stddz > 0.5 m does not apply here. The dxy-diagram reveals low displacements of about 0.5 m after the first scarp (80-140 m) and displacements up to 2.3 m after the second scarp at 170 m. From there until the end they are decreasing continuously down to 0.5 m. Besides the unreliable peak at the beginning, the stddz shows two peaks at the steepest flanks of dxy-change. The ellipticity (ell) images the two scarp at 60 and 120 m and shows an increase at the end, probably due to the channel morphology there, leading to matching uncertainties in channel direction (the inverse case of scarps). The diagonally cross-section in Figure 4.22 exhibit the concave shape of the active region and the highest displacements at the lowest part.

Mas d'Avignonet Figure 4.23 shows the enlarged area indicated as Z2 in the overview map of Avignonet (Fig. 4.21). The displacement-map seems to be quite complex and erroneous. However, the northern half seems to be more active than the southern part. The GPS-displacements are mostly comparable with the Lidar-displacements. Some problems seem to exist at point 45 with highly varying displacements in the vicinity.

Looking at the cross-section thru the village Mas d'Avignonet P10 in Figure 4.24, it can be seen that from 100-320 m the vectors pointing into the ground with very low displacements around 0.1-0.2 m and the last 50 m they pointing upwards the ground with higher displacements at 0.5 m. This suggests a rotational slide, but is very unreliable due to the low displacements. In the upper part of the profile at 60 m, where it crosses the road, higher displacements directing southwards which seems very unlikely. The elevated ellipticity at this point reveals the linearity of the road structure and could explain the derived displacements in that direction. However, if the sharpness (sharp) in that direction would be too low, it would have been sorted out by the quality-filtering. This indicates, that probably the sharp-threshold is to low in that case and other parts at Avignonet which show equally erogenous displacements.

The cross-section P11, also indicates a rotational block by displacement-vectors pointing into the ground in the upper half and pointing more upwards in the lower part. Also the decrease of displacement between this two zones could be explained by the rotational center of the block. The maximum displacements goes up to nearly 0.7 m.

Gorge outlet N Avignonet Figure 4.25 gives the detailed vector-field of the active area at the gorge outlet in the northern part of Avignonet indicated as Z3 in Figure 4.21. Besides some erroneous displacements in the NW corner, again associated with the road, the map looks quite reasonable. The displacements pointing in general towards the outlet at the gorge and show larger movements at steeper slopes. The GPS-points 11, 12, 21 and 22 are in very good agreement with the Lidar-displacements. Interestingly, only looking at the GPS-displacements would suggest a quite stable area in the SW of the map, which is not the case when looking at the Lidar-displacements. The displacements are increasing just a few meters away from the GPS-points. At the GPS-points 1, 2 and 3 the agreement is quite bad. Point 1 is surrounded by non-reliable Lidar-displacements, so the remaining Lidar-displacements are likely just below the threshold contain also larger errors.

Near the top of profile P13 is a bundle of large displacements facing the opposite direction than the surrounding displacements pointing upslope. Looking at the cross-section in Figure 4.26a, the sharpness (sharp) is going down very near to the threshold of $0.8 \cdot 10^{-5}$. So the area is prone to mis-match due to a smooth terrain. Also this area is a camping-site with variable structures which could have lead to the large mis-matches.

The profile P14 is going down a slope which is divided in three major steps. Looking at the cross-section and dxy-diagram in Figure 4.26b, only the middle block seems to have moved about 0.6 m, the upper and lower are relatively stable. But the displacement-vectors in the overview-map just south of P14T do not approve this impression from the profile as there are movements above 0.5 m.

Finally the profile P12 starts at erroneous displacements, crosses the road and directly goes down a slope with increased displacements. Figure 4.27 shows the corresponding cross-section and diagrams. The large erroneous displacements in the uppermost part above the road before 80 m, does not show up in the cross-section as they pointing perpendicular to the profile plane, but the displacements are seen in the dxy-diagram. A hint for the mis-matching behavior of the displacement-extraction could be the low sharpness (sharp), but other plausible looking parts of the profile show the same low sharpness. It is not clear how to detect those mis-matching displacements without loosing presumingly correct results. The road at 80 m seems to be fairly stable showing only displacements below 0.1 m. But at the slope just below the road, the displacements climb to 0.7 m until the end of the profile.

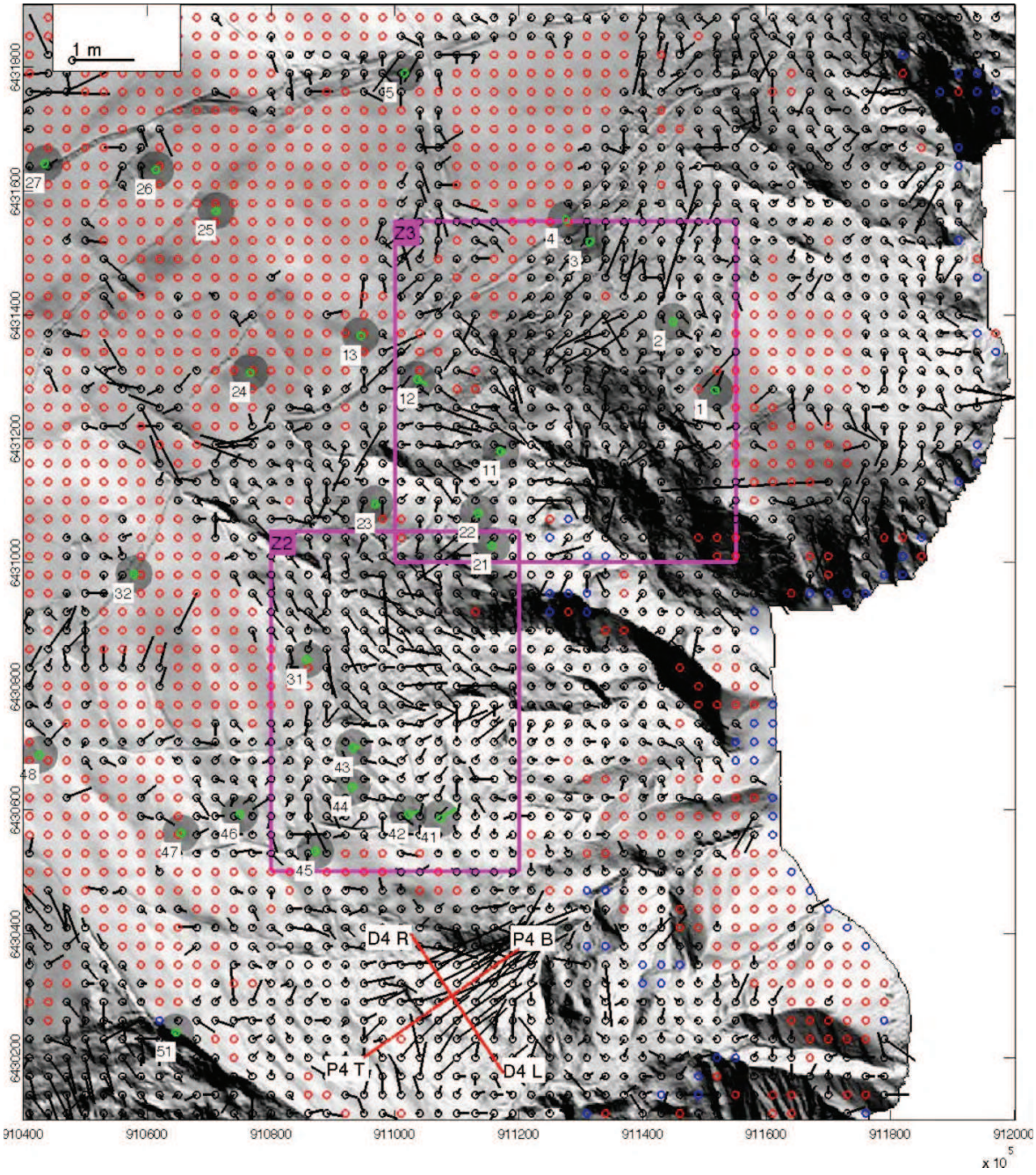

Figure 4.21: Map of horizontal displacements (at 30 m spacing) of the Avignonet landslide after quality-filtering. The displacement vectors are draped on the shaded Lidar-DTM. Blue dots are points with chaotic displacements (stddz > 0.5 m) and therefore no meaningful displacement. Areas with insufficient point distributions (pol < 80 %) or to smooth morphology (sharp < 0.8) are marked as red dots. The regions Z2 and Z3 are shown in higher detail in the Figures 4.23 and 4.25. The red-lines are Profiles, which are shown on the right page in Figure 2.26d. "T" and "B" for top and bottom. The grey highlighted green displacements are based on GPS-measurements (see Appendix A.5). Coordinates are in meter in Lambert93.

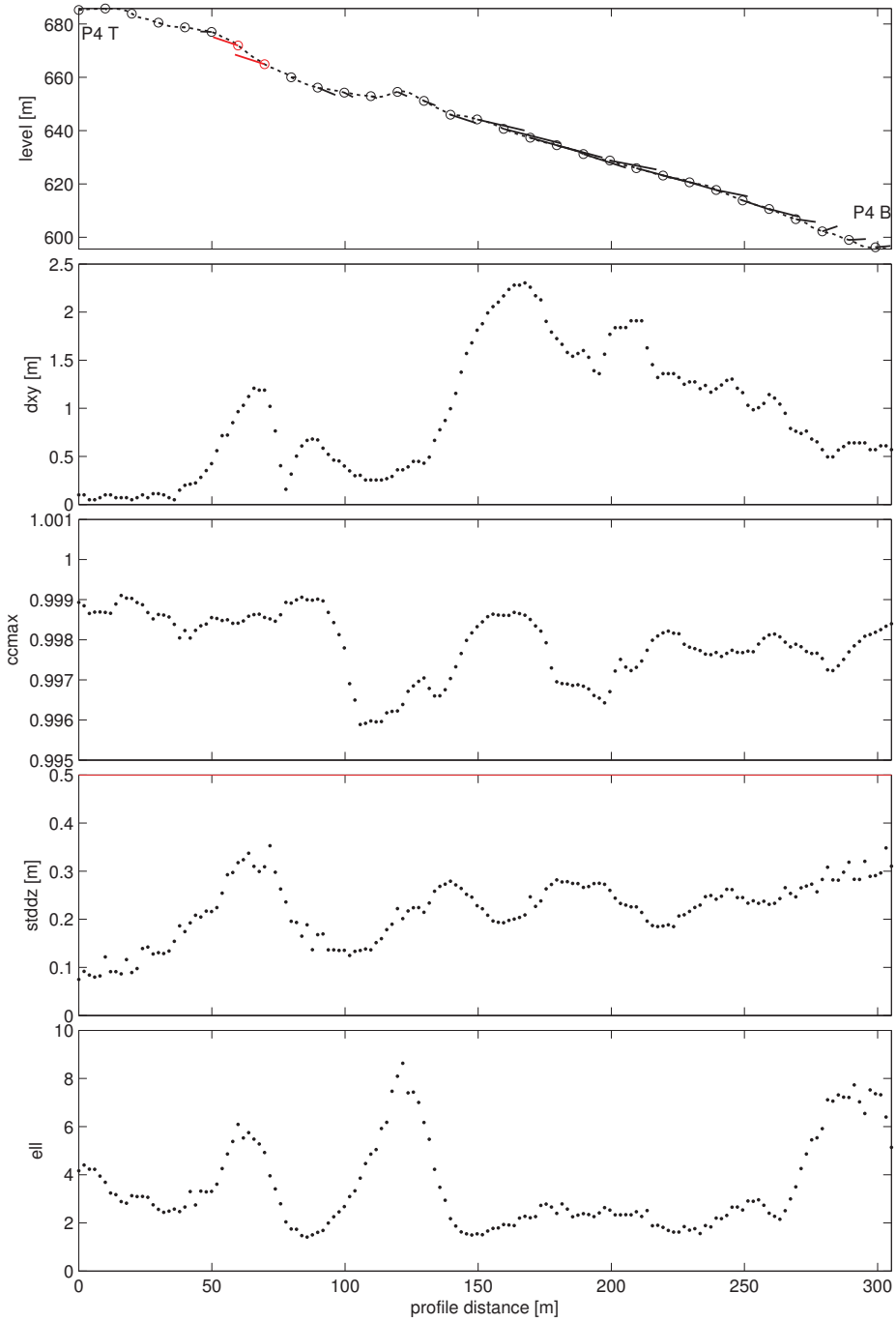

(a) P4

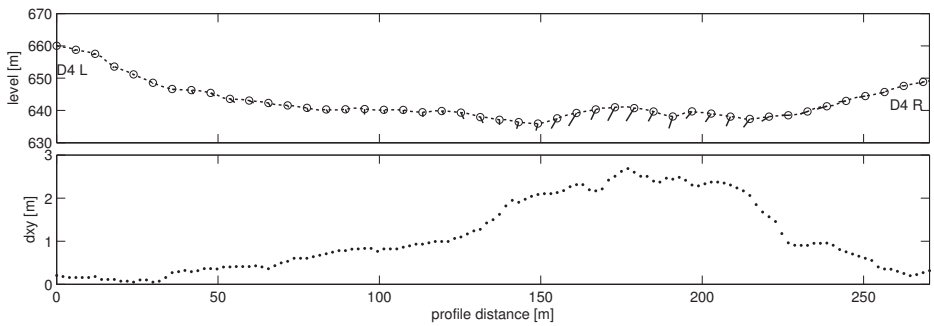

(b) D4

Figure 4.22: Profiles P4 and D4 thru the most active part of Avignonet in the S. Locations are shown in Figure 4.21 on the left page.

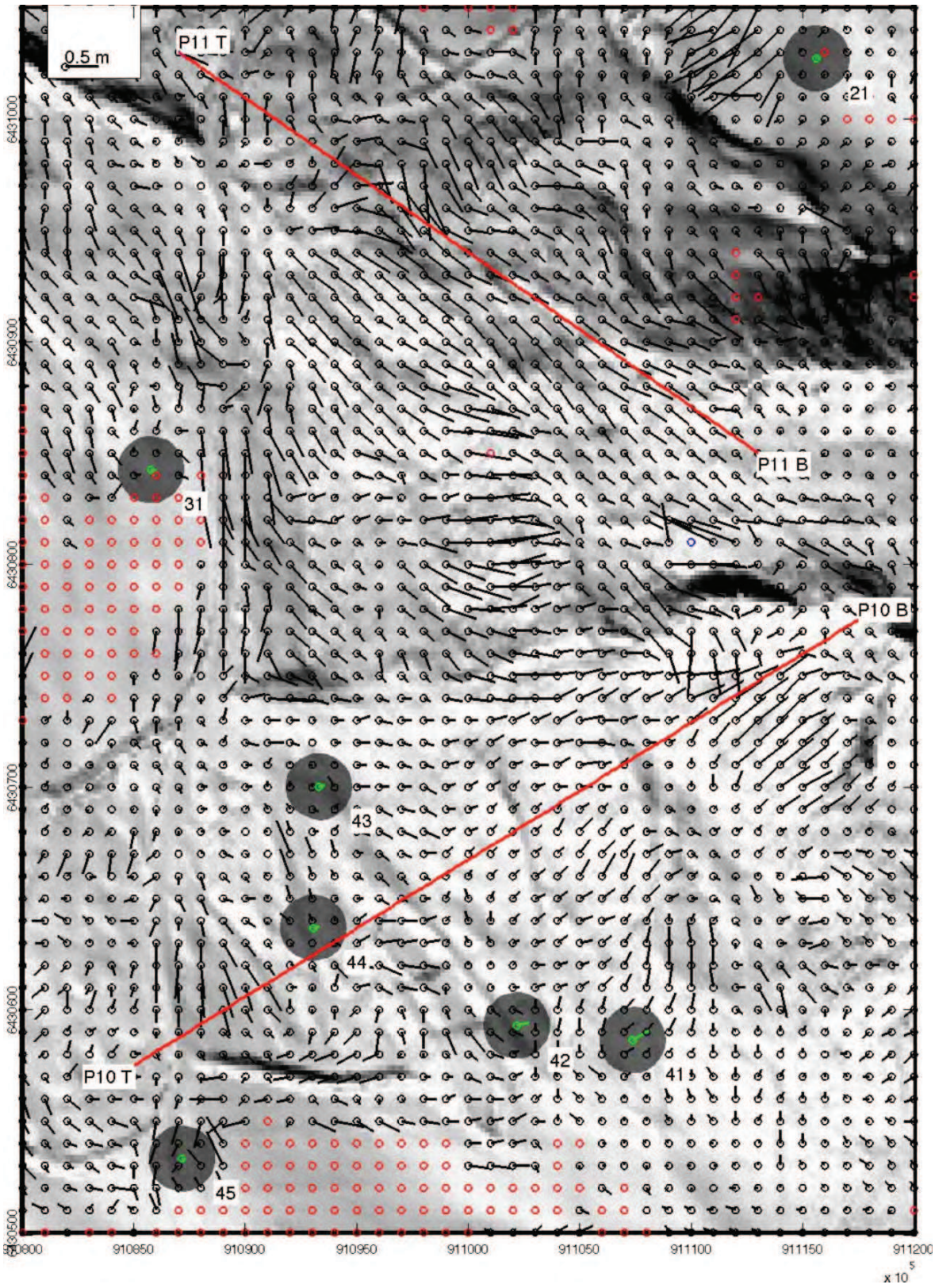

Figure 4.23: Zoom on horizontal displacements at the village Mas d'Avignonet. The location is shown as Z2 in Figure 4.21 The red lines are the locations of the profiles on the right page (Fig. 4.24). Coordinates are in meter in Lambert93.

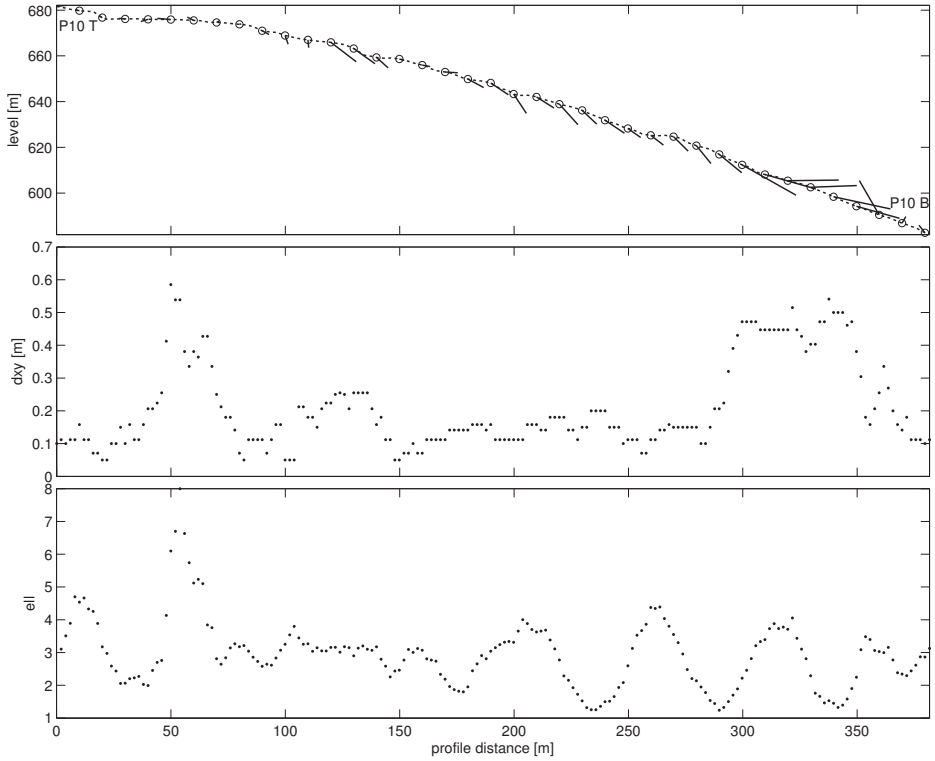

(a) P10

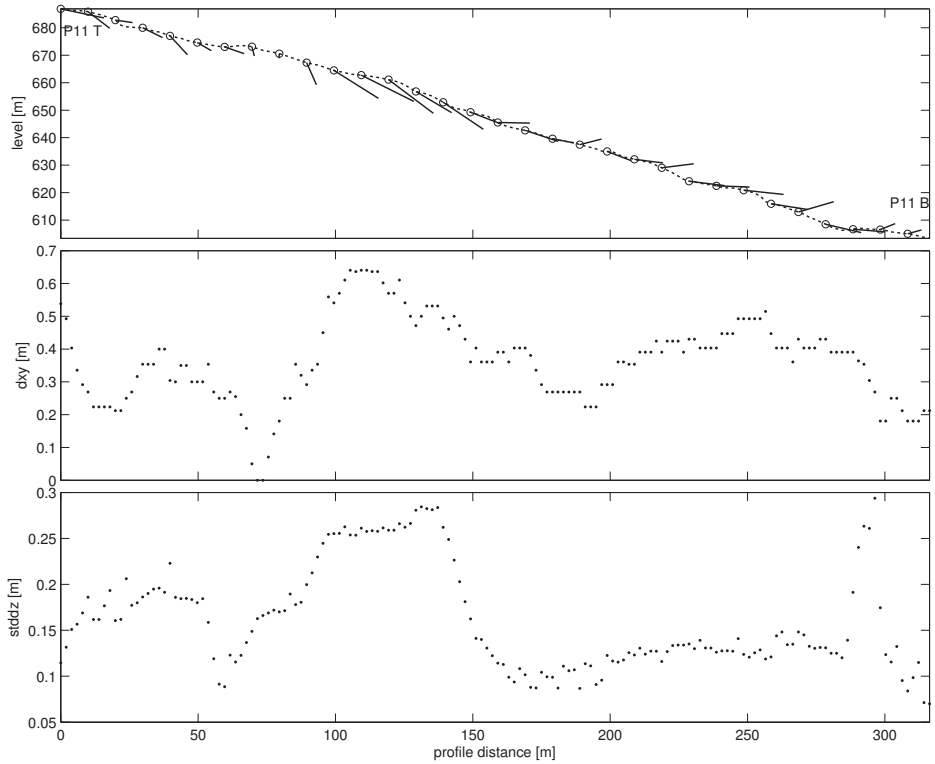

(b) P11

Figure 4.24: Profiles P10 and P11. Locations are shown in Figure 4.19 on the left page. (a) Profile from top to bottom along the slope direction. (b) Profile from left to right looking uphill.

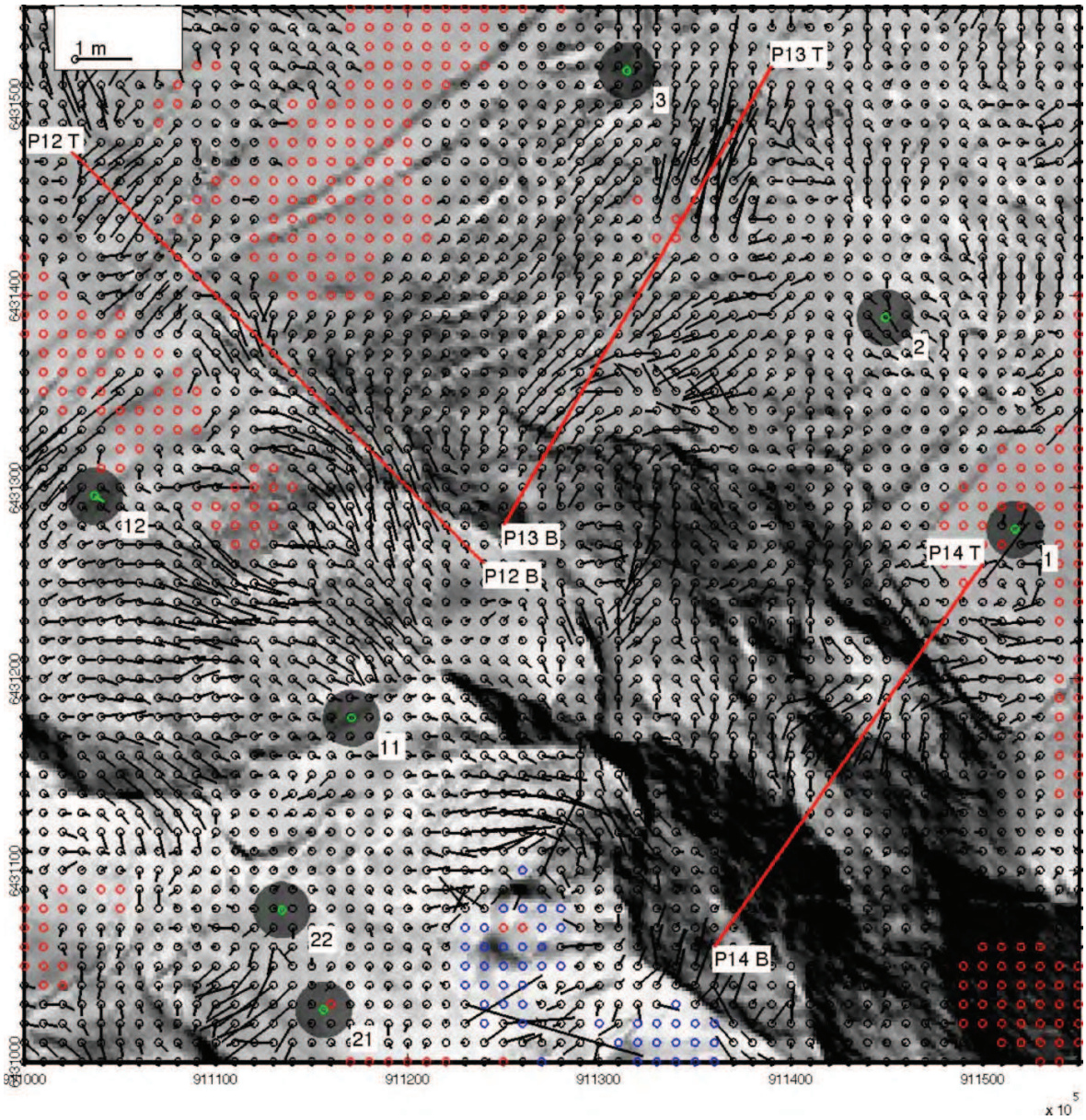

Figure 4.25: Zoom on horizontal displacements at the northern active region on the Avignonet landslide. The location is shown as Z3 in Figure 4.21 The red lines are the locations of the profiles on the right page (Fig. 4.26) and on Figure 4.27. Coordinates are in meter in Lambert93.

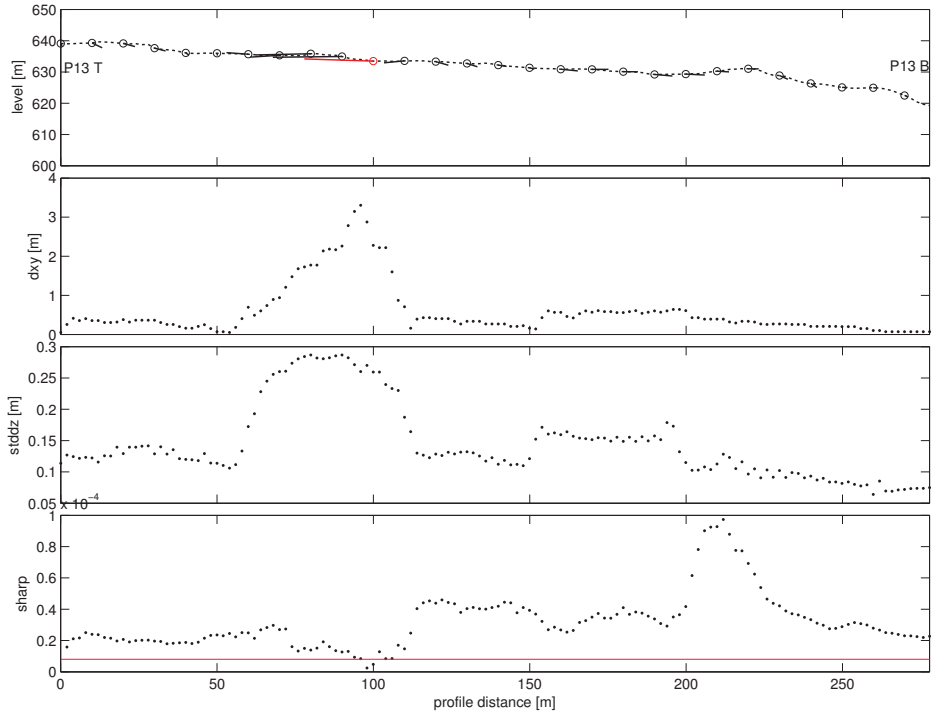

(a) P13

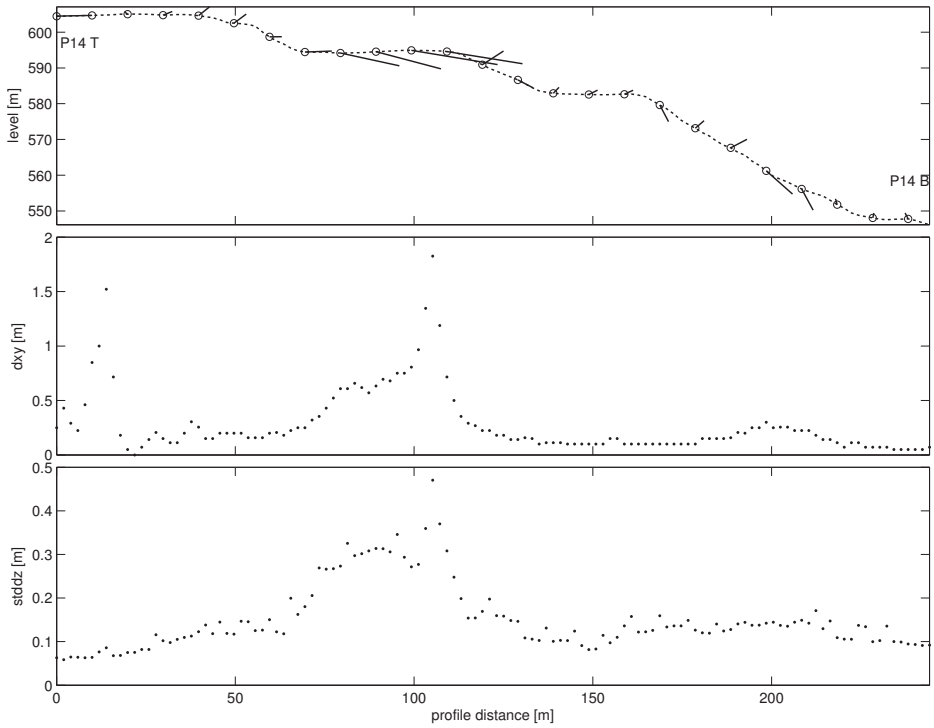

(b) P14

Figure 4.26: Profiles P13 and P14. Locations are shown in Figure 4.25 on the left page. (a) P13. (b) P14.

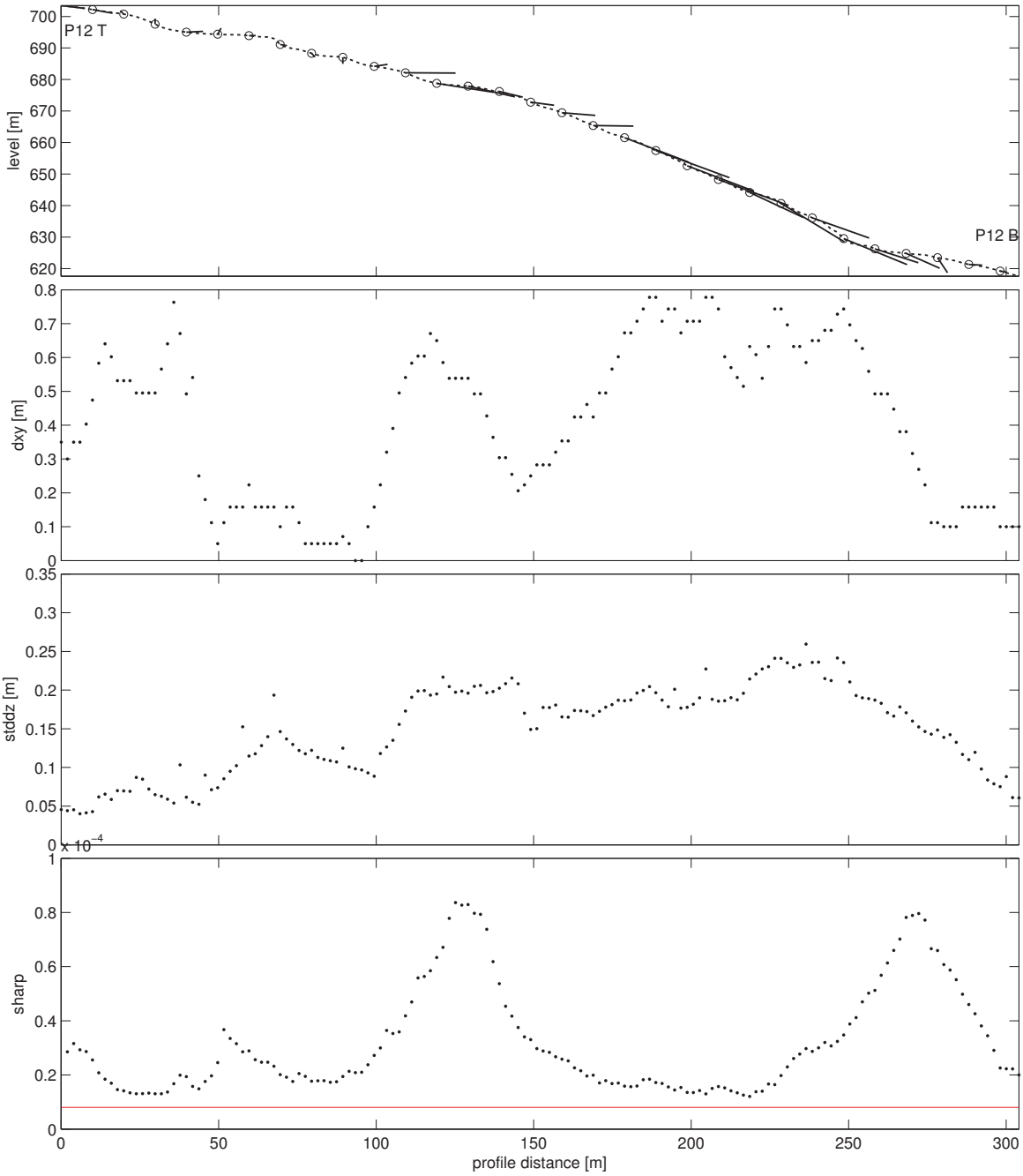

Figure 4.27: Profile P12 at the headscarp of Harmalière showing the variability of quality measures at a location with chaotic displacements. Locations are shown in Figure 4.25. Profile is from top (P12 T) to bottom (P12 B) along the slope direction.

4.2.4 Discussion

Displacements between two aerial Lidar-sets of the Avignonet and Harmalière landslide could be obtained. The derived accuracy is about 0.2 m at its best, but varies with the complexity of the morphology and the point-cloud densities. Also the vertical component could be extracted by using the height difference of the matched kernels. The advantage to direct measurements on the ground like permanent or repeated GPS-measurements or extensiometers are the spatial distribution. However the accuracy is not as high and the temporal resolution is also limited by the costs per Lidar-campaign, but the accuracies will raise and the costs will decrease with future technological progress. Also no direct access is needed for the monitoring, which could be essential in tough terrain or fast moving landslides. Compared to the extraction from aerial photos, the advantages are the ability of filtering vegetation and the direct access to the coordinates of the point cloud. Aerial photos are always in need of an extra DEM for ortho-rectification and ground control points for a proper georeferencing. On the other hand, the extraction is assumed to be much better at smooth terrain, because it will be based on intensities (or colors) instead of morphological features. This means, aerial photos are a potential good replacement in areas where the Lidar-DTM extraction does not work satisfactory due to insignificant morphologies. The potential weaknesses of the Lidar-DTM extraction method are the loss of information at the gridding step, the inability of detecting movements in smooth terrain and the evaluation of the accuracy of the results. The loss of information during the gridding is due to two facts, first the transformation from 3D to 2D will average vertical formations, and second the resolution will be finite which can finally influence the extraction at sharp edges. The lack of robustness in smooth terrain can not easily be solved, as only higher point densities and higher resolutions could lead to significant morphologies at smaller scale, but would decrease the signal/noise-ratio of the Lidar-measurements (accuracy approx. 10 cm). Consequently, displacements of too low robustness should at least effectively sorted-out by reasonable criteria. In order to find suitable thresholds for the quality measures, a reference area should be included in the Lidar-coverage preferable containing all different kinds of occurring terrain-types and no displacements or well known displacements for the examined time-period. This is necessary for a proper statistical analysis to determine error-ranges and thresholds for recognizing mis-matches.

Another problem for the interpretation of vertical displacements could come from erosion and accumulation of material. If this change is relatively small or the erosion/accumulation is very regular throughout the kernel size, the match will be robust, but the vertical component, defined by the average difference between the kernel heights, will be altered. This concerns especially the case when interpreting displacevectors in cross-sections as indicators for rotational blocks, because erosion at the top of the slope would lower the vertical component resulting in vectors pointing into the ground and accumulation at the bottom of the slope would raise the vertical component and lead to vectors biased upwards. As an example the following calculation can be made in profile P1 (Fig. 4.20a) for the fourth vector from the top, which points into the ground. The horizontal component (dxy) is 0.74 m and the vertical component (dz) is -0.48 m, resulting in a vector pointing downwards at 33°. The slope angle is 19°. The difference is 14°, which is the downward orientation of the vector relative to the ground. How much regular erosion over the kernel area (20x20 m) would be needed to explain this downward orientation? The vertical component would have needed to be decreased by 0.23 m, which would be equivalent to an erosion rate of about 10 cm per year. This can be seen as the lower limit of the problem, as in the most other cases the

displacements are larger and/or the difference to the slope-direction is bigger. As erosion usually increases with steeper slopes and accumulation appears at gentler slopes, the said angle-difference would correlate with the slope-angle. Also, as erosion and accumulation is mostly not spatially equal distributed especially in rough terrain, this effect would show up in the stddz-value.

Finally some ideas can be given, how the extraction of displacements from Lidar point clouds could be improved:

1. The Lidar point-clouds usually contain also the intensity, which could be included in the cross-correlation to improve the quality of matches between kernels. To improve the process, the already described quality-measure or new ones could be used to weight the match based on the DTM and the match based on the intensity in order to use the best combination of both depend on the terrain-type. For example in smooth terrain the match could be more judged by the intensity correlation and in rough terrain more by the DTM correlation.

2. The DTM cross-correlation could be extended to affine matches, allowing for scaling, rotation and shearing. This would lead to lower stddz-values in transition zones between stable and unstable blocks and give direct information about affine deformations of blocks. However, the computation-time would be extremely increased, without serious efforts in code-optimization.

3. The horizontal displacement extraction can be based, instead of the direct height-values, on derivatives of the DTM, like the gradient or the shaded relief to be independent of the absolute height.

4. During the development of the displacement extraction software, instead of the normalized cross-correlation (NCC), also the discrete Fourier-transforms (DFT) were used to obtain the correlation matrix in order to increase the speed of the cross-correlation and to be able to derive subpixel displacements using the whole kernels, not only the upsampled correlation peak. But as this approach is highly sensitive to general slopes, which leads to correlation peaks at the highest absolute elevations, the derived displacements were not satisfying. Also the use of detrended kernels by removing linear or polynomal surfaces could not avoid those mis-matches. This path of using the DFTs could be approached by either using derivatives of the DTM as proposed in the previous point or by incorporating a normalization in the cross-correlation of the DFTs.

5. Another approach is to extract the displacements directly from the 3D-point clouds by finding a method describing the similarity between point-clouds and using a kernel cube to find the best fit inside a search cube. Or simple geometries (planes, cubes, lines, curved planes, corners etc.) could be fitted in both point-clouds to calculate the deformation parameters between them. For example Figure 4.28 shows a perspective view of the Lidar point-cloud at the village Mas D'Avignonet and a fitted plane in one of the roofs. By doing so in both Lidar-sets the displacement perpendicular to the plane could be extracted. By using nearby planes with different orientations the displacements could be combined to a 3D displacement. The used software for this example is LidarViewer[2]

[2]LidarViewer-2.5 developed by C. Bowles and O. Kreylos at the Computational Science and Engineering division of the UC Davis (`http://wiki.cse.ucdavis.edu/keckcaves:lidar_viewer`)

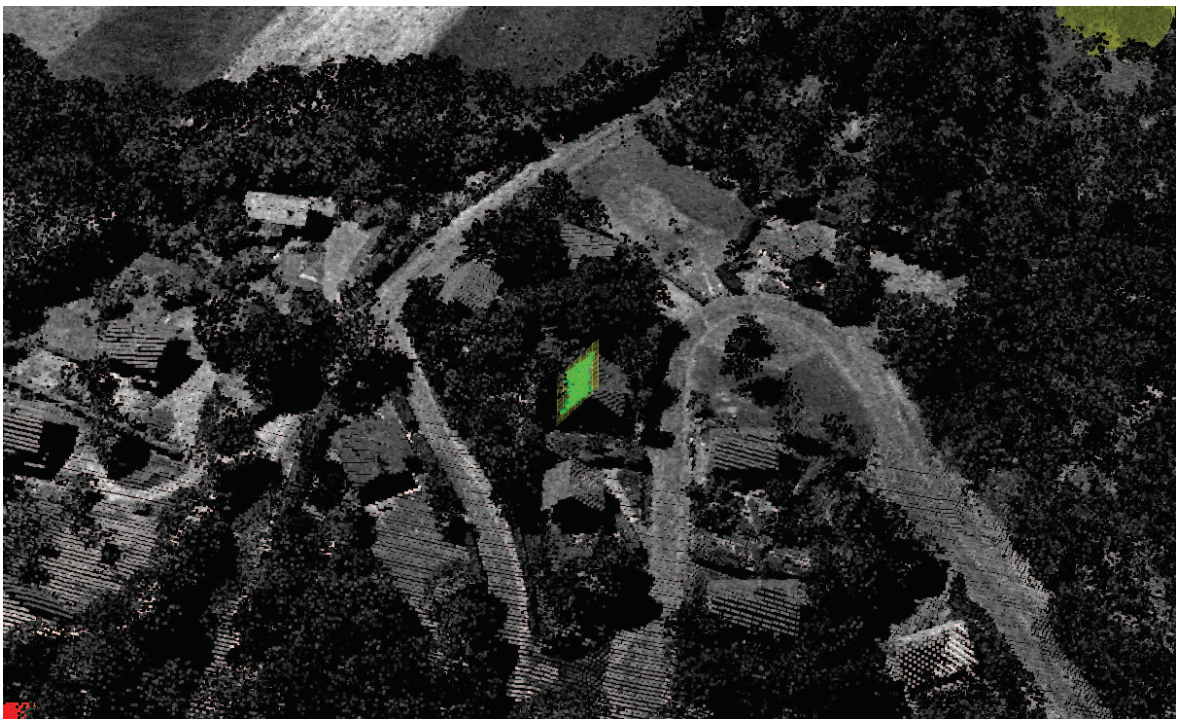

Figure 4.28: Perspective view of the 2006 Lidar point cloud showing the village of Mas d'Avignonet. The point brightness represents the reflectivity of the Lidar points. At one house a plane (yellow) is fitted into the roof using the green points.

4.3 Insar

ERS1 and ERS2 SAR images between 1992 and 2000 are analysed using Persistent Scatterer Insar (PSI). The processing covers the whole chain from the raw satellite data to landslide displacements. The steps from the raw data to the co-registered SLC images is covered in Section 2.7.4 for the Grenoble study site, because the same images also cover the Avignonet and Harmalière landslide (see Fig. 2.37). The same "standard" processing chain of the GAMMA[3]-software is applied to the SLC subset covering the area of the two landslides and the differences and difficulties compared to the Grenoble case are highlighted (Sec. 4.3.1). Due to the limited results of the Gamma-"standard" solution and the difficulties to alter the processing inside of Gamma, the processing is extended in Section 4.3.2 using Matlab. In Section 4.3.2.5 the results are interpreted as displacements in slope direction and compared to GPS-displacements. Finally the PSI-processing is critical discussed in Section 4.3.3.

Figure 4.29 shows the features seen in a multilook SAR-image of the Avignonet-Harmalière study site, in order to provide a better orientation in multiple other figures of this chapter, where this image is used as a background. The extent of this subsection is shown on the topographical map in Figure 2.27 and on the whole original SAR image in Figure 2.27.

[3]Gamma is a SAR processing software by Gamma Remote Sensing `http://www.gamma-rs.ch/`

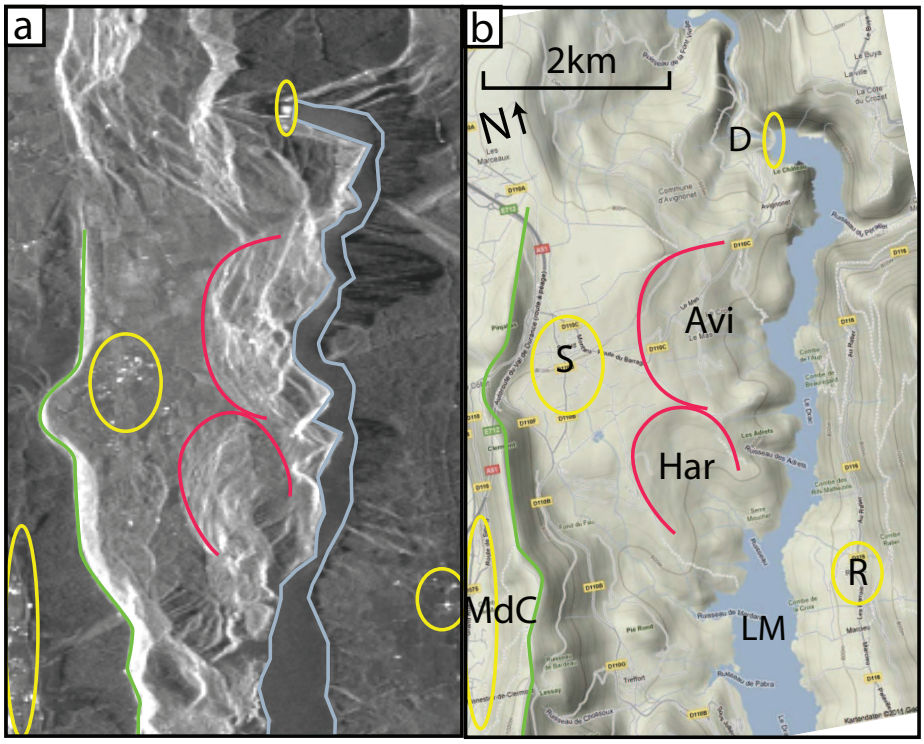

Figure 4.29: (a) Multilook SAR image (1:5) and (b) topographic map of the sub-frame for the Avignonet/Harmalière study site, highlighting the headscarps of the Avignonet (Avi) and Harmalière (Har) landslides (red), the villages Sinard (S), Monestier-de-Clermont (MdC), Rouac (R) and the dam (D) (yellow), the Lake Monteynard (LM) (blue) and the Pinjallas-Clermont-mountain range (green).

4.3.1 Standard solution at Avignonet and Harmalière

Starting point for the processing are the SLCs already computed from the raw data in the Grenoble case. The master image is also the same (ERS2 from 15.3.1997), but cropped to the region of Avignonet and Harmalière with an extent of 200 x 1600 pixel, which is about 4 x 6.4 km (see the extent on the map in Fig. 2.27 and on the whole interferogram in Fig. 2.36). In Gamma the minimum size to perform the co-registration is 512 pixel, therefore first the master image was cropped to 550 x 1600 pixel, then all images are co-registered and finally all images are cropped equally to 200 x 1600 pixel. At the co-registration step offsets are obtained like in the Grenoble case at 1024 equally distributed points (32 x 32 grid). In average at half of the points offsets could be obtained (389 to 826 of 1024) with mean accuracies of 0.07 - 0.12 pixel in range and 0.17 - 0.65 pixel in azimuth direction. Compared to the Grenoble case, these errors are about two times higher in range and up to 5 times higher in azimuth. Also in azimuth it exceeds the suggested 0.2 pixel of the Gamma-user guide. The higher errors are expected due to the highly mountainous terrain including areas of shadow, overlay and water. These areas contain partly random information in the intensity images, which leads to mismatches in the co-registration step. However, PSI-results are limited to the non-problematic areas where the co-registration is expected to be much better (like in the Grenoble case).

For the DEM a combination of the 50 m IGN-DEM (A.4) and the 2 m Lidar-DEM is used to increase the accuracy of DEM-information in the landslide area. The area in the IGN-DEM covered by Lidar is replaced with the Lidar-DEM and the whole DEM is resampled with 10 m spacing.

From the co-registered SLCs PSI-point candidates are obtained using the same criteria as in the Grenoble case leading altogether to 1329 point candidates, which are about 0.42 % of all points. Not surprisingly this is about 3-4 times lower than in Grenoble due to the low availability of good reflectors in the area. Figure 4.30 shows statistics of different properties of the co-registered SLCs together with the used thresholds to illustrate the influence of thresholds on the obtained number of point candidates. The number of point candidates is represented on a logarithmic scale, which already illustrates that small changes of the threshold can lead to high changes of the derived point candidates (in a) and c)). However, at this step it was tried to increase the number of point candidates by lowering the thresholds, which lead to more point candidates, but could not increase the number of final results (due to the psigma-threshold of the regression analysis).

In next step is to chose a reference point of good quality. Therefore several single regressions are calculated and illustrated using the Gamma-function “dis_ipta”. Good reference candidates are chosen by high average intensity values (white dots in the MLI) and the quality of the linear regressions towards several target points is judged based on the linear fit with respect to the baseline and linear deformation. The reference point is at the coordinates 149, 816 (range, azimuth), which is inside the village Sinard. Figure 4.31 shows the Gamma standard solution after the regression analysis within the allowed limits of 30 m height correction and deformation rates of 2 cm/a in both directions (towards and away from the satellite). The sigma threshold for solutions is 1.2, which finally lead to 106 points inside the whole image. Most of them are inside the village Sinard. A few points (not distinguishable in the figure) are at the small village inside the Avignonet landslide, one in the north of Avignonet and non inside the Harmalière landslide. The obtained linear deformations are between -0.1 cm/a and 1.2 cm/a. The result fits to the hypothesis of a stable plateau in the west (blue

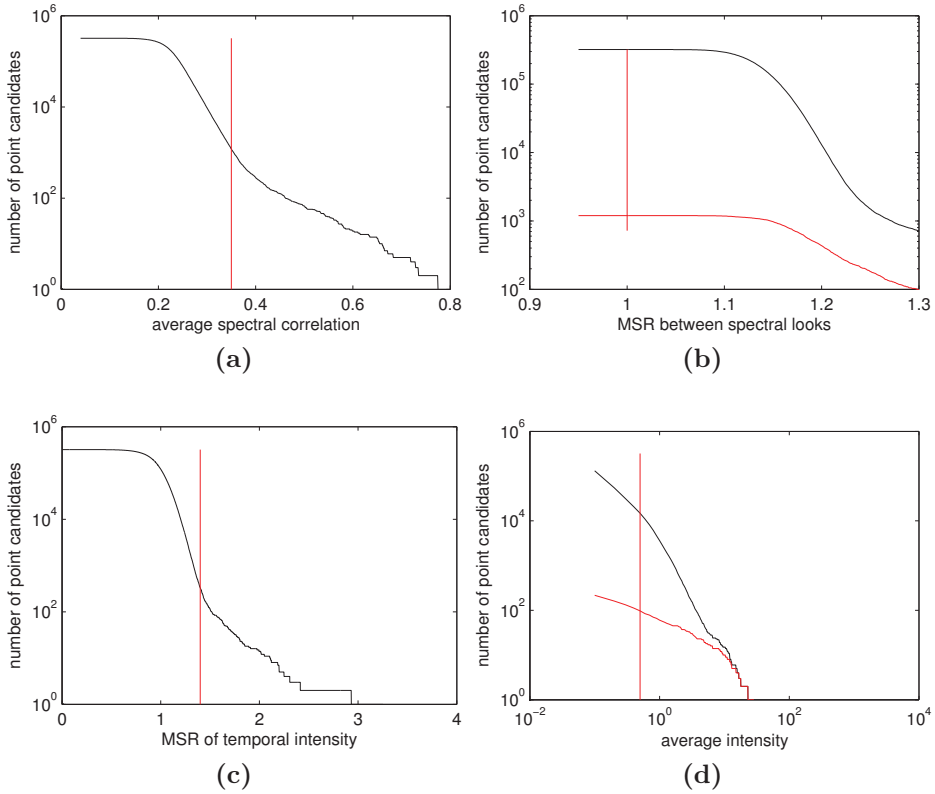

Figure 4.30: Properties of co-registered SLCs for the selection of point candidates of the Gamma PSI processing. The figures show the potential derived point candidates in dependence of chosen thresholds of different statistical properties of the co-registered SLC stacks. a) and b) are based on the non-temporal properties. a) shows the average spectral correlation and the finally chosen threshold of 0.35 in red leading to 1145 point candidates. b) shows the mean-square-root (MSR) between spectral looks in black for the whole image and in red for the subset of point candidates using the threshold in a). The final threshold of 1.0 here has no influence on the number of point candidates because all values are already higher. c) and d) are based on the temporal properties of points. c) shows the MSR of the point intensity over time with the finally chosen threshold of 1.4 in red leading to 328 point candidates. d) shows the average intensity in black for the whole image and in red for the subset of point candidates using the threshold in d). The threshold here (red vertical line) is at 0.5, leading to finally 96 point candidates. In d) the absolute value of point candidates does not reflect the Gamma-result, because it does not include the normalization of average intensities between the images. With respect to that, Gamma leaves 252 point candidates.

dots) and unstable areas at the border of the plateau, here on the Avignonet landslide (yellow dot) and some areas north of it (cyan dots indicating slightly negative values $>$ -0.1 cm/a). The height corrections shown in (b) are between -17 m and 18 m and are less high on flat terrain (Sinard, plateau) and higher at areas of higher topographical complexity (i.e. white areas indicating higher slopes due to layover). This is consistent with the assumption that the 20 m-DEM, which is already included in the calculation, is less accurate at more complex topography, so that corrections are higher. The solutions for deformation rates and height corrections are all far away from the given limits (0.2 cm/a, 30 m), which indicates that the limits are sufficiently high for this area. In (c) the sigma value, which shows the error from the linear fit, does not vary much with values near the given threshold of 1.2 (yellow dots) with an exception in the Sinard village (magenta dot) of higher quality, probably due to the direct neighborhood to the reference point. Because many points are near the given threshold, it could be

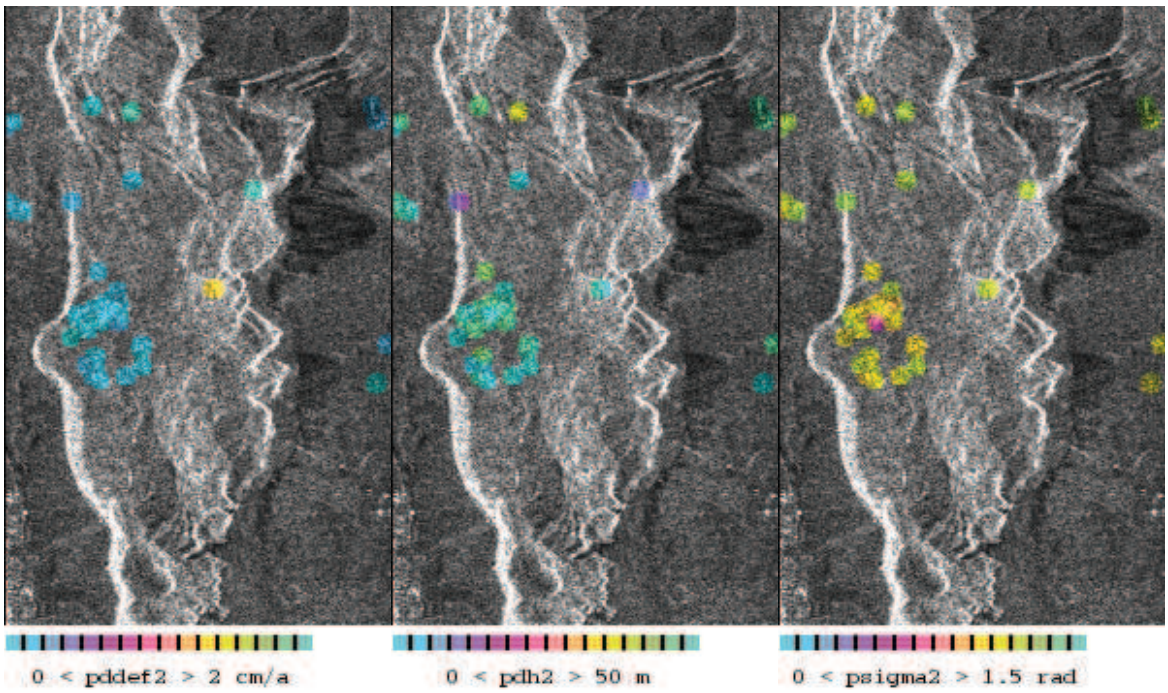

Figure 4.31: Gamma standard solution at Avignonet and Harmalière area using 65 images between 1992-2000 with allowed height correction of 30 m and linear deformation rate up to 2 cm/a. The left and right values below the colorbar indicate the equivalent values for the colors at the edges. The colorbar is circular, which means negative values starting with the most right color as zero and going to the left with decreasing values. a) average linear deformation rate, result values are between -0.1 cm/a and 1.2 cm/a towards the satellite. b) height correction, result values are between -18 and 17 m. c) psigma, the error from the linear fit, with values between 0 and 1.5.

assumed to derive more solution by setting the psigma-value higher.

However, the processing using Gamma is stopped at this point due to several reasons:

1. The lack of control and quality assessment of the regression analysis.
2. The indirect access of the solutions for proper visualization and post-processing.
3. The limited possibilities of developing processing strategies adjusted to the special properties of the area.

Instead the processing is recalculated and advanced using self-written code in Matlab starting from the differential interferograms of the co-registered SLCs (usually called "diff0" in the Gamma manuals).

4.3.2 Extended processing at Avignonet and Harmalière

4.3.2.1 Pre-requisite

Starting point for the extended processing are the differential interferograms. These are the interferograms between all co-registered SLCs and the master SLC corrected by the phase due to the topography and the orbits (perpendicular baselines). Due to the unavoidable errors when simulating the topographic and orbital phase just from the

external DEM and the orbital parameters, the differential interferograms still contain significant errors depending on the topography and perpendicular baseline. The basic idea of the PSI processing can be explained by looking at the different components of the interferometric phase between two points:

$$\phi_{int} = \phi_0 + \phi_{topo} + \phi_{def} + \phi_{res} \tag{4.1}$$

ϕ_{int} is the interferometric phase of the two differential phases of the points. ϕ_0 is a constant phase only depending on the reference image. ϕ_{topo} is the phase depending on the topography (and perpendicular baseline). ϕ_{def} is the phase depending on a linear deformation and ϕ_{res} summarizes all residual phases (i.e. atmospheric, decorrelation, non-linear deformation etc.). The regression analysis is done by minimizing the residual phase while modeling ϕ_0, ϕ_{topo} and ϕ_{def}. The modeling is possible due to the linear relations between the topographic phase and the perpendicular baseline on one hand and between the linear deformation phase and time on the other hand. By using the stack of interferometric phases from different images, the linear relation can be revealed. Basically the modeled phase can be written as:

$$\phi_{mod} = \phi_0 + a_1 \cdot db(i) + a_2 \cdot dt(i) \tag{4.2}$$

The modeled phase ϕ_{mod} is composed of a constant phase ϕ_0, a phase with a linear dependency on the perpendicular baseline of the image $a_1 \cdot db(i)$ and a phase with a linear dependency on the date of the image $a_2 \cdot dt(i)$ (i is an index into the images). Figure 4.32 shows an overview of the perpendicular baselines of the ERS1/2-database. The constant phase ϕ_0 is in the limits of one circle $(0 - 2\pi)$. a_1 is connected with the height correction of the DEM between the two points and can be calculated using the factor $f_1 = 1/1525\,m^{-1}$. This factor is obtained from Gamma and depends on the geometry of the orbits of the satellites. a_2 is connected with the relative linear deformation rate between two points in LOS (line of sight of the satellite) and can be calculated using the factor $f_2 = 4\pi/\lambda$. This factor depends only on the Radar-wavelength of the satellite, which is 5.656 cm for the ERS satellites. These factors are essential for the start of the calculation in order to convert the given limits for the height correction in limits for a_1 and the limits for the linear deformation in limits for a_2. And after the computing to convert the results back into usable values. These factors are verified by comparing the solutions of Gamma with solutions of the self-developed code.

The most essential measure of the quality of the fit is psigma, the RMS of the residual phase:

$$psigma = \sqrt{\overline{\phi_{res}^2}} \tag{4.3}$$

If psigma is low, the interferometric phase can be good explained by the model. If psigma is high, the phase contains other components, which could be due to atmospheric distortions, vegetation change, non-linear displacements, precipitation conditions, badly co-registered SLCs etc..

The Figures 4.33, 4.34 and 4.35 show 3 different examples of solutions from the phase regression analysis. The figures are each composed of 4 subfigures showing details of the solution. The location of the pairs shown on the MLI image in the lower right by the yellow line with the two dots. The lower left figure shows the color-coded psigma-values of all possible models tried in the initial step. The image shows only the solution-plane at the a0-value of the final solution. The full solution matrix would be a cube. The model parameters with the lowest psigma is then further optimized by

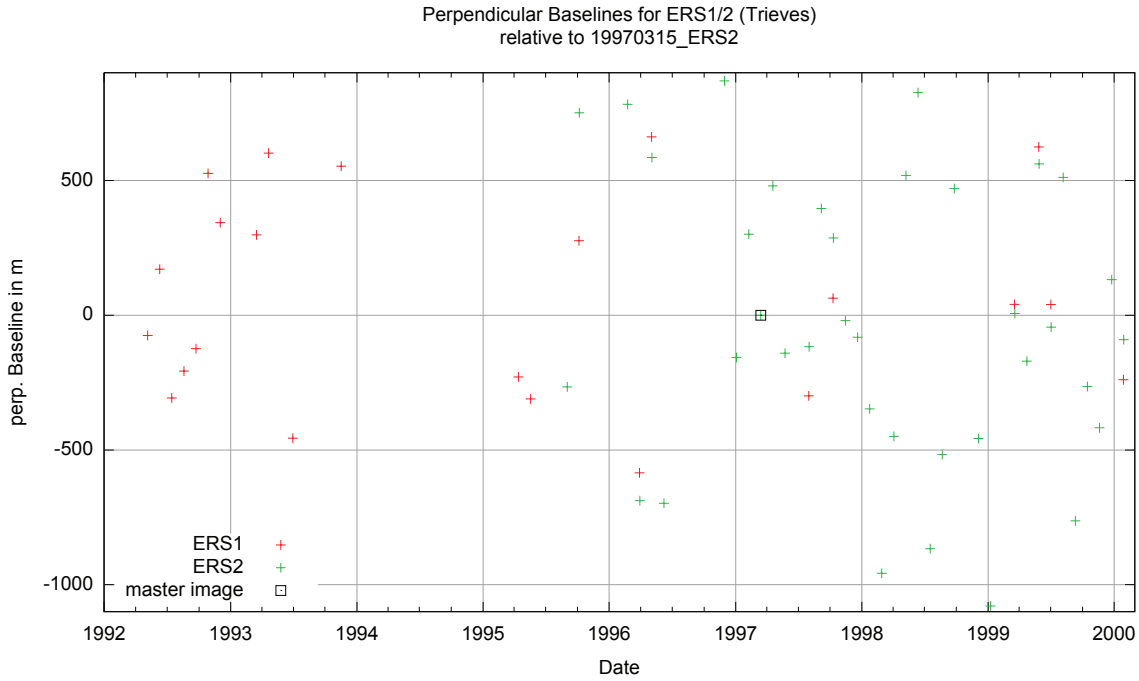

Figure 4.32: Perpendicular baselines of ERS1 and ERS2 images from 1992-2000 relative to the chosen master-image of 15.03.1997.

an iterative process in order to find the final solution at the minimum of psigma (the center of the most blue valley in the image). The two plots at the top show the phase plots with the best linear fit in red. The phase in the top left plot shows the variation with time and is corrected from the topographic phase. And the phase in the top left plot shows the variation relative to the perpendicular baselines and is corrected from the phase due to the linear deformation.

Figure 4.33 shows the best solution of the whole image from two nearby stable points in the village Monestier de Clermont. The psigma-matrix shows a clear minimum leading to an unambiguous final fit at a deformation rate of about 0.4 mm/a. Figure 4.34 shows a solution between a stable point in the village Sinard and an unstable point in the center of the Avignonet landslide. The values in the psigma-matrix are much higher than in the previous solution, but still contain a relative unambiguous solution (blue valley). The continues alignment of the red fit in the phase-time plot suggests that the deformation is really linear without major changes thru time.

The last example in Figure 4.35 shows a very ambiguous solution. The phase-matrix contains several psigma-depressions with similar values of about 1.4. The lowest depression leads to a solution of a highly negative deformation rate and a high height correction (blue valley in the upper left). But other solutions like the blue valley near the matrix center would be equally sufficient. Also the two phase-plots at the top confirm that impression as the red fitting line seems fairly random. This solution could be considered as false.

4.3.2.2 processing strategy

The whole processing strategy is based only on a low psigma. No other criterias are considered, which is different to the Gamma approach where point candidates are preselected using other statistically properties. The easiest way would be to calculate all possible pairs inside the image, which would be about 51 Gpairs (Giga-pairs = $51 \cdot 10^9$

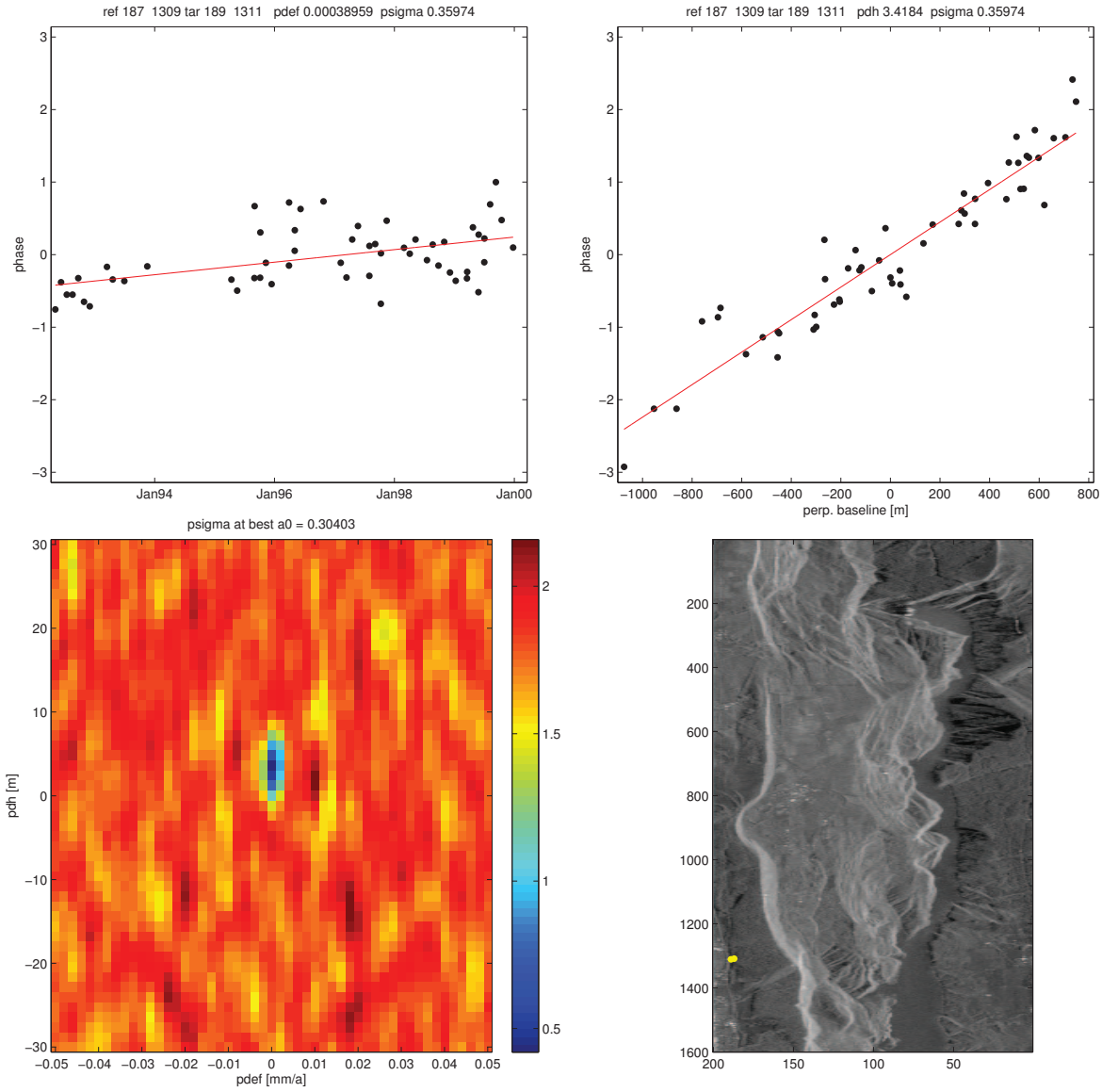

Figure 4.33: Example of the best solution from the whole image of the phase regression analysis. psigma is 0.36. The linear deformation rate is 0.4 mm/a. The point distance is about 41 m (2.8 pixel). TopLeft) phase versus time. TopRight) phase versus perpendicular baseline. BottomLeft) psigma-matrix for initial regression-models at a0 of best model. The model limits are 30 m height correction and 5 cm/a deformation rate. BottomRight) Location of the pair in the MLI.

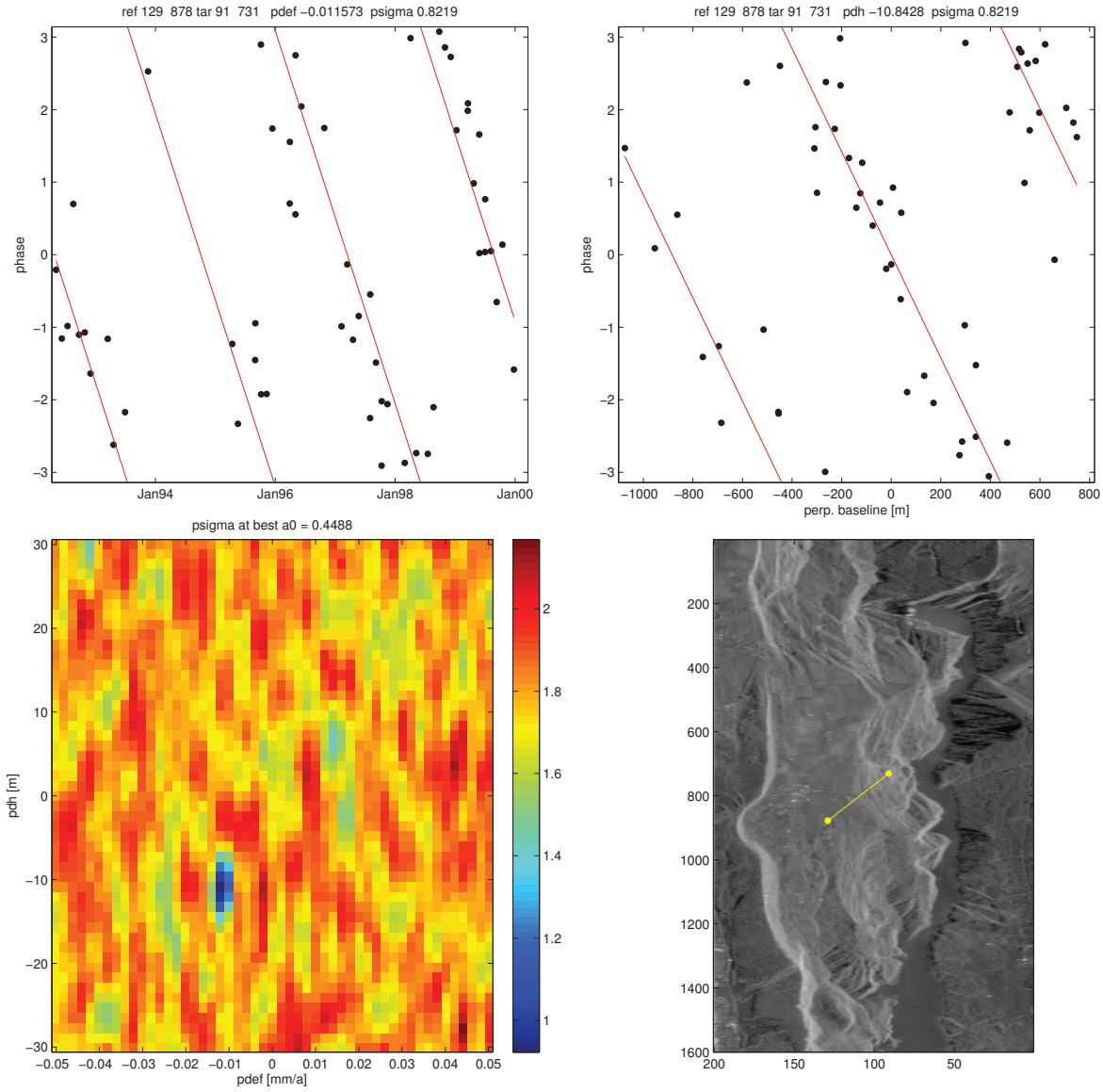

Figure 4.34: Example of a high quality solution of the phase regression analysis with a high linear deformation rate in Avignonet. psigma is 0.82. The linear deformation rate of the point in Avignonet is 1 cm/a towards the satellite. The point distance is about 2944 m (152 pixel). TopLeft) phase versus time. TopRight) phase versus perpendicular baseline. BottomLeft) psigma-matrix for initial regression-models at a0 of best model. The model limits are 30 m height correction and 5 cm/a deformation rate. BottomRight) Location of the pair in the MLI.

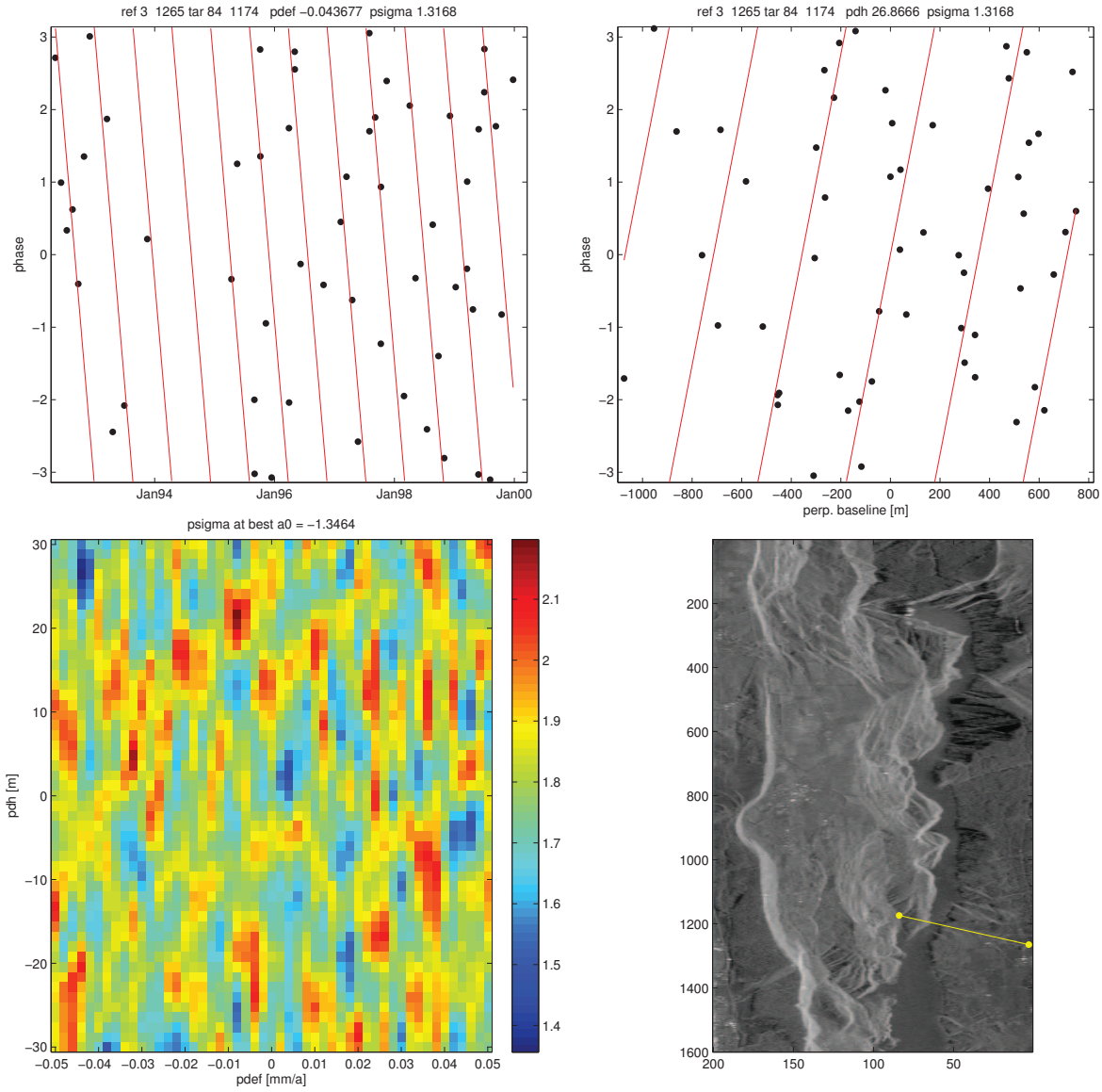

Figure 4.35: Example of a low quality solution of the phase regression analysis in Harmalière. psigma is 1.32. The linear deformation rate would be 4.4 cm/a. The point distance is about 1849 m (122 pixel). TopLeft) phase versus time. TopRight) phase versus perpendicular baseline. BottomLeft) psigma-matrix for initial regression-models at a0 of best model. The model limits are 30 m height correction and 2 cm/a deformation rate. BottomRight) Location of the pair in the MLI.

pairs). The non-optimized code is able to compute about 3 Mpairs/day using Gamma on a normal office computer (Dual processor at 2GHz). This would result in about 50 years of processing time. The estimated potential for code-optimization is high, but is not the aim of this work, so the number of pairs should be reduced. The final goal is to obtain as much as possible solutions inside the landslide area (P_u) relative to stable points outside of the landslide (P_s). The reason to have more than one solution for a single point inside the landslide is to verify the robustness by analyzing the different solutions towards a single point. Each step of the strategy is based on a condensation of a set of solutions (pairs) into a set of points of higher quality, which consists of the following operations:

1. Calculation of all pairs between a set of reference points and a set of target points. Both sets can be overlapping or equal. Additionally a minimum and maximum distance between the points can be defined, which means that only pairs within this limits are considered. The minimum distance can avoid to consider pairs of neighboring pixels which may depend on the same dominant reflector and therefore are not independent. The minimum is always set to 2.5 pixel.

2. Reduction of the number of pairs by a soft psigma threshold to lower the processing time for the next step.

3. If searching for stable points, filtering of solutions with deformation rates higher than 1 mm/a.

4. Keeping the best individual pairs, which means to sort the solutions by psigma and to remove pairs containing a point already present in a pair with a lower psigma. This step is necessary to not be biased towards pairs containing the same point with very good reflective properties.

5. Only keeping the top best individual pairs, either defined by a constant number or a psigma threshold (probably a stronger than at step 2).

6. Using all points of the leftover pairs as a new set of reference or target points.

To find the stable points P_s the following strategy is implemented (see Figure 4.36 for illustration):

1. Defining regions of potential stable points P_s^0 with higher quality (Fig. 4.36a). These regions are the villages Sinard, Monestier de Clermont, la Morte and Rouac, the dam of Lake Monteynard and a street along the cliff at the NE-side of the lake.

2. Condensation of a subset of points P_s^2 from solutions within the stable regions ($P_s^0 \rightarrow P_s^0$). For Sinard and Monestier a maximum distance of 5 pixel in range and 15 pixel in azimuth is set and the resulting point-set P_s^1 is again calculated against P_s^0 and condensed to P_s^2 to lower processing time. For the other smaller regions this intermediate step is not necessary.

3. Condensation of the solution $P_s^2 \rightarrow P_{\neg u}^0$. $P_{\neg u}^0$ are all points outside the unstable region. This point-set P_s includes stable points outside the predefined regions. For this step only a subset of P_s^2 is used in order to reduce processing time. The final set of stable points P_s includes all points of P_s^2.

To find the unstable points P_u the following strategy is implemented:

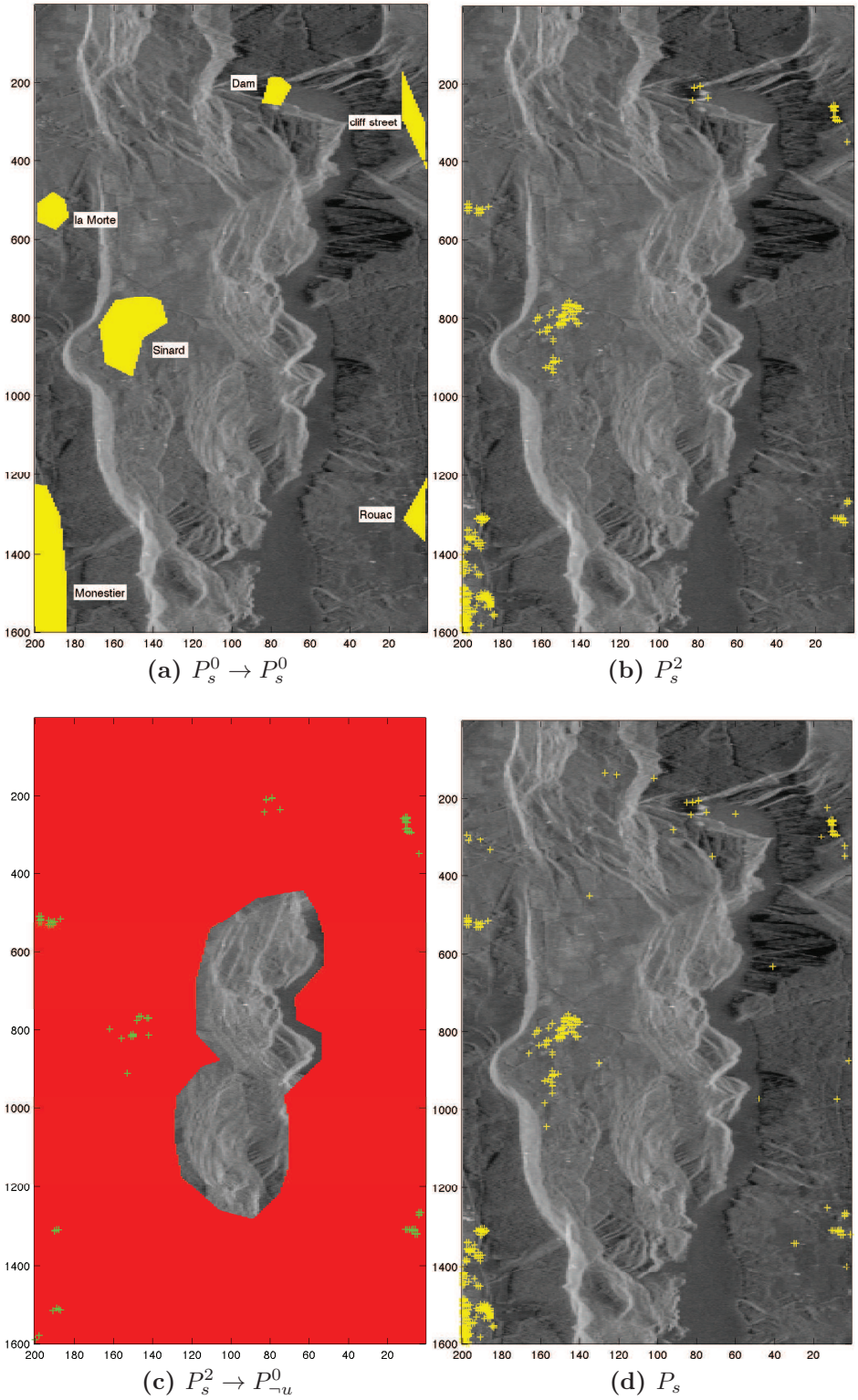

(a) $P_s^0 \rightarrow P_s^0$ **(b)** P_s^2

(c) $P_s^2 \rightarrow P_{\neg u}^0$ **(d)** P_s

Figure 4.36: Reference and target points for PSI processing strategy of stable points. The left images show the reference points (green) and target points (red) of the pair calculations. If the reference points and target points are the same they are plotted in yellow. The right images show the condensed points from the solutions of the corresponding pairs on the left. (a) Stable regions with expected higher density of PS. (b) Condensed points from solution of (a). (c) Pair calculation from predefined stable points to the whole area outside Avignonet and Harmalière. (d) Condensed stable points from solution (c).

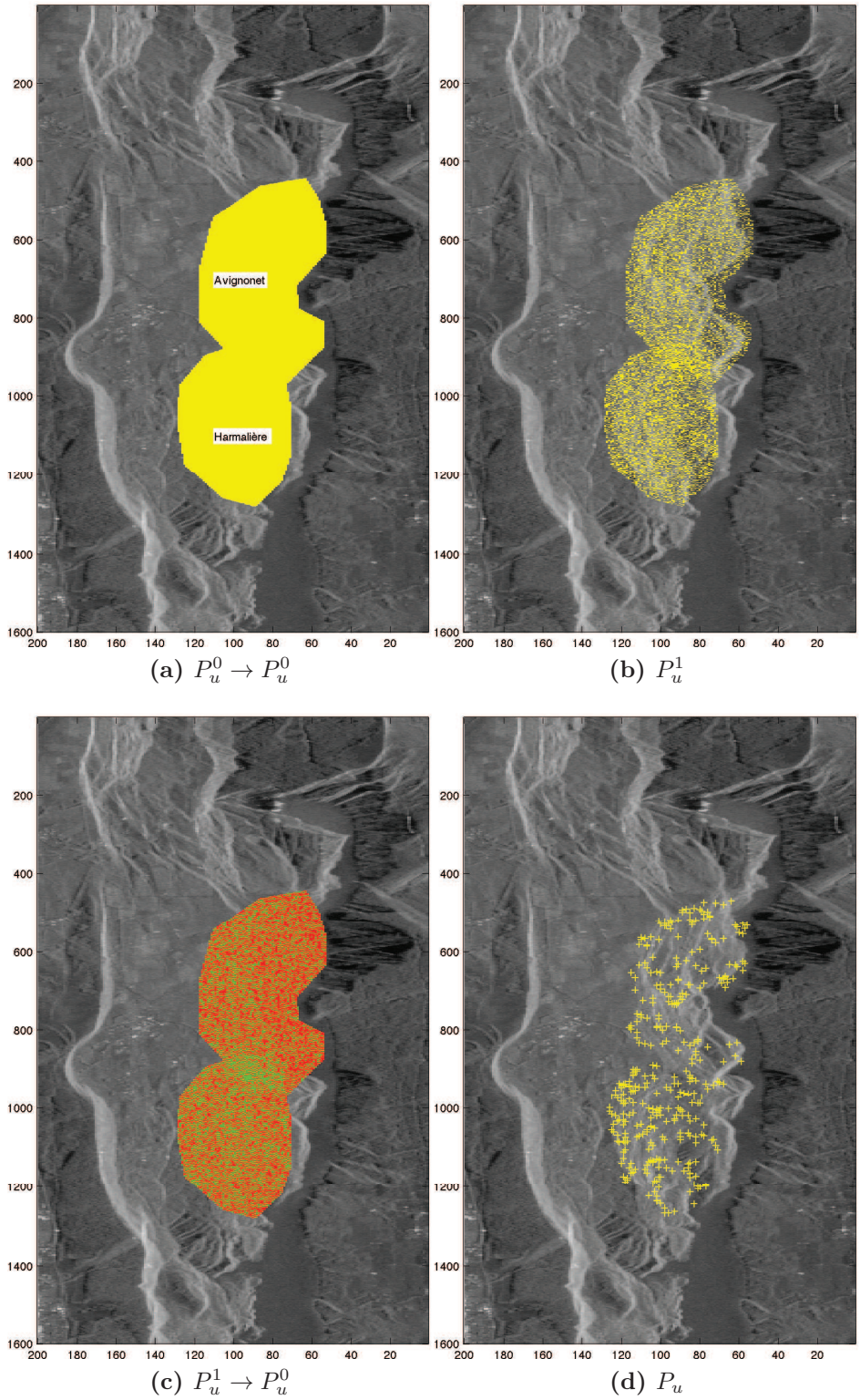

(a) $P_u^0 \rightarrow P_u^0$ **(b)** P_u^1

(c) $P_u^1 \rightarrow P_u^0$ **(d)** P_u

Figure 4.37: Reference and target points for PSI processing strategy of unstable points. The left images show the reference points (green) and target points (red) of the pair calculations. If the reference points and target points are the same they are plotted in yellow. The right images show the condensed points from the solutions of the corresponding pairs on the left. (a) Landslide regions with potential unstable points. (b) Condensed points from solution of (a) using a soft psigma-threshold. (c) Pair calculation from the subset of unstable points to the whole area of Avignonet and Harmalière. (d) Condensed unstable points from solution (c).

1. Defining the region of interest P_u^0, i.e. the area of the Avignonet and Harmalière landslide (Fig. 4.37a).

2. Condensation of a first subset of points P_u^1 from solutions within the landslides ($P_u^0 \rightarrow P_u^0$) and a maximum distance of 5 pixel in range and 15 pixel azimuth. A soft psigma-threshold is used in order to keep as most points as possible for the next step.

3. Condensation of the solution $P_u^1 \rightarrow P_u^0$. This point-set P_u includes also individual points of higher quality because there is no distance limitation.

The final solutions are calculated using the best 60 stable points (P_s) and the best 160 unstable points (P_u) resulting in 9600 solutions (pairs). The reference and target points are shown in Figure 4.38a. In order to judge the quality of the results a second calculation is done using the same points and parameters for the regression analysis but with random interferometric phases. Figure 4.38b shows the linear deformation rate and psigma for the real solutions (black) and the random solutions (red). The figure shows for the random solutions a main psigma-band approximately between 1.25 and 1.4 with some psigmas as low as 1.1. The real solutions show the same band but additionally some concentrations at distinct deformation rates between -12 mm/a and +5 mm/a. Another slightly increasing number of psigma can be seen at a deformation rate around 40 mm/a, but all psigmas there are still higher than the lowest psigma of the random solutions. From that figure it can be concluded that a psigma-threshold of 1.05 would be relatively safe in order to only keep real solutions. Any filtering of the solutions by a higher psigma-threshold would also include random solutions without any meaning and needs additional quality tests. Figure 4.38c and d show maps of solutions after filtering by a strong psigma-threshold of 1.05 (120 pairs, 15 target points) and by a soft psigma-threshold of 1.25 (1033 pairs, 180 target points). The target points of the certain solutions (c) are limited to the center and north of the Avignonet landslide, most likely due to the buildings present in these areas. The deformation rates (colors) seem to be similar for adjacent points. No point is situated in the Harmalière landslide. The more uncertain solution map (d) (attention for the different colorbar) does reveal at least two patches of points in Harmalière with similar low deformation rates, which could be an indication of meaningful solutions. However, the overall distribution of points seems highly random.

In order to extract useful deformation rates of the landslides the solutions are filtered and condensed in Section 4.3.2.4. In Section 4.3.2.5 the extracted deformation rates (in the direction of the LOS) are interpreted as landslide movements.

4.3.2.3 Detection of erroneous image dates

The residual phase of a pixel with a dominant reflector of a co-registered SLC can be influenced by several factors. If the quality of a whole image is reduced, the psigma-value for all solutions is generally raised and therefore more difficult to distinguish from random noise (e.g. Fig. 4.38b). Therefore it can be helpful for the whole processing to exclude the most erroneous image-dates from the calculations, which on the other hand decreases the statistical robustness of the regression analysis. Some factors which could explain an overall decrease of the reflective quality of an image are:

- the presence of snow or higher soil moisture due to snow-melting or rainfall,

- decreased quality of the SLC co-registration or

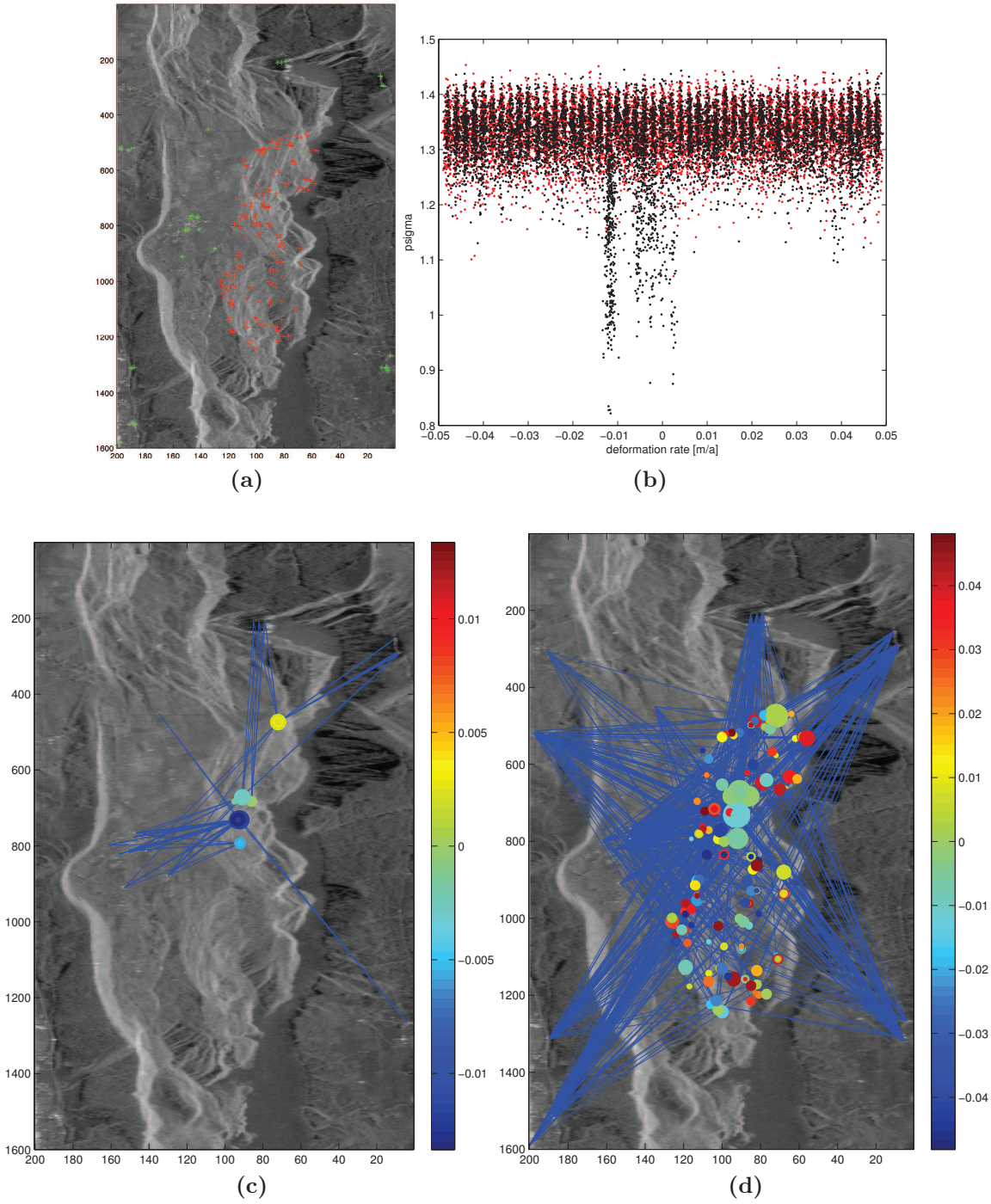

Figure 4.38: Raw final solution of 2-dimensional phase-regression analysis between 60 stable reference points and 160 unstable target points in the area of the Avignonet and Harmalière landslide. (a) Point overview on top of the average MLI. Stable reference points in green. Unstable target points in red. (b) deformation and psigma of all solutions (black) in comparison to a set of completely random solutions (red). (c) Solution map after filtering with a strong psigma-threshold of 1.1. (d) Solution map after filtering with a soft psigma-threshold of 1.25. The solution map is drawn on top of the average MLI. Each solution is represented by a blue line from the reference point to the target point and a colored circle at the target point. The diameter of the circle corresponds to psigma, so that solutions with a low psigma are represented by a big circle (because they are more probably to be true) and solutions with a high psigma are drawn with a smaller circle (less sure). The color represents the linear deformation rate in m/a in LOS direction away from the satellite, which would translate on a horizontal plane westwards for positive values and eastwards for negative values.

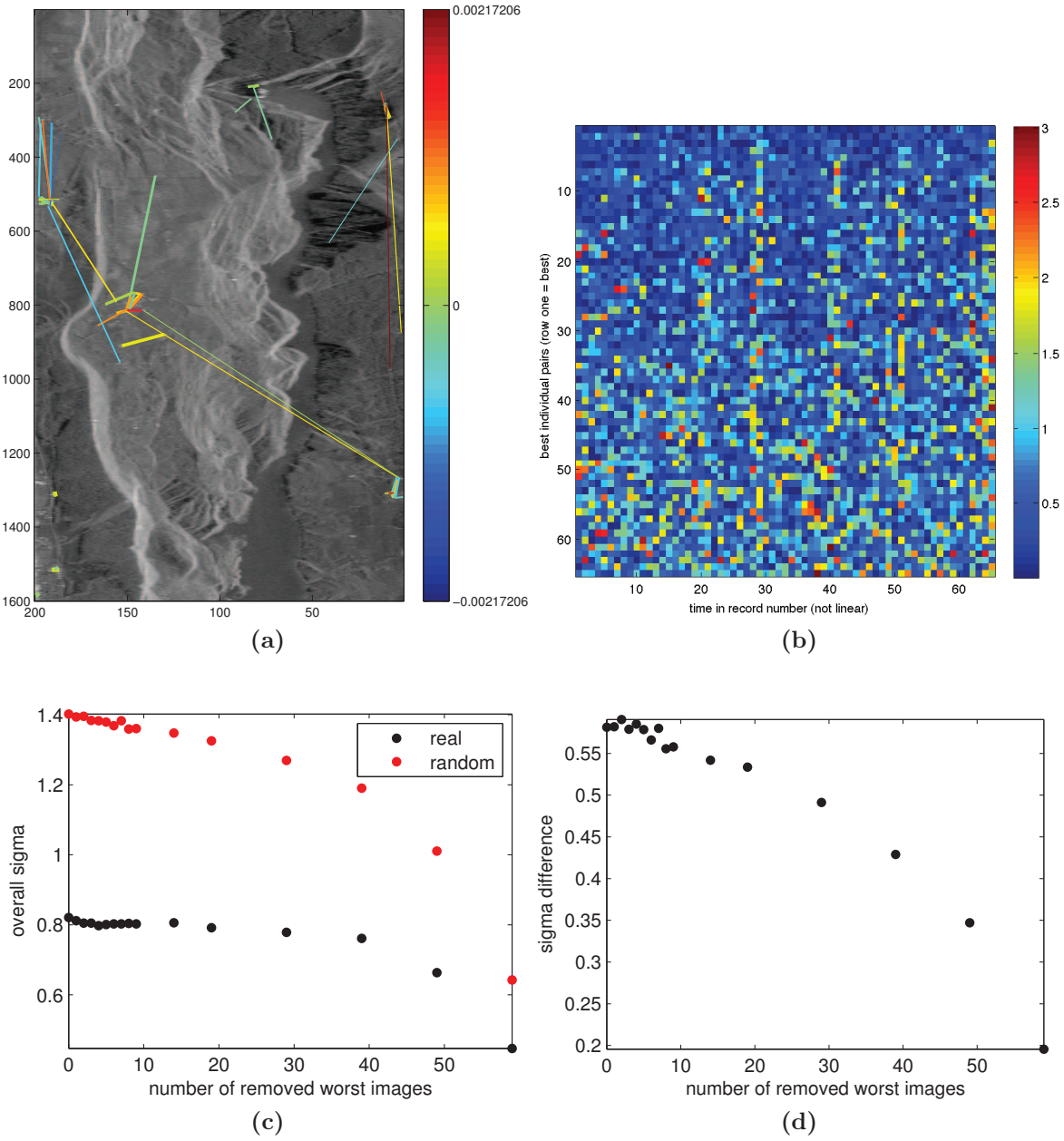

Figure 4.39: Phase quality per image-date with dependence on snow-fall and co-registration quality. a) Solution map of the pairs used for the time analysis on top of the MLI. Each line represents a solution between the connected points. The thickness of the line depends on psigma and is thicker for a lower psigma. The color shows the linear deformation rate indicated at the colorbar. b) Absolute residual phases per solution and image dates. The solution quality increases from the top to the bottom. c) Average sigma over all solutions and dates using a decreasing number of images. d) Sigma difference of (d)

- turbulent atmospheric conditions.

A good measure for the overall image quality is the RMS of the residual phase, but not over all dates per solution (= psigma), but instead over all solutions per date (= tsigma). In order to minimize the influence of spatial variance of the residual phase (like decorrelation and non-linear displacements) only solutions from stable points and below a strong psigma-threshold are used. Therefore the best individual pairs of the solutions from the regression analysis from stable points to stable points ($P_s^2 \rightarrow P_{\neg u}^2$, Fig. 4.36c) with linear deformation rates below 2.5 mm/a are used. These 65 solutions

are shown in Figure 4.39a. The pairs are distributed over the whole image and can be assumed to be representative. Figure 4.39b shows the absolute residual phase per date and solution. The RMS per row is psigma and the RMS per column is tsigma. The variability of the residuals increases from the top to the bottom because the solutions are sorted by psigma. More important is the observation that some columns contain higher residuals than others (vertical lines). This is a direct indication that some images are of lower quality and tsigma is a good measurement for it.

The overall quality of the regression analysis can probably increased by removing the worst images. In order to test the increase of the overall regression quality, the regression analysis for all solutions is repeated after removing the always next worse image with the highest tsigma from the database. The black dots in Figure 4.40c show the decrease of the overall sigma when removing the images. If too many images are removed, the regression thru the leftover phase-values can result in lower psigmas, but the robustness of the regression is also lowered. The extreme end would be the removal of all but two images and the regression thru two points would lead always to a psigma of zero. This means that there is a natural decrease of psigma just because of a decreasing number of images. Therefore a second database of random values is build-up and calculated in parallel. When removing the same dates of that random database the sigma is also decreasing as seen by the red dots in Figure 4.40c. As the goal of the whole regression analysis is to distinguish between random solutions and real solutions by a psigma threshold, the difference between the sigmas from the random and real database need to be maximized. Figure 4.40d shows this difference. The main observation is that there is no clear optima of the difference, but about 10 images can be removed without decreasing the sigma difference. In order to decide wether to remove those images or not, the cause of the decreased image-quality is analyzed.

Figure 4.40a shows tsigma, the measure of the image-quality, versus the image-dates. At least for the years from 1996 to 2000 tsigma seems to be elevated during the winter seasons. This impression can be confirmed when looking at Figure 4.40c, which shows the image quality dependent on the seasons (day of the year). In this plot tsigma-values are only higher than 1.0 from the days 1 - 60 (Jan-Feb) and above day 330 (Dec), leads to the assumption that the image quality is decreased in the winter season due to snow. Figure 4.40b shows the database of daily fresh snow for the same time period derived from a nearby meteorological station[4]. Figure 4.40d shows the relation between tsigma and the fresh snow of the same day as the image acquisition. This plot does not reveal a clear relation between snowfall and image-quality. The linear correlation coefficient R (after Pearson) is 0.18. The reason could be that only fresh snow of the same day is taken in consideration, but snow-fall before the date of image acquisition is expected to have a major influence as well. Data of absolute height of snow was not available at this station. Therefore R is calculated between tsigma and an accumulated snow taking 0 - 30 days before the image acquisition into account (Fig. 4.40e). The maximum correlation ($R = 0.75$) is reached when considering 8 days of fresh snow before the image-date. Figure 4.40f shows this accumulated snow versus the image quality (tsigma). It confirms the dependency of the image quality on the presence of snow. All images (except 1 out of 10) with tsigma > 1.0 are from dates with at least 15 cm (black line) of accumulated snow in the 8 days before image acquisition. These 10 images are finally removed from the database even if the overall increase of quality could not be proved. The reason is that for the image-quality statistic only the

[4]Meteorological station no. 38242001 at Monestier de Clermont (village in the SE of the SLC, see Fig. 4.36a). Daily fresh snow thickness (Hneigef, 24H). The station altitude is 800 m.

best stable solutions of the whole image are used, but the influence of snow is maybe stronger on solutions from pixels with less dominant scatterers. The final number of images for the further processing is 55.

4.3.2.4 Quality filtering of the final solution

The final solution $P_s \rightarrow P_u$ is done using the best 60 stable points and the 160 best unstable points, resulting in 9600 solutions of very different quality (Fig. 4.38). Each target point in the landslide area (P_u) is part of 60 pairs, which need to be condensed into one deformation rate per point. The variability of solutions per target point can help to estimate the quality of that deformation rate. Figure 4.41 shows 4 representative examples of different quality in order to highlight the problems of judging the quality of a result. The plots show the regression error (psigma) versus the linear deformation rate (pdef). The vertical lines indicate an extracted linear deformation rate using different 3 different methods: (1) the average pdef of all solutions as dotted line, (2) the pdef at the most frequent appearance in black and (3) the pdef with the lowest psigma in red. The example (a) shows the solutions at a target point of higher quality with a low deformation rate (2.9 mm/a). The average psigma is 1.13. The standard deviation of pdef as a measure for the consistency between the solutions, is 0.014 m/a. All solutions below a psigma of 1.25 show a similar pdef and just a few solutions with a high psigma are widespread over the whole range of possible pdefs. All three methods to extract the deformation rate for that target point are very close. However, the mean pdef is influenced by the bad solutions with the higher psigmas and therefor too low. In example (b) this problem is more obvious. There is a clear linear accumulation of pdef-solutions near 0.036 m/a reaching psigmas down to 1.15, but the mean pdef is about 0.01 m/a. The two other methods (black and red line) are more accurate here. The standard deviation of pdef is with 0.030 m/a about twice as high as in example (a) an reflects very well the inconsistency between the single solutions. Example (c) reveal a high (negative) deformation rate of -1.3 cm/a with a high consistency (standard deviation of pdef is 0.013. Example (d), a target point of very low quality, highlights two problems: First, the peak-method and best-method can be very different. Second, the standard deviation of pdef is with 0.025 lower than in example (b), but the plot of solutions suggests that it is not possible to extract a meaningful deformation rate, which seems still possible in example (b).

However, from the examples it is concluded that the most robust technique to extract the deformation rate is to take the pdef at the most frequent appearance (peak-method). In order to judge the quality of a target point, the average psigma and standard deviation of pdef is used. Figure 4.42a gives an overview about these quality values for all target points. The black dots represent all 160 targets and the red dots show the same number of points from the random database. Two thresholds are chosen in a way that all random results (red dots) are kept in quadrant D. All real results in quadrant D are assumed to be random or not distinguishable from non-random results and are therefore sorted out. The results from the other 3 quadrants are shown in the maps 4.42d-f.

The results in quadrant A are expected to be relatively robust. The accompanying map (4.42d) shows the positions of the target points and their deformation rates. Quadrant B contains the results with psigmas equally high as random results. The question is here, is a higher consistency (lower standard deviation of pdef) sufficient to proof their robustness? The theoretical answer was yes, because the higher psigma can be related to non-linear displacements, but would be consistent when looking from

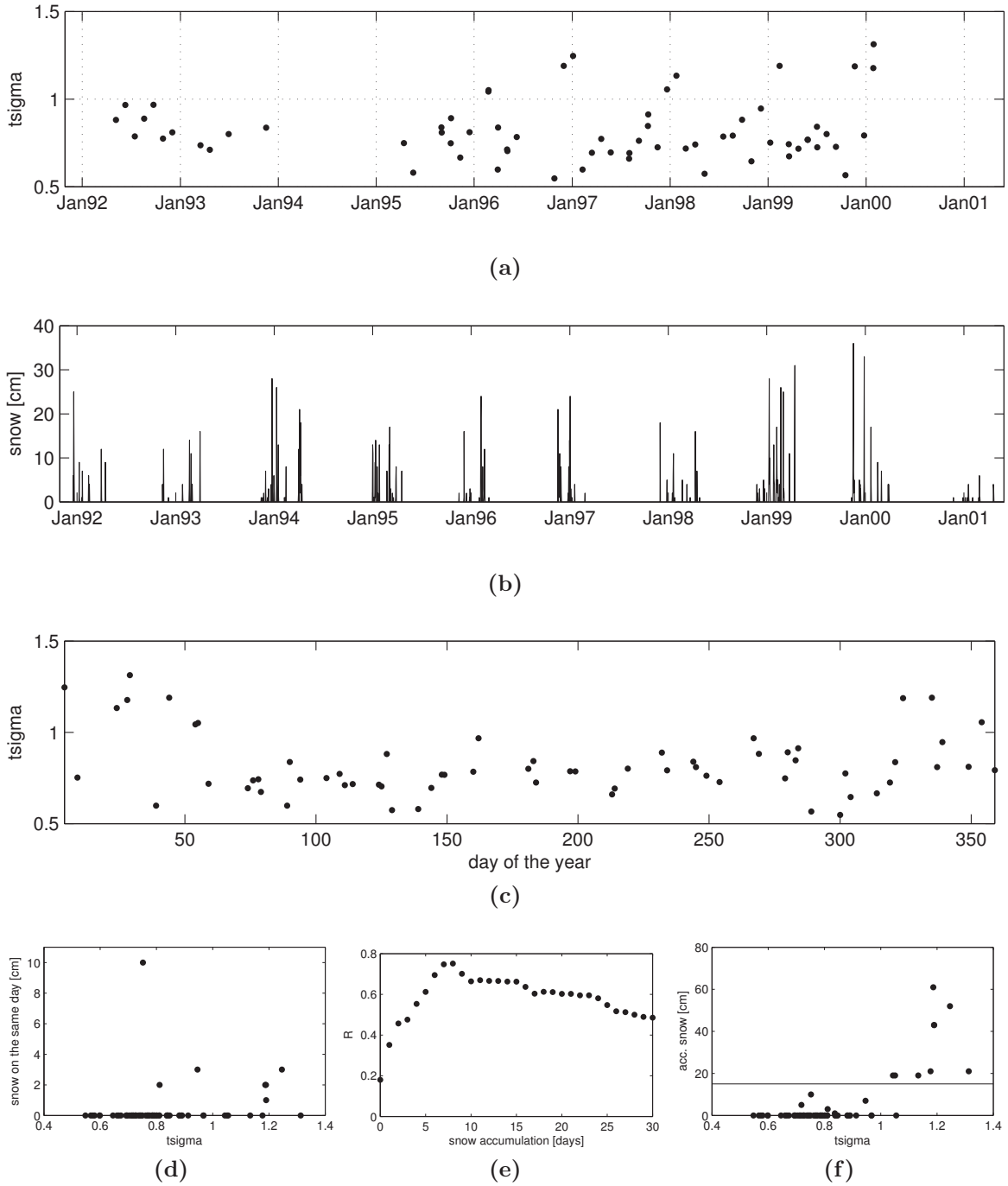

Figure 4.40: Dependency of overall phase quality on snowfall. a) Image quality (tsigma) per image-date. b) Height of fresh snow per day. c) Image quality (tisgma) depending on the season (day of the year). d) Fresh snow of the image acquisition date versus the image quality. $R = 0.18$. e) Linear correlation (R) between accumulated snow and image quality (tsigma) dependent on the days taken into account before the image-date. Best correlation (R = 0.75) is reached when summarizing the fresh snow of 8 days before the image acquisition. f) Accumulated snow of 8 days before the image acquisition versus the image quality (tsigma). The black line indicates the snow-threshold used to remove images of lower quality.

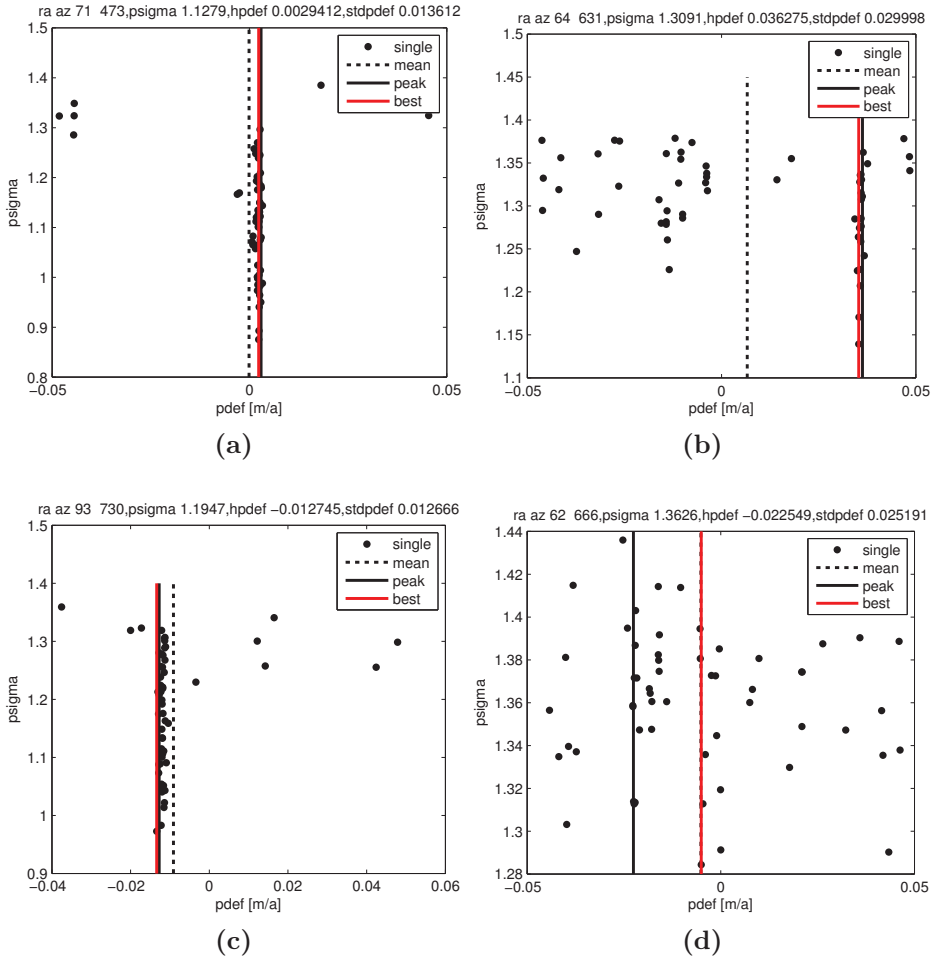

Figure 4.41: Consistency of solutions from 60 stable points towards single points in the landslide area. a) High quality point with low deformation rate. b) Medium quality point with high deformation rate. c) High quality point with high (negative) deformation. d) Low quality point with non-extractable deformation rate.

different reference points. The map of the results of Quadrant B (Fig. 4.42e) shows 16 points distributed over the Avignonet and Harmalière landslides. The distribution of deformation rates gives no hint wether these are plausible results or not. Due to the fact that also the standard deviation of pdef is higher than all results of quadrant A, the results should be considered as relatively unreliable. Quadrant C contains only 3 points with very high displacement rates ($> 2.5\,\mathrm{cm/a}$) and high psigmas (> 1.28) near the psigma threshold. These results are dismissed for the further analysis.

Figure 4.42b shows the standard deviation of the deformation rate (pdef) versus the deformation rate itself. It can be observed that points with higher deformation rates are only present at higher standard deviations. Above the threshold (red line) the results contain all possible deformation rates. Figure 4.42c shows the psigmas versus the deformation rate. All deformation rates below the threshold (red line) stay in a relatively narrow band of deformation rates between -0.15 and $+0.05\,\mathrm{cm/a}$, except the three (dismissed) values of quadrant C.

4.3.2.5 Interpretation of LOS displacements

The displacement rates shown in Figure 4.42d and c only contain the part of the displacement in a 3D-space in the direction of LOS (line of sight of the satellite). For the

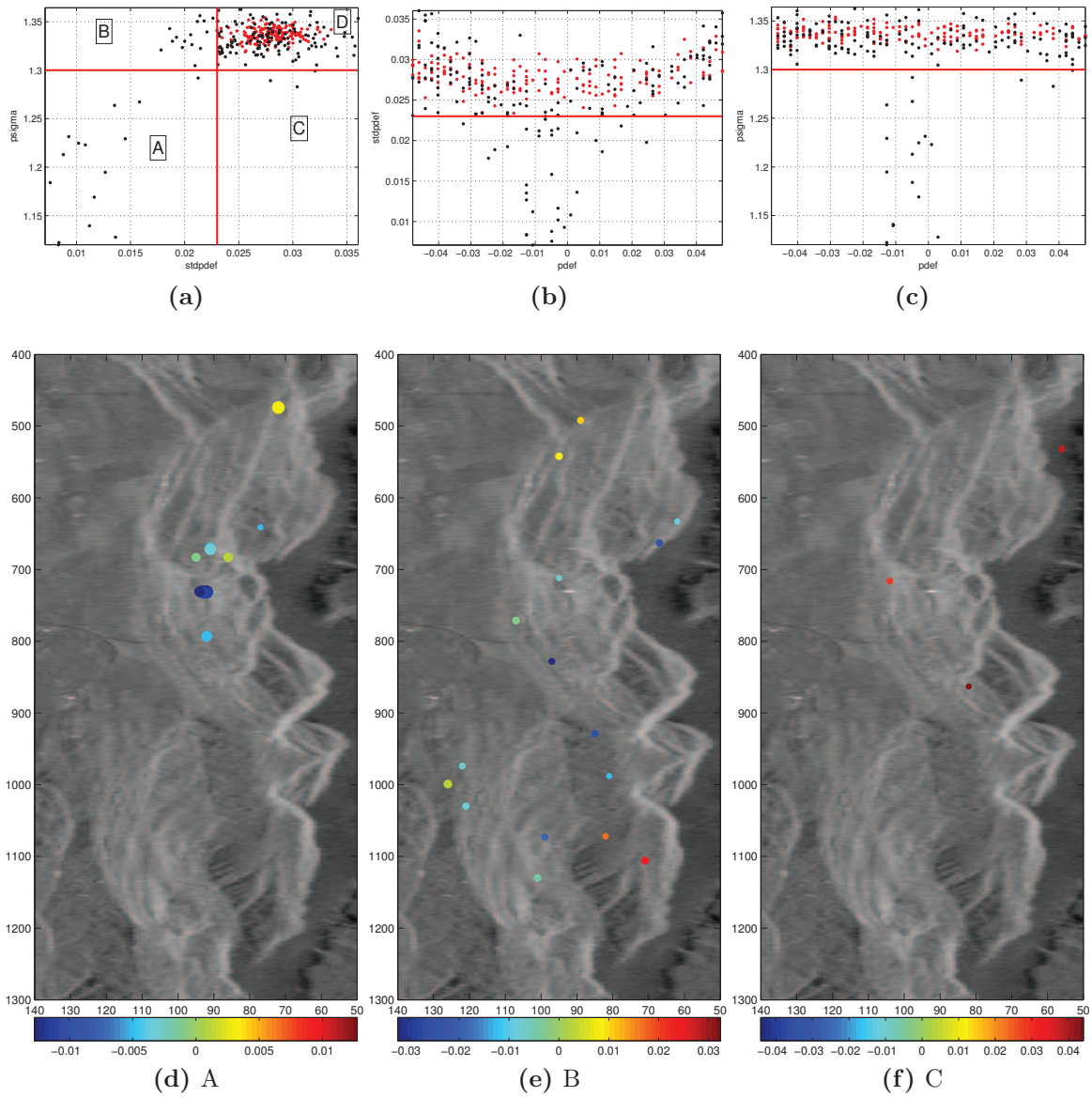

Figure 4.42: Quality filtering of PSI-results

ERS satellites the horizontal component of this vector is perpendicular (right looking) to the descending flight direction (8.55°, NNE→SSW) of the satellite, which is 8.55° counterclockwise from W. The vertical component is inclined by 21.29° (± 0.1°) for the whole image. This value is obtained from the Gamma-software during the co-registration of the SLCs. As seen in the GPS-data and Lidar results the direction of landslide movements at the Avignonet and Harmalière landslides are usually along the down-slope direction. In order to derive comparable displacement rates from the PSI results, the LOS-displacement rates are translated in landslide movements assuming they are along the slope. This leads to velocity vectors elongated by a factor greater than 1 relative to the original velocity in the direction of the LOS. The slope directions are extracted from the same DEM used for the processing of the differential interferometric phases described in Section 2.7.4.3.

In order to illustrate the problems arising from such an interpretation, Figure 4.43 shows the two essential geometrical factors for all SLC-pixel. Figure 4.43a shows the slope angle in LOS-direction. This is the relevant angle for layover and shadowing

effects and directly related to the intensity-values as seen in the averaged MLI (e.g. Fig. 4.39a). Low angles (< -40°, blue) show areas of shadowing. Theoretically full shadows appear below angles of -68.71°, but also higher angles already leading to very low signal reflection. These parts of the images are usually badly co-registered and therefore do not contain utilizable data. Because of that, also the DEM-coregistration is there highly erroneous and leads to wrong altitudes and geographical coordinates in general. That explains also the pixel-wise higher slope angles (red dots in (a)) at the west-ward orientated slopes at the east shore of the lake. if these areas contain results, they are likely to be of random nature and should not be considered. Figure 4.43b shows the exaggeration factor for each image pixel, if a LOS-displacement rate would be interpreted as a landslide velocity along the slope. In the polar plot in Figure (c) every dot represents the slope orientation, slope angle and exaggeration factor of one pixel of (b). The slope orientation is given by the direction from the center and the slope angle is the distance from the center. The solid circles are drawn for the angles 10°, 20° and 30°. For example a flat surface would be represented by a dot in the center and a north-dipped slope by 30° at the top center of the plot. The color represents the exaggeration factor for the conversion from LOS displacement rates into landslide velocities in slope direction. Slope vectors perpendicular to the LOS can not be interpreted in that way because they would lead to an infinite exaggeration factor. In other words a displacement rate in LOS can not be caused by a movement perpendicular to it. The dotted circle shows all slopes matching that condition. Interpreted velocities near that slope conditions should be used carefully because small errors will be seriously exaggerated. And also, if displacement rates are partly due elevation or subsidence of blocks (e.g. due to rotational landslides), the interpreted velocity would be highly misleading especially near that critical slopes. As an example, a displacement rate of 2 cm/a on a slope of 18° towards E would be interpreted as a landslide velocity of 40 cm/a (factor 20). If 1 cm/a of that displacement rate is due to an elevation of the sliding block, the landslide velocity would be only 20 cm/a. Another problem arises for flat areas in the center of the plot. On flat areas the orientation of slopes is less robust, e.g. rotation of the surface by 1° can change the orientation from 0.5° towards E to 0.5° towards W. As the exaggeration factor highly varies around the plot center, small changes in slope orientation will lead to very large changes of the interpreted landslide velocity. As a conclusion of this short discourse it can be said, PSI results near the red areas of Figure 4.43b and at gentle slopes should be interpreted with caution.

Finally the PSI displacement rates are interpreted as landslide velocities and are shown in Figure 4.44. The map in (a) shows the velocities from the 16 high-quality points of category A in blue and the 16 low-quality points of category B in red (see Figure 4.42a for the definition of A and B). The interpreted velocities are between 0.6 cm/a and 35 cm/a. The blue results seem somehow consistent with a few exceptions probably due to the interpretation step. The results of A are shown in the circular plot (b). The color represents the slope angle in LOS direction would therefor indicate problematic slope orientations with respect to layover and shadowing. All results are not affected by layover (red) or serious shadowing (blue). For the interpretation step, the slope orientations need to be not near the critical slopes indicated by the dotted circle. Some of the slopes dipping nearly 20° eastwards and are prone to an ambiguous interpretation. It should be highlighted that for the eastwards oriented slopes (almost all in the Avignonet landslide) an upslope velocity (like the one in the very NE) could also be a subsidence. The ambiguous interpretations will be addressed in the following by comparing them with GPS-derived velocities along profiles. The low-quality results (red lines) seem to be not plausible for the majority of points. But as no other results

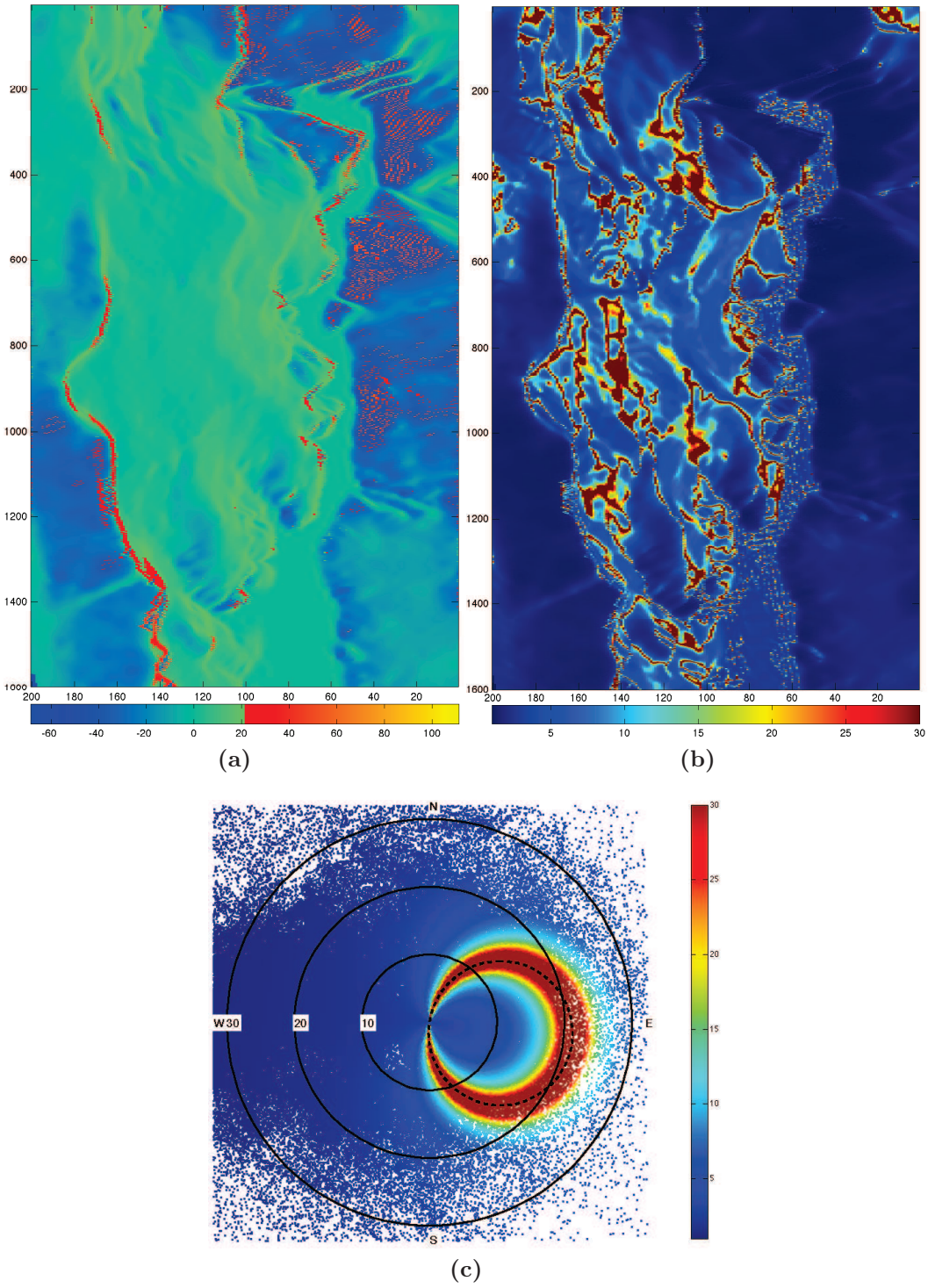

Figure 4.43: Geometrical factors for the interpretation of LOS-displacement rates into landslide velocities in slope direction. a) Slope angle in LOS-direction per pixel of the SLC. It reflects the theoretical quality of the reflected Radar-signal from the satellite. The discontinuity in the colorbar reflects the critical inclination angle of the satellite (21.29°). b) Exaggeration factor in each SLC pixel if the displacement rate is interpreted as a landslide velocity in a general slope direction. c) Polar plot of the exaggeration factor from (b). The distance from the center is the slope angle, the direction from the center is the slope orientation and the color represent the exaggeration factor. The dotted circle indicates the critical slopes where the factor would be infinite.

are available in Harmalière some of them will be more carefully addressed if they are reliable. The circular plot (c) reveals that no results are in a layover area (red), but two results are more close to shadowing (blue) with slope angles in LOS direction as low as -23° and -12° (44° and 33° with the LOS vector). Also some of them are highly ambiguous for the interpretation along the slope (very near to the dotted circle).

In the following the PSI-results from category A will be discussed at four locations (A1-A4) in greater detail. The positions of A1-A4 are shown in Figure 4.44a. The first location A1 is at an ensemble of farm-houses in the center of the Avignonet landslide. Figure 4.45a shows a 200x200 m close-up of the Lidar-derived shaded relief including houses and trees. This location contains 7 PSI-landslide velocities between 9 and 31 cm/a which are shown in blue. The shaded relief reveals the shapes of houses near the PSI results which are surely the origin of the permanent scatterers. However the PS-positions differ from the positions of the houses by about 40 m, which are about 2 pixel in azimuth in the SLC. This seems to be in a reasonable magnitude of error considering that the coordinate transformation from SLC-geometry to geographical coordinates is based on the co-registration of a DEM with 50 m resolution. The red velocity vector is coming from biannual GPS-measurements(App. A.5). The distance to the houses, the source of the PSI results, is less than 40 m and therefore feasible for a comparison. The circular plot (b) shows the slope orientations of the PSI positions (blue). The PSI-points closer to the critical slopes (dotted circle) correlate with the ones E of the road (7, 8, 9) because they are are on steeper slopes. The red GPS-point shows the direction of the velocity (and not the slope orientation at the GPS position), which is on the critical circle. That means the velocity-vector obtained by GPS is steeper than the slope. The problem here is, the GPS-velocity can not explain the PSI-displacements or the other way around, the PSI-results could not interpreted as velocities along the GPS-vector. This is also illustrated in the profile view (c). The profile is obtained along the green line in (a). The red GPS-vector is steeper than the slope. The LOS-displacements in LOS direction are almost identical between 1.1 and 1.3 cm/a (barely visible small black lines at the blue PSI vectors). But the interpreted PSI-velocities (blue vectors) increase rapidly with increasing slope angles from W to E. An interpretation of the PSI-displacements along the slope is here misleading, but the discrepancy between the GPS- and PSI-results remains. The only interpretation of the PSI-displacements resulting in more feasible absolute velocities (near the GPS-velocity) would be in an upwards direction (relative to the slope). Figure (d) addresses the question if the PSI-results contain information about the non-linearity of displacements. This is done by comparing the GPS-displacements in LOS-direction (red) with the residuals of the PSI-solutions (black and blue). As the GPS-measurements started in 1996 and the PSI-results end in 2000, only the relatively short overlapping is shown. The black lines are the residuals of the 7 PSI-solutions and the blue line is the average of them. Two negative peaks of the GPS-displacements at Autumn 1997 and Autumn 1998 seem to correlate with positive peaks of the PSI-residuals, but considering the whole timeline it remains highly speculative.

The location A2 is situated in the small village in the southern part of the Avignonet landslide. Figure 4.46a shows a 200x200 m close-up of the shaded unfiltered Lidar DEM showing the shapes of several houses near the two PSI-results (blue). Considering the positional uncertainty at A1, it can not be said which house exactly is the source for the PSI. The next available GPS displacements (red) are within 100 m. The circular plot (b) shows slope-directions at the PSI positions of about 10° and not near the critical slopes (dotted circle). An interpretation of LOS-directions in velocities along slope direction is therefore more robust. The exaggeration factors for that interpretation

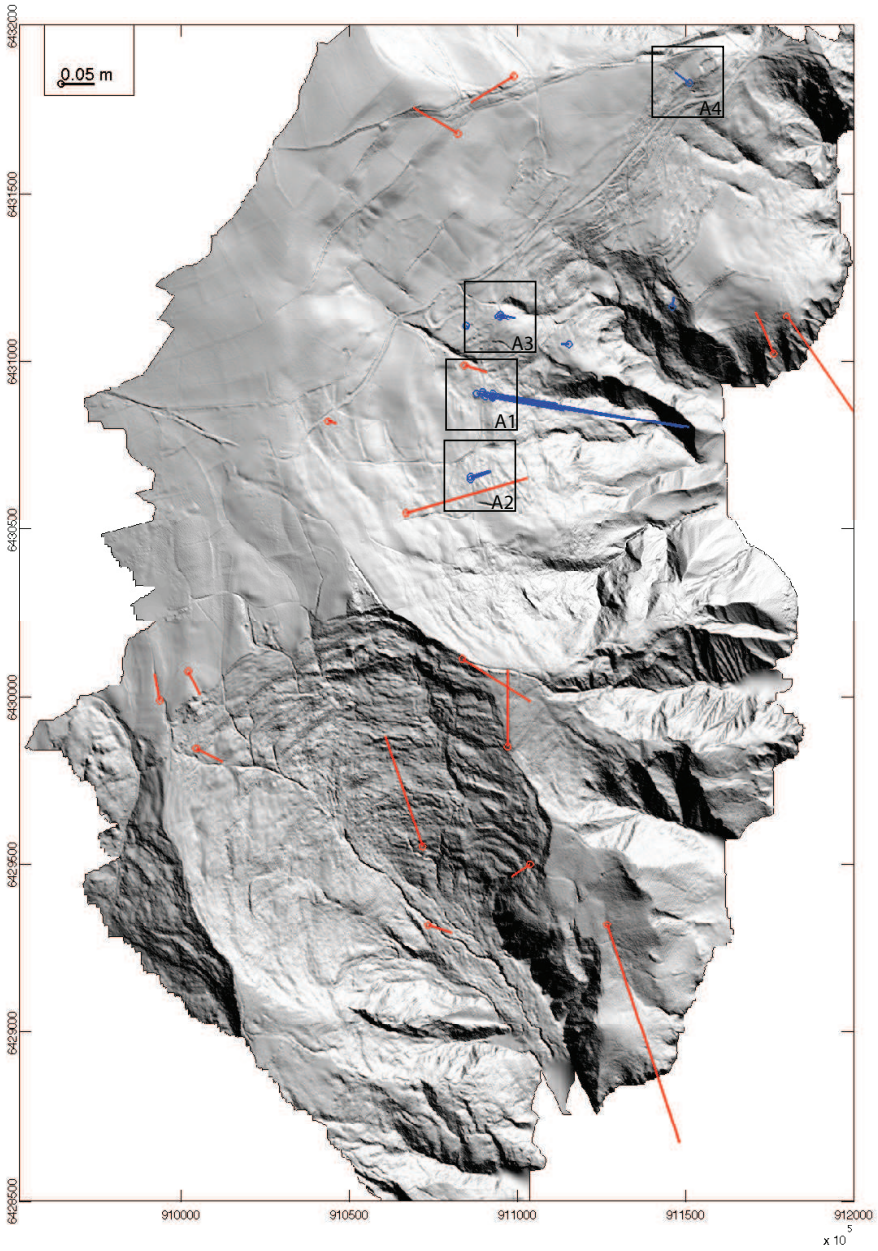

(a)

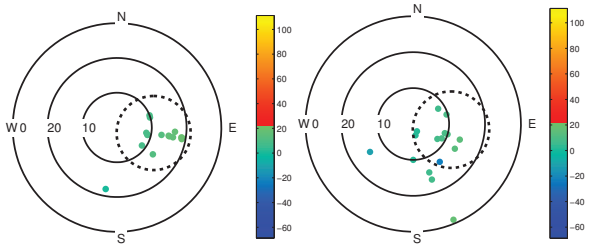

(b) A, blue **(c)** B, red

Figure 4.44: Landslide velocities interpreted from PSI displacement rates. a) Map of Avignonet and Harmalière landslide with landslide velocities from results of quadrant A (blue, higher quality) and quadrant B (red, lower quality). See Figure 4.42 for the distinction between A and B. b+c) Circular plots of slope orientation. The color represents the slope angle in LOS direction and indicates slopes prone to layover (red) and shadowing (blue). The dotted circle marks slopes perpendicular to the LOS.

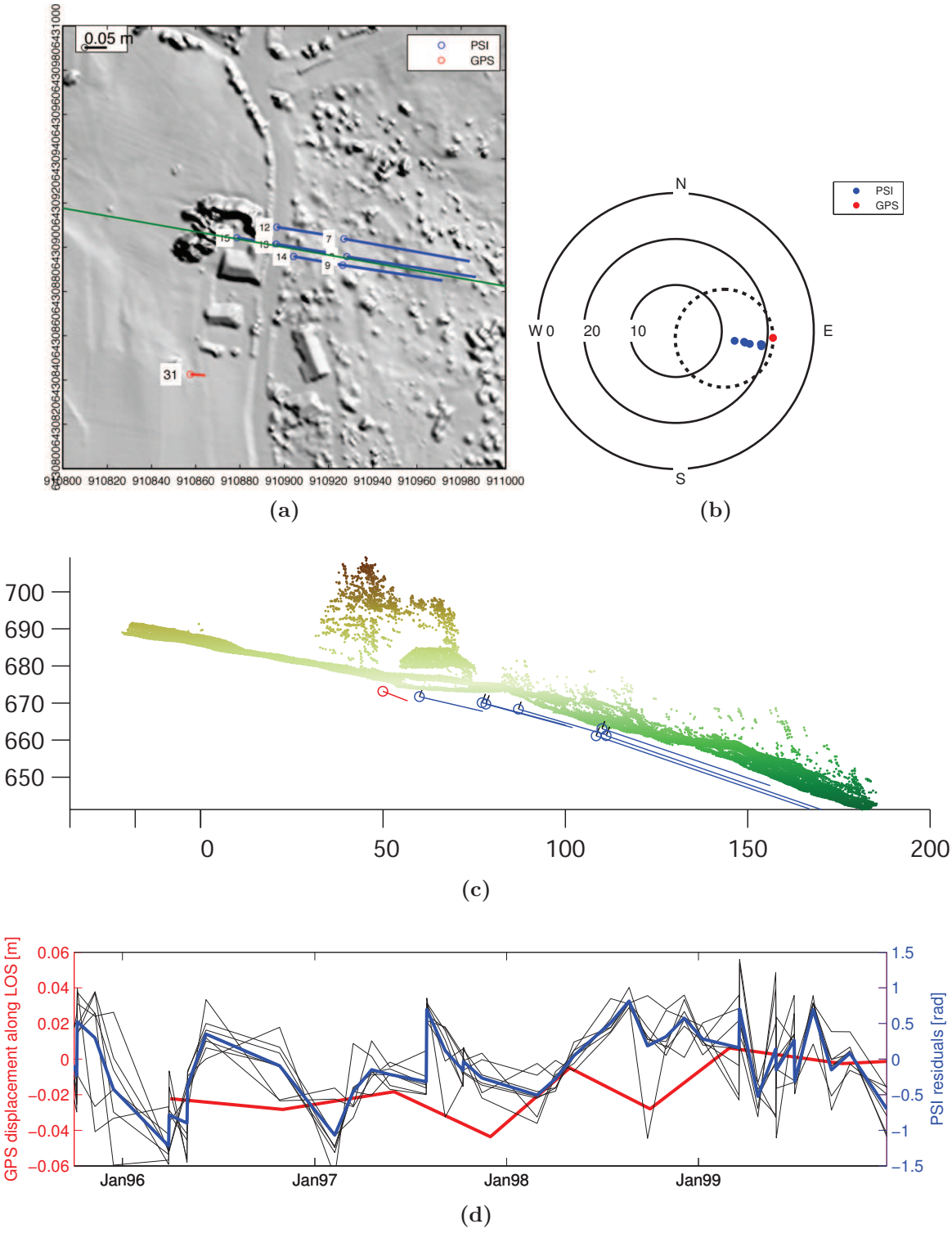

Figure 4.45: PSI results at A1 (overview in Fig. 4.44) a) unfiltered Lidar DEM with interpreted LOS-displacements (blue), GPS-displacement (red) and profile location (green) b) circular plot of PSI- and GPS-displacement orientation c) DEM cross-section with PSI- and GPS-displacements, the displacements are plotted below the terrain-surface for better visualisation, the shorter black lines at the PSI-displacements indicate the LOS-displacements. d) time-series of the portion in LOS-direction from the GPS-displacement (red), the PSI-residual phases per point (black) and the average PSI-residuals (blue)

are 6.1 and 6.6. The velocities shown in the profile (c) from the PSI (3 cm/a) and the GPS (4 cm/a) are comparable. Even the increased velocity down-slope follows the general trend of that area. The comparison of GPS-displacements in LOS-direction with PSI-residuals in (d) does not reveal any relationship.

The location A3 is situated at a small ensemble of houses about 300 m north of A1. The shaded relief 4.47a shows 3 PSI-results (blue) about 50 m NE of their probably source, the two bigger houses together with the paved road in front of them, which form a right-angled structure more or less towards the LOS (SE). Also a GPS-point (red) is available within 50 m. The circular plot shows that an interpretation of the PSI-results (blue) along the slope direction is robust (not near the dotted circle). However, a interpretation in the direction of the GPS-vector would be difficult (red dot is near the dotted circle). The profile (c) shows an increased slope angle (18°) eastwards of the road and a well aligned GPS-vector along that slope. The PSI-results are at a more gentle slope (10°). The LOS-displacements are between 0.3 and 0.5 cm/a exaggerated to in-slope velocities of 1.3-2.3 cm/a. The GPS-velocity is 2.9 cm/a. The timeline of GPS-displacements and PSI-residuals (d) does not show any relation.

The location A4 is at the north limits of the Avignonet landslide. The 200x200 m shaded relief map 4.48a shows this single PSI-results and about 40 m SE its probable source, a single house at the paved main road. Less likely the two houses in the NE, 100 m away from the PSI-result could be the source too. (b) reveals a general slope towards SE with angle of 13° (blue dot). As seen in the profile (c) the PSI-deformation rate of 0.3 cm/a is, unlike in the cases A1-A3, away from the satellite (black line at blue dot). Strictly interpreted in slope direction the resulting velocity would be 3 cm/a up-slope (blue vector). As this is not feasible at all, the swarm of black lines shows possible interpretations of the LOS-displacement in other directions. For example a down-slope direction combined with subsidence would be a much more feasible interpretation.

From the analysis of the locations A1-A4, it can be concluded that a detailed analysis of PSI-results is only possible if (1) the PSI-results are reliable in itself (low psigma and low stdpdef), (2) the PSI-results are spatially reliable (a cluster of PSI-results with similar displacements) and (3) movement directions are available from other sources like GPS. Even if all these conditions are met, the interpretation remains highly speculative. For an analysis of single PSI-results from the lower quality points of category B, all three conditions are worse. (1) The PSI-results in itself are less reliable (higher psigma and stdpdef), (2) the PSI-results can not be proven for its spatially reliability because they are not clustered (see Fig. 4.44a) and (3) especially for the more interesting results of Harmalière no other measurements are available. The Lidar-displacements can not be used for that, because (1) they are obtained more than 6 years after the SAR images and (2) at slow movements (< 10 cm/a) as observable by PSI-techniques they are quite vague. The weak points of the PSI-technique used in this work are reviewed in the next section together with suggestions for improvements.

4.3.3 Discussion

Several aspects of the used PSI technique and its applicability to slow moving landslides needs to be addressed, (1) the conditions of the ground for permanent scatterers, (2) the geometry of the slopes, (3) non-linear displacements and (4) the quality control (or error analysis). The ideal conditions are right-angles of big concrete structures like a paved road with adjacent houses with orientation towards the look direction of the satellite. Together with perfectly linear displacement rate, the sigma would be near zero. More interesting is the lower end of the conditions. In order to analyze this properly it

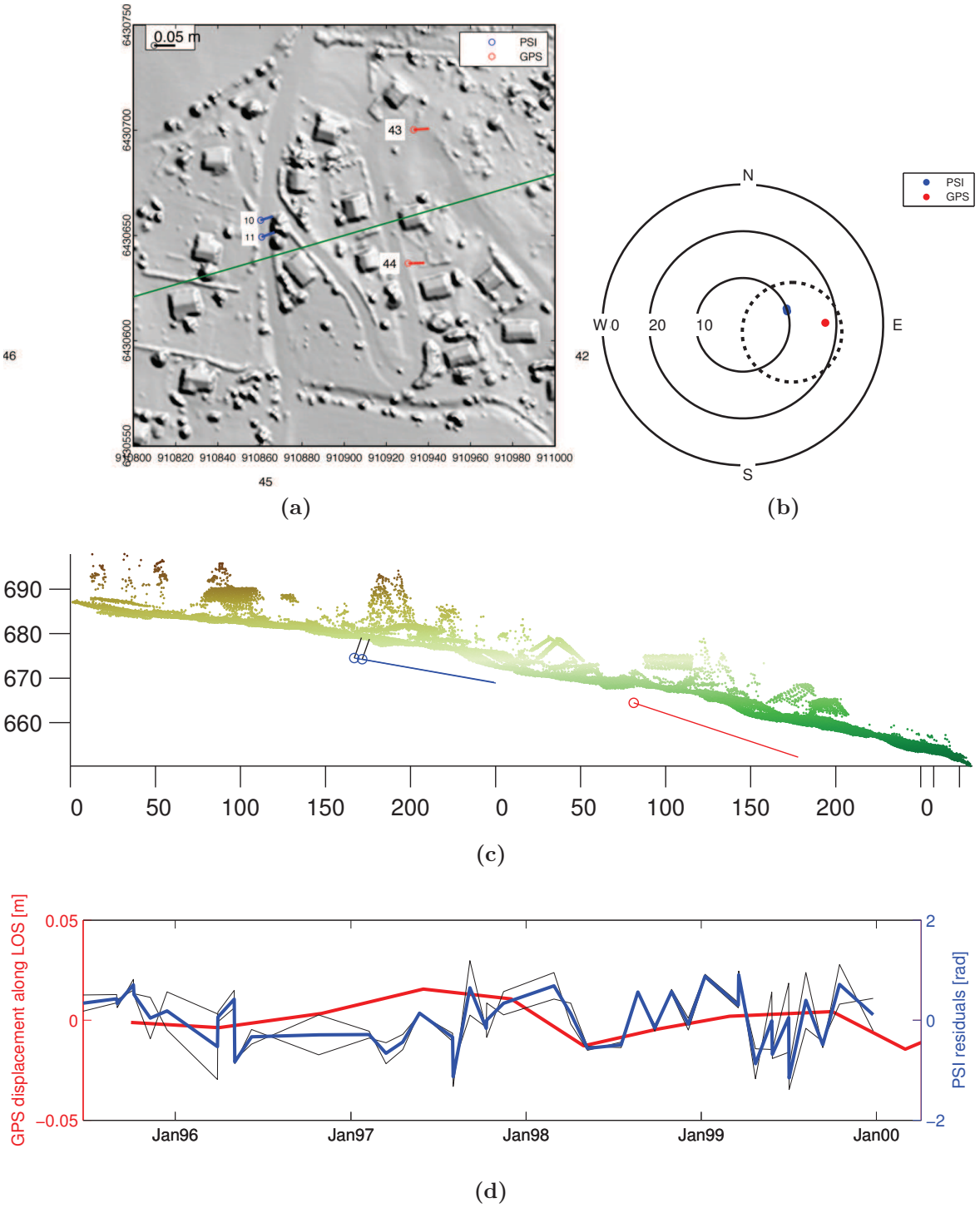

Figure 4.46: PSI results at A2 (overview in Fig. 4.44) a) unfiltered Lidar DEM with interpreted LOS-displacements (blue), GPS-displacement (red) and profile location (green) b) circular plot of PSI- and GPS-displacement orientation c) DEM cross-section with PSI- and GPS-displacements, the displacements are plotted below the terrain-surface for better visualisation, the shorter black lines at the PSI-displacements indicate the LOS-displacements. d) time-series of the portion in LOS-direction from the GPS-displacement (red), the PSI-residual phases per point (black) and the average PSI-residuals (blue)

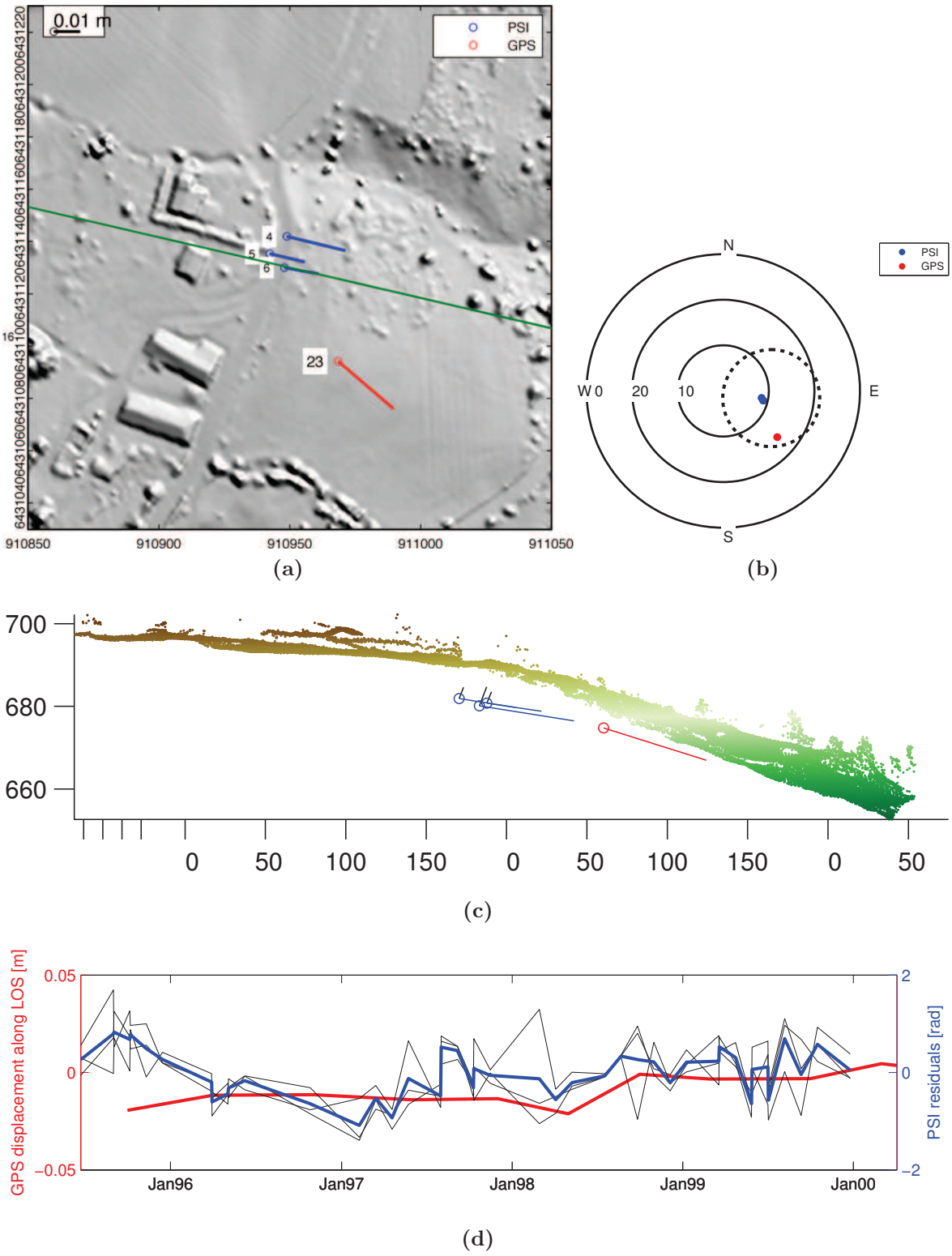

Figure 4.47: PSI results at A3 (overview in Fig. 4.44) a) unfiltered Lidar DEM with interpreted LOS-displacements (blue), GPS-displacement (red) and profile location (green) b) circular plot of PSI- and GPS-displacement orientation c) DEM cross-section with PSI- and GPS-displacements, the displacements are plotted below the terrain-surface for better visualisation, the shorter black lines at the PSI-displacements indicate the LOS-displacements. d) time-series of the portion in LOS-direction from the GPS-displacement (red), the PSI-residual phases per point (black) and the average PSI-residuals (blue)

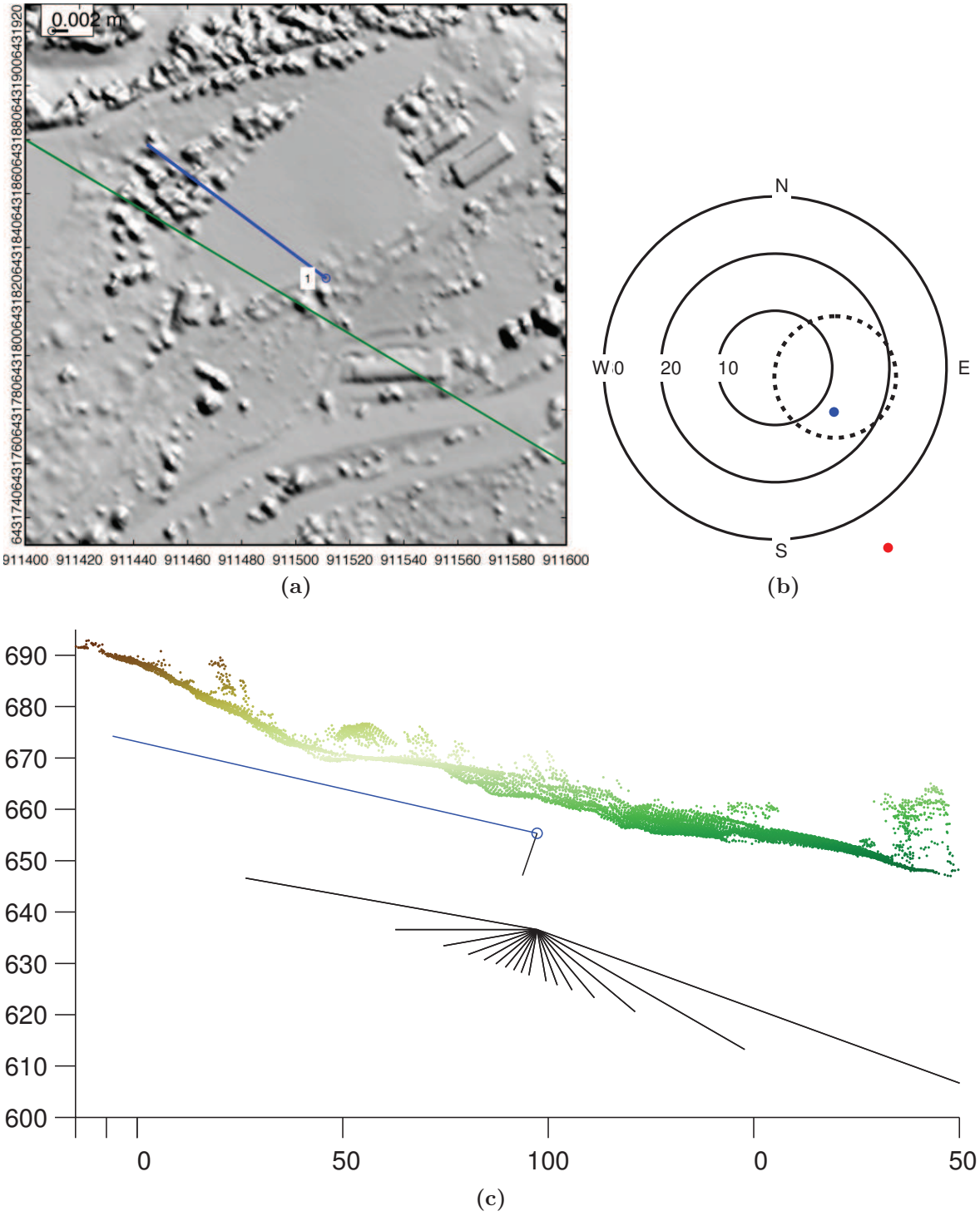

Figure 4.48: PSI results at A1 (overview in Fig. 4.44) a) unfiltered Lidar DEM with interpreted LOS-displacement (blue), GPS-displacement (red) and profile location (green) b) circular plot of PSI- and GPS-displacement orientation c) DEM cross-section with PSI- and GPS-displacements, the displacements are plotted below the terrain-surface for better visualisation, the shorter black lines at the PSI-displacements indicate the LOS-displacements. The fan of black lines represent the ambiguity of interpretations of the LOS-displacement in other directions than the terrain slope.

could be helpful to test the detection of PS in a test area as free as possible from influences leading to residual phases, like ground movements, atmospheric turbulences and mountainous areas. A parallel geometric analysis of a Lidar-derived DSM from that area in comparison with the derived PS-points could clarify the minimum preconditions necessary for the detection of PS-points.

The next problem is the ambiguity of the derived LOS-displacement. In cases like the subsidence of Grenoble this is less a problem, because the direction vector of the phenomena is relatively clear. For landslides the direction of the movement is usually more complex. One solution could be the analysis of ascending and descending SLCs in order to derive to displacement vectors along two different LOS. Starting from a surface point at a landslide the knowledge of one LOS-displacement leads to the ambiguity of the moved point on a planar in the 3d-space. With the knowledge of a second LOS-displacement from that same surface point the ambiguity is limited to a linear in the 3d-space. In order to derive an unambiguous solution towards a single point it can be assumed that the movement takes place along a vertical planar in slope direction. The point of intersection between the linear and the planar would give the final displacement direction in the 3d-space. The necessity of a ascending and descending PS-point for the same location would likely decrease the amount of derived displacements, because (1) the geometrical orientation of the slope would have to meet the restrictions for both orbits (layover, shadowing) and (2) the derived PS-points from both orbits need to be at the same geographical location. The narrow passage at the Avignonet landslide is probably the second restriction, because many of the PS-points are maybe related to an eastwards oriented right-angle between a road and a house (see examples A1-A4). Looking from an ascending orbit (approximately from W) it can be expected that for the most of those locations no accompanying PS-points will be found.

As the detection of PS is based on a low sigma of a linear regression depending on a linear deformation rate, any non-linearity in the movement of the landslide decreases the chance of finding a PS. Figure 4.49 illustrates on the left four examples of displacements using the classical approach of one linear regression using all images, (1) a linear displacement which leads to a low sigma and would be successfully detected (green), (2) a non-linear displacement for example due to a larger movement on a specific date, (3) a discontinued displacement due to the loss of a PS for example due to a grown tree in front of a building and (4) a seasonal movement for example because of a geometrical change of the permanent scatterer due to temperatures. A seasonal accelerating of a landslide would still fit in the first linear case, because an acceleration would not lead to movements back and forth, but all soil and structural movements due to changes in temperature, groundwater level or even air moisture could lead to seasonal effects. An approach to still find permanent scatterers affected by non-linear displacements could be to search for linear regressions using shorter time-windows. An idea about the minimum image-number used per sub-set gives Figure 4.39c. The sigma value of the random dataset (red) decreases more rapidly when removing more than 40-50 images from the whole dataset of 65 images. This means that using time-windows with less than 15 images could more easily lead to false detected linear regression at random points without any meaning. The average time-span for the ERS-dataset is 45 days, so the time windows should not be shorter than about 2 years, but could be realized by a moving window e.g. with an offset of 45 days. In order to find PS affected by seasonal movements, the linear regression could be made using sub-sets of image-dates depending on the season. The seasonal behavior of the GPS displacement at A1 (Fig. 4.45d, red curve) could be a hint that such effects actual exists at the study site. All Figures 4.45d, 4.46d and 4.47d of the locations A1-A3 could not show

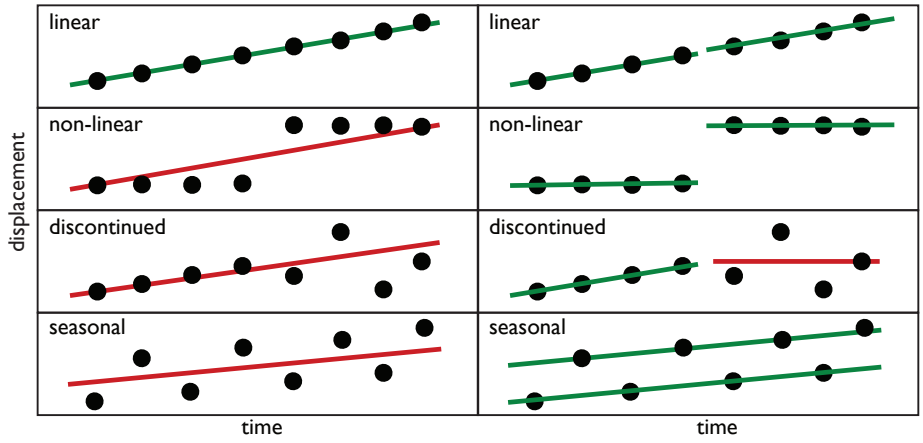

Figure 4.49: Effect of non-linear displacements on sigma in the PSI approach. Each point represents a phase (or displacement) of a permanent scatterer at one date. The lines show the best linear fit. Red lines are bad fits with a high sigma and green lines are good fits with a low sigma. The left examples using all dates for one fit, the examples on the right using multiple fits on sub-sets of dates.

a good correlation between GPS-displacements and PSI-residuals. On the one hand the overlapping time is too short for a statistical evidence, on the other hand the biannual sample-resolution of the GPS is too low to redraw the peaks of the PSI-residuals. In theory, if the PSI-residuals are exclusively due to non-linearity of displacements, downward peaks in the GPS-displacement timeline would lead to positive peaks in the residuals. This is maybe the case at the already mentioned location A1, but remains highly speculative. A longer and displacement time-line of higher resolution, e.g. from a permanent GPS, near a permanent scatterer would be needed for a proper analysis of such a relation.

Another important issue is the quality control of the PSI-results. Figure 4.42a on page 171 shows that the stdpdef-value of the category B solutions is relatively high, but below the solutions from the random dataset. It means that the majority of pairs towards one of those target points leading to a similar deformation rate pdef. The question is why are many other pairs leading to wrong solutions. Looking at the sigma-matrix of a single solution of lower quality like the one in Figure 4.35 on 160, it can be seen that there are several minima. The lowest minima is used to determine the best model. But for example the model at the second lowest sigma could be the right one. The idea is to correct the network of reference points to a single height and ϕ_0 before doing the regression towards a target point. By doing that the sigma-matrices of all solutions towards a target could be stacked and if their is a non-random minima it should become visible. Sigma minima at random pdefs would be insignificant in the stack even if they are dominant in a single solution.

4.4 Discussion

In the previous sections it was shown that the aerial photos, Insar technique and most of all the Lidar displacements provide some new information on the landslide kinematics. In this section those results will be first compared to the previous acquired GPS data and the derived displacement zonation on which have relied some of the recent risk management decision in Avignonet (Requillart and Moulin, 2004). Then conclusions are made about the present geometry and kinematics by connecting new insights with previous results from literature. Finally, the present state is compared to the long-term evolution of the basin in order to shape a coherent explanation for the spatial and temporal development of the two landslides since the last ice-age and what that could mean for the future.

Figure 4.50 shows a topographic map of the populated part of the Avignonet landslide containing three major settlements, the camp site in the north, le Cros in the middle and le Mas in the south, which was newly built starting in 1970 (Requillart and Moulin, 2004). After the main event of the Harmalière landslide in 1981 and increasing damages (cracks, deformation) at houses and infrastructures in Avignonet, drainage systems were established between 1984-1991 (blue lines and dots) in order to decrease the pore-pressure and the sliding possibilities at the shallow rupture surfaces. It turned out to be not sufficient. From 1995, biannual GPS-measurements have been performed in order to quantify and monitor the landslide velocities. The GPS-velocities together with borehole inclinometer measurements were used to define four zones with different levels of deformation rate (Fig. 4.50). West of Zone 1 the displacements are insignificant (<1 cm/a) (green), Zone 1 moves with 1-3 cm/a (yellow), Zone 2 with 3-9 cm/a (orange), Zone 3 with 9-16 cm/a (red) and Zone 4 does not significantly move (green). To explain the downward increase of velocity, an interpretation is that there are imbricated surface ruptures at different depths (Fig. 4.51b). There are evidences of such localised shear zones from observation of the inclinometric tubes. Shallow slip surfaces are coexisting with deeper slip surfaces so that their cumulative displacements produce a downhill increase of surface displacement from zone 1 to zone 3. Zone 4 would not show significant displacement because of the disappearance of the clay, uncovering the compact alluvial layer.

These zones are compared to the recent Lidar displacements and GPS-velocities using the same timespan from Oct-Nov 2006 until April 2009. The colours of the circles of the GPS-measurements represent the zones to which they would belong using the categories mentioned above. The same four colours are used for the Lidar displacements in the background. As the Lidar displacements reveal also higher velocities than Zone 3 (>16 cm/a), such areas are coloured in magenta. Requillart and Moulin (2004) mentioned an acceleration of the Zone 3 up to 20 cm/a starting in 1999. The recent GPS-measurements instead show that there is no velocity which would fall into Zone 3, suggesting a slow-down. Furthermore all GPS-measurements in Zone 2 are in 2006-2009 below 3 cm/a (yellow) which would relate to Zone 1. In Zone 1 the velocities match with one exception in the west of le Mas. Following the logic of Figure 4.51 it would mean the movement along the rupture surface between Zone 1 and Zone 2 has stopped or nearly stopped moving.

Coming to the Lidar displacements it should be mentioned that the reliability is 0.2 m as its best (see Sec. 4.2.4) which is equivalent to about 10 cm/a. Consequently, Zones 1-3 are indistinguishable using the Lidar-results and only velocities above 16 cm/a (magenta) can carefully be considered to be significant. At first glance,

velocities seem to be much higher than those provided by GPS. But looking closely at the GPS-positions, almost everywhere the velocity from the Lidar-displacements are similar in the direct vicinity. While the lidar displacements are not robust enough to improve the zonation, they can help to understand the mechanisms on a broader view.

Figure 4.51a shows a typical section across a slope in laminated clays based on observations of various landslides in the Trièves (Giraud et al., 1991). It consists mainly of three types of movements: (A) surface movements, slow to more-or-less rapid mudflows with a lobate shape wherein the original laminated clay structure has been completely destroyed, (B) planar sliding with rupture surface parallel to the slope, controlled by seasonal changes of the pore-pressure with rainfall and melt-water infiltration along fissures, which opened up in dry periods, (C) deep rotational slides, usually with continuous slow movements along slip surfaces deeper than 20 m (Giraud et al., 1991). It is tried to identify these movements along the cross-section of the Avignonet landslide (Fig. 4.51b) using scarps, GPS-velocities, slip surfaces in inclinometer data and Lidar surface displacement vectors. The scarps F1-8 were identified on the shaded Lidar-DEM (Fig. 3.19) and on the slope-map (Fig. 3.16). Because of their spatial extend they need to be related to the deeper movements of type B or C. Displacement rates are calculated for scarps F1-8 by subtracting the velocities of GPS-measurements (G40-G48) of the adjacent blocks. If several GPS-stations are on one block the average value of those GPS-stations is taken. The main clay body west of F1 is assumed to be stable. Because the block between F2 and F3 contains no GPS-station, the difference between the GPS-velocities of G46/47 and G48 can not be clearly assign to F2 or F3. The slip-surface appearing at F4 can be assumed to be dormant, because the adjacent blocks contain similar velocities and the scarp height is not as significant as the others. T0-T2 represent boreholes with slip-surfaces identified in inclinometer measurements. The compacted alluvial layers (CAL) which outcrops in the east are found at the bottom of T1 and T2. Finally slip-surfaces are interpreted from all significant scarps F1-8 ($>$ 1cm/a) so that they match with the slip-surfaces found in the boreholes. The resulting geometry suggests a slow deep seated rotational sliding along F1 which outcrops near the top of the alluvial layers. The maximum depth is 43 m at T0. The second intermediate slip-surface F2 seems to be of type B, resulting in intersected blocks sliding along the planar slip-surface. The lowest distinctive block below F5 is affecting le Mas. Below F6 the movements are dominated by shallow, fast and more irregular movements indicated by the higher variability of velocities from the GPS-measurements (G41, G42) and the Lidar displacements (Zone 3, Fig. 4.50). The Lidar displacement vectors (taken from Fig. 4.23 and 4.24) shown above the toe of the landslide indicate small rotational movements of higher velocity (up to 20 cm/a). Before coming to possible scenarios for the future of the Avignonet landslide, some aspects about the general evolution of the landslide since the last ice-age needs to be addressed.

Figure 4.51c shows a cross-section of the Avignonet landslide in a larger context. The whole valley is 3-4 km wide based on jurassic bedrock. As shown in chapter 3, the valley is divided by a paleo-topographic bulge. The compacted alluvial layers on top and east of that bulge are from the former Drac de Cros deposited until the end of the Riss glacial period (Monjuvent, 1973). They will be called CAL1 in the following. The compacted alluvial layers west of the bulge, deposited during the Würm glacial period from the Drac de Sinard and were later covered by the laminated clays of the Lake

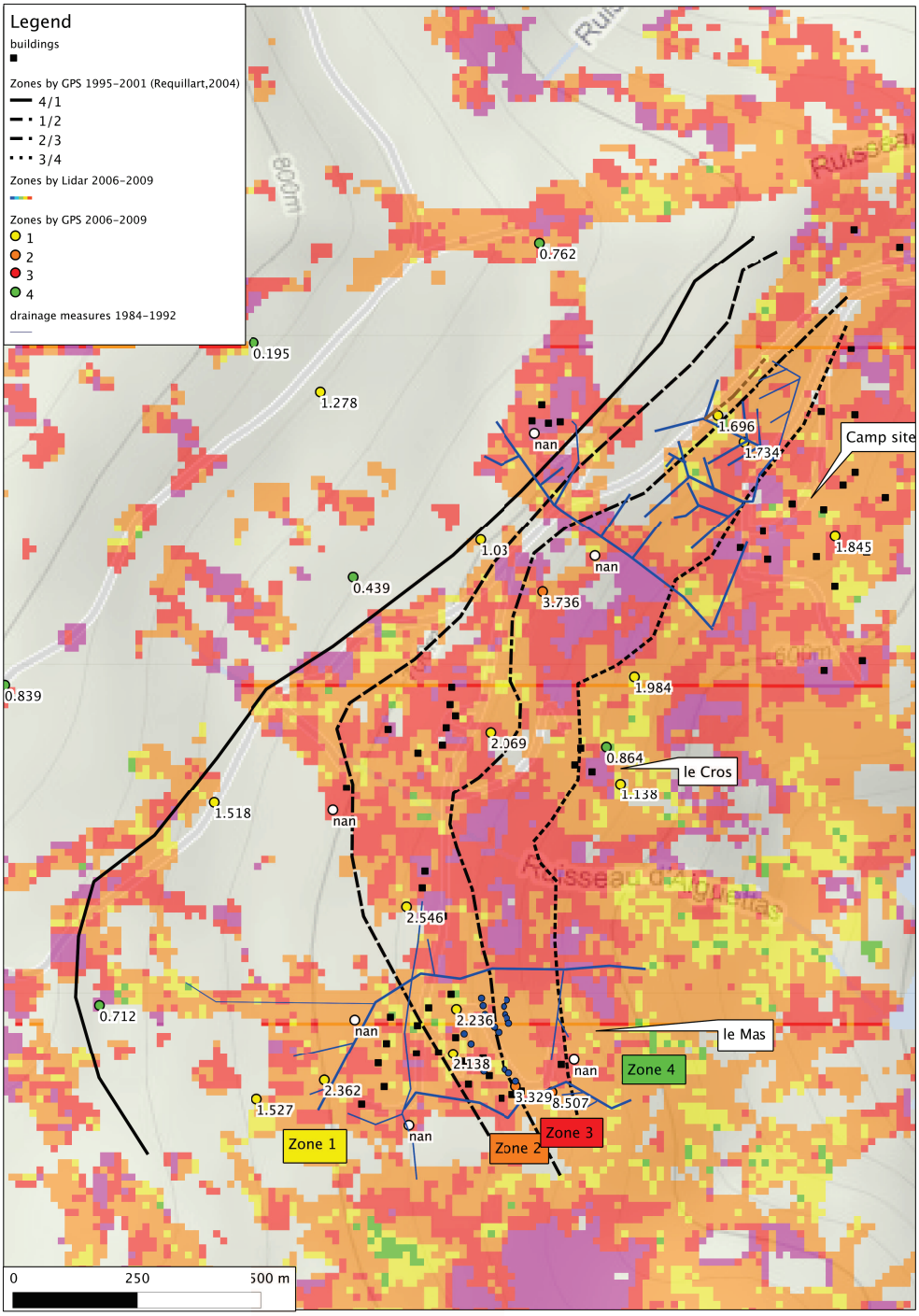

Figure 4.50: Displacement rate zones at Avignonet by landslide velocities as defined in Requillart and Moulin (2004): Zone 1: 1-3 cm/a (yellow), Zone 2: 3-9 cm/a (orange), Zone 3: 9-16 cm/a (red), Zone 4: non significant (green). The 4 black lines show these zones from (Requillart and Moulin, 2004), which are based on GPS-measurements between 1995-2001. The round circles show the locations of the GPS-measurements colored after the same velocities, but using the GPS-data of the timespan between the Lidar campaigns (2006-2009). The GPS-points are labeled with the GPS-velocities in cm/a. The partially colored background shows the zonation obtained from the Lidar displacements. Lidar displacements show that same color scheme than GPS except for those higher than 16 cm/a are colored in magenta. Note that only the magenta Lidar measurement are really significative according to the incertainty level reported in section 4.2. Areas without Lidar-results are left out and reveal the underlying topographic map with contour lines and streets. The blue lines and dots represent drainage measures installed between 1984 and 1992.

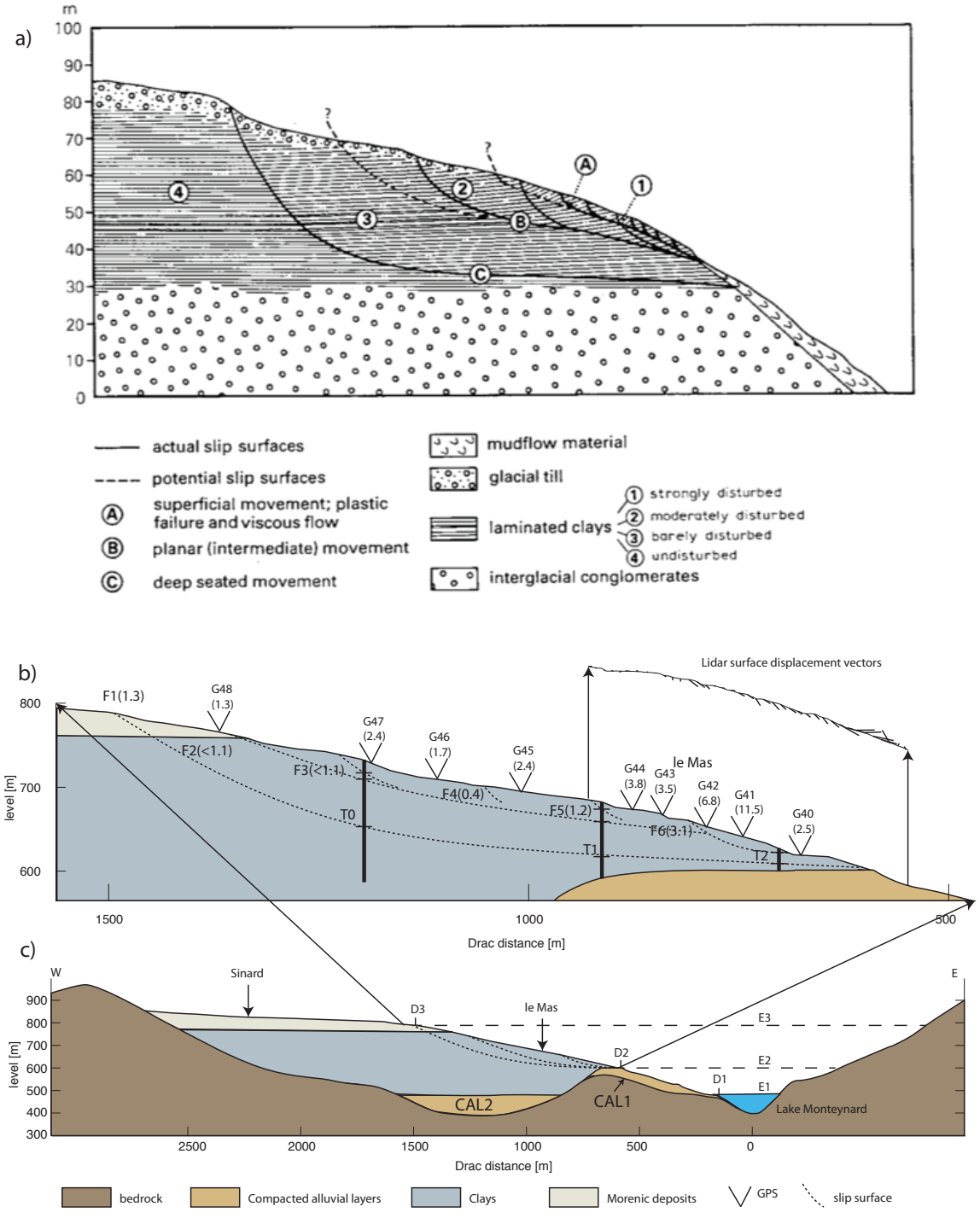

Figure 4.51: a) Idealised section across a slope in laminated clays to show potential and actual slip surfaces.(Giraud et al., 1991) b) Interpreted cross-section of the Avignonet landslide. G40-48 show the average GPS-velocities from 1995 - 2009 in cm/a. F1-6 are scarps identified on the shaded Lidar-DEM. In brackets an average displacement rate calculated from the difference of GPS-velocities of the accompanying blocks. T0-T2 are boreholes with inclinometric measurements and slip surfaces marked as small horizontal lines. c) Extended cross-section after (Monjuvent, 1973; Bièvre, 2010). D1: contact bedrock/CAL, D2: contact CAL/clays, D3: upper landslide limit, E1-3: accompanying elevation levels before incision.

Trièves due to the impoundment of the Drac by the Isère glacier. They will be called CAL2. Finally during the retreat of the glacier some morainic deposits remained on the top (Monjuvent, 1973, 1978; Brocard et al., 2003). The retreat of the Isère glacier started between 23 000 BP and 14 000 BP (Brocard et al., 2003) generating the incision of the Drac into the morainic deposits and laminated clays. After Brocard et al. (2003) the incision rate into the clays is at least 6 cm/a. That means that the Drac has incised the 200 m from E3 to E2 (Fig. 4.51) in about 3300 years. Assuming that the compacted alluvial layers filled the whole valley up to E2, the Drac incised the CAL down to the bedrock, whose top is probably more irregular, but is approximately near the today shore of the lake Monteynard at the E1 level. After Brocard et al. (2003) the incision rate into the CAL is about 0.8 cm/a to 1.1 cm/a, which leads to a incision time for the 120 m from E2 to E1 of about 11-15 ka. The further incision in the bedrock can be assumed to be much slower due to the high resistivity of the bedrock.

The Drac incision can be correlated with the retreat of the headscarp of Avignonet, assuming that the general slope angle of the sliding clay was constant. The slope angle of the Avignonet landslide is about 13°. During the incision from E3 to E2 the headscarp retreated 900 m from the Drac within 3300 years, which gives a retreat rate of about 30 cm/a. Afterward, the incision and therefore the retreat of the headscarp slowed down. Assuming the CAL-slope (D2-D1) was approximately the same at that time as today (17°), the retreat would be 500 m in 11-15 ka, which gives a retreat rate of 3-5 cm/a. But the problem here is, that the CAL-slope can not be assumed to be constant due to the rigid character of the cliffs. It is more likely that the slope was much higher until the Drac reaches the bedrock at E1. Then the incision rate dramatically decreased even further and the CAL slope decreased due to erosion from the valley sides, preferably at the exposed cliff at the top of the CAL. That means that the (long-term) evolution of the Avignonet landslide today is controlled by the retreat of the CAL-top (D2), which in itself is not controlled anymore by the incision of the Drac river. But how fast is the retreat of that cliff at the CAL-top and with that the retreat of the Avignonet headscarp? The maximum can be assumed to be the 3-5 cm/a calculated above.

Another approach is to extrapolate the recent movements of Avignonet. The major scarps at Avignonet (F1-6 in Fig. 4.51) are separated by about 100 m with an offset by about 15 m. The displacement rate for the uppermost block is 1.3 cm/a (G48) with approx. 0.25 cm/a in the vertical direction. This would mean the block needs about 6000 years for the 15 m and a new headscarp 100 m further is created only every 6000 a, which would reflect a retreat rate of 1-2 cm/a. But this would mean that the Avignonet landslide had only time to develop 2-3 scarps, which is not the case. Therefore this suggests that the landslide velocities do not reflect the long-term behaviour, which leads to assumption that the Avignonet landslide has seen and probably will see times of higher activity. These accelerations are likely to be linked with typical triggering factors of landslides like extreme rainfall, snow-melting or earthquakes.

The present-day morphology and spatial distribution of landslide velocities seems to support the thesis that the Avignonet landslide is controlled by the retreat of the CAL-top. Figure 4.52 shows both landslides with the Lidar-derived recent landslide velocities, shown a different colour-scale in order to highlight the areas where the velocities are significantly above the uncertainty. The figure also contains the contour line at 600 m asl (blue dotted line), which matches the top of the compacted alluvial layers (CAL) at three locations (blue solid line on the contour line) and therefore would indicate the top limit of the alluvial layers if it would be a continues horizontal plane. The blue-green alternating line at the west-shore of the lake indicates the outcropping

geological formation (blue = CAL, green = bedrock) as interpreted from the IGN-aerial photos of 2010 (via Google maps, maps.googe.com) and field-visits. On these images the level of the artificial Monteynard lake is exceptional low and therefore reveals a wide stripe of exposed rock along the lake which would be usually under water. The arrows OC1 to OC4 indicate the view of the photos in Figure 4.53, which show the appearance of the top of the alluvial layers in the landscape as a continuous sharp cliff.

Three areas of higher velocity can be observed in the Avignonet landslide (A, B, C). These locations are concentrated where the 600 m contour line exhibits a concave shape. On the other hand velocities are relatively low at the convex shapes, between A and B, B and C and south of C. This suggests that the relatively compact alluvial layers are a controlling factor of the Avignonet landslide: Where the CAL-cliffs stick out eastwards the landslide is blocked or at least slowed down; where the alluvial layers are retreated westwards the landslide is more active. The same pattern can be seen with the alluvial layers and bedrock at the lake-shore. The bedrock crops out at the convex shapes of the shore-line as it is more resistant.

The development of the Harmalière landslide during the incision of the Drac river into the clays can be assumed to be similar to the Avignonet landslide with an East-West orientation perpendicular to the Drac river, retreating westwards. But the Drac de Sinard has eroded the CAL1 from the Drac de Cros, flew westwards of the bulge and deposited its CAL2 at a lower elevation up to approx. 500 m (Fig. 4.51c). This means that the Drac of today incised SE of the Harmalière landslide into clays and tap the landslide from the SE through the former channel of the Drac de Sinard. This presumedly lead to a rotation of the Harmalière landslide towards the SE in the time after the Drac started incising into the CAL1. The question is what is the driving force today for the Harmalière landslide and has it changed with the filling of the Monteynard lake? At the Avignonet landslide it was suggested that the erosion of the CAL1-top is the triggering factor from the toe of the landslide. For Harmalière this could similarly be the erosion of the CAL2-top (before the filling of the lake), which is unlikely due to the following observations: (1) There is no evidence that the CAL2-top was already reached by the incision of the Drac river of today, due to the lack of outcrops mainly because of the filling of the lake and the filling of the outlet channel from the Harmalière landslide with the mudflow from the main event of 1981 and subsequent ones. (2) Even if the CAL2-top was reached, it can be assumed to have been levelled immediately, because the height relative to the level of the Drac river could not be higher than 50 m, the distance from the Drac river to the toe of surface rupture is with about 800 m relative long (see the geomorphological map in Fig. 3.21) and the whole watershed, which is almost as big as the one of the Avignonet landslide, is draining through the one narrow outlet channel (see the drainage map in Fig. 3.22). (3) Dissimilar to the Avignonet landslide, the recent activity of the Harmalière landslide is distributed over the whole landslide (Fig. 4.52). Also the aerial photos before the main event of 1981 (Fig. A.1-A.4 in the Appendix) show cracks, suggesting that the landslide is not only triggered by removing material at the bottom, but also by gravitational push from the head. Although the cracks showed up even before the creation of the lake in the 1960s, the filling of the lake itself could have been a triggering factor for the main event in 1981, because as seen on the aerial photos of 1970 (Fig. A.3), the lake sticks far out into the channel and could have raised the groundwater level, increasing the chance of failure at intense rainfall events. Another influence could have made the clearing of the forrest for a powerline at the eastern

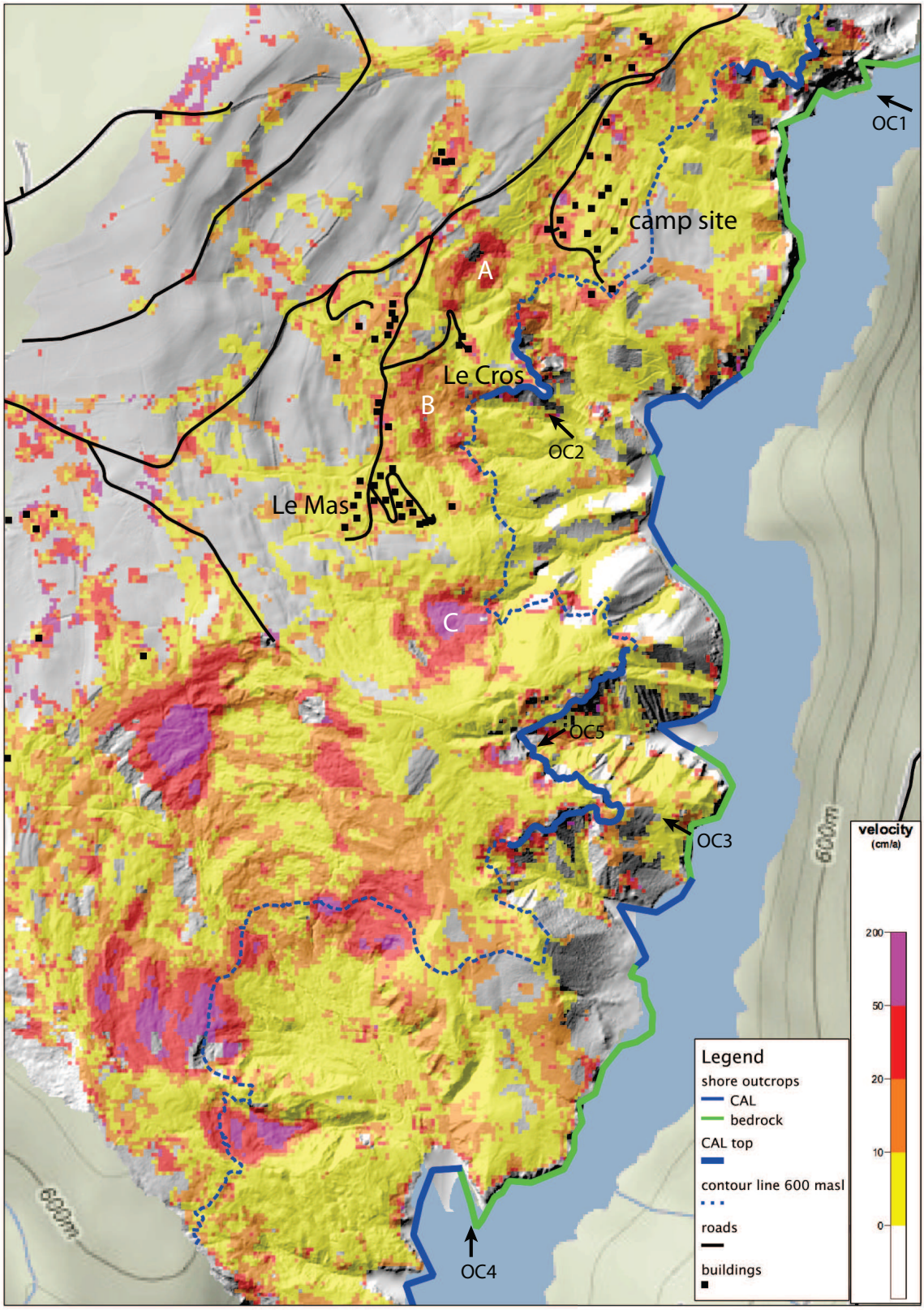

Figure 4.52: Landslide velocities derived from Lidar displacements on top of the shaded relief map.

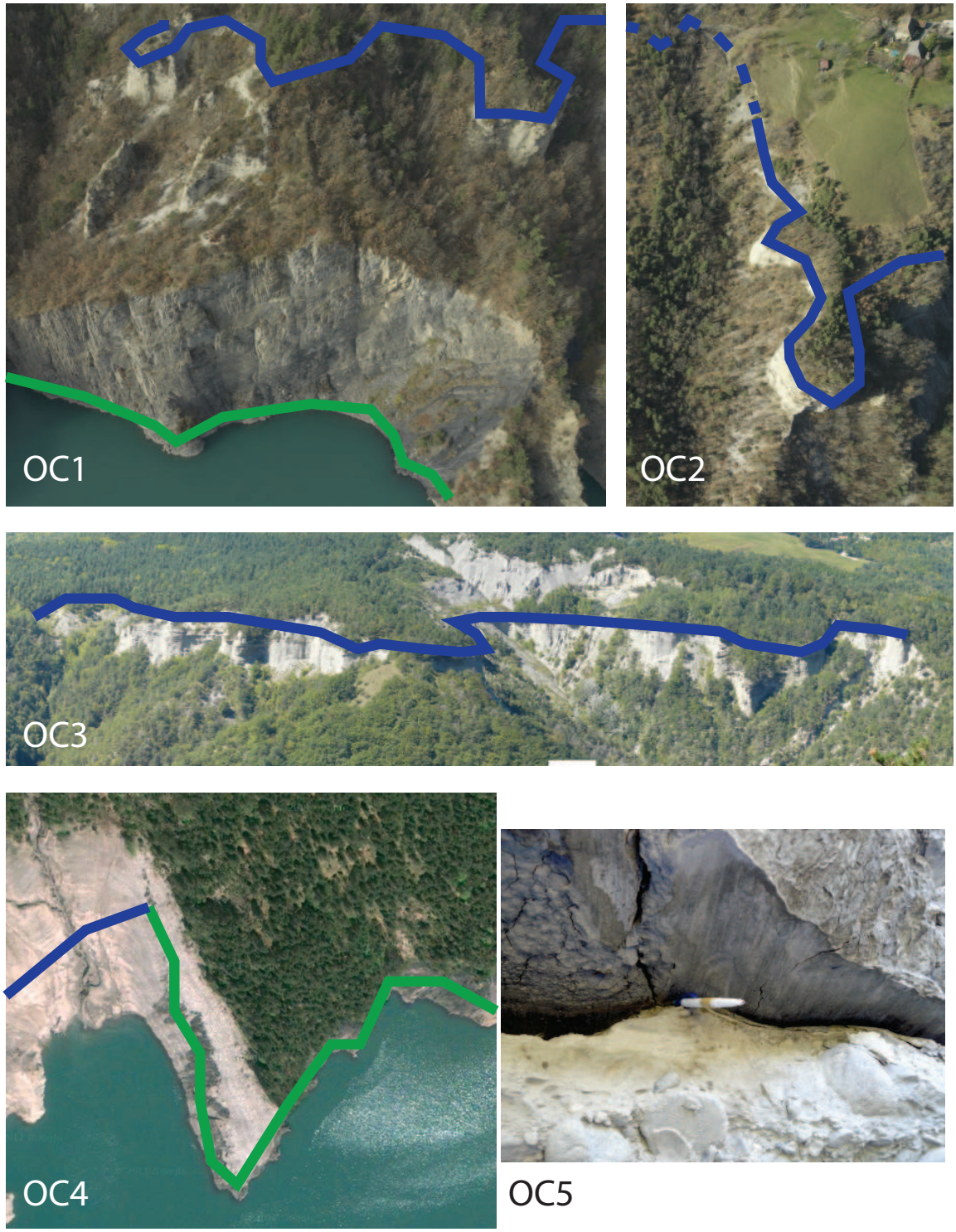

Figure 4.53: Outcrop photos

border of the later failed main section of the event in 1981.

The recent activity, seen in the Lidar displacements of Figure 4.52, show that the main middle part of the Harmalière landslide, which collapsed in 1981 and subsequent events, is less active than the flanks east and west from it. This could be due to the two main natural drainages at both sides of that section. In the mudslide at the lower end, these drainage paths join and incised already several meters into the debris since the last event in 2001. The moving block near the headscarp in the NW and the opening cracks behind it suggest further retreat of the headscarp in the NW direction towards the village Sinard. A very rough estimation of the retreat-rate can be assumed from the average retreat of the Harmalière landslide since the start of the tapping from the SE mentioned above at the time the Drac river reached the CAL1-top about 20 000-11 000 BP. The distance is about 1500 m which leads to an average retreat-rate of about 7-14 cm/a. However, the events since 1981 proofed that the average retreat of the headscarp can be as fast as 30 m/a over two decades.

CHAPTER 5

Conclusions

Three remote sensing techniques, aerial photogrammetry, Lidar and PS-Insar, were applied to the Trièves area in order to analyse the spatial-temporal behaviour of the two clayey landslides Avignonet and Harmalière. DEMs and ortho-photos have been produced from aerial photos of 1948 to 2003. Denuded areas have been mapped on the ortho-photos as an indicator for shallow landslide activity. In all photos the percentage of denuded surface is much larger in Harmalière than in Avignonet with 13 - 20% versus 3 - 5%, indicating a higher activity over the last 60 years. Although the DEMs from the most recent photos (2001, 2003) show elevation accuracies below 0.5 m, DEMs and ortho-photos from older photos reveal major inaccuracies of up to 20 m and therefore are not suitable for proper mass balance calculations or direct displacement extraction for such slow moving landslides.

The application of helicopter based Lidar on the landslides provides a high resolution bare earth DEM (approx. 0.5 m resolution), which is used for the morphological characterisation of the landslides. In opposite to optical imagery, the main advantage is the high absolute accuracy (15 cm) and the automatic filtering of vegetation. The HR-DEM and its derivatives (slope, aspect, shaded relief, drainage system) allowed a geomorphological interpretation with higher detail than it was possible before, revealing also structures in forested areas. The surface roughness, as defined by the RMS-deviation, is calculated at different scales (2 m and 20 m) along two directions - in slope direction and perpendicular to the slope - on small profiles (20 m and 200 m) over the whole HR-DEM. Directional roughness appears to be a good indicator for landslide activity, which is evidenced by down-slope roughness (created by perpendicular-to-slope scarps), while erosion, generating drainage downslope paths, is shown by roughness along contour lines. Several parts of the Harmalière landslide, as well as some regions along the lake, exhibit unpronounced directional roughness and are not easily classified.

Displacement-vectors were derived from two DEMs of 2006 and 2009, using cross-correlation techniques and developing a filter-strategy in order to detect erroneous displacements. Three main factors could be identified as the main reasons for mismatches at the correlation step and are sorted-out using different quality-measures: (1) Insufficient data-density in one or both DEMs, detected by a low point-overlapping, which takes into account the variability of the point-cloud densities on which the DEMs are based. (2) Irregular change, caused for example by chaotic movements or manmade earthworks. It can be detected by a high standard deviation of the difference between the matched DEM-kernels. (3) Insignificant morphology (e.g. flat terrain), detectable by a indistinct peak in the cross-correlation matrix. The final displacements show

accuracies up to 0.2 m depending on the complexity of morphology and the point-cloud densities. The displacement field reveals distinct areas in the Harmalière landslide, which moved up to 3 m with or without rotational component, or which exhibited relative low activity (<0.4 m) like in the main sliding channel caused by the events from 1981-2001. In the Avignonet landslide, the highest activity is obtained in a non-rotational sliding area in the south with displacements up to 2.5 m. On the whole rest of the landslide the displacements increase towards the toe with rotational and non-rotational components. The highest values are concentrated near the main drainage outlets with displacements up to 1 m.

The PS-Insar technique was applied, using 65 SAR-images from the ERS-satellites of the years 1992-2000. The decreased quality of 10 images shows significant correlation with the accumulated snowfall of 8 days before the acquisition of the image and are not used for further processing. The remaining 55 images were processed using a two-dimensional phase regression analysis, in order to determine stable points outside the two landslides and potential unstable points of high reflective quality inside the landslides. Finally, 16 reliable displacement-rates in the line of sight away from the satellites could be obtained inside the Avignonet landslide, ranging from -3 to 13 mm/a. In Harmalière no reliable results were obtained. Among the 16 points, 12 points are concentrated in three groups near the center of the Avignonet landslide and 4 are situated in the middle and northern part. All points can be related to buildings acting as reflector. The vectors in line of sight of the satellite are further interpreted as displacements along the slope direction, but this interpretation remains highly ambiguous due to the orientation of the slope nearly perpendicular to the incidence angle of the satellite.

Interpretation of all the remote sensing data and previous works has led to the following conclusions:

- The Harmalière landslide is and has been more active than the Avignonet landslide at least since 1950. The major cause seems to be the N-S ridge of hard sediments (Jurassic bedrock and/or compact alluvial layers) on the eastern side of the Avignonet landslide, which prevents the Avignonet landslide to develop new deeper sliding surfaces.

- This ridge disappears at the outlet of the Harmalière landslide and makes place to what can be interpreted as a NW-SE oriented paleovalley of the river Drac.

- The Avignonet landslide seems to be controlled by the slow retreat of the top of the compact alluvial layers, resulting in increasing velocities at the toe of the landslide near the drainage paths, where the top of the alluvial layers is eroded further towards the west. The landslide is moving along slip surfaces with increasing depths (superficial to 45 m) from the toe to the head and exhibiting decreasing velocities (50 cm/a to 1 cm/a).

- The Harmalière landslide shows higher activity distributed over the whole area, with the development of cracks behind the headscarp before the main events. At present, the main channel, which played a major role in the 1981 and subsequent events, is less active due to the filling of the outlet channel towards the lake by the mudslide deposits and probably by the natural drainage paths developed at the side of this body.

- Concerning the long-term evolution of the landslides since the retreat of the Isère glacier, it can be assumed that both landslides were similarly controlled by the incision of the Drac river into the clays and were oriented both perpendicular to it. After the Drac reached the top of the compacted alluvial layers of the former Drac de Crôs after about 3300 years, the incision slowed down, along with the regression of the landslide headscarp. At that time the Drac started to erode the channel of the former Drac de Sinard, leading finally to a rotation of the Harmalière landslide towards the SE. Since the Drac reached the bedrock after another 11-15 ka, the incision slowed down again stopping to directly controlling the landslide evolutions.

- From recent activity, the average retreat rate of the Avignonet headscarp is estimated to 1-5 cm/a. This value would also hold for the long-term past activity. For Harmalière, the long-term retreat rate is estimated to be 7-14 cm/a, but the events from 1981-2001 showed temporally a regression as high as 30 m/a for the northern part of the headscarp.

This work has highlighted several issues that could be further investigated. In aerial photogrammetry an integrated model refinement at the image registration process of photos from different dates and the extraction of displacements directly from the source images without calculating separate ortho-photos (Ayoub et al., 2009) should be tested. However, displacements derived from old aerial photos will much likely not reach accuracies better than one meter and only in non-vegetated areas.

The extraction of displacement-vectors from multi-temporal Lidar campaigns by cross-correlation techniques is also of high potential for further development and is easily adaptable to different landslide velocities and spatial extents. In this study only the lower end of detectable displacements are explored. Landslides with higher displacements should also be investigated in order to develop a pyramidical processing strategy, which dynamically adapts the kernel size, search distance and grid resolution with the local conditions. Other suitable Lidar data-sets were started to investigate but could not be treated in time, two plane-based Lidar campaigns from the Trièves covering a larger spatial extent and aerial laser-scans from two other study-sites within the Mountain Risks project: the Super Sauze landslide (French Alps) and the Valoria landslide (Appennines, Italy) with Lidar-sets from 3 different years each. Also, the integration of the intensity of the Lidar-data could help to increase the reliability, especially in flat terrain. Another approach could be the extraction of 3D-displacements based on geometrical patterns matched into the non-filtered point-clouds.

The Insar method using permanent scatterers should be further investigated for its potential to show non-linear behaviour of slow movements and the combination of ascending and descending orbits to solve the ambiguity when interpreting the LOS-displacements. The method is generally better suited for landslides which contain structures with high reflectivity properties (e.g. buildings, hard-rocks), but results can maybe significantly improved using new processing strategies by combing small-baseline and permanent-scatterer approaches (Hooper, 2008; Ferretti et al., 2011) and/or using data from recently launched satellites (TerraSarX, CosmoSkymed) with higher resolution (1 m), low return times (4 days) and steerable SAR-instruments (variable incidence angle and left/right looking capabilities).

Bibliography

Abellan, A., Vilaplana, J. M., and Martinez, J. (2006). Application of a long-range terrestrial laser scanner to a detailed rockfall study at Vall de Nuria (Eastern Pyrenees, Spain). *Engineering Geology*, 88:136–148.

Angeli, M.-G., Pasuto, A., and Silvano, S. (2000). A critical review of landslide monitoring experiences. *Engineering Geology*, 55(3):133–147. TY - JOUR.

Antoine, P., Giraud, A., and Monjuvent, G. (1981). Les argiles litées du Trièves (Isère); conditions de glissement et exemples de propriétés géotechniques. *Bulletin de la Société géologique de France*, pages 117–127.

Antoine, P., Monnet, J., Rai, N. E., Moulin, C., and Meriaux, P. (1991). Resultats de cinq annees d'auscultation sur un glissement dans les argiles glacio-lacustres du trieves (sud-est de la france). Technical report, IRIGM.

Antonello, G., Casagli, N., Farina, P., Leva, D., Nico, G., Sieber, A., and Tarchi, D. (2004). Ground-based sar interferometry for monitoring mass movements. *Landslides*, 1(1):21–28.

Axelsson, P. (2000). Dem generation from laser scanner data using adaptive tin models. *International Archives of Photogrammetry and Remote Sensing*, 33(B4/1; PART 4):111–118.

Ayoub, F., Leprince, S., and Avouac, J. (2009). Co-registration and correlation of aerial photographs for ground deformation measurements. *ISPRS Journal of Photogrammetry and Remote Sensing*, 64:551–560.

Baltsavias, E., Li, H., Stefanidis, A., and Sinning, M. (1996). Automatic dsms by digital photogrammetry. *Surveying World*, 4(2):18–21.

Bard, P.-Y. (1998). Microtremor measurements: a tool for site effect estimation? In Irikura, K., Kudo, K., Okada, H., and Sasatani, T., editors, *The Effects of Surface Geology on Seismic Motion*, pages 1251–1279. Balkema, Rotterdam.

Barlow, J., Franklin, S., and Martin, Y. (2006). High spatial resolution satellite imagery, dem derivatives, and image segmentation for the detection of mass wasting processes. *Photogrammetric Engineering & Remote Sensing*, 72(6):687–692.

Berardino, P., Fornaro, G., Lanari, R., and Sansosti, E. (2002). A new algorithm for surface deformation monitoring based on small baseline differential sar interferograms. *Geoscience and Remote Sensing, IEEE Transactions on*, 40(11):2375–2383.

Bièvre, G. (2010). *Caractérisation de versants argileux instables dans des conditions hydrogéologiques hétérogènes. Approche géophysique*. PhD thesis, Université de Grenoble.

Bievre, G., Kniess, U., Jongmans, D., Pathier, E., Schwartz, S., van Westen, C. J., Villemin, T., and Zumbo, V. (2011). Paleotopographic control of landslides in lacustrine deposits (trièves plateau, french western alps). *Geomorphology*, 125(1):214–224.

Blanchet, F. (1988). *Etude géomécanique de glissements de terrain dans les argiles glaciolacustres de la vallée du Drac*. PhD thesis, Université Joseph Fourier, Grenoble, France, Grenoble, France.

Bonci, L., Bozzano, F., Calcaterra, S., Eulilli, V., Ferri, F., Gambino, P., Manuel, M. R., Martino, S., and Scarascia Mugnozza, G. (2004). Geological control on large seismically induced landslides: the case of Cerda (Southern Italy). In *Proceedings of the 9th International Symposium on Landslides*, pages 985–991.

Bonnefoy-Claudet, S., Cornou, C., Bard, P.-Y., Cotton, F., Moczo, P., Kristek, J., and Fäh, D. (2006). H/v ratio: a tool for site effects evaluation. results from 1-d noise simulations. *Geophysical Journal International*, 167:827–837.

Bozzano, F., Lenti, L., Martino, S., Paciello, A., and Scarascia Mugnozza, G. (2008). Self-excitation process due to local seismic amplification responsible for the reactivation of the Salcito landslide (Italy) on 31 October 2002. *Journal of Geophysical Research*, 113:B10312.

Briese, C., Pfeifer, N., and Dorninger, P. (2002). Applications of the robust interpolation for DTM determination. In *IAPSIS XXXIV*, volume 3A, pages 55–61.

Brocard, G. (2003). *Origine, variabilite spatio-temporelle et signature morphologique de l'incision fluviale dans les Alpes Dauphinoises (se France)*. PhD thesis, UJF Grenoble.

Brocard, G. Y., van der Beek, P. A., Bourles, D. L., Siame, L. L., and Mugnier, J. L. (2003). Long-term fluvial incision rates and postglacial river relaxation time in the french western alps from 10be dating of alluvial terraces with assessment of inheritance, soil development and wind ablation effects. *Earth and Planetary Science Letters*, 209(1-2):197–214.

Brovelli, M., Cannata, M., and Longoni, U. (2002). Managing and processing lidar data within grass. In *Proceedings of the Open source GIS-GRASS users conference, Trento, Italy*. Citeseer.

Bruckl, E., Brunner, F. K., and Kraus, K. (2006). Kinematics of a deep-seated landslide derived from photogrammetric, gps and geophysical data. *Engineering Geology*, 88(3-4):149–159.

Casson, B. (2004). *Apports de l'imagerie optique haute resolution pour l'étude 3D des glissements de terrain*. PhD thesis, Université Claude Bernard Lyon.

Casson, B., Delacourt, C., Baratoux, D., and Allemand, P. (2003). Seventeen years of the "la clapiere" landslide evolution analysed from ortho-rectified aerial photographs. *Engineering Geology*, 68(1-2):123–139. TY - JOUR.

Chadwick, J., Dorsch, S., Glenn, N., Thackray, G., and Shilling, K. (2005). Application of multi-temporal high-resolution imagery and gps in a study of the motion of a canyon rim landslide. *ISPRS Journal of Photogrammetry and Remote Sensing*, 59(4):212–221. TY - JOUR.

Chatelain, J.-L., Guéguen, P., Guillier, B., Fréchet, Bondoux, F., Sarrault, J., Sulpice, P., and Neuville, J. M. (2000). Cityshark: A user-friendly instrument dedicated to ambient noise (microtremor) recording for site and building response studies. *Seismological Research Letters*, 71:698–703.

Chen, R., Chang, K., Angelier, J., Chan, Y., Deffontaines, B., Lee, C., and Lin, M. (2006). Topographical changes revealed by high-resolution airborne lidar data: The 1999 tsaoling landslide induced by the chi-chi earthquake. *Engineering geology*, 88(3-4):160–172.

Cheng, K. S., Wei, C., and Chang, S. C. (2004). Locating landslides using multi-temporal satellite images. *Advances in Space Research*, 33(3):296–301. TY - JOUR.

Clark, P. U., Dyke, A. S., Shakun, J. D., Carlson, A. E., Clark, J., Wohlfarth, B., Mitrovica, J. X., Hostetler, S. W., and McCabe, A. M. (2009). The last glacial maximum. *Science*, 325(5941):710–714.

Colesanti, C. and Wasowski, J. (2006). Investigating landslides with space-borne synthetic aperture radar (sar) interferometry. *Engineering geology*, 88(3-4):173–199.

Corsini, A., Borgatti, L., Coren, F., and Vellico, M. (2007). Use of multitemporal airborne LiDAR surveys to analyse postfailure behaviour of earthslides. *Canadian Journal of Remote Sensing*, 33(2):116–120.

Corsini, A., Cervi, F., Daehne, A., Ronchetti, F., and Borgatti, L. (2008). Coupling geomorphic field observation and lidar derivatives to map complex landslides. In Malet, J.-P., Remaître, A., and Bogaard, T., editors, *Proceedings of the Landslide Processes Conference, Strasbourg 6-7 February, 2008*.

Costa-Cabral, M. and Burges, S. (1994). Digital elevation model networks (demon): A model of flow over hillslopes for computation of contributing and dispersal areas. *Water Resources Research*, 30(6):1681–1692.

Crosnier-Leconte, J., Bordet, C., and Duffaut, P. (1953). Séparation de deux anciens lits successifs dans la vallée du Drac à Monteynard (Isère). *Comptes-Rendus Sommaires de la Société Géologique de France*, 12:221–223.

Crowley, J., Hubbard, B., and Mars, J. (2003). Analysis of potential debris flow source areas on mount shasta, california, by using airborne and satellite remote sensing data. *Remote Sensing of Environment*, 87:345–358.

Cruden, D. and Varnes, D. (1996). Landslide types and processes. Special Report 247, Transportation Research Board, National Research Council, Washington.

Debelmas, J. (1967). La Chapelle-en-Vercors. In *Carte géologique de la France au 1/50000*. BRGM Éditions, Orléans, France.

Delacourt, C., Allemand, P., Berthier, E., Raucoules, D., Casson, B., Grandjean, P., Pambrun, C., and Varel, E. (2007). Remote-sensing techniques for analysing landslide kinematics: a review. *Bulletin De La Societe Geologique De France*, 178(2):89–100. Delacourt, Christophe Allemand, Pascal Berthier, Etienne Raucoules, Daniel Casson, Berangere Grandjean, Philippe Pambrun, Claude Varel, Eric.

Delacourt, C., Allemand, P., Casson, B., and Vadon, H. (2004). Velocity field of "la clapiere" landslide measured by the correlation of aerial and quickbird satellite images. *Geophysical Research Letters*, 31(15):15619.

Delacourt, C., Raucoules, D., Le Mouélic, S., Carnec, C., Feurer, D., Allemand, P., and Cruchet, M. (2009). Observation of a large landslide on la reunion island using differential sar interferometry (jers and radarsat) and correlation of optical (spot5 and aerial) images. *Sensors*, 9(1):616–630.

Delgado, J., López Casado, C., Estévez, A., Giner, J., Cuenca, A., and Molina, S. (2000). Mapping soft soils in the Segura river Valley (SE Spain); a case study of microtremors as an exploration tool. *Journal of Applied Geophysics*, 45(1):19–32.

Deparis, J., Fricourt, B., Jongmans, D., Villemin, T., Effendiantz, L., and Mathy, A. (2008). Combined use of geophysical methods and remote techniques for characterizing the fracture network of a potential unstable cliff site (the "Roche du Midi", Vercors massif, France). *Journal of Geophysical Engineering*, 5:147–157.

Dikau, R., Brunsden, D., Schrott, L., and Ibsen, M.-L. (1996). *Landslide Recognition. Identification, Movement and Courses*. Wiley & Sons, Chichester, etc.

Dilley, M. (2005). *Natural disaster hotspots: a global risk analysis*. Number 5. World Bank Publications.

Eilertsen, R. S., Hansen, L., Bargel, T. H., and Solberg, I.-L. (2008). Clay slides in the Målselv valley, northern Norway: Characteristics, occurrence, and triggering mechanisms. *Geomorphology*, 93(3-4):548–562.

Elmqvist, M. (2002). Ground surface estimation from airborne laser scanner data using active shape models. *INTERNATIONAL ARCHIVES OF PHOTOGRAMMETRY REMOTE SENSING AND SPATIAL INFORMATION SCIENCES*, 34(3/A):114–118.

Ercanoglu, M. (2005). Landslide susceptibility assessment of se bartin (west black sea region, turkey) by artificial neural networks. *Natural Hazards and Earth System Sciences*, 5(6):979 – 992.

Evans, J. and Hudak, A. (2007). A multiscale curvature algorithm for classifying discrete return lidar in forested environments. *IEEE Transactions on Geoscience and Remote Sensing*, 45(4):1029.

Eyers, R., Moore, J., Hervas, J., and Liu, J. (1998). Integrated use of landsat tm and spot panchromatic imagery for landslide mapping: case histories from southeast spain. *Engineering Geology Special Publications*, 15(1):133.

Ferretti, A., Fumagalli, A., Novali, F., Prati, C., Rocca, F., and Rucci, A. (2011). A new algorithm for processing interferometric data-stacks: Squeesar. *Transactions on Geoscience and Remote Sensing, IEEE*, 99.

Ferretti, A., Prati, C., Rocca, F., and ed Inf, D. (2000). Nonlinear subsidence rate estimation using permanent scatterers indifferential SAR interferometry. *Geoscience and Remote Sensing, IEEE Transactions on*, 38(5 Part 1):2202–2212.

Franceschetti, G. and Lanari, R. (1999). *Synthetic aperture radar processing*. CRC.

Freeman, T. (1991). Calculating catchment area with divergent flow based on a regular grid. *Computers & Geosciences*, 17(3):413–422.

Fruneau, B., Achache, J., and Delacourt, C. (1996). Observation and modelling of the saint-etienne-de-tinee landslide using sar interferometry. *Tectonophysics*, 265(3-4):181–190. TY - JOUR.

Fruneau, B., Michel, S., Kniess, U., Pathier, E., Cornou, C., Ménard, G., Casagli, N., and Bard, P.-Y. (2010). Subsidence of the grenoble urban area (french alps) from insar and its relationship to basin sedimentary deposits. In *ESA Living Planet Symposium*.

Geomatics, P. (2003). Pci geomatics. *Geomatica OrthoEngine Users Guide, PCI Geomatics Enterprises Inc., Richmond Hill (2003)*, 158.

Geudtner, D. (1995). Interferometric processing of ers-1 sar data. *Cologne, Germany: Deutsche Forschungsanstalt fuer Luft- und Raumfahrt(DLR Forschungsbericht 95-28), 1995.*

Gili, J. A., Corominas, J., and Rius, J. (2000). Using global positioning system techniques in landslide monitoring. *Engineering Geology*, 55(3):167–192. TY - JOUR.

Giraud, A., Antoine, P., Van Asch, T., and Nieuwenhuis, J. (1991). Geotechnical problems caused by glaciolacustrine clays in the french alps. *Engineering Geology*, 31(2):185–195.

Glade, T., Anderson, M., and Crozier, M. (2005). *Landslide hazard and risk*. J. Wiley.

Glenn, N. F., Streutker, D. R., Chadwick, D. J., Thackray, G. D., and Dorsch, S. J. (2006). Analysis of lidar-derived topographic information for characterizing and differentiating landslide morphology and activity. *Geomorphology*, 73(1-2):131–148.

Greco, R., Sorriso-Valvo, M., and Catalano, E. (2007). Logistic regression analysis in the evaluation of mass movements susceptibility: The aspromonte case study, calabria, italy. *Engineering Geology*, 89(1-2):47–66.

Green, A. G., Maurer, H., Spillmann, T., Heincke, B., and Willenberg, H. (2007). High-resolution geophysical techniques for improving hazard assessments of unstable rock slopes. *The Leading Edge*, 25(3):311–316.

Guéguen, ., Cornou, C., Garambois, S., and Banton, J. (2007). On the limitation of the H/V spectral ratio using seismic noise as an exploration tool: application to the Grenoble valley (France), a small apex ratio basin. *Pure and Applied Geophysics*, 164(1):115–134.

Guillier, B., Cornou, C., Kristek, J., Bonnefoy-Claudet, S., Bard, P., Fah, D., , and Moczo, P. (2006). Simulation of seismic ambient vibrations: does the H/V provide quantitative information in 2D-3D structure? In *ESG2006*, Grenoble.

Guizar-Sicairos, M., Thurman, S., and Fienup, J. (2008). Efficient subpixel image registration algorithms. *Optics Letters*, 33(2):156–158.

Haneberg, W., Creighton, A., Medley, E., and Jonas, D. (2005). Use of lidar to assess slope hazards at the lihir gold mine, papua new guinea. In *Landslide Risk Management. Proceedings of International Conference on Landslide Risk Management, Vancouver, Canada*, volume 31.

Haskell, N. A. (1960). Crustal reflexion of plane SH waves. *Journal of Geophysical Research*, 65:4147–4150.

Hein, A. (2004). *Processing of SAR data: fundamentals, signal processing, interferometry*. Springer Verlag.

Heincke, B., Maurer, H., Green, A. G., Willenberg, H., Spillmann, T., and Burlini, L. (2006). Characterizing an unstable mountain slope using shallow 2D and 3D seismic tomography. *Geophysics*, 71(6):B241–B256.

Henry, J., Malet, J., Maquaire, O., and Grussenmeyer, P. (2002). The use of small-format and low-altitude aerial photos for the realization of high-resolution dems in mountainous areas: application to the super-sauze earthflow (alpes-de-haute-provence, france). *Earth Surface Processes and Landforms*, 27(12):1339–1350.

Hervas, J., Barredo, J. I., Rosin, P. L., Pasuto, A., Mantovani, F., and Silvano, S. (2003). Monitoring landslides from optical remotely sensed imagery: the case history of tessina landslide, italy. *Geomorphology*, 54(1-2):63–75. TY - JOUR.

Hilley, G. E., Burgmann, R., Ferretti, A., Novali, F., and Rocca, F. (2004). Dynamics of slow-moving landslides from permanent scatterer analysis. *Science*, 304(5679):1952–1955.

Hofmann-Wellenhof, B., Lichtenegger, H., and Collins, J. (2001). *GPS theory and practice*. New York, NY.

Hooper, A. (2008). A multi-temporal insar method incorporating both persistent scatterer and small baseline approaches. *Geophys. Res. Lett*, 35:L16302.

Hooper, A., Zebker, H., Segall, P., and Kampes, B. (2004). A new method for measuring deformation on volcanoes and other natural terrains using InSAR persistent scatterers. *Geophysical Research Letters*, 31(23).

Huff, W. D. (1974). Mineralogy and provenance of Pleistocene lake clay in an alpine region. *Geological Society of America Bulletin*, 85:1455–1460.

Ibs-von Seht, M. and Wohlenberg, J. (1999). Microtremor measurements used to map thickness of soft sediments. *Bulletin of the Seismological Society of America*, 89(1):250–259.

IGN (2007). Coordinate systems, projections and geodetic systems. Technical report, Institut Geographique National de France.

IGN Institut Geographique National (2006). Projet Lambert 93. http://lambert93.ign.fr.

IPF (2004). Software SCOP++. http://www.inpho.de/index.php?seite=index_scope.

Jaboyedoff, M., Couture, R., and Locat, P. (2009). Structural analysis of turtle mountain (alberta) using digital elevation model: toward a progressive failure. *Geomorphology*, 103(1):5–16.

Jaboyedoff, M., Oppikofer, T., Abellán, A., Derron, M., Loye, A., Metzger, R., and Pedrazzini, A. (2010). Use of lidar in landslide investigations: a review. *Natural Hazards*, pages 1–24.

Jackson, M., Bodin, P., Savage, W., and Nel, E. (1996). Measurement of local horizontal velocities on the slumgullion landslide using the global positioning system. *US Geol. Surv. Bull*, 2130:93–95.

Jongmans, D., Bièvre, G., Schwartz, S., Renalier, F., and Beaurez, N. (2009). Geophysical investigation of the large Avignonet landslide in glaciolacustrine clays in the Trièves area (French Alps). *Engineering Geology*, 109:45–56.

Jongmans, D. and Garambois, S. (2007). Geophysical investigation of landslides: a review. *Bulletin de la Société Géologique de France*, 178(2):101–112.

Kääb, A. (2002). Monitoring high-mountain terrain deformation from repeated air- and spaceborne optical data: examples using digital aerial imagery and aster data. *ISPRS Journal of Photogrammetry and Remote Sensing*, 57(1):39–52.

Kampes, B. (2005). *Displacement parameter estimation using permanent scatterer interferometry*. DLR, Bibliotheks-und Informationswesen.

Kasperski, J., Delacourt, C., Allemand, P., Potherat, P., Jaud, M., and Varrel, E. (2010). Application of a terrestrial laser scanner (tls) to the study of the séchilienne landslide (isère, france). *Remote Sens.*, 2:2785–2802.

Kimura, H. and Yamaguchi, Y. (2000). Detection of landslide areas using satellite radar interferometry. *Photogrammetric engineering and remote sensing*, 66:337–344.

Kitanidis, P. K. (1997). *Introduction to Geostatistics: Applications in Hydrogeology*. Cambridge University Press, Cambridge.

Kjekstad, O. (2007). The challenges of landslide hazard mitigation in developing countries. In Turner, A. K. and Schuster, R. L., editors, *Landslide and society. Keynote and invited presentations at the 1st North American Landslide Conference,*, AEG Special Publicacion No. 22, Vail, Colorado, June 3-8, 2007. The Association of Environmental & Engineering Geologists.

Koller, M. G., Chatelain, J.-L., Guillier, B., Duval, A.-M., Atakan, K., Lacave, C., and Bard, P.-Y. (2004). Practical user guidelines and software for the implementation of the H/V ratio technique: measuring conditions, processing method and results interpretation. In *Proceedings of the 13th world conference in earthquake engineering, Vancouver, Canada*.

Konno, K. and Ohmachi, T. (1998). Ground-motion characteristics estimated from spectral ratio between horizontal and vertical components of microtremor. *Bulletin of the Seismological Society of America*, 88(1):228–241.

Kraus, K. and Pfeifer, N. (2001). Advanced dtm generation from lidar data. *INTERNATIONAL ARCHIVES OF PHOTOGRAMMETRY REMOTE SENSING AND SPATIAL INFORMATION SCIENCES*, 34(3/W4):23–30.

Kruse, F., Boardman, J., and Huntington, J. (2003). Comparison of airborne hyperspectral data and eo-1 hyperion for mineral mapping. *Geoscience and Remote Sensing, IEEE Transactions on*, 41(6):1388–1400.

Lambert, A. and Monjuvent, G. (1968). Quelques vues nouvelles sur l'histoire quaternaire de la vallee du drac. *Geologie Alpine*, 44:117–137.

Lapenna, V., Lorenzo, P., Perrone, A., Piscitelli, S., Rizzo, E., and Sdao, F. (2005). 2d electrical resistivity imaging of some complex landslides in the lucanian apennine chain, southern italy. *Geophysics*, 70(3):B11–B18.

Le Roux, O., Schwartz, S., Gamond, J.-F., Jongmans, D., Tricart, P., and Sebrier, M. (2008). Interaction between tectonic and erosion processes on the morphogenesis of an Alpine valley: geological and geophysical investigations in the lower Romanche valley (Belledonne massif, western Alps). *International Journal of Earth Sciences*, pages 1437–3254.

Lea, N. (1992). An aspect driven kinematic routing algorithm in overland flow. *Hydraulics and Erosion Mechanics, edited by AJ Parsons and AD Abrahams, Chapman and Hall, New York*.

Lee, S. and Evangelista, D. (2006). Earthquake-induced landslide-susceptibility mapping using an artificial neural network. *Natural Hazards and Earth System Sciences*, 6(5):687 – 695.

Lee, S. and Lee, M.-J. (2006). Detecting landslide location using kompsat 1 and its application to landslide-susceptibility mapping at the gangneung area, korea. *Advances in Space Research*, 38(10):2261–2271.

Lejot, J., Delacourt, C., Piégay, H., Fournier, T., Trémélo, M., and Allemand, P. (2007). Very high spatial resolution imagery for channel bathymetry and topography from an unmanned mapping controlled platform. *Earth Surface Processes and Landforms*, 32(11):1705–1725.

Leprince, S. (2008). *Monitoring Earth Surface Dynamics with Optical Imagery*. PhD thesis, California Institute of Technology.

Lewis, J. (1995). Fast normalized cross-correlation. In *Vision Interface*, volume 10, pages 120–123. Citeseer.

Li, Z., Ding, X., Huang, C., Wadge, G., and Zheng, D. (2006). Modeling of atmospheric effects on insar measurements by incorporating terrain elevation information. *Journal of atmospheric and solar-terrestrial physics*, 68(11):1189–1194.

Lorier, L. and Desvarreux, P. (2004). Glissement du mas d'avignonet. In *Proceedings of the workshop Ryskhydrogeo, Program Interreg III, LaMure (France)*.

Malet, J. P., Maquaire, O., and Calais, E. (2002). The use of global positioning system techniques for the continuous monitoring of landslides: application to the super-sauze earthflow (alpes-de-haute-provence, france). *Geomorphology*, 43(1-2):33–54. TY - JOUR.

Mantovani, F., Soeters, R., and van Westen, C. J. (1996). Remote sensing techniques for landslide studies and hazard zonation in europe. *Geomorphology*, 15(3-4):213–225. TY - JOUR.

Mark, D. (1988). Network models in geomorphology. *Modelling Geomorphological Systems. John Wiley and Sons New York. 1988. p 73-97, 11 fig, 3 tab, 60 ref. NSF Grant SES-8420789*.

Mather, P. and Koch, M. (2004). *Computer processing of remotely sensed images: an introduction*. Wiley.

McKean, J. and Roering, J. (2004). Objective landslide detection and surface morphology mapping using high-resolution airborne laser altimetry. *Geomorphology*, 57(3-4):331–351.

Méneroud, J.-P., Duval, A.-M., Vidal, S., Fréchet, J., Gamond, J.-F., Beck, C., Tardy, M., Bard, P.-Y., Barnichon, E., and Gaboriaud, J.-M. (1995). Franchissement de l'Ébron, étude de l'aléa sismique local. Technical Report 93/95666/74, CETE Méditerranée.

Meng, X., Wang, L., Silván-Cárdenas, J., and Currit, N. (2009). A multi-directional ground filtering algorithm for airborne lidar. *ISPRS Journal of Photogrammetry and Remote Sensing*, 64(1):117–124.

Méric, O., Garambois, S., Malet, J.-P., Cadet, H., Gueguen, P., and Jongmans, D. (2007). Seismic noise-based methods for soft-rock landslide characterization. *Bulletin de la Societé Géologique de France*, 178(2):137–148.

Metternicht, G., Hurni, L., and Gogu, R. (2005). Remote sensing of landslides: An analysis of the potential contribution to geo-spatial systems for hazard assessment in mountainous environments. *Remote Sensing of Environment*, 98(2-3):284–303.

Michel, S., Cornou, C., Pathier, E., Ménard, G., Collombet, M., Knieß, U., and Bard, P.-Y. (21–23 April 2010). May subsidence rate serve as proxy for site effects? In *Seismological Society of America annual meeting*.

Mitasova, H., Mitas, L., and Harmon, R. (2005). Simultaneous spline approximation and topographic analysis for lidar elevation data in open-source gis. *IEEE Geoscience and Remote Sensing Letters*, 2(4):375–379.

Mondino, E. B., Giardino, M., and Perotti, L. (2009). A neural network method for analysis of hyperspectral imagery with application to the cassas landslide (susa valley, nw-italy). *Geomorphology*, 110(1-2):20–27.

Monjuvent, G. (1973). transfluence durance-isere: Essai de synthese du quaternaire du bassin du drac (alpes francaises). *Geologie Alpine*, 49:57–118.

Monjuvent, G. (1978). *Le Drac, morphologie, stratigraphie et chronologie quaternaires d'un bassin alpin.* PhD thesis, UJF-Grenoble, France.

Moulin, C. and Chapeau, C. (2004). Le glissement de la Salle en Beaumont (Isère). In *Proceedings of the workshop Ryskhydrogeo, Program Interreg III, La Mure (France)*, page 9 p.

Moulin, C. and Robert, Y. (2004). Le glissement de Harmalière sur la commune de Sinard. In *Proceedings of the workshop Ryskhydrogeo, Program Interreg III, LaMure (France)*.

Nichol, J. E., Shaker, A., and Wong, M.-S. (2006). Application of high-resolution stereo satellite images to detailed landslide hazard assessment. *Geomorphology*, 76(1-2):68–75.

Nicoud, G., Royer, G., Corbin, J.-C., Lemeille, F., and Paillet, A. (2002). Creusement et remplissage de la vallée de l'Isère au Quaternaire récent. Apports nouveaux du forage GMB1 (1999) dans la région de Grenoble (France). *Géologie de la France*, 4:39–49.

O'callaghan, J. and Mark, D. (1984). The extraction of drainage networks from digital elevation data. *Computer vision, graphics, and image processing*, 28(3):323–344.

Oppikofer, T., Jaboyedoff, M., and Keusen, H.-R. (2008). Collapse at the eastern Eiger flank in the Swiss Alps. *Nature Geoscience*, 1:531–535.

Paine, D. and Kiser, J. (2003). *Aerial photography and image interpretation.* Wiley.

Pambrun, C. and Nocquet, J. (2005). Monitoring of the clapiere landslide (french alps) by comtinuous gps. In *Geophysical Research Abstracts*, volume 7, page 07640.

Pathier, E. (2003). *Apports de l'interférométrie radar différentielle à l'étude de la tectonique active de Taiwan.* PhD thesis, Université de Marne-La-Vallée.

Perrone, A., Zeni, G., Piscitelli, S., Pepe, A., Loperte, A., Lapenna, V., and Lanari, R. (2006). Joint analysis of sar interferometry and electrical resistivity tomography surveys for investigating ground deformation: the case-study of satriano di lucania (potenza, italy). *Engineering Geology*, 88(3-4):260–273.

Pesci, A., Fabris, M., Conforti, D., Loddo, F., Baldi, P., and Anzidei, M. (2007). Integration of ground-based laser scanner and aerial digital photogrammetry for topographic modelling of vesuvio volcano. *Journal of Volcanology and Geothermal Research*, 162(3-4):123–138.

Petley, D. (2008). The global occurrence of fatal landslides in 2007. In *International Conference on Management of Landslide Hazard in the Asia–Pacific Region. Japan Landslide Society, Tokyo, Japan*, pages 590–600.

Pfeifer, N., Stadler, P., and Briese, C. (2001). Derivation of digital terrain models in the scop++ environment. In *Proceedings of OEEPE Workshop on Airborne Laserscanning and Interferometric SAR for Detailed Digital Terrain Models, Stockholm, Sweden*, volume 3612.

Pugin, A. J.-M., Pullan, S. E., Hunter, J. A., and Oldenborger, G. A. (2009). Hydrogeological prospecting using P- and S-wave landstreamer seismic reflection methods. *Near Surface Geophysics*, 7:315–327.

Quinn, P., Beven, K., Chevallier, P., and Planchon, O. (1991). The prediction of hillslope flow paths for distributed hydrological modeling using digital terrain models. hydrol. *Proc. 5*, pages 59–79.

Renalier, F., Jongmans, D., Bièvre, G., Schwartz, S., and Orengo, Y. (2007). Characterisation of a landslide in clay deposits using Vs measurements. In *Near Surface 2007, EAGE meeting, 03-04 September 2007, Istanbul, Turkey.*

Requillart, J. and Moulin, C. (2004). Glissement du mas sur la commune d'avignonet (france) etat de la gestion du risque en octobre 2004. Technical report, RTM de l'Isère.

Roch, K. H., Chwatal, E., and Brückl, E. (2006). Potential of monitoring rock fall hazards by gpr: considering as example of the results of Salzburg. *Landslides*, 3:87–94.

Roggero, M. (2001). Airborne laser scanning-clustering in raw data. *INTERNATIONAL ARCHIVES OF PHOTOGRAMMETRY REMOTE SENSING AND SPATIAL INFORMATION SCIENCES*, 34(3/W4):227–232.

Rosser, N. J., Petley, D. N., Lim, M., Dunning, S. A., and Allison, R. J. (2005). Terrestrial laser scanning for monitoring the process of hard rock coastal cliff erosion. *Quarterly Journal of Engineering Geology*, 38:363–375.

Rott, H., Scheuchl, B., Siegel, A., and Grasemann, B. (1999). Monitoring very slow slope motion by means of SAR interferometry: A case study from a mass waste above a reservoir in the Ötztal Alps, Austria. *Geophysical Research Letters*, 26:1629–1632.

Rowlands, K., Jones, L., and Whitworth, M. (2003). Landslide Laser Scanning: a new look at an old problem. *Quarterly Journal of Engineering Geology and Hydrogeology*, 36(2):155–157.

Rutledge, D., Gnipp, J., and Kramer, J. (2001). Advances in real-time gps deformation monitoring for landslides, volcanoes, and structures. In *Proceedings of the 10th FIG International Symposium on Deformation Measurementsm, Orange, California, March*, pages 19–22.

Sassa, K. and Canuti, P. (2008). *Landslides: disaster risk reduction.* Springer.

Schulz, W. H. (2007). Landslide susceptibility revealed by LiDAR imagery and historical records, Seattle, Washington. *Engineering Geology*, 89(1-2):67–87.

Shepard, M. K., Campbell, B. A., Bulmer, M. H., Farr, T. G., Gaddis, L. R., and Plaut, J. J. (2001). The roughness of natural terrain: A planetary and remote sensing perspective. *J. Geophys. Res.*, 106:–.

Sidle, R. and Ochiai, H. (2006). *Landslides: processes, prediction, and land use*, volume 18. Amer Geophysical Union.

Simons, M. and Rosen, P. (2007). *Treatise on Geophysics - Volume 3 - Geodesy*, chapter Interferometric Synthetic Aperture Radar Geodesy, pages 391–446. Elsevier Press.

Sithole, G. and Vosselman, G. (2001). Filtering of laser altimetry data using a slope adaptive filter. *INTERNATIONAL ARCHIVES OF PHOTOGRAMMETRY REMOTE SENSING AND SPATIAL INFORMATION SCIENCES*, 34(3/W4):203–210.

Sithole, G. and Vosselman, G. (2004). Experimental comparison of filter algorithms for bare-earth extraction from airborne laser scanning point clouds. *ISPRS Journal of Photogrammetry and Remote Sensing*, 59(1-2):85–101.

Smith, K. and Petley, D. (2009). *Environmental Hazards: Assessing Risk and Reducing Disaster.* Routledge.

Sohn, G. and Dowman, I. (2002). Terrain surface reconstruction by the use of tetrahedron model with the mdl criterion. *INTERNATIONAL ARCHIVES OF PHOTOGRAMMETRY REMOTE SENSING AND SPATIAL INFORMATION SCIENCES*, 34(3/A):336–344.

Squarzoni, C., Delacourt, C., and Allemand, P. (2003). Nine years of spatial and temporal evolution of the la valette landslide observed by sar interferometry. *Engineering Geology*, 68(1-2):53–66.

Squarzoni, C., Delacourt, C., and Allemand, P. (2005). Differential single-frequency gps monitoring of the la valette landslide (french alps). *Engineering Geology*, 79(3-4):215–229.

Strozzi, T., Farina, P., Corsini, A., Ambrosi, C., Thüring, M., Zilger, J., A., W., Wegmüller, U., and Werner, C. (2005). Survey and monitoring of landslide displacements by means of L-band satellite SAR interferometry. *Landslides*, 2:193–201.

Tarboton, D. G. (1997). A new method for the determination of flow directions and upslope areas in grid digital elevation models. *Water Resour. Res.*, 33:–.

Tarchi, D., Casagli, N., Fanti, R., Leva, D. D., Luzi, G., Pasuto, A., Pieraccini, M., and Silvano, S. (2003). Landslide monitoring by using ground-based sar interferometry: an example of application to the tessina landslide in italy. *Engineering Geology*, 68(1-2):15–30. TY - JOUR.

Thoma, D. P., Guptab, S. C., Bauerc, M. E., and Kirchoff, C. E. (2005). Airborne laser scanning for riverbank erosion assessment. *Remote Sensing of Environment*, 95:493–501.

Uebayashi, H. (2003). Extrapolation of irregular subsurface structures using the horizontal-to-vertical spectral ratio of long-period microtremors. *Bulletin of the Seismological Society of America*, 93(2):570–582.

Usai, S. (2001). *A New Approach for Long Term Monitoring of Deformations by Differential SAR Interferometry*. PhD thesis, Technical University of Delft.

Vallet, J. and Skaloud, J. (2004). Development and experiences with a fully-digital handheld mapping system operated from helicopter. *The International Archives of the Photogrammetry, Remote Sensing and Spatial Information Sciences*, XXXV(Commission 5):Part B.

Van den Eeckhaut, M., Poesen, J., Verstraeten, G., Vanacker, V., Moeyersons, J., Nyssen, J., Van Beek, L. P. H., and Vandekerckhove, L. (2007). Use of LiDAR-derived images for mapping old landslides under forest. *Earth Surface Processes and Landforms*, 32:754–769.

van Westen, C., Castellanos, E., and Kuriakose, S. (2008). Spatial data for landslide susceptibility, hazard, and vulnerability assessment: An overview. *Engineering Geology*, 102(3-4):112–131.

Vanderbecq, A. (2000). Potentiel de l'interférométrie en zones montagneuses. *DEA Dynamique de la Lithosphere, Grenoble*.

Varnes, D. J. (1978). Slope movements types and processes. In Schuster, R. L. and Krizek, R., editors, *Landslides: Analysis and Control. Special Report 176*, pages 11–33. Transportation Research Board, National Academy of Sciences, Washington, D.C.

Vosselman, G. (2000). Slope based filtering of laser altimetry data. *International Archives of Photogrammetry and Remote Sensing*, 33(B3/2; PART 3):935–942.

Wack, R. and Wimmer, A. (2002). Digital terrain models from airborne laser-scanner data-a grid based approach. *INTERNATIONAL ARCHIVES OF PHOTOGRAMMETRY REMOTE SENSING AND SPATIAL INFORMATION SCIENCES*, 34(3/B):293–296.

Walstra, J., Chandler, J., Dixon, N., and Dijkstra, T. (2004). Time for change–quantifying landslide evolution using historical aerial photographs and modern photogrammetric methods. *International Archives of Photogrammetry and Remote Sensing*, 35(4):474–480.

Wathelet, M., Jongmans, D., and Ohrnberger, M. (2004). Surface-wave inversion using a direct search algorithm and its application to ambient vibration measurements. *Near Surface Geophysics*, 2:211–221.

Webley, P., Bingley, R., Dodson, A., Wadge, G., Waugh, S., and James, I. (2002). Atmospheric water vapour correction to insar surface motion measurements on mountains: results from a dense gps network on mount etna. *Physics and Chemistry of the Earth*, 27(4-5):363–370.

Wegmüller, U., Werner, C., and Strozzi, T. (2003). *Gamma Interferometric Point Target Analysis Software (IPTA): User Guide*. Gamma Remote Sensing.

Wegmüller, U., Werner, C., Strozzi, T., and Wiesmann, A. (2004). Multi-temporal interferometric point target analysis. In *Proceedings of the Second International Workshop on the Analysis of Multi-Temporal Remote Sensing Images: Multitemp 2003, Joint Research Centre, Ispra, Italy, 16-18 July 2003*, page 136. World Scientific Pub Co Inc.

Weirich, F. and Blesius, L. (2007). Comparison of satellite and air photo based landslide susceptibility maps. *Geomorphology*, 87(4):352–364.

Weng, Q. and Quattrochi, D. (2007). *Urban remote sensing*. CRC.

Werner, C., Wegmüller, U., Strozzi, T., Wiesmann, A., Sensing, G., and Muri, S. (2003). Interferometric point target analysis for deformation mapping. *Geoscience and Remote Sensing Symposium, 2003. IGARSS'03. Proceedings. 2003 IEEE International*, 7.

Whitman, D., Zhang, K., Leatherman, S., and Robertson, W. (2003). Airborne laser topographic mapping: Application to hurricane storm surge hazards. *Earth Sciences in the Cities, G. Heiken, R. Fakundiny, and J. Sutter, editors, American Geophysical Union*, pages 363–378.

Zhang, K., Chen, S., Whitman, D., Shyu, M., Yan, J., Zhang, C., et al. (2003). A progressive morphological filter for removing nonground measurements from airborne lidar data. *IEEE Transactions on Geoscience and Remote Sensing*, 41(4):872–882.

Zhang, K. and Whitman, D. (2005). Comparison of three algorithms for filtering airborne lidar data. *Photogrammetric Engineering and Remote Sensing*, 71(3):313–324.

Zogning, A., Ngouanet, C., and Tiafack, O. (2007). The catastrophic geomorphological processes in humid tropical africa: A case study of the recent landslide disasters in cameroon. *Sedimentary Geology*, 199(1-2):13–27.

APPENDIX A

Used Datasets

A.1 IGN aerial photos

- Description: Aerial photos with stereo overlapping
- Dates: 1948, 1956, 1970, 1978, 1985, 2001, 2003
- Source: Institut Geographique National (IGN - `www.ign.fr`)
- Format: Digitised film-positives
- Metadata: see Table A.1
- Spatial extent: N 6428041-6432620 E 908821-912705 Z 483-1168 (RGF93, ellipsoid heights)

year	mission No	mission name	scale	available col/bw
2003	FD 38	department Isere	1/25.000	col
2001	FD 26	department drome	1/25.000	col+bw
1998	FD 38	department Isere	1/25.000	col
1997	F 3336	la mure	1/30.000	bw
1995	F 3235-3240	Grenoble-Sederon	1/30.000	bw
1993	FD 38	department Isere	1/20.000	col+bw
1989	F 3236-3336	la chapelle - la mure	1/30.000	bw
1985	F 3136-3236	le Charpey - la chapelle	1/30.000	bw
1981	IFN 38	Trieves	1/15.000	bw
1978	F 3136-3236	le Charpey - la Chapelle	1/30.000	bw
1970	1959/150 P-IR		1/15.000	bw(pancr. + IR)
1969	F 3236	la Chapelle	1/25.000	bw
1956	F 3234-3237	Grenoble - Mens	1/25.000	bw
1948	F 3234-3237	Grenoble - Mens	1/28.000	bw

Table A.1: Database of Aerial photos available from IGN for the Avignonet-Harmalière study site.

Figure A.1: 1948

Figure A.2: 1956

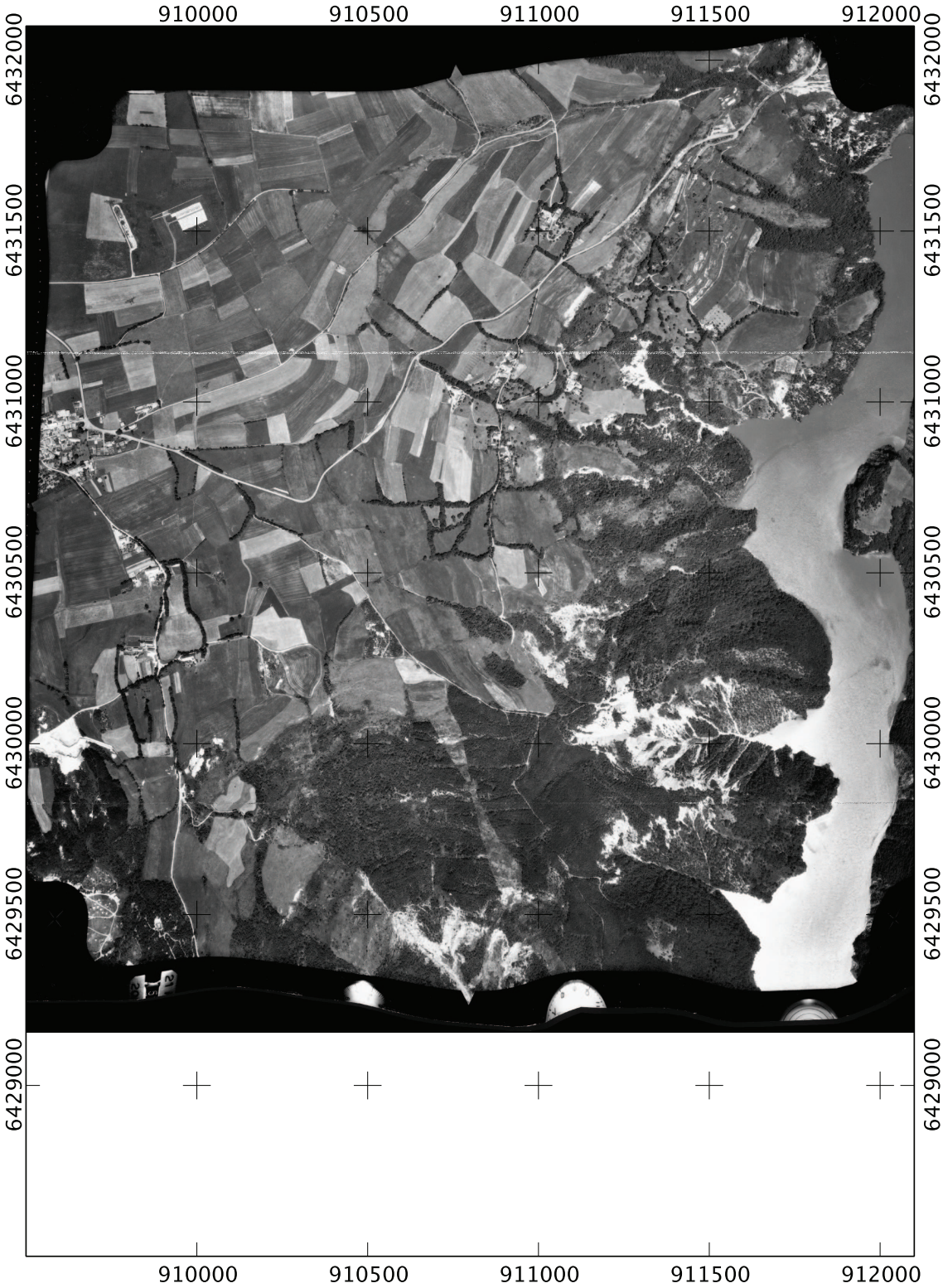

Figure A.3: 1970

Figure A.4: 1978

Figure A.5: 1985

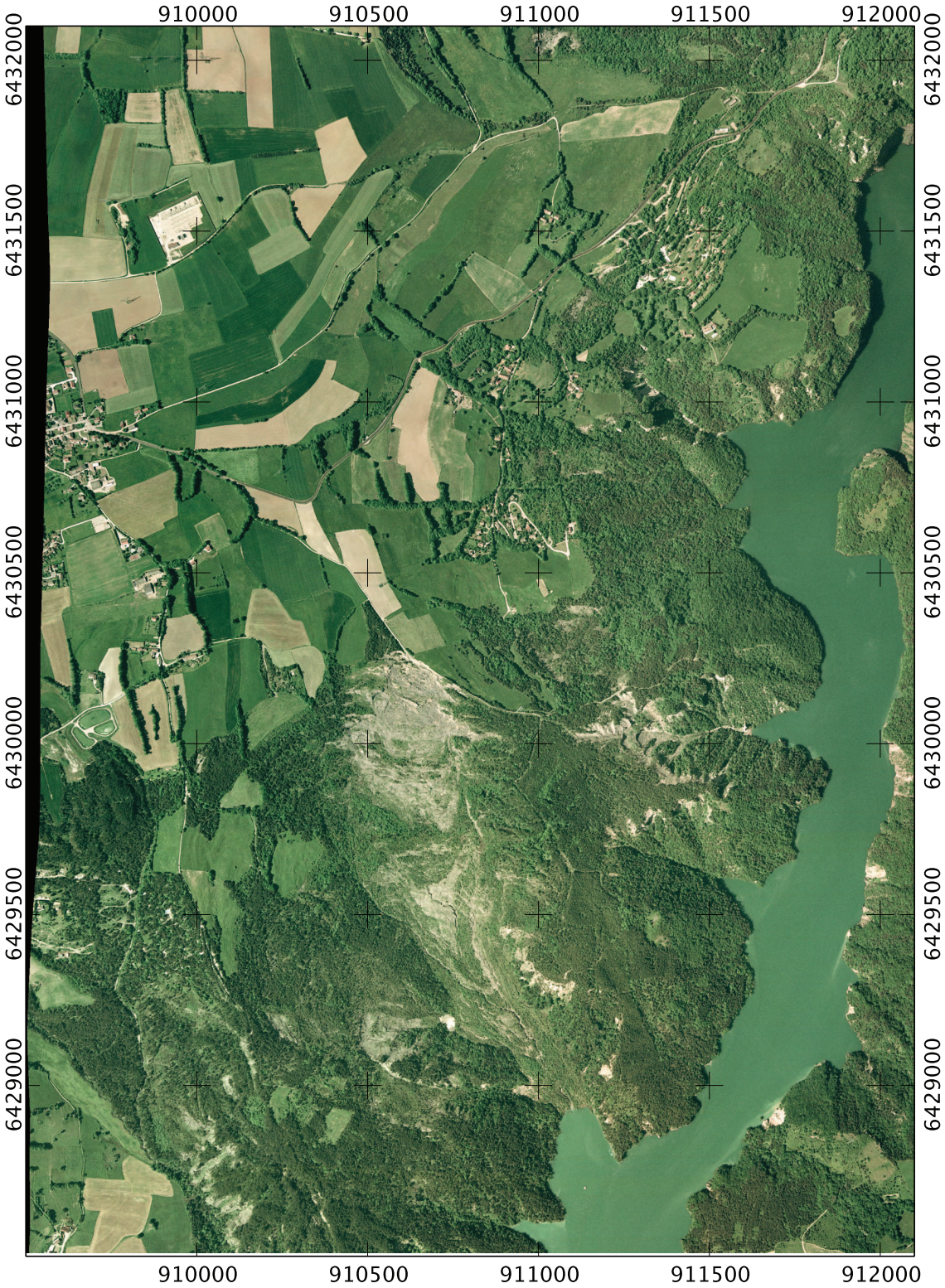

Figure A.6: 2001

Figure A.7: 2003

A.2 Lidar 2006

- Description: Handheld aerial laser scan from helicopter, see Figure 3.13 for an overview
- Date: Nov 2006
- Source: Helimap - `helimap.ch`
- Format: Point-cloud (xyzi)
- Metadata: number of points 36 154 656, last pulse only, average point density 5 pts/m^2
- Spatial extent: N 6428041-6432620 E 908821-912705 Z 483-1168 (RGF93, ellipsoid heights)

A.3 Lidar 2009

- Description: Handheld aerial laser scan from helicopter, see Figure 3.13 for an overview
- Date: Apr 2009
- Source: Sintegra - `www.sintegra.fr`
- Format: Point-cloud (xyzi)
- Metadata: number of points 26 214 244, last pulse only, average point density 5 pts/m^2
- Spatial extent: N 6432415-6428074 E 909516-912326 Z 461-1185 (RGF93, ellipsoid heights)

A.4 IGN 50m DEM

- Description: Elevation data of the Departement Isère
- Source: Institut Geographique National (IGN - `www.ign.fr`)
- Format: DEM (grd and xyz)
- Metadata: resolution 50 m, elevation reference NGF, projection Lambert2/3
- Spatial extent: Departement Isère

A.5 Sintegra GPS points

- Description: GPS campaign points
- Dates: biannual since 1994
- Source: Sintegra - `http://sintegra.fr`)
- Format: Microsoft Excel sheets
- Metadata: local coordinate system, average velocities 1-13 cm/y (see Figure A.9)
- Spatial extent: 30 points at the Avignonet landslide (see Figure A.8)

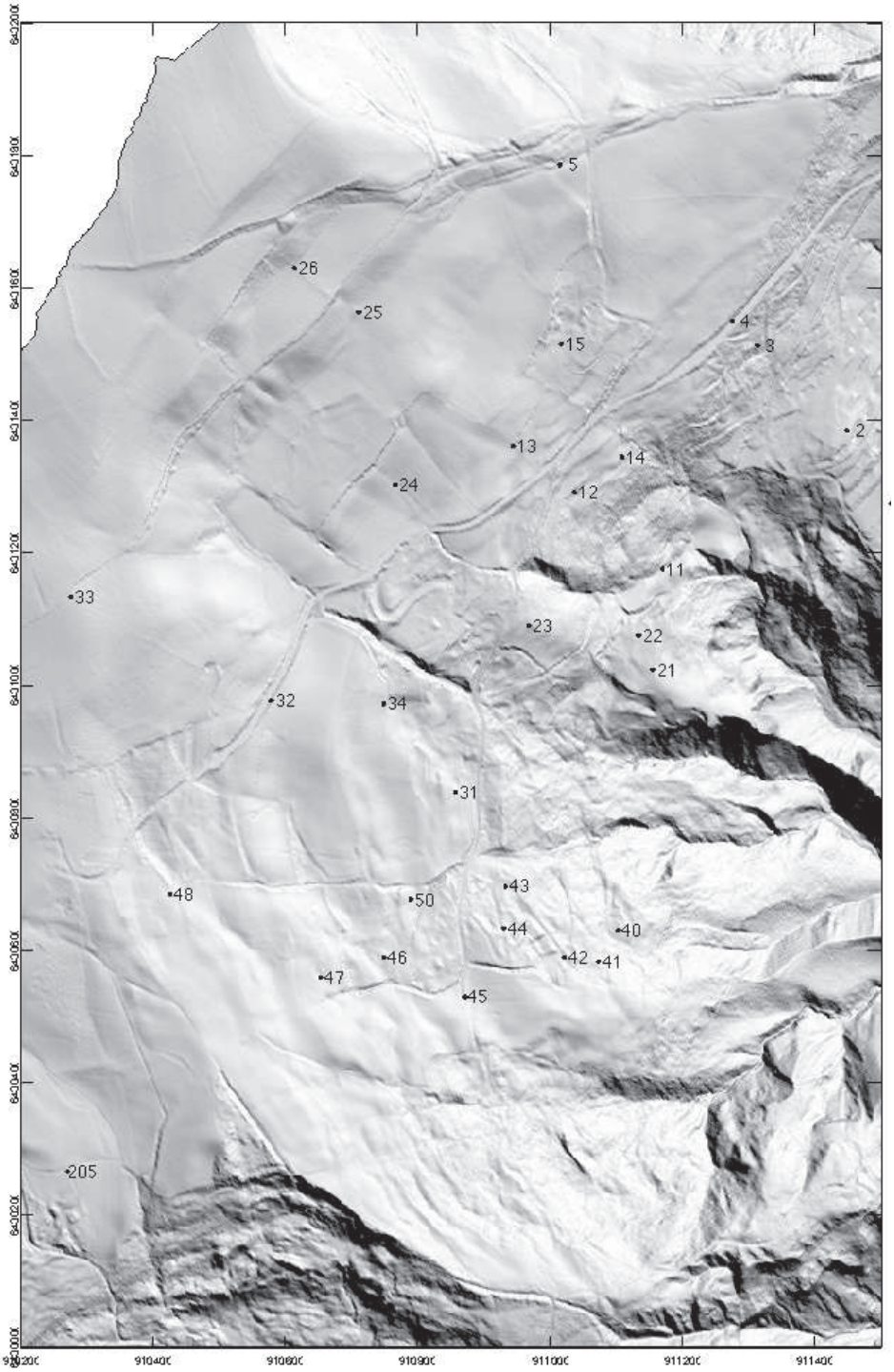

Figure A.8: Sintegra GPS points on the Avignonet landslide

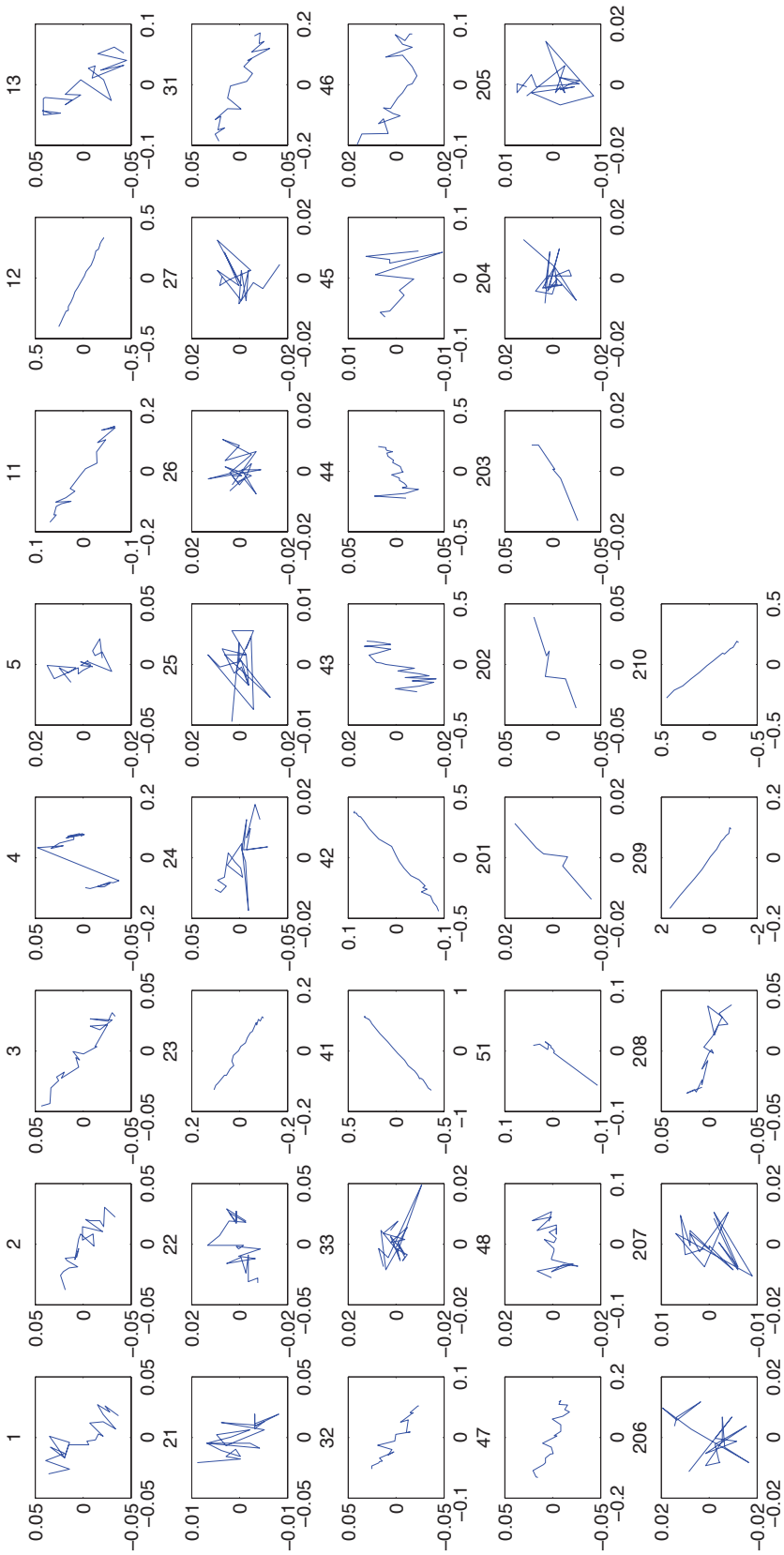

Figure A.9: Displacements horizontal displacements in meter of the Sintegra GPS points on the Avignonet landslide. One line shows the displacement in half a year. Orientation is approx. X = East, Y=North.

APPENDIX B

Coordinate systems and projections

B.1 Geodetic datums

To determine quantitatively a position on earth a referential is needed. One way to do it, is to use a geodetic datum in which geographical coordinates (latitude, longitude) are well defined. A geodetic datum is defined by a set of geodetic points on the earth surface associated with a set of parameters including a reference ellipsoid. Table B.1 lists some geodetic systems commonly used in France with their associated ellipsoids defined by their semi-major axis and semi-minor axis. The reference ellipsoid is a mathematical model aiming to describe the geoid as best as possible as the shape of an oblate spheroid. Because the best fit of this ellipsoid varies if the geoid of the whole earth is taken into account or only a region limited to a country or continent, it exists many different reference ellipsoids that should always be mentioned when using geographical coordinates. The most commonly used is the WGS84-ellipsoid natively used by the Global Positioning System (GPS). Longitudes are usually given relative to the Greenwich meridian, but in older french systems the Paris meridian may be used, which is $2^\circ\,20'\,14.025''$ E of the Greenwich one. Every geographical coordinates of the form latitude, longitude and height can be expressed as cartesian coordinates with its origin in the earth center (the center of the corresponding ellipsoid). Using a seven-parameter-coordinate transformation (Helmert-transformation), coordinates can be switched from one system to another but may contain errors up to several meters. By using local grids of transformation parameters, higher accuracy can be reached. Such transformation grid can be derived from the geodetic points which build up the datums and whose coordinates are known in both systems. According to the software Circé from IGN (Institut Geographique National, France) the accuracy of the transformation from the old NTF system to the new RGF93 system using the grid-transformation is below 5 cm in horizontal and vertical direction.

The elevation can be measured relatively to the reference ellipsoid or to the mean sea-level. Usually coordinates in the NTF system are given in sea-level altitude (which are defined for France in the altimetric system IGN69). In the new RGF93 system elevations are sometimes given as ellipsoid heights (which would be the GRS1980 ellipsoid) and not in sea-level altitude (which is the same in NTF and RGF93). The ellipsoid height lies in average 51.76 m above the altitude in the study area, but is not constant due to dependency of the IGN69 system on the geoid. As seen in Figure B.1 the maximum gradient at the study area is about 5 cm over a distance of 1 km downwards in NW direction. Therefore the difference between the two elevations varies

geodetic system	associated reference ellipsoid	a	b	f
NTF	Clarke 1880 IGN	6378249.2	6356515.0	293.466021
ED50	Hayford 1909	6378388.0	6356911.9	297.000000
WGS84	IAG GRS 1980	6378137.0	6356752.3	298.257222
RGF93	IAG GRS 1980	6378137.0	6356752.3	298.257222

Table B.1: Typical geodetic systems used in France with their associated reference ellipsoids and parameters. a is the semi-major axis, b the semi-minor axis and f the flattening defined by $\frac{a-b}{a}$. NTF: Nouvelle Triangulation Française, ED50: European Datum 1950, WGS84: World Geodetic System 1984, RGF93: Réferentiel Géodésique Français 1993. (data from IGN (2007))

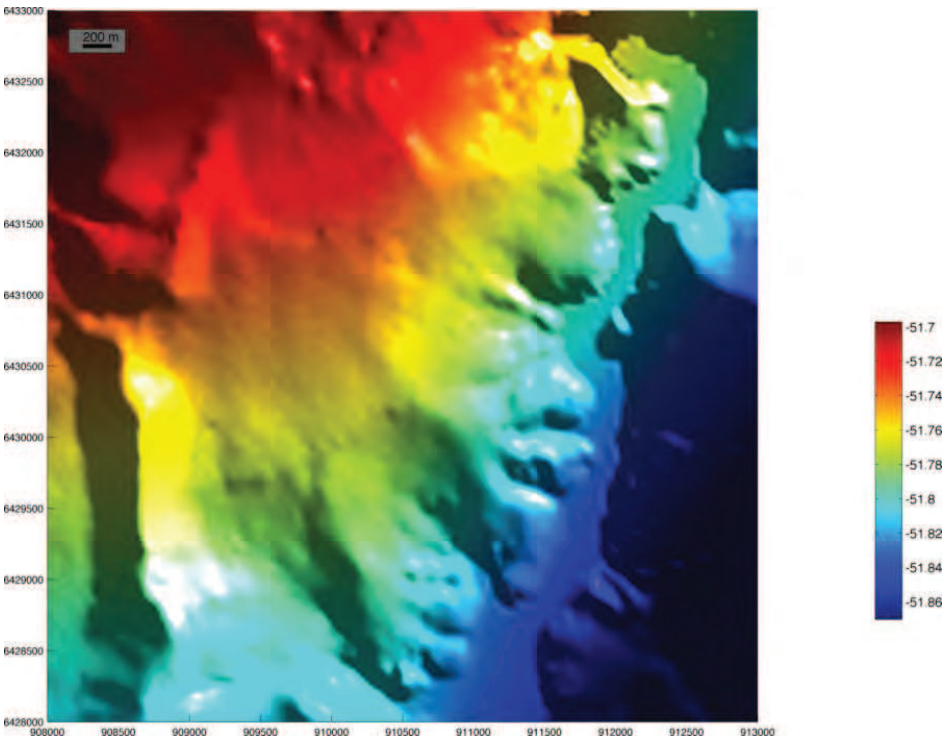

Figure B.1: Difference between ellipsoid height (GRS1980) and sea-level altitude (IGN69) in the study area draped on the shaded relief of the 50 m IGN DEM. The altitude in the study area is $52.76\,m \pm 6\,cm$ below the ellipsoid height. Colorbar is in meter. Coordinates are in meter, in Lambert93 map projection.

between 51.82 m in the South of Harmalière and 51.70 m in the North of Avignonet, which is 12 cm and not always negligible.

B.2 Projections

A map projection defines how the bended earth surface is represented on a 2D-map. Table B.2 lists the main projections used in France. Today Lambert-93 (based on the RGF93 datum) is the official one for national use. It is a single projection valid for the whole of France (without oversea departments).

To project the spherical geographical coordinates on a 2D-plane or map a mathematical transformation is needed that is a map-projection. All projections distort the mapped surface. The "best" projection depends on the region to display and the purpose of the map. Some projections preserve distances, some preserve angles and

projection	system	X0	Y0	ref. meridian	ref. parallel(s)
Lambert I	NTF	600 000 m	200 000 m	0° Paris	49° 30′ N
Lambert II	NTF	600 000 m	200 000 m	0° Paris	46° 48′ N
Lambert III	NTF	600 000 m	200 000 m	0° Paris	44° 06′ N
Lambert IV	NTF	234 358 m	185 861.369 m	0° Paris	42° 09′ 54″ N
Lambert II ext	NTF	600 000 m	2 200 000 m	0° Paris	46° 48′ N
UTM 30/31/32	ED50	500 000 m	0 m	-3°/3°/9° E	0°
UTM 30/31/32	WGS84	500 000 m	0 m	-3°/3°/9° E	0°
Lambert-93	RGF93	700 000 m	6 600 000 m	3° E	44°/49° N

Table B.2: Typical map-projections used in France with their usually associated geodetic systems and parameters. X0 and Y0 are the false easting and northing and the reference median 0° Paris is at 2° 20′ 14.025″ E. Note that the UTM projection is worldwide typically used in WGS84 but can be used with other geodetic systems as well, like ED50 in France. (data from IGN (2007))

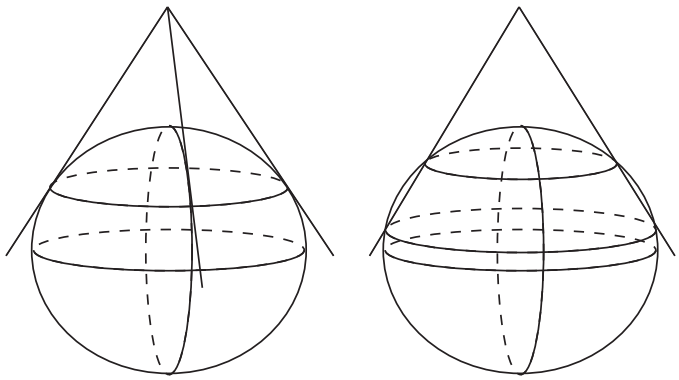

Figure B.2: Lambert conformal conic projection as used for all french Lambert map-projection. (a) shows the tangential version used in Lambert I-IV and Lambert II extended and (b) the secant version used in Lambert-93. (Figure after IGN (2007))

some both. In France, the most commonly used is the Lambert conformal conic (LCC) projection.

As seen in figure B.2 the projection superimposes a cone over the sphere of the Earth. The cone touches the earth only at one reference parallel in the tangent case (a) and intersecting it at two reference parallels in the secant case (b). Along the standard parallels there is no distortion, but it increases further from the parallels. Other usual projections are the cylindrical Universal Transverse Mercator (UTM) projections. It is a system of projections covering systematically the whole globe. France falls into three of them. The Trièves can be covered by either UTM 31 and UTM 32. An overview about the projections used in France is given in table B.2. The official geodetic system in France today is the RGF93 with the linked map-projection Lambert-93. All the different french systems and projections are included in PROJ.4[1] since version 4.4.6.1. PROJ.4 is an open-source software library for geodetic transformations used in several GIS-applications. Also some specialised software utilities for coordinate transformations including CIRCE have been developed by (IGN) (IGN

[1]PROJ.4 - `http://trac.osgeo.org/proj/`

Institut Geographique National, 2006) and are available on their website[2].

For this thesis, all datasets have been transformed into Lambert-93 to be comparable. The projections of the former NTF system covering the Trièves area are "Lambert III" or "Lambert II ext".

[2] lambert93.ign.fr

APPENDIX C

Abstracts of communications

C.1 Subsidence in Grenoble - B. Fruneau 2010

Fruneau, B., Michel, S., Kniess, U., Pathier, E., Cornou, C., Ménard, G., Casagli, N., and Bard, P.-Y. (2010). Subsidence of the grenoble urban area (french alps) from insar and its relationship to basin sedimentary deposits. In *ESA Living Planet Symposium*

We use InSAR time series analysis from ERS1-2 (1993-2000) and ENVISAT (2002-2008) data to estimate subsidence rate of the Grenoble city and its suburbs (more than 400,000 inhabitants) located in the French Alps. About 80 ERS dates and 45 ENVISAT dates have been used applying both Permanent Scatterers and StaMPS approaches. The number of available images and the urbanized land cover allow good quality results. The two approaches gives comparable results. The mean velocity maps are also in agreement with leveling data. Area of maximum of subsidence (2-3mm/year) is located in the middle of the valley. There is no clear correlation with the documented lateral variations of the subsurface deposits (gravel, sand, silt or clays). In contrast, there is a clear correlation between subsidence rate and thickness (that can reach 1 km) of the young sedimentary fill of the Grenoble basin. As, in numerous basins, sediment thickness maps are not well known, this observed correlation opens interesting perspectives to use subsidence rate map as a proxy for thickness map, where conditions are favorable.

C.2 Subsidence in Grenoble - S. Michel 2010

Michel, S., Cornou, C., Pathier, E., Ménard, G., Collombet, M., Knieß, U., and Bard, P.-Y. (21–23 April 2010). May subsidence rate serve as proxy for site effects? In *Seismological Society of America annual meeting*

There is a growing interest to incorporate site effects in seismic hazard estimates (e.g. shaking maps, earthquake scenario, insurance models). The current practice is to use for site classification the average shear-wave velocity in the upper 30 meters (Vs30). As site conditions are usually not known with the appropriate spatial coverage, a growing attention is paid to proxies. Recently, Wald and Allen (2007) proposed to use as a proxy for Vs30 the surface topography: a large slope is related to rock or stiff soil, while a small slope testify of soft soils. Cadet et al. (2008) proposed the use of resonance frequencies with or without information on the shallow shear-wave velocity as an alternative for site classification. Recent studies have shown the ability of INSAR Permanent Scatterer approach to densely map present-day ground motion in urban area with a millimetric precision for relative average annual displacement rate. Except anthropogenic causes (pumping, underground infrastructure), the subsidence is caused by compaction of sediments due to increasing overburden. Since both resonance periods and subsidence rate increase with thickness and softness of soil, both data should be correlated. We test this simple idea on Grenoble city which is located in a valley filled with thick late quaternary deposits and for which all necessary data are available: SAR images, resonance frequencies, bedrock depth, shear-wave velocities, geotechnical and geological drillings, levelling data. Results show that subsidence rates (d), ranging from 0 to -6 mm/year, are linearly correlated with the resonance periods (T) through the following regression law: d (mm/an) = -0.36 T (s) -1. The linear correlation between subsidence rate and bedrock depth together with analysis of geotechnical drillings indicate that subsidence is mostly caused by compaction of the entire sedimentary column.

Abstract

Three remote sensing techniques, Lidar, satellite radar interferometry and aerial photogrammetry are applied to quantify the spatial and temporal evolution of two clayey landslides (Avignonet and Harmalière, located in the Trièves area, French Alps) in complement to in-situ instrumentations. A geomorphological analysis based on Lidar-derived filtered DEM, coupled to analysis of ortho-photos dating back to 1948 and geophysical investigations, shows that the different evolution of the neighbouring landslides could be partly controlled by the paleotopography of the bedrock underlying the clay layer. Directional roughness is shown to help distinguishing between landsliding and gully erosion patterns. Cross-correlation technique adapted to DEMs has been developed to derive 3D-displacement-vectors between two Lidar acquisitions (2006 and 2009), paying attention on measure quality assessment. The displacement map reveals that, at the Harmalière landslide, the main sliding channel, very active from 1981 - 2001, is now relatively slow (< 0.4 m over 3 years), in contrast with four surrounding distinct areas of large movements (up to 3 m) partly with rotational components. At the Avignonet landslide, displacements generally increase towards the toe (up to 1 m near the drainage outlets). Persistent Scatterers Interferometry technique allows to derive new reliable displacement-rates (1992 - 2000) at 16 points of the Avignonet landslide, consistent with GPS time-series. The long-term average headscarp retreat rates are estimated to 1 - 5 cm/y at Avignonet and 7 - 14cm/y at Harmalière. The retreat of the Avignonet landslide seems to be controlled by the erosion of the top of the underlying compacted alluvial layers. The presence of a paleovalley (Drac river) below the Harmalière toe could explain the difference of kinematics between the two landslides.

Résumé

Trois méthodes de télédétection (Lidar, interférométrie radar satellitaire et photogrammétrie aérienne) ont été appliquées pour quantifier les évolutions spatiales et temporelles de deux glissements argileux (Harmalière et Avignonet, situés dans la région du Trièves, Alpes françaises) en complément d'instrumentation in-situ. Une analyse géomorphologique a été réalisée à partir d'ortho-photos (depuis 1948) et du MNT Lidar filtré. Couplée à des reconnaissances géophysiques, elle a montré que la cinématique différente des deux glissements contigus était partiellement contrôlée par la paléotopographie sur laquelle s'est déposée la couche d'argile. La rugosité directionnelle a permis de distinguer les processus d'érosion résultant de mouvements gravitaires et de ravinement. Une technique de corrélation d'images adaptée aux MNT a été développée pour obtenir les vecteurs de déplacement 3D entre deux acquisitions Lidar (2006 - 2009), avec une attention particulière portée à l'évaluation de la qualité des mesures. La carte des déplacements obtenue montre que la zone la plus active du glissement de Harmalière entre 1981 et 2001 est maintenant relativement lente (déplacement < 0.4 m en 3 ans), contrairement à d'autres zones proches montrant des mouvements importants atteignant 3m avec une composante rotationnelle. Pour le glissement d'Avignonet, les déplacements déduits augmentent généralement vers le pied du glissement et peuvent atteindre 1 m. La technique des réflecteurs permanents en interférométrie radar a permis de déterminer de nouvelles valeurs de taux de déplacements (entre 1992 et 2000) en 16 points du glissement, qui sont cohérentes avec les données GPS existantes. Le taux moyen de recul à long terme de l'escarpement principal a été estimé à 1-5 cm/an à Avignonet et entre 7 et 14 cm/an à l'Harmalière. La régression du glissement d'Avignonet semble contrôlée par l'érosion du sommet de la couche d'alluvions compactes reposant sur le substratum. La présence d'une paleovallée du Drac sous le pied du glissement de l'Harmalière pourrait expliquer cette différence de cinématique entre les deux glissements.